Integral Line-of-Sight Guidance and Control of Underactuated Marine Vehicles

Walter Caharija
PhD Candidate, NTNU

A dissertation submitted to the Norwegian University of Science and Technology
for the degree of Doctor of Philosophy

To my parents, Peter and Nadia, and my little sister, Elisabetta, for their support. And to my dear friend Zinajda, for never ever giving up on me.

Summary

This dissertation presents an extensive analysis of the integral line-of-sight (ILOS) guidance method for path following tasks of underactuated marine vessels and vehicles, operating on and below the sea surface. It is shown that thanks to the embedded integral action, the guidance law makes the vessels follow straight lines in presence of environmental disturbances such as currents, wind and waves. The analysis develops linearly with a growth of complexity that spans from simple two and three dimensional (2-3D) kinematic models to full kinematic-dynamic models for surface and underwater vehicles including environmental disturbances of different nature. Furthermore, the problem of steering a vehicle against the ocean current or with the ocean current is addressed as well.

The ILOS guidance is first applied to a simple kinematic model of surface vessels that neglects the vehicle dynamics. It is shown, using simple and intuitive mathematical tools, that current compensation for underactuated surface vessels reduces to a pure vectorial sum and has one possible solution that identifies the only heading the ship can hold to compensate for the drift. The relative velocity of the vessel is kept constant and compensation is achieved through side-slipping. It is proved that path following of straight lines is obtained. A discussion involving intuitive as well as practical aspects of the ILOS law is also given. A 3D version of the same ILOS is then applied to a kinematic model of underactuated underwater vehicles, thus extending the same concepts and the same analysis to 3D.

The following step in complexity consists of including the underactuated dynamics into the Lyapunov analysis of the 2D ILOS guidance law. Disturbances in the form of constant irrotational ocean currents and constant dynamic, attitude dependent, forces are taken into account. The mathematical complexity of the analysis increases significantly compared to the pure kinematic cases, yielding explicit bounds on the guidance law gains to guarantee stability.

Next, the complete kinematic and dynamic closed loop system of the ILOS guidance law for path following purposes of underactuated surface vessels is analyzed. The actuated surge and yaw dynamics are included in the analysis and it is shown that the resulting closed loop system forms a cascade. The properties of uniform global asymptotic stability (UGAS) and uniform local exponential stability (ULES) are shown for the closed loop cascaded system. In this case disturbances in the form of irrotational ocean currents are considered only. Results from simulations and experiments are presented to support and illustrate the theoretical results where the ILOS guidance is applied to the CART vehicle for sea trials.

The possibility of extending the ILOS guidance law proposed for underactuated surface marine vehicles to fully actuated marine vehicles with saturated transverse actuators is analyzed as well. Low-speed path following of straight lines is considered and the proposed solution is inspired by practical issues faced when operating remotely operated vehicles (ROVs) at sea. As a result, a solution combining the ILOS guidance law with a nonlinear bounded sway feedback controller is designed. UGAS and ULES for the origin of the closed loop system are proved and the theoretical results are supported by simulations.

It is furthermore shown that the ILOS guidance law successfully compensates for combined kinematic and dynamic disturbances, thus further extending the previous results. To this end, a 3 degrees-of-freedom (DOFs) maneuvering model for control design purposes that includes both the kinematic and dynamic disturbing effects of currents, wind and waves is presented. The ILOS guidance method is extended with adaptation and it is analytically shown that the resulting control scheme successfully compensates for both kinds of disturbances and hence guarantees path following of underactuated surface vessels in different sea conditions with UGAS and ULES stability properties. The theoretical results are supported by simulations.

The complete kinematic and dynamic closed loop system of the 3D ILOS guidance law is analyzed as well, hence extending the developed analysis to underactuated AUVs for 3D straight-line path following applications in the presence of constant irrotational ocean currents. The closed loop stability analysis concludes UGAS and ULES and gives explicit conditions on the guidance law parameters. The proposed 3D ILOS guidance control scheme is applied to the LAUV autonomous underwater vehicle and results from simulations and sea trials are shown to support the theoretical findings.

This dissertation addresses the problem of steering a marine vessel against the ocean current or with the ocean current as well and hence two guidance laws for counter-current and co-current guidance of underactuated marine vehicles in 3-DOFs are presented. The guidance laws are based on the relation between the relative and absolute velocities and show different stability properties: local exponential stability (LES) for the first and uniform semiglobal exponential stability (USES) for the second. In both the cases the closed loop system reveals multiple stable/unstable equilibrium points, corresponding to the counter-current/co-current directions depending on the setting. Simulation results support the theoretical findings.

Preface

This thesis is submitted in partial fulfillment of the requirements for the degree of Doctor of Philosophy (PhD) at the Norwegian University of Science and Technology (NTNU).

The presented work has been carried out at the Department of Engineering Cybernetics and the Center for Autonomous Marine Operations and Systems (AMOS) at NTNU, in the period from January 2011 to June 2014, under the supervision of Professor Kristin Ytterstad Pettersen of the Department of Engineering Cybernetics. Professor Jan Tommy Gravdahl (Dept. of Eng. Cybernetics, NTNU), Professor Asgeir Johan Sørensen (Dept. of Marine Technology, NTNU) and PhD Even Børhaug (Kongsberg Maritime AS - Horten) were appointed as co-advisors. Financial support has been provided by the Research Council of Norway though the Center of Excellence funding scheme and the Strategic University Program.

Acknowledgments

As I am writing these very last lines of my dissertation almost four years have passed since my first meeting, then a job interview, with Prof. Kristin Y. Pettersen. Shortly after that meeting I was offered of a PhD position at the Dept. of Eng. Cybernetics under her supervision. I read the proposal with a bittersweet mix of satisfaction and apprehension since I knew that it implied a significant decision from my side. The dilemma was: hold on to a safe job and a familiar environment or move to Norway and accept a new challenge that meant working on something new, quite far from my own educational background. Instinct said the latter was the thing to do, and I followed it, bold and confident that someway, somehow I would make it.

Now, four years later, I do not regret that decision and Kristin has been a great supervisor. She believed in me, guided me through ups and downs and supported all the key ideas and projects I worked on during the course of my PhD and that are now part of this dissertation. Her combination of giving the example and believing in my own skills has payed off and pushed me to give my best. She has given me the chance to grow professionally and personally, and she kept commenting my papers and helped me even when other issues, far more serious, required her attention. This is something I will never forget!

I will always remember my co-advisor Prof. Jan Tommy Gravdahl for his optimism and his “Go for it!” sentence he would pronounce every time we were about to publish some results. I had a great time in Australia with him and his family, and during the pizza dinner they later organized here in Trondheim with Kristin and all their PhD students. Last but not least, I have to sincerely thank him for keeping track of my work in unfortunate circumstances that then however turned out for the best.

As this adventure approaches its end I wonder whether I will ever have the chance to work again with anyone as committed and fair as my co-advisor Prof. Asgeir J. Sørensen. I honestly doubt it. From every meeting I had with him there is always an advice or sentence I remember. Wise words that helped me to hold the balance on the thin edge between my deep hunger for challenges and ambitions, and the reality of accomplishing a PhD. I am sure this is a valuable experience I will carry on to the next challenge.

I would also like to thank my co-advisor PhD Even Børhaug from Kongsberg Maritime AS. His precious doctoral thesis represented the starting point of my PhD and his advice was very valuable. Furthermore, I enjoyed the visit in Horten where I could see the HUGIN AUV in operation.

During these three and a half years I had the pleasure to work with very clever and motivated researchers from NTNU and other institutions. Often, what started as a professional relation developed into a genuine friendship. Therefore I would like to thank Milan Milovanović (Rolls Royce Marine AS), Signe Moe (NTNU, ITK), Esten Ingar Grøtli (Sintef IKT) and Mauro Candeloro (NTNU, IMT).

I often relied on the expertise and skills of external institutions to test our guidance algorithms. In particular, I had the unique opportunity to work with two excellent research groups: the LSTS Laboratory of the University of Porto, Portugal and the CNR-ISSIA Institute in Genova, Italy. Therefore, I would like to express my gratitude to Pedro Calado, José Braga and João B. Sousa from LSTS for giving me the opportunity of testing the ILOS algorithm on their LAUV vehicle. I am also very grateful to Marco Bibuli, Enrica Zereik, Gabriele Bruzzone and Massimo Caccia from CNR-ISSIA for making it possible in a very short time to successfully test the ILOS algorithm on their CART vehicle in Murter, Croatia. It has been a great experience to work with all of you!

My co-advisor Asgeir J. Sørensen once told me: "Your best advisor is often another PhD student". He was so right and I was so lucky to have colleagues and friends around who supported me and with whom I could share opinions, experiences and ideas. Hence, I would like thank Giancarlo Marafioti, Anders Fougner, Francesco Scibilia, Christian Holden, Morten Breivik, Johannes Tjønnås, Øyvind N. Stamnes and Luca Pivano, all former ITK PhD students. From the current generation of ITK - IMT PhD students I would like to express my gratitude to Eleni Kelasidi, Anne Mai Ersdal, Bjarne Grimstad, Ulrik Jørgensen, Øivind K. Kjerstad, Christoph J. Backi, Lorenzo Fusini, Aleksander Veksler, Serge Gale, Sergey Kolyubin, Anders Willersrud, Parsa Rahmanpour, Ehsan Rezapour, Andres C. Duarte, Hodjat Rahmati, Øyvind F. Auestad, Daniel de A. Fernandes, Tor Aksel N. Heirung, Morten D. Pedersen and Brage R. Knudsen. We had some wonderful time together and I wish you good luck for accomplishing your own PhDs.

To successfully lead and administrate a department like ours is no easy task. No doubt that Morten Breivik, Tove K. B. Johnsen, Unni Johansen, Bente S. Lindquist, Eva L. Amdahl and Janne K. Hagen hold most of the credit for this. Thanks a lot to all of you!

How to forget cageball: thanks to Stefano Bertelli and Torkel Hansen for organizing the epic cageball tournaments every given Friday! Given my poor technical football skills and my aggressive, hard tackling playing style, I am not sure how much you will actually miss me... Moreover, as an active member, I wish to thank the NTNUI Svømmegruppa - Swimming Team for the great time together, the intense training sessions and the unforgettable parties!

Last but not least, I would like to thank my entire family and my closer friends for their support and encouragement during my doctoral studies that kept me away from home for such a long time.

`Walter Caharija, June 2014`

Contents

List of Figures

List of Tables

Chapter 1.

Introduction

"Effort and hard work build a bridge between dreams and reality."
— Roberto Baggio, Football Player

This thesis presents an extensive analysis of an Integral Line-of-Sight (ILOS) guidance and control method for path following purposes of marine vehicles. The very first part of the dissertation is meant to give a proper perspective for the presented work motivated by the ongoing research in the field of marine control systems. In addition it recalls the major improvements in this area witnessed by the last decades. The contribution of this work is then framed within the described context.

1.1. Background and Motivation

1.1.1. Motivation

Sailors, seamen, and naval architects have faced challenges represented by wind, waves and sea currents since the early days of coastal navigation, world exploration and merchant shipping. The unavoidable occurrence of dealing with heavy seas and the need to guarantee ship maneuverability as well as safety of the crew on board has lead to improved vessel hulls, smarter navigation techniques and better meteorological/oceanographic forecasts. Environmental forces and disturbances such as ocean currents, wind and waves that affect ships, offshore structures and coastal installations are often referred to as sea loads

[50] and their effect can significantly undermine maritime activities and pose serious threats to the people involved.

Many of the areas that are of interest for ship traffic, fishing and oil and gas operations are characterized by hostile environmental conditions. For instance, storms regularly hit the North Sea and the North Atlantic, whereas hurricanes are more and more often disrupting the activities in the Gulf of Mexico. Moreover, given the shrinking of the arctic icecap and the consequent opening of the Northern Sea Route, new challenges are arising and are setting higher safety and robustness standards for ships and maritime activities. As a response to these challenges, the last decades have witnessed substantial improvements in naval engineering, marine propulsion, navigation techniques and automation. It is an ongoing activity and the technological development is today focusing on automation and integration of on-board systems and operations at sea. This trend is well established worldwide since any improvements in these fields can significantly improve safety, sustainability and effectiveness of activities such as offshore hydrocarbon production and exploration, shipping, fishing, offshore wind power production and environmental monitoring. Given the world's increasing demand for energy and food, the offshore oil and gas industry has positioned itself at the forefront of this trend [101] but other activities are following close.

Today the shipping industry relies more and more on heavily automated container carriers, crude carriers and other merchant vessels. Moreover, drilling rigs, supply vessels, anchor handling vessels and floating production units involved in offshore operations are often fitted with state of the art control systems to help the crew handle a wide set of operations in different sea states. It is also seen that automation helps reduce cost and risk since less people performing dangerous jobs are needed on board. This is becoming a key factor for other industries as well. For example, reducing the need for manned maintenance operations may determine the economical success of offshore wind farms and floating wind turbines [102].

The origin of automation on board regular manned vessels dates back to the 19th century with the introduction of the steam engine and and the propeller. A steam engine was first mounted on a boat by Scottish engineer William Symington in 1802 in Glasgow, Scotland, while the propeller was first invented and tested by Czech inventor Josef Ressel in 1829 in Trieste, then Austrian Empire. But the real waves of marine control had yet to come: in 1911 a gyro-compass was installed on-board of a US war ship by entrepreneur Elmer Sperry. Sperry was then able to design a ship autopilot. Unaware of this development, Russian-born engineer Nicolas Minorsky published his famous first theoretical analysis of a PID controller in 1922 after installing an automatic steering device on-board the battleship *USS New Mexico*. Hence, the theoretical and practical foundations for the successful application of ship autopilots in the following years were laid [16]. Today every commercial ship is fitted with advanced autopilots, GPS based navigation systems, speed controllers and radar systems, and the development continues.

Recently, unmanned marine vehicles have been introduced. Unmanned vehicles make it possible to operate in otherwise hazardous and unaccessible areas for humans, for instance in deep waters or under the ice. The remotely operated vehicles (ROVs) for underwater operations were first introduced by the US Navy in the 1970s and by the 1980s ROVs were essential for the offshore oil and gas industry when the developed fields exceeded the reach of human divers. Soon, other classes of vehicles, unattached to the mothership and hence providing limited or even no human interaction, showed up: the unmanned surface vessels (USVs) and the autonomous underwater vehicles (AUVs). USVs and AUVs require a higher level of autonomy since they must be capable of accomplishing tasks on their own, independently. At first, USVs and AUVs were used for a few number of tasks, often limited to scientific or military purposes. Today, with the development of more advanced processing capabilities and high yield power supplies, USVs and AUVs are employed more and more often in civilian applications with roles and missions constantly evolving.

Although ROVs today represent the core platform for deep-water activities, AUVs are becoming more popular and are starting to replace ROVs in activities such as search and rescue, surveying and pipeline inspection [119]. The trend is expected to last since AUVs are unattached, work independently of the ship and can collect geo-referenced data. Moreover, AUVs can perform repeatable pre-planned operations regardless of the conditions on the surface and their inspection speed is often higher than 2 [knots], which gives high coverage rates [67].

The unmanned USVs are also experiencing a significant development phase, since their applications appear not to be limited to scientific or military purposes anymore. For instance, [22] demonstrates that cooperating USVs can perform emergency ship towing operations in the open sea or in a confined harbor, while [84] presents an innovative approach for search and rescue operations where a USV is used to retrieve overboard personnel. Furthermore, the joint use of Unmanned Surface and Aerial Vehicles (USVs and UAVs) and AUVs shows very promising results and tools to successfully run different integrated missions are available [115].

1.1.2. Underactuated Marine Vessels

Most marine surface vessels are underactuated since cost, design simplicity, low energy consumption, robustness and cargo capacity are often the driving factors considered by naval architects. In particular, they are equipped with fixed stern propellers and steering rudders, or alternatively with azimuth thrusters only. Even when tunnel thrusters are installed, such actuators are effective exclusively at low maneuvering speeds [78]. As a result, the absence of actuation in sway poses significant challenges on the control system design side in path following and trajectory tracking scenarios, especially when the vessel is subject to disturbances acting in the underactuated transverse direction.

Similar arguments apply to underwater vehicles: in general, design simplicity is preferred to minimize energy consumption and guarantee robustness, hence most existing AUVs are torpedo shaped and underactuated. In particular, they are equipped with stern propellers, steering rudders and diving rudders only [68, 40, 69]. Although providing design simplicity, the absence of actuation in sway and heave poses significant challenges on the control system design side. Furthermore, unmanned underwater vehicles operate in challenging environments where sea currents significantly affect their speed and maneuverability. As a result, an efficient and reliable compensation strategy is required to reduce the impact of currents on underwater activities.

1.1.3. Path Following Control of Marine Vessels

Whether on the surface or under the surface, many offshore activities involve path following tasks of marine vessels. Path following is a motion control scenario where a vessel or underwater vehicle has to follow a predefined path without any time constraints. Therefore, path following problems differ from trajectory tracking, since there the goal is to track a time varying reference trajectory. See [47, 1, 39, 52] for a discussion on the fundamental differences between different motion control scenarios. Path following is indeed a very wide concept that covers, among others, applications of wheeled mobile robots, marine vehicles and aerial vehicles (see for instance [128, 13, 127, 135]).

A review of different approaches to path following and other control problems of marine vehicles and vessels is given in [9, 108] where both linear and nonlinear control strategies are used. Since the dynamics of marine vehicles are inherently nonlinear, classic linear approaches lead to local results while the use of nonlinear techniques may yield global results. Also, linear approximations of the underactuated marine vessels are typically not controllable in all degrees of freedom, while the physical systems indeed are controllable. This makes control approaches based on nonlinear models attractive and recent research focuses on taking into account the dominating nonlinear behavior. For instance, fully actuated surface vessel are considered in [53] where a backstepping controller that takes into account the actuator dynamics is introduced for trajectory tracking purposes. In [70] a passivity based controller is developed to make fully actuated ships follow parametrized paths while path following of fully actuated ships in presence of parameter uncertainties is addressed in [81]. Finally, a Jacobian task priority-based approach for path following purposes is introduced in [137].

A class of underactuated surface vessel described by a 3 Degrees-of-Freedom (DOFs) nonlinear model is considered in [61] where a path following controller is designed with the simplifying assumption of diagonal inertia and damping matrices. The output space is reduced from 3-DOFs to 2-DOFs where the heading of the vessel is left uncontrolled. A controller is then developed to make the vessel follow straight and circular paths with global exponential stability properties of the origin of the closed loop system. Finally, boundedness is shown for the zero dynamics represented by the sway velocity and the yaw rate. This procedure reduces the output space so that its dimension corresponds to the dimension of the control input space, thus obtaining a reduced-state stabilization problem.

The work of [111] presents one of the first solutions to the full-state stabilization problem of underactuated 3-DOFs surface vessels. In [111], the controllers are designed to make the vessel follow a 2-Dimensional (2D) path as well as to stabilize the heading dynamics. The proposed control strategy however can be applied only to paths having non-zero curvature and global exponential stability is only achieved under the condition that the commanded yaw rate is Persistently Exciting (PE). This restricts the type of paths that can be followed. The stringent conditions of [111] are relaxed in [112] and extended to trajectory tracking in [89] where the the tracking error dynamics are shown to hold exponential stability properties. Motivated by [111], [74] and [72] present a path following control solution for a 3-DOFs underactuated marine vehicle required to follow a straight line. Assuming that the vessel holds a constant and positive surge speed and that the system matrices are diagonal, the proposed controller sets the yaw rate and guarantees global asymptotic stability of the origin of the closed loop system, including the geometrical errors, the heading and the sway velocity. These results are extended to underactuated underwater vehicles for path following of 3D curves in [75]. Furthermore, in

[4] and [5] position control of underactuated underwater vehicles is considered and a vector field is defined such that a virtual fully actuated vehicle would exponentially converge to the desired configuration. Afterwards, a steering law for the underactuated vessel is derived. Notice that the approach of [4] and [5] considers a pure kinematic unicycle-like model of the vehicle. The Lyapunov direct method and backstepping techniques are exploited for full-state stabilization problems of underactuated 3-DOFs surface vessels for tracking and path following scenarios in [44], [41] and [92]. In [44] the stringent conditions of [111] are again relaxed while [41] proposes a unified framework for tracking problems and in [92] a feedback dominance backstepping technique is implemented showing improved robustness with respect to model uncertainties. These three methods have however the limitation of considering the matrices of the system dynamics diagonal.

Stabilizing all the DOFs of an underactuated vehicle using a single controller is an ambitious and powerful approach since it gives complete control over the vehicle. It may however restrict the type of paths that can be followed, as discussed above. Moreover, the full state stabilization approach often leads to extensive mathematical analysis and to complex control laws lacking of clear physical interpretations. For this reason, reduced-state stabilization control approaches, where only the actuated subset of the degrees of freedom is directly stabilized, are sometimes preferred. For instance, exploiting the results of [121] and [98], [48] proposes a nonlinear controller for 2D path following tasks of 3-DOFs underactuated marine vehicles. The controller is designed to stabilize only a reduced subset of the DOFs but the zero dynamics are shown to remain well behaved. The work of [48] is further developed in [46] and [87], where 3D and 2D path following of underactuated underwater vehicles is considered. In the work of [87] a virtual target that the vehicle has to follow is introduced and the initial position of the vehicle is not restricted to lie inside a tube centered on the path, which was the major shortcoming of [48]. Along the same line of research, a hybrid adaptation scheme is used in [86] to increase robustness with respect to uncertainties of the vessel model. Path following problems of underactuated marine vehicles are also addressed in [1] where switching supervisory control is implemented with parametric model uncertainties. This control strategy is inspired by [123] where maneuvering control for a class of nonlinear systems is considered.

This dissertation focuses on the nonlinear Line-of-Sight (LOS) guidance principle. The nonlinear LOS law is widely used to solve practical path following problems of marine vehicles due to its simplicity and intuitiveness: it imitates a helmsman steering the vessel toward a point lying at a constant distance ahead of the ship along the desired path. In particular, it is used in [107, 66, 110, 54, 17, 58] for path following control in 2D of fully actuated as well as underactuated ships. In [54] the LOS guidance law is combined with a heading controller for path following control purposes of 3-DOFs underactuated surface vessels. Although the heading controller is shown to track the reference LOS heading with asymptotic convergence properties, the zero dynamics and the cross-track error dynamics are not analyzed. The proposed controllers are however tested on a model ship. The work of [54] is further developed in [17] and extended to 3D path following scenarios in [21] and [18]. The complete kinematic/dynamic closed loop behavior of a LOS guidance system is analyzed in detail with a full state approach in [58] where explicit stability conditions upon the guidance law parameters are given. The preliminary results of [58] are validated with experiments in [59] and the work presented in [59] can be seen as an extension of [110]. The LOS guidance is used in [27] and [25] for 3D path following control of underactuated underwater vehicles where a full-state stabilization approach is followed to show stability. In [24] formation control and path following of underactuated marine surface vessels is considered where each ship is equipped with a LOS reference generator. The idea of employing a time varying look-ahead distance is mentioned in [23] and developed in [90], without however analyzing the underactuated sway dynamics. Notice that most of the contributions listed so far do not consider environmental disturbances.

Environmental disturbances such as currents, wind and waves have significant effects on marine operations and constant irrotational ocean currents represent a widely accepted model for slowly varying disturbances [52, 51]. Observers as well as adaptive techniques are widely used to compensate for the drift. For instance, in [7] an adaptive law is introduced to add robustness with respect to unknown ocean currents in tracking scenarios of underwater vehicles, while in [99] a current estimator is integrated into a sensor based navigation filter for AUVs. Currents are considered in [49] where disturbance estimators are added to guarantee 2D path following of underactuated surface vessels. Adaptive techniques are applied to compensate for ocean currents in [43] to obtain path following of underactuated AUVs. Position feedback and integral action are used in [45] to achieve path following in presence of constant disturbances. In [6] adaptive/integral action is introduced to control the AUV in 6-DOFs and add robustness with respect to ocean currents and model uncertainties. In [113] it is shown that a least-squares planar path following technique guarantees some robustness with respect to ocean currents as well. To render the LOS guidance robust with respect to ocean currents, [2] proposes a modification based on measurements of the AUV velocity, while [10] suggests to directly control the relative velocity of the vehicle and to estimate the necessary side-slip angle.

Both the contributions refer to planar motion. Planar motion is also considered in [26, 19] where integral action is added to the LOS reference generator to compensate for ocean currents without the need for velocity measurements nor disturbance estimators. In [19] the possibility of spatial and temporal integral effects is mentioned, while [26] shows convergence with an extensive mathematical full-state stabilization approach since absolute velocities as well as relative velocities are present in the system dynamics, forcing the introduction of adaptive techniques, and thus increasing complexity and weakening stability. Course control and integral action are added to the LOS of [90] in [91] and a reduced-state stabilization approach is followed, without however analyzing the underactuated sway dynamics of the ship.

1.1.4. Bounded Control Problems

The path following control problem addressed in Chapter 7 of this thesis is in part a bounded control problem since some saturation constraints are taken into account. Actuator saturation and other constraints on control inputs lead to bounded control problems. The main purpose of bounded control is to stabilize closed loop systems with bounded feedback controllers. Backstepping methods with bounded feedbacks have been developed: the nested saturation control laws proposed in [133] are exploited by [134] and [60] while Lyapunov-based design is used in [97]. The results from [97] are extended to time-varying systems in [96]. The extension to time-varying systems is applied to aircraft control in [63].

1.1.5. Counter Current and Co-Current Guidance

In this thesis the problem of steering a marine vessel against the ocean current or with the ocean current is addressed as well. This is indeed an interesting problem since an autonomous marine vehicle capable of sensing the current and follow the flow could exploit the drift when exact positioning is not as critical as energy efficiency, as shown in [124, 125, 79]. In fact, such a guidance law makes the vehicle determine the direction that guarantees the minimum energy consumption for a given absolute speed. Moreover, an underwater vehicle that can turn against the flow could, for instance, help locate a hydrothermal vent [136, 77] or detect hydrocarbon leaks from subsea oil and gas installations. Furthermore, a control law for counter-current guidance can be integrated into more complex Weather Optimal Heading/Positioning Control systems (WOHC-

WOPC) since it is meant to steer the vessel against the disturbance. The WOHC and WOPC concepts are thoroughly defined by [57] where a pendulum analogy is introduced and the ship is forced to move along a circular path until the optimal position and orientation to face the unknown environmental forces are determined. In [57] nonlinear adaptive backstepping is used to design the WOPC system. Alternatively, [114] obtain WOPC for large tankers with PID feedback controllers where only derivative action is used in the heading autopilot. Finally, a novel implementation of WOHC and WOPC is proposed in [83] for fully actuated as well as underactuated vessels.

1.1.6. Mathematical Modeling of Marine Vessels

In this thesis a set of mathematical models of surface vessels and underwater vehicles are defined for control design purposes. Mathematical descriptions of marine vessels in the form of point-mass models are powerful tools to design, test and simulate complex marine control systems. Accurate models, increasing computational power, better simulation tools and the introduction of Hardware-in-the-Loop (HIL) simulators reduce the developing time and the risk for incidents [131, 132].

Mathematical modeling of marine systems and vessels is a multidisciplinary field and depending on the operational conditions models can be classified into low velocity/station keeping or high velocity/maneuvering models [52]. Models are also classified according to their purpose and complexity. In particular, [130, 117] define two classes of mathematical models: the process plant models and the control plant models. A process plant model is a comprehensive description of the actual vessel. Its main purpose is to simulate the vessel dynamics with a high degree of accuracy and it often includes noise effects, disturbances, sensor responses and actuator dynamics. The process plant model is mostly used to assess the robustness and the performance of the control systems. A control plant model represents a simplified mathematical description of the vessel. It is meant for control design purposes and therefore it includes only the main physical properties of the vehicle. Notice that the control plant model may also be part of the designed controller. The control plant model is used in analytical stability analysis, such as the Lyapuonv analysis, as well. Since accurate models of the vessel dynamics are not always available or suffer from high parameter uncertainties, control plant models are often used as process plant models. In these cases a critical approach towards the results obtained from simulations becomes fundamental.

1.2. Contributions and Scope of This Thesis

This dissertation focuses on the Integral Line-of-Sight solution for motion control of marine vehicles in the presence of environmental disturbances and therefore its main contributions are related to path following of straight lines. However, some of the obtained results closely relate to bounded control and modeling of marine crafts. Furthermore, the problem of steering a vehicle against the ocean current or with the ocean current is addressed as well.

1.2.1. Mathematical Modeling of Marine Vessels

A class of maneuvering control plant models that include the main disturbing effects of the environmental forces at sea are developed in Chapter 2 to design and analyze robust guidance systems. The presented control plant models describe the effects of the environmental disturbances as a constant irrotational ocean current [52] where an additional dynamic bias term is sometimes added to include heading dependent disturbances and model uncertainties. The fact that the unknown ocean current is assumed constant and irrotational makes it possible to define the presented models in terms of the relative velocity vector. Moreover, as done in [23], a translation of the equations of motion is introduced to remove the effect of the yaw control on the sway dynamics for the 3-DOFs maneuvering models. An analogous translation of the equations of motion for the 5-DOFs maneuvering models is used to remove the effects of the pitch and yaw control terms on the heave and sway dynamics. Such transformations, inspired by [42] and further developed [59], are useful in underactuated control design for surface vessels and underwater vehicles

1.2.2. The ILOS Guidance Law for Path Following Control of Underactuated Marine Vessels

This thesis aims to improve, revisit, extend and validate the ILOS guidance law first presented in [26]. In particular, [67, 52] show that the vessel model can be redefined in terms of its relative velocity vector in presence of constant irrotational ocean currents. This property is used in this thesis and it is shown that it leads to a simpler control system with stronger stability properties compared to [26]. Planar motion of underactuated marine vessels is considered first and the ILOS guidance is then extended to 3D path following of underactuated underwater vehicles with similar theoretical results. Furthermore, the ILOS guidance is shown to be robust with respect to disturbances in the underactuated sway/heave directions. This property is exploited in two occasions: first, it is proved that the ILOS control scheme can successfully handle combined kinematic and dynamic disturbances. Second, it is shown that the ILOS guidance can be extended to fully actuated marine vehicles with saturated transverse actuators. Finally, the theoretical results are validated with extensive simulations and full scale sea trials using underactuated unmanned surface and underwater vehicles.

In this dissertation the ILOS guidance law is first studied in a kinematic perspective in Chapters 3 and 4, and the level of complexity is gradually increased by adding the underactuated dynamics in Chapter 5. Both the underactuated/actuated dynamics are added in Chapters 6, 8 and 9 to analyze the complete problems of underactuated vehicles subject to environmental disturbances in 3-DOFs and 5-DOFs. Notice that the problems solved in Chapters 6, 8 and 9 follow along the line of research set by [110, 59, 25, 26] and represent full-state stabilization problems where stability is shown for both the actuated as well as the underactuated dynamics. Lyapunov theory [82], elements of robust control [57] and control of nonlinear systems in cascaded form [105, 104] are used in the proofs.

A Kinematic Approach to Current Compensation and the ILOS Guidance Law

The ILOS guidance for planar motion from [26] is applied to a simple kinematic model of a vessel in Chapter 3. It is shown, using simple and intuitive mathematical tools, that current compensation for underactuated surface vessels reduces to a vectorial sum and has one possible solution that identifies the only heading the ship can hold to side-slip and compensate for the drift. The relative velocity of the vessel is kept constant and compensation is achieved through side-slipping. Path following of straight lines is obtained. It is furthermore shown that the ILOS guidance law executes the sum between the relative velocity of the vehicle and the ocean current velocity to compensate for the drift. This provides a useful practical explanation of the role that the integral term plays in the guidance law. This kinematic approach is similar to [3, 71] where the well known unicycle model is used, or to [100] where steering of miniature air vehicles is considered.

In Chapter 4 a 3D version of the same ILOS guidance system is presented and applied to a kinematic model of underactuated underwater vehicles. Path following of straight lines is considered and the explanation follows along the lines of Chapter 3. In particular, it is shown that current compensation for underactuated underwater vehicle reduces to a 3D vectorial sum that has one possible solution. This solution identifies the only attitude the vehicle can hold to compensate for the drift. Again, the relative velocity of the vessel is kept constant and compensation is achieved using the control surfaces only. The stability of the closed loop kinematic system is successfully analyzed. Similar kinematic approaches to solve guidance, control and ranging problems of underactuated underwater vehicles are found in [5, 73, 8], while autonomous aircraft are described with 3D kinematic models in [120] to develop collision avoidance strategies.

The Underactuated Dynamics in ILOS Guidance Schemes

In Chapters 3 and 4 the analysis of the ILOS kinematic closed loop systems gives explicit bounds on the integral gains but does not give any guidelines on how to choose the look-ahead distances. It is argued that the look-ahead distances should be ‘long enough’ to avoid overshoots and hence make the underactuated sway and heave dynamics neglectable. In Chapter 5 explicit bounds for the choice of the ILOS guidance look-ahead distance are derived. This is done by including the underactuated dynamics into the Lyapunov analysis. Disturbances in the form of constant irrotational ocean currents and constant dynamic, attitude dependent, forces are taken into account. Furthermore, more precise bounds upon the integral gains are obtained as well. A 3-DOFs planar motion scenario is considered with sway being the underactuated dynamics and the actuated dynamics are not taken into account.

Path Following Control of Underactuated Vehicles in the Presence of Ocean Currents

In Chapter 6 the complete kinematic and dynamic closed loop system of the ILOS guidance law for path following purposes of underactuated surface vessels is analyzed. The actuated surge and yaw dynamics are included in the analysis and combined with the results from Chapter 5. It is shown that the resulting closed loop system forms a cascade where the actuated dynamics perturb the combined sway-guidance system. In this case disturbances in the form of irrotational ocean currents are taken into account, while dynamic heading dependent environmental disturbances are not taken into account. Path following of straight lines is considered and the underactuated vessel is made to side-slip in order to compensate for the drift since no actuation is available in sway to counteract for the components of the disturbances acting in the transverse direction. The dynamics of the vessel are expressed in terms of its relative velocity, where the relative velocity of the vessel is its velocity with respect to the water. This is possible since the current is assumed constant and irrotational in the inertial frame. Compared to [26] the stronger stability properties of Uniform Global Asymptotic Stability (UGAS) and Uniform Local Exponential Stability (ULES) (alternatively global κ-exponential stability [129]) are shown for the closed loop cascaded system and the stability margins for the guidance law parameters are increased. The control approach in [26] includes both absolute and relative velocities, while here it is based on relative velocities only with direct control over the ship relative speed. It is hence not necessary to use adaptive techniques to estimate the unknown kinematic drift in the ship surge and yaw controllers. Furthermore, it is shown that in steady state it is possible to estimate the unknown current by combining the integral term of the ILOS guidance with the measurements of the absolute and relative speeds of the vessel.

In Chapter 9 the underactuated and the actuated dynamics are included in the analysis of the 3D ILOS guidance law from Chapter 4. The results from Chapter 6 are hence extended to underactuated AUVs for 3D straight line path following applications in the presence of constant irrotational ocean currents acting in any direction of the inertial frame. The 3D ILOS guidance law from Chapter 4 with integral action in both the vertical and horizontal directions is shown to solve the task together with three feedback controllers in a cascaded configuration. The control approach is based on relative velocities with direct control over the AUV relative speed. It is shown that redefining the AUV dynamics in terms of relative velocities makes it possible to prove the stability properties of UGAS and ULES for the 3D AUV case as well. Compared to Chapter 4, both the kinematic and dynamic levels of the problem are addressed and explicit bounds on all of the guidance law parameters are given to guarantee stability.

Results from Full Scale Sea Trials

Results from simulations and field experiments are presented that support and illustrate the theoretical results of Chapters 6 and 9. In Chapter 6 the analyzed 2D ILOS guidance scheme is applied to the CART Unmanned Semi-Submersible Vehicle (USSV) for sea trials [22], while the model of an underactuated supply vessel is used for simulation purposes since a model of the CART USSV is not yet available. First, the model of the supply vessel is used to simulate the control system and to assess its robustness with respect to parameter uncertainties and process noise. Next, the model is scaled to match the dimensions of the CART USSV in order to have simulation results that can be directly compared with the experiments. Finally, experimental results from sea trials are presented and a back to back comparison between simulations and experimental results is given. Furthermore, different combinations of the guidance law parameters are tested for different speeds/thrust levels.

In Chapter 9 the analyzed 3D ILOS guidance is applied to the LAUV autonomous underwater vehicle [126]. First, simulations are run using a mathematical model of the LAUV vehicle to analyze the guidance law response and tune the ILOS controllers. The simulations include an example of a 3D underwater path following case and a 2D underwater way-point following case, analogous to the sea trial runs, for a back-to-back comparison. Next, experimental results from full scale underwater 2D way-point following tests are shown. Finally, the ILOS guidance law is compared to the vector field guidance law for path following purposes from [100]. The comparison is based on experiments.

Path Following Control of Underactuated Surface Vessels in the Presence of Multiple Disturbances

The 2D ILOS guidance method developed in Chapter 6 is extended with adaptation in Chapter 8 where it is analytically shown that the resulting control scheme successfully compensates for a combination of kinematic and dynamic disturbances and hence guarantees path following of underactuated surface vessels in different sea conditions. Path following of straight lines is considered. Compared to [26] the control approach is again based on relative velocities with direct control over the ship relative speed. It is hence not necessary to use adaptive techniques to estimate the unknown kinematic drift in the ship surge and yaw controllers, whereas adaptation is still required to estimate and compensate for the dynamic disturbances. The combined effect of kinematic and dynamic disturbances is analyzed assuming that the dynamic disturbance is known in direction but unknown in magnitude. It is shown that the ILOS guidance in a cascaded configuration with an adaptive speed-heading controller guarantees UGAS and ULES for the closed loop system. The results are supported by simulations.

ILOS in Bounded Control Problems

The possibility of extending the ILOS guidance law proposed for underactuated surface marine vehicles in Chapter 6 to fully actuated marine vehicles with saturated transverse actuators is discussed in Chapter 7. Low-speed path following of straight lines is considered and the proposed solution combines the ILOS guidance law with a nonlinear bounded sway feedback controller. A fully actuated surface vessel described by a 3-DOFs maneuvering model is considered and the guidance law is derived from the underactuated case described in Chapter 6. Compared to Chapter 6, it is shown that the additional use of the transverse actuators for disturbance compensation reduces the side-slip angle the vessel has to hold. The problem addressed is partially a bounded control problem since saturation is considered for the transverse actuators while the surge and yaw control inputs are considered unconstrained. The proposed control system is based on relative velocities with direct control over the vehicle relative speed as done in Chapter 6. UGAS and ULES of the origin of the closed loop system are proved giving full-state stabilization, and explicit bounds on the guidance law parameters are given to guarantee stability. Results from simulations are presented to verify and illustrate the theoretical results.

1.2.3. Counter Current and Co-Current Guidance

In Chapter 10 the problem of steering a marine vessel against the ocean current or with the ocean current is addressed. Two guidance laws for counter-current and co-current guidance of underactuated marine vehicles in 3-DOFs are presented in Chapter 10. The proposed solutions can be applied to surface vessels or to underwater vehicles and are designed to perform counter-current or co-current guidance in presence of constant and irrotational ocean currents. The guidance laws are based on the relation between the relative and absolute velocities. In particular, it is shown that the counter-current direction and the co-current direction are two possible steady-state headings having zero absolute sway velocity and zero sway current component. In the first guidance law the absolute sway velocity is the error signal of the guidance system, while in the second guidance law the sway current component is the error signal. The two laws show different stability properties: local exponential stability (LES) for the first and uniform semiglobal exponential stability (USES) for the second. In both cases the closed loop system reveals multiple stable/unstable equilibrium points, corresponding to the counter-current/co-current directions depending on the setting. Lyapunov theory [82, 65] is used in the proofs. Simulation results support the theoretical findings.

1.2.4. Delimitation

The theoretical results presented in this dissertation are based on the assumption that the considered models are known, free of uncertainties and free of modeling errors. It is moreover assumed that any measured signals are noise and drift free, and that the necessary analog/digital signal processing has been performed by dedicated systems. The design of systems without these assumptions is beyond the scope of this thesis. Furthermore, no explicit saturation constraints are added into the theoretical analysis, except for the bounded sway controller of Chapter 7. The effects of saturation are however taken into account through numerical simulations and experiments. Furthermore, robustness of the ILOS guidance scheme for surface vessels with respect to model uncertainties and process noise is also analyzed through simulations in Chapter 6.

1.2.5. Publications

The main results of this thesis have been published in several international conferences and journals:

Journal Papers

- W. Caharija, K. Y. Pettersen, P. Calado, J. Braga and M. Milovanović, "Path following control of underactuated AUVs in the presence of ocean currents: theory, simulations and experiments," *IEEE Transactions on Control System Technology*, 2014, (to be submitted).
- W. Caharija, K. Y. Pettersen, M. Bibuli, E. Zereik, J. T. Gravdahl, A. J. Sørensen and G. Bruzzone, "Integral LOS for path following control of underactuated surface vessels: theory, simulations and experiments," *IEEE Transactions on Control System Technology*, 2014, (submitted).
- W. Caharija, K. Y. Pettersen, A. J. Sørensen, M. Candeloro and J. T. Gravdahl, "Relative velocity control and integral LOS for path following of ASVs: Merging intuition with theory," *Proc. of the Institution of Mechanical Engineers, Part M: Journal of Engineering for the Maritime Environment*, 228(2):180-191, 2014.

Conference Papers

- W. Caharija, E. I. Grøtli and K. Y. Pettersen, "Improved countercurrent and co-current guidance of underactuated marine vehicles with semiglobal stability properties", In *Proc. of IFAC World Congress*, Cape Town, South Africa, Aug 2014 pp. 12166-12173.

- M. Bibuli, W. Caharija, K. Y. Pettersen, G. Bruzzone, M. Caccia and E. Zereik, "ILOS guidance - experiments and tuning", In *Proc. of the 19th IFAC World Congress*, Cape Town, South Africa, Aug 2014, pp. 4209-4214.
- W. Caharija, K. Y. Pettersen and J. T. Gravdahl, "Path following of underactuated surface vessels in presence of uknown constant environmental forces: Preliminary results," In *Proc. of the 9th IFAC Conference on Control Applications in Marine Systems*, Osaka, Japan, Sept 2013, pp. 85-90.
- W. Caharija, K. Y. Pettersen and J. T. Gravdahl, "Counter-current and co-current guidance of underactuated unmanned marine vehicles," In *Proc. of the 8th IFAC Symposium on Intelligent Autonomous Vehicles*, Gold Coast, QLD, Australia, June 2013, pp. 184-191.
- W. Caharija, K. Y. Pettersen and J. T. Gravdahl, "Path following of marine surface vessels with saturated transverse actuators," In *Proc. of American Control Conference*, Washington DC, USA, June 2013, pp. 546-553.
- W. Caharija, K. Y. Pettersen, J. T. Gravdahl and E. Børhaug, "Path following of underactuated autonomous underwater vehicles in the presence of ocean currents," In *Proc. of the 51st IEEE Conference on Decision and Control*, Maui, HI, USA, Dec 2012, pp. 528-535.
- W. Caharija, M. Candeloro, K. Y. Pettersen and A. J. Sørensen, "Relative velocity control and integral LOS for path following of underactuated surface vessels," In *Proc. of the 9th IFAC Conference on Manoeuvring and Control of Marine Craft*, Arenzano, Italy, Sept 2012 pp. 380-385, *Best Student Paper Award.*
- W. Caharija, K. Y. Pettersen, J. T. Gravdahl and E. Børhaug, "Integral LOS guidance for horizontal path following of underactuated autonomous underwater vehicles in the presence of vertical ocean currents," In *Proc. of American Control Conference*, Montreal, Canada, June 2012, pp. 5427-5434.
- W. Caharija, K. Y. Pettersen, J. T. Gravdahl and A. J. Sørensen, "Topics on current compensation for path following applications of underactuated underwater vehicles," In *Proc. of the 3rd IFAC Workshop on Navigation, Guidance and Control of Underwater Vehicles*, Porto, Portugal, April 2012, pp. 184-191.

Other publications, related to but not part of this thesis

- S. Moe, W. Caharija, K. Y. Pettersen and I. Schjølberg,"Path Following of Underactuated Underwater Vehicles in the Presence of Unknown Ocean Currents", In *Proc. of the 33th International Conference on Ocean, Offshore and Arctic Engineering*, San Fransisco, CA, USA, June 2014.
- S. Moe, W. Caharija, K. Y. Pettersen and I. Schjølberg, "Path Following of Underactuated Marine Surface Vessels in the Presence of Unknown Ocean Currents", In *Proc. of American Control Conference*, Portland, OR, USA, June 2014, pp. 3856-3861.

1.3. Outline of the Thesis

This dissertation is in organized in 11 chapters and 3 appendices. The arrangement is such that a linear growth of complexity is held throughout the thesis, where the analysis of the ILOS guidance scheme is first limited to kinematic models and then step by step extended to more complex kinematic-dynamic models. Additional short appendices are also given at the end of some chapters. This is done to give the thesis a modular structure so that each chapter is not excessively dependent on the previous ones.

Chapter 2: presents the control plant models used in this dissertation.

Chapter 3: applies the ILOS guidance for surface vessels to a simple 2D kinematic model. An intuitive and practical explanation of the current of compensation problem follows.

Chapter 4: applies the ILOS guidance for 3D path following of underwater vehicles to a simple 3D kinematic model. An intuitive and practical explanation of the current of compensation problem follows.

Chapter 5: the underactuated sway dynamics is added to the 2D kinematic system introduced in Chapter 3 and kinematic as well as dynamic disturbances are included. A detailed and well commented proof of stability of the sway-guidance closed loop system is given, where the actuated dynamics are not taken into account. The proof represents the backbone of the thesis and is used in the following chapters.

Chapter 6: analyzes the complete case of an underactuated vessel in 3-DOFs subject to irrotational ocean current disturbances and equipped with an ILOS controller. The actuated dynamics are added to the sway-guidance system discussed in Chapter 5 in a cascaded configuration. The theoretical results are supported by simulations and experiments.

Chapter 7: explores the possibility of extending the ILOS guidance to fully actuated surface vessels with saturated sway actuators to shrink the side-slip angle. The full closed loop system (kinematics/dynamics) is analyzed and simulation results are included.

Chapter 8: extends the case of Chapter 6 where the underactuated vessel is under the influence of irrotational ocean currents and dynamic heading dependent forces generated by wind. The theoretical results are supported by simulations.

Chapter 9: applies the 3D ILOS guidance from Chapter 4 to underactuated underwater vehicles where the underactuated and actuated dynamics are included in the 5-DOFs analysis. Disturbances in the form of irrotational ocean currents are considered and a multiple cascaded structure is obtained. The theoretical results are supported by simulations and experiments.

Chapter 10: presents two guidance laws for co-current and counter-current guidance of underactuated marine vehicles in 3-DOFs

Chapter 11: conclusions and future work.

Bibliography

Appendix A: summarizes the stability concepts, definitions and theorems that are significant for this dissertation.

Appendix B: presents the simulation models of the vehicles used in this dissertation.

Appendix C: gives the wind load coefficients for supply vessels from [15].

Chapter 2.

Modeling of Marine Vehicles for Control Design Purposes

"One learns more from listening than speaking. And both the wind and the people who continue to live close to nature still have much to tell us which we cannot hear within university walls."
— Thor Heyerdahl, Explorer

The design and development of control systems for marine vehicles requires a certain degree of knowledge of the underlying physics governing the motion of the vessel. The breadth and depth of the required knowledge depends on the application, the type of vessel, the desired level of robustness and cost issues. Trade offs often arise between these requirements and experience suggests that on-the-field tuning and testing is widely accepted for smaller systems such as unmanned marine vehicles, while controllers for large scale systems such as ships, drilling rigs or floating productions units (FPUs) require a significantly higher level of modeling, analysis and simulation for obvious cost and risk issues. Therefore, detailed and consistent modeling of marine vessels represents a cutting edge research line in the field of marine technology worldwide.

Detailed mathematical rigid body models based on classical mechanics are used to design and simulate controllers for manned and unmanned marine vehicles. Although the mathematical models differ in their parameters and level of complexity according to the type of vessel (supply ship, crude carrier, FPU) and application (station keeping or maneuvering), the models found in literature are also classified according to their purpose. In particular, [130, 117] define two classes of mathematical models: the process plant models and the control plant models. A process plant model represents a comprehensive description of the actual vessel. Its main purpose is to simulate the vessel dynamics with a high degree of accuracy and it often includes noise effects, disturbances, sensor responses and actuator dynamics. The process plant model is mostly used to assess the robustness and the performance of the control systems. A control plant model represents a simplified mathematical description of the vessel. It is meant for control design purposes and therefore it includes only the main physical properties of the vehicle that are relevant in control design. Notice that the control plant model may also be part of the designed controller. The control plant model is used in analytical stability analysis, such as the Lyapuonv analysis, as well. Since accurate models of the vessel dynamics are not always available or suffer from high parameter uncertainties, control plant models are often used as process plant models. In these cases a critical approach towards the results obtained from simulations becomes fundamental.

In this chapter the class of control plant models used throughout this dissertation is introduced. In particular, the main topic addressed by this thesis is disturbance compensation in path following control problems of underactuated marine vessels. Therefore, certain maneuvering control plant models that include the main disturbing effects of the environmental forces at sea are developed to design and analyze robust guidance systems. The presented control plant models describe the effects of the environmental disturbances as a constant irrotational ocean current [52] where an additional dynamic bias term is sometimes added to include heading dependent disturbances and model uncertainties. The fact that the the unknown ocean current is assumed constant and irrotational makes it possible to define the presented models in terms of the relative velocity vector only, where the relative velocity is the velocity with respect to the water. Moreover, as done in [23], a translation of the equations of motion is introduced to remove the effect of the yaw control input on the sway dynamics for the 3 degrees of freedom (DOFs) two dimensional (2D) maneuvering models. An analogous translation of the equations of motion for the 5-DOFs 3D maneuvering models is used to remove the effects of the pitch and yaw control inputs on the heave and sway dynamics. Such transformations, inspired by [59], have proved useful in underactuated control design for surface vessels and extended to underwater vehicles in [25], as they simplify the controller design as well as the stability analysis. However, possible physical interpretations of the proposed transformations and the possibility of preserving the ship model in the matrix form introduced by [52] are only shortly discussed in [23] for the 3-DOFs case. The 3-DOFs as well as the 5-DOFs transformations proposed in this thesis are yet based on [59] and it is shown in details that they correspond to a translation of the equations of motion. This makes the presented models suitable for several control design purposes.

This chapter is organized as follows: in Section 2.1 the general rigid body model of marine vehicles is presented and discussed. The definition of underactuated and fully actuated systems is briefly recalled in Section 2.2 while in Section 2.3 the class of control plant models for surface vessels and underwater vehicles moving in a plane is introduced. In Section 2.4 the class of control plant models for underwater vehicles moving in the 3D space is introduced. Some of the results from [33, 29, 30] are presented in this chapter.

2.1. The Rigid Body Model of Marine Vessels and Vehicles

According to [52] the marine craft equations of motion can be written in a vectorial form:

$$\dot{\boldsymbol{\eta}} = \boldsymbol{J}(\boldsymbol{\eta})\boldsymbol{\nu}, \tag{2.1}$$

$$\boldsymbol{M}_{RB}\dot{\boldsymbol{\nu}} + \boldsymbol{C}_{RB}(\boldsymbol{\nu})\boldsymbol{\nu} + \boldsymbol{M}_{A}\dot{\boldsymbol{\nu}}_r + \boldsymbol{C}_{A}(\boldsymbol{\nu}_r)\boldsymbol{\nu}_r + \boldsymbol{D}(\boldsymbol{\nu}_r)\boldsymbol{\nu}_r + \boldsymbol{g}(\boldsymbol{\eta}) = \boldsymbol{\tau} + \boldsymbol{w}. \tag{2.2}$$

Before defining the terms found in (2.1-2.2) it is important to emphasize the fact that the model (2.1-2.2) describes the motion of the ship with a rigid body approximation. It is a mass damper spring model where two reference frames are used to describe the motion of the vessel: the inertial North-East-Down (NED) frame i and the body frame b, as shown in Figure 2.1. Notice that the body frame b is fixed to the vehicle and is generally in motion with respect to i.

The vector $\boldsymbol{\eta} \triangleq [x, y, z, \phi, \theta, \psi]^T$ is defined in i and represents the position and the orientation of the vessel with respect to the inertial frame i, where x, y and z are the Cartesian coordinates of the vessel. The ϕ, θ and ψ angles are the roll, pitch and yaw Euler angles, and describe the attitude of the craft with respect to the inertial frame i. The term $\boldsymbol{\nu} \triangleq [u, v, w, p, q, r]^T$ is the generalized velocity vector defined in b where u is the surge velocity, v is the sway velocity, w is the heave velocity, p is the roll rate, q is the pitch rate and r is the yaw rate. The term $\boldsymbol{\nu}_r \triangleq \boldsymbol{\nu} - \boldsymbol{\nu}_c$ is the relative velocity of the vessel in b and is defined as the velocity of the craft with respect to the ocean current. The vector $\boldsymbol{\nu}_c$ is the ocean current velocity expressed in b. The matrix $\boldsymbol{J}(\boldsymbol{\eta})$ is the velocity transformation matrix, $\boldsymbol{M}_{RB} = \boldsymbol{M}_{RB}^T > 0$ is the rigid body inertia matrix, $\boldsymbol{C}_{RB}(\boldsymbol{\nu})$ is the rigid body Coriolis and centripetal matrix, $\boldsymbol{M}_A = \boldsymbol{M}_A^T > 0$ is the hydrodynamic added mass matrix, $\boldsymbol{C}_A(\boldsymbol{\nu}_r)$ is the added mass Coriolis and centripetal matrix, $\boldsymbol{D}(\boldsymbol{\nu}_r)$ is the hydrodynamic damping matrix and $\boldsymbol{g}(\boldsymbol{\eta})$ is the gravity vector. The term $\boldsymbol{\tau}$ is the control input vector in b. The vector $\boldsymbol{w}$ is defined in b and contains the dynamic forces and moments that the environment produces on the vessel (winds, waves, currents).

Detailed and comprehensive discussions about the structure of the above mentioned matrices and coefficients can be found in a large number of publications, such as [52, 130, 117]. Furthermore, they are defined case by case in the following sections and chapters of this thesis. Therefore, a detailed definition of the terms in the model (2.1-2.2) is here omitted. Instead, focus is put on the aspects of (2.1-2.2) that are significant for the definition of the control plant models used in this dissertation.

The model (2.1-2.2) is a rigid body model and as such it is a lumped mechanical model. However the environment interacts with the hull and the superstructure in a distributed fashion: for instance, environmental disturbances such as wind, waves and currents generate distributed loads. The interactions water-vessel and wind-vessel can be described using the laws of hydrodynamics and aerodynamics, leading to very complex distributed models [50, 15]. Hence, given the high level of complexity and the distributed nature of these phenomena, numerical approaches are used [52]. To integrate the effects of the interaction water-vessel into the lumped model (2.1-2.2) the added mass $\boldsymbol{M}_A$ matrix and the damping $\boldsymbol{D}(\boldsymbol{\nu}_r)$ matrix are introduced. Notice that the coefficients of $\boldsymbol{M}_A$ and $\boldsymbol{D}(\boldsymbol{\nu}_r)$ are often the result of extensive numerical simulations or model identification

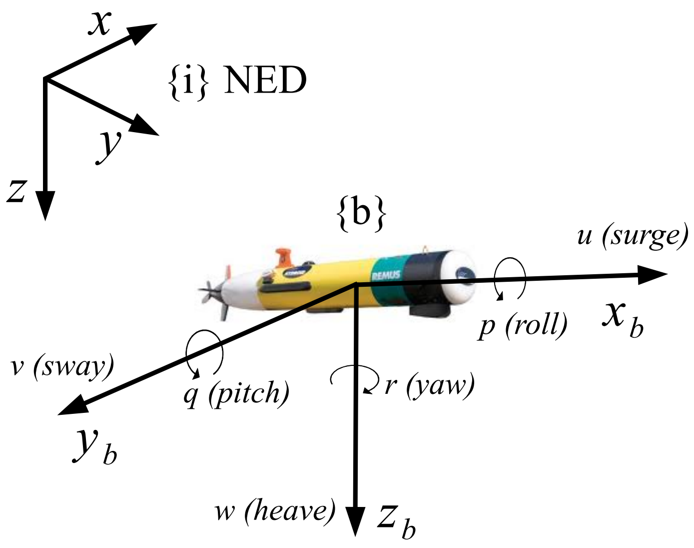

Figure 2.1.: The inertial NED frame and the body frame used to describe the motion of a marine craft in 6-DOF.

analysis, and may suffer from high parametric uncertainties. The effects of environmental disturbances like wind, waves and currents are integrated into the lumped model (2.1-2.2) through the relative velocity vector $\boldsymbol{\nu}_r \triangleq \boldsymbol{\nu} - \boldsymbol{\nu}_c$ and the environmental load vector $\boldsymbol{w}$. It is hence the terms $\boldsymbol{M}_A$, $\boldsymbol{D}(\boldsymbol{\nu}_r)$, $\boldsymbol{\nu}_r$ and $\boldsymbol{w}$ that represent the connection between the distributed nature of the environment and the lumped rigid body representation given in (2.1-2.2).

This dissertation focuses on the design of guidance control systems capable of compensating for the disturbances in transit and maneuvering operations of marine vessels. Therefore, adequate control plant models have to be derived from (2.1-2.2) where the most significant effects of the environmental disturbances have to be extracted from the terms $\boldsymbol{\nu}_c$ and $\boldsymbol{w}$ in relation to the guidance and control objectives. In straight line path following control scenarios of underactuated marine vehicles it is fundamental to keep the vessel on the desired course. Hence, field experience from sailors and seamen suggests that there are two major effects pushing the vessel away from the desired path: a kinematic velocity bias that will affect the boat independently of its heading and a heading dependent dynamic bias. Several environmental forces may contribute to the two disturbing effects and it is generally believed that currents and slowly varying drifting effects can be treated as a kinematic bias, while the average wind pressure represents the main heading dependent dynamic disturbance. Notice that this discussion implicitly neglects the zero mean oscillating effects caused by waves and wind gusts since they are often filtered out through wave filtering or by the inertia of the vessel, and therefore are not significant for path following control purposes.

In this thesis the constant irrotational ocean current model is used to define the kinematic bias, where the term $\boldsymbol{\nu}_c$ is defined as described in Section 2.1.1. The vector $\boldsymbol{w}$ is defined in Section 2.1.2 and it represents the bias term that embodies unmodeled dynamics and dynamic, heading dependent disturbances caused by currents, winds and waves. In this context, the significant effect of constant wind disturbances is assumed to dominate in $\boldsymbol{w}$.

2.1.1. The Constant and Irrotational Ocean Current

The ocean current is defined in the inertial frame i and is assumed constant, irrotational and bounded. Hence, for underwater vehicles $\boldsymbol{V}_c \triangleq [V_x, V_y, V_z]^T$ and there exists a constant $V_{\max} > 0$ such that $V_{\max} \geq \sqrt{V_x^2 + V_y^2 + V_z^2}$. For surface vessels $\boldsymbol{V}_c \triangleq [V_x, V_y, 0]^T$ and $V_{\max} \geq \sqrt{V_x^2 + V_y^2}$.

The constant and irrotational ocean current model is widely accepted to describe the effects of slowly varying disturbances and it represents a good approximation when closed loop control is implemented on-board of marine vehicles [51, 52]. Hence, the drifting effect of currents, tides, low frequency swells and second order wave-induced forces can be included into the ocean current vector $\boldsymbol{V}_c$. Notice that the vector $\boldsymbol{V}_c$ defines an irrotational and incompressible flow field and thus it is clearly not meant for detailed hydrodynamic modeling of the interaction water-hull. Nevertheless, it represents a good approximation of the effects of the disturbances in rigid body models for control design purposes. The generalized ocean current velocity of an irrotational fluid in the moving frame b is:

$$\boldsymbol{\nu}_c = [u_c, v_c, w_c, 0, 0, 0]^T, \tag{2.3}$$

where u_c, v_c and w_c represent the linear velocity of the current in b: $\boldsymbol{v}_c \triangleq [u_c, v_c, w_c]^T$. Moreover, $\boldsymbol{v}_c$ relates to $\boldsymbol{V}_c$ as:

$$\boldsymbol{v}_c = \boldsymbol{R}(\phi, \theta, \psi)^T \boldsymbol{V}_c, \tag{2.4}$$

where $\boldsymbol{R}(\phi, \theta, \psi)$ is the rotation matrix from b to i, parametrized using Euler angles. It is shown in [67] and [52] that if the current is constant and irrotational in the inertial frame i, the rigid body kinetics satisfy:

$$\boldsymbol{M}_{RB}\dot{\boldsymbol{\nu}} + \boldsymbol{C}_{RB}(\boldsymbol{\nu})\boldsymbol{\nu} = \boldsymbol{M}_{RB}\dot{\boldsymbol{\nu}}_{\boldsymbol{r}} + \boldsymbol{C}_{RB}(\boldsymbol{\nu}_r)\boldsymbol{\nu}_r. \tag{2.5}$$

The property (2.5) can be used to simplify the equations of motion (2.1-2.2) where the state of the vessel is now represented by the relative velocity $\boldsymbol{\nu}_r$:

$$\dot{\boldsymbol{\eta}} = \boldsymbol{J}(\boldsymbol{\eta})\boldsymbol{\nu}_r + [\boldsymbol{V}_c^T, 0, 0, 0]^T, \tag{2.6}$$

$$\boldsymbol{M}\dot{\boldsymbol{\nu}}_r + \boldsymbol{C}(\boldsymbol{\nu}_r)\boldsymbol{\nu}_r + \boldsymbol{D}(\boldsymbol{\nu}_r)\boldsymbol{\nu}_r + \boldsymbol{g}(\boldsymbol{\eta}) = \boldsymbol{\tau} + \boldsymbol{w}. \tag{2.7}$$

Equation (2.4) is used to derive (2.6) and the matrices $\boldsymbol{M}$ and $\boldsymbol{C}(\boldsymbol{\nu}_r)$ are defined as $\boldsymbol{M} \triangleq \boldsymbol{M}_{RB} + \boldsymbol{M}_A$ and $\boldsymbol{C}(\boldsymbol{\nu}_r) \triangleq \boldsymbol{C}_{RB}(\boldsymbol{\nu}_r) + \boldsymbol{C}_A(\boldsymbol{\nu}_r)$.

This choice of model has direct implications for the choice of adequate control objectives and control design. In particular, the model expressed in terms of the relative velocity vector (2.6-2.7) makes it natural to choose the control input $\boldsymbol{\tau}$ in order to control the relative velocity $\boldsymbol{\nu}_r$. Therefore, the absolute speed with respect to the inertial frame i is not directly controlled, but is instead determined by the sum between the relative speed and the current velocity. This result is less surprising as one could think: actuators such as propellers, tunnel thrusters, azimuth thrusters and pump-jets create local pressure differences in the fluid that push the water particles [116]. Hence, motion is obtain with respect to the water and the speed through water of the vessel is roughly proportional to the rotation rate of the propeller. Moreover, until space-based satellite navigation systems were not operational water speed was often the only measurement available on board, provided by sensors such as doppler speed logs, pitometer logs, paddle meters and, in the very old days, ship logs. Finally, notice that relative velocity control is not the ideal choice if speed profile planning/tracking scenarios were considered. However, controlling the relative velocity of the ship gives direct control over the energy consumption as hydrodynamic damping depends on $\boldsymbol{\nu}_r$, and also it removes the term $\boldsymbol{\nu}_c$ from the velocity feedback loop.

2.1.2. The Environmental Load Vector $\boldsymbol{w}$

The vector $\boldsymbol{w}$ represents a bias term that embodies unmodeled dynamics and dynamic, heading dependent disturbances caused by currents, winds and waves. For control system design purposes it is common to assume the principle of superposition when considering the effects of different disturbances [52]. In particular the effects of wind on surface vessels is extensively analyzed with simulations and wind tunnel tests in [76, 103, 15] while wave-induced forces are studied in [109].

In this context, the significant effect of constant wind disturbances is assumed to dominate in $\boldsymbol{w}$ when motion on the sea surface is analyzed. Motivated by [15] and [52], the overall effect of wind is modeled as a constant pressure P_e acting on the vessel in a constant direction β_e. The mean and slowly varying drifting effect caused by wind is considered, while highly oscillating zero mean effects due to wind gusts are not taken into account since they are often removed through filtering. Furthermore, the vessel inertia has low pass filtering effects as well. The forces and moments generated by the wind pressure P_e on the ship are proportional to the frontal and lateral projected areas above the waterline of the ship, and to some well defined load coefficients. The areas above the waterline are considered since the effect of wind is limited to the surface. The loading coefficients depend on the geometry of the ship hull and superstructure, and are functions of the disturbance angle of attack. They are usually obtained through interpolation of data from simulations and wind tunnel tests for different types of ships

[76, 103, 15]. The environmental load vector $\boldsymbol{w}$ is then defined as:

$$\boldsymbol{w} \triangleq \begin{bmatrix} P_e A_{Fw} C_X(\gamma_e) \\ P_e A_{Lw} C_Y(\gamma_e) \\ P_e A_{Lw} L_{oa} C_N(\gamma_e) \end{bmatrix}, \tag{2.8}$$

where A_{Fw} is the frontal projected area above the waterline, A_{Lw} is the lateral projected area above the waterline and L_{oa} is the length overall of the vessel (maximum length of the vessel hull). The term $\gamma_e \triangleq \psi - \beta_e - \pi$ is the angle of attack of the wind. The terms $C_X(\gamma_e)$, $C_Y(\gamma_e)$ and $C_N(\gamma_e)$ are the load coefficients. The coefficients from [15] are included in this dissertation due to their wide use to assess wind loads on ships, and can be found in Appendix B.

2.2. The Underactuated Marine Vehicles

Since this dissertation focuses heavily on underactuated marine vessels, the following definition of underactuated mechanical systems, adapted from [62], is quoted from [1]. Consider an affine mechanical system described by:

$$\ddot{\boldsymbol{q}} = \boldsymbol{F}(\boldsymbol{q}, \dot{\boldsymbol{q}}) + \boldsymbol{G}(\boldsymbol{q})\boldsymbol{u}, \tag{2.9}$$

where $\boldsymbol{q}$ is a vector of independent generalized coordinates, $\boldsymbol{F}$ is a vector field that describes the dynamics of the system, $\boldsymbol{G}$ is the input matrix and $\boldsymbol{u}$ is the vector of generalized inputs. The system (2.9) is:

- *Fully actuated*: if the rank of $\boldsymbol{G}$ is equal to the dimension of $\boldsymbol{q}$.
- *Underacuated*: if the rank of $\boldsymbol{G}$ is smaller than the dimension of $\boldsymbol{q}$.
- *Overactuated*: if the rank of $\boldsymbol{G}$ is larger than the dimension of $\boldsymbol{q}$.

Hence, an underactuated marine vehicle is a vehicle having more degrees of freedom than independent control inputs and therefore it cannot independently control all its degrees of freedom simultaneously. Moreover, [122] and [16] introduce two operational spaces to help define different motion control scenarios:

- *The work space*: the physical space in which the vehicle moves (2D space for a car, 3D space for an airplane).

- *The configuration space*: the set of variables sufficient to specify all the points of a rigid body vehicle in the work spaces. Each degree of freedom is a configuration variable.

Based on the definitions above, it is possible to conclude that an underactuated vehicle is generally unable to achieve arbitrary tasks in its configuration space but it can still achieve meaningful tasks in its work space.

Notice that in practice most marine vessels are underactuated when moving at high speed since the thrusters facilitating full actuation become ineffective at speeds higher than $1-2$ [m/s] ($3-4$ [knots]) [95, 16].

2.3. A Class of Control Plant Models in 3-DOFs

In this section the class of control plant models in 3-DOFs used in this thesis is defined. It describes the kinematics and dynamics of surface vessels as well as underwater vehicles moving in the horizontal plane and the models are designed for maneuvering control purposes.

2.3.1. Model Assumptions

Assumption 2.1. The motion of the vessel can be described by 3-DOFs, that is surge, sway and yaw.

Assumption 2.2. The vessel is port-starboard symmetric.

Assumption 2.3. The body fixed coordinate frame b is located on the center line of the vessel.

Assumption 2.4. The ocean current is defined in the inertial frame i and is assumed constant, unknown, irrotational and bounded. Hence, $\boldsymbol{V}_c \triangleq [V_x, V_y, 0]^T$ and there exists a constant $V_{\max} > 0$ such that $V_{\max} \geq \sqrt{V_x^2 + V_y^2}$.

2.3.2. The Control Plant Model

The state of the surface vessel is given by the vector $[\boldsymbol{p}^T, \boldsymbol{\nu}_r^T]^T$ where $\boldsymbol{p} \triangleq [x, y, \psi]^T$ describes the position and the orientation of the vehicle with respect to the inertial frame

i. The vector $\boldsymbol{\nu} \triangleq [u, v, r]^T$ contains the linear and angular velocities of the ship defined in the body-fixed frame b, where u is the surge velocity, v is the sway velocity and r is the yaw rate. The ocean current velocity in the body frame b, $\boldsymbol{\nu}_c \triangleq [u_c, v_c, 0]^T$, is obtained from $\boldsymbol{\nu}_c = \boldsymbol{R}^T(\psi)\boldsymbol{V}_c$ where $\boldsymbol{R}(\psi)$ is the rotation matrix from b to i. According to Assumption 2.4 the ocean current is constant and irrotational in i and hence $\dot{\boldsymbol{V}}_c = \boldsymbol{0}$, and $\dot{\boldsymbol{\nu}}_c = [rv_c, -ru_c, 0]^T$. In navigation problems involving ocean currents it is useful to describe the state of the vessel with the relative velocity vector: $\boldsymbol{\nu}_r \triangleq \boldsymbol{\nu} - \boldsymbol{\nu}_c = [u_r, v_r, r]^T$. The vector $\boldsymbol{\nu}_r$ is defined in b, where u_r is the relative surge velocity and v_r is the relative sway velocity. This thesis considers the class of marine vehicles described by the following 3-DOF maneuvering model:

$$\dot{\boldsymbol{p}} = \boldsymbol{R}(\psi)\boldsymbol{\nu}_r + \boldsymbol{V}_c, \tag{2.10}$$

$$\boldsymbol{M}\dot{\boldsymbol{\nu}}_r + \boldsymbol{C}(\boldsymbol{\nu}_r)\boldsymbol{\nu}_r + \boldsymbol{D}(\boldsymbol{\nu}_r)\boldsymbol{\nu}_r = \boldsymbol{B}\boldsymbol{f} + \boldsymbol{w}. \tag{2.11}$$

The model (2.10-2.11) can describe the kinematics and dynamics of surface vessels as well as underwater vehicles moving in the horizontal plane. The vector $\boldsymbol{f} \triangleq [T_u, T_r]^T$ is the control input vector, containing the surge thrust T_u and the rudder angle T_r. Notice that the model (2.10-2.11) is underactuated in its configuration space since it has fewer control inputs than DOFs. The matrix $\boldsymbol{M} = \boldsymbol{M}^T > 0$ is the mass and inertia matrix and includes hydrodynamic added mass. The matrix $\boldsymbol{C}$ is the Coriolis and centripetal matrix, $\boldsymbol{D} > 0$ is the hydrodynamic damping matrix and $\boldsymbol{B} \in \mathbb{R}^{3\times 2}$ is the actuator configuration matrix. For maneuvering control purposes, the matrices $\boldsymbol{R}(\psi)$, $\boldsymbol{M}$, and $\boldsymbol{B}$ are considered to have the following structures [52]:

$$\boldsymbol{R}(\psi) \triangleq \begin{bmatrix} \cos(\psi) & -\sin(\psi) & 0 \\ \sin(\psi) & \cos(\psi) & 0 \\ 0 & 0 & 1 \end{bmatrix}, \tag{2.12}$$

$$\boldsymbol{M} \triangleq \begin{bmatrix} m_{11} & 0 & 0 \\ 0 & m_{22} & m_{23} \\ 0 & m_{23} & m_{33} \end{bmatrix}, \quad \boldsymbol{B} \triangleq \begin{bmatrix} b_{11} & 0 \\ 0 & b_{22} \\ 0 & b_{32} \end{bmatrix}. \tag{2.13}$$

The particular structure of $\boldsymbol{M}$ is justified by Assumptions 2.1-2.3. The actuator configuration matrix $\boldsymbol{B}$ has full column rank and maps the control inputs T_u and T_r into forces and moments acting on the vessel. The Coriolis and centripetal matrix $\boldsymbol{C}$ is obtained from $\boldsymbol{M}$ as [52]:

$$\boldsymbol{C}(\boldsymbol{\nu}_r) \triangleq \begin{bmatrix} 0 & 0 & -m_{22}v_r - m_{23}r \\ 0 & 0 & m_{11}u_r \\ m_{22}v_r + m_{23}r & -m_{11}u_r & 0 \end{bmatrix}. \tag{2.14}$$

The damping term $\boldsymbol{D}(\boldsymbol{\nu}_r)$ is here left unspecified and its definition is considered case by case in the following chapters of this dissertation. The same applies to the body fixed environmental load vector $\boldsymbol{w} \triangleq [w_u, w_v, w_r]^T$.

Remark 2.1. Given the model (2.10-2.11) one can choose to consider both the proposed disturbances, $\boldsymbol{V}_c$ and $\boldsymbol{w}$, or only one, depending on the application, type of vessel and the environmental conditions.

2.3.3. Translation of the Equations of Motion

In the model (2.10-2.11) the yaw control T_r affects not only the yaw dynamics but also the underactuated sway dynamics. This complicates the controller design and the subsequent stability analysis. To overcome the problem, it is useful to modify the model using coordinate transformations as done in [25] for an underwater vehicle and in [59] for a surface vessel. The transformation is here redefined as a translation of the equations of motion, similarly to [23]. In [59] it is shown that the following transformation removes the effect of the yaw control on the sway motion:

$$\bar{u}_r = u_r, \quad \bar{v}_r = v_r + \epsilon r, \quad \bar{r} = r. \tag{2.15}$$

The transformed velocity vector is $\bar{\boldsymbol{\nu}}_r \triangleq [\bar{u}_r, \bar{v}_r, \bar{r}]^T$ while ϵ is a constant given by:

$$\epsilon \triangleq -\frac{m_{33}b_{22} - m_{23}b_{32}}{m_{22}b_{32} - m_{23}b_{22}}. \tag{2.16}$$

Notice that ϵ is well defined as long as the system is controllable in yaw. It is straightforward to define the corresponding transformation matrix $\boldsymbol{H}_{\mathrm{3DOF}}$ such that $\boldsymbol{\nu}_r = \boldsymbol{H}_{\mathrm{3DOF}}\bar{\boldsymbol{\nu}}_r$:

$$\boldsymbol{H}_{3DOF} \triangleq \begin{bmatrix} 1 & 0 & 0 \\ 0 & 1 & -\epsilon \\ 0 & 0 & 1 \end{bmatrix}. \tag{2.17}$$

The linear transformation is invertible since all the diagonal elements of $\boldsymbol{H}_{\mathrm{3DOF}}$ are nonzero. The transformation corresponds to a physical translation of the equations of motion (2.10-2.11) along the center line of the ship for a distance ϵ (see [52]). In particular, the supply ship described by the model given in Appendix B has $\epsilon \cong 1.67$ [m]. Therefore, without any loss of generality, the vehicle model (2.10-2.11) is transformed to describe the motion of a point $\boldsymbol{P}$ located $\boldsymbol{r}_P \triangleq [\epsilon, 0, 0]^T$ from the original one. Notice that $\boldsymbol{r}_P$ is given in b and represents a translation along the center line of the vessel. The translation of the origin of the body fixed frame b to $\boldsymbol{P}$ is done as described in [52] and

(2.10-2.11) becomes:

$$\dot{\boldsymbol{p}} = \boldsymbol{R}(\psi)\boldsymbol{\nu}_r + \boldsymbol{V}_c, \tag{2.18}$$

$$\boldsymbol{M}^P\dot{\boldsymbol{\nu}}_r + \boldsymbol{C}^P(\boldsymbol{\nu}_r)\boldsymbol{\nu}_r + \boldsymbol{D}^P(\boldsymbol{\nu}_r)\boldsymbol{\nu}_r = \boldsymbol{B}^P\boldsymbol{f} + \boldsymbol{w}, \tag{2.19}$$

where $\boldsymbol{M}^P = \boldsymbol{H}_{\mathrm{3DOF}}^T\boldsymbol{M}\boldsymbol{H}_{\mathrm{3DOF}}$, $\boldsymbol{D}^P(\boldsymbol{\nu}_r) = \boldsymbol{H}_{\mathrm{3DOF}}^T\boldsymbol{D}(\boldsymbol{\nu}_r)\boldsymbol{H}_{\mathrm{3DOF}}$ and $\boldsymbol{B}^P = \boldsymbol{H}_{\mathrm{3DOF}}^T\boldsymbol{B}$. The vectors $\boldsymbol{p}$ and $\boldsymbol{\nu}_r$ in (2.18-2.19) now describe the motion of the point $\boldsymbol{P}$. This convention will be used in the following sections and chapters unless diversely specified. Furthermore, the translation does not change the structure nor the properties of the inertia, damping and actuator configuration matrices. It is straightforward to show that the matrices $\boldsymbol{M}^P$ and $\boldsymbol{B}^P$ are such that:

$$(\boldsymbol{M}^P)^{-1}\boldsymbol{B}^P\boldsymbol{f} = \begin{bmatrix} \frac{b_{11}}{m_{11}}T_u \\ 0 \\ \frac{m_{22}b_{32}-m_{23}b_{22}}{m_{22}m_{33}-m_{23}^2}T_r \end{bmatrix}. \tag{2.20}$$

Therefore, the influence of the yaw control input T_r has been removed from the sway dynamics. This makes the model (2.18-2.19) suitable for several control design purposes and in the following chapters, whenever referring to single matrix elements, they are from the model in $\boldsymbol{P}$. Finally, since it is often necessary to expand the transformed model into its components, the component form control inputs τ_u and τ_r are defined and related to T_u and T_r through the following transformation:

$$\begin{bmatrix} \tau_u \\ \tau_r \end{bmatrix} \triangleq \begin{bmatrix} \frac{b_{11}}{m_{11}} & 0 \\ 0 & \frac{m_{22}b_{32}-m_{23}b_{22}}{m_{22}m_{33}-m_{23}^2} \end{bmatrix} \begin{bmatrix} T_u \\ T_r \end{bmatrix}. \tag{2.21}$$

Remark 2.2. Notice that (2.21) is well defined as long as $\boldsymbol{M}$ is non-singular.

2.4. A Class of Control Plant Models in 5-DOFs

In this section the class of control plant models in 5-DOFs used in this thesis is defined. It describes the kinematics and dynamics of underwater vehicles moving in a 3D space, below the wave affected zone.

2.4.1. Model Assumptions

Assumption 2.5. The body-fixed coordinate frame b is located along the center-line of the vessel.

Assumption 2.6. The roll motion is passively stabilized through fins or by gravity and therefore can be neglected. Hence, the motion of the vehicle is described in 5-DOFs, that is surge, sway, heave, pitch and yaw.

Assumption 2.7. The vehicle is neutrally buoyant and the center of gravity (CG) and the center of buoyancy (CB) are located along the same vertical axis in b.

Assumption 2.8. The AUV is xz plane symmetric with a large length-to-width ratio.

Assumption 2.9. The surge mode is decoupled from the other degrees of freedom and only dominating interconnections between sway and yaw, and between heave and pitch are considered.

Remark 2.3. Assumptions 2.6, 2.7, 2.8 and 2.9 are common assumptions in maneuvering control of slender body AUVs [52]. They also hold for the LAUV and HUGIN vehicles [25, 40].

Assumption 2.10. The ocean current in the inertial frame i, $\boldsymbol{V}_c \triangleq [V_x, V_y, V_z]^T$, is constant, irrotational and bounded. Hence, there exists $V_{\max} > 0$ such that $V_{\max} \geq \sqrt{V_x^2 + V_y^2 + V_z^2}$.

2.4.2. The Vehicle Control Model

Following Assumption 2.6 the state of the underwater vehicle is given by the vector $\boldsymbol{\eta} \triangleq [x, y, z, \theta, \psi]^T$ which describes the position and the orientation of the AUV with respect to the inertial frame i. In particular, θ is the vehicle pitch angle and ψ is the vehicle yaw angle. The vector $\boldsymbol{\nu} \triangleq [u, v, w, q, r]^T$ contains the linear and angular velocities of the vehicle defined in the body-fixed frame b where u is the surge velocity, v is the sway velocity, w is the heave velocity, q is the pitch rate and r is the yaw rate. According to Assumption 2.10 the ocean current is irrotational in i and its velocity in the body frame b, $\boldsymbol{\nu}_c \triangleq [u_c, v_c, w_c, 0, 0]^T$, is obtained from $[u_c, v_c, w_c]^T = \boldsymbol{R}^T(\theta, \psi)\boldsymbol{V}_c$ where $\boldsymbol{R}(\theta, \psi)$ is the rotation matrix from b to i, defined using the zyx convention [52]. Furthermore, the fact that $\dot{\boldsymbol{V}}_c = \boldsymbol{0}$ gives $\dot{\boldsymbol{\nu}}_c = [rv_c - qw_c, -ru_c, qu_c, 0, 0]^T$. In marine control problems involving ocean current it is useful to introduce the relative velocity. The relative velocity is defined as the velocity of the vehicle with respect to the flow: $\boldsymbol{\nu}_r \triangleq \boldsymbol{\nu} - \boldsymbol{\nu}_c = [u_r, v_r, w_r, q, r]^T$. The vector $\boldsymbol{\nu}_r$ is defined in b where u_r is the relative surge velocity, v_r is the relative sway velocity and w_r is the relative heave velocity. The underwater vehicles described by the following 5-DOF maneuvering model are considered [52]:

$$\dot{\boldsymbol{\eta}} = \boldsymbol{J}(\boldsymbol{\eta})\boldsymbol{\nu}_r + [\boldsymbol{V}_c^T, 0, 0]^T, \tag{2.22}$$

$$\boldsymbol{M}\dot{\boldsymbol{\nu}}_r + \boldsymbol{C}(\boldsymbol{\nu}_r)\boldsymbol{\nu}_r + \boldsymbol{D}(\boldsymbol{\nu}_r)\boldsymbol{\nu}_r + \boldsymbol{g}(\boldsymbol{\eta}) = \boldsymbol{B}\boldsymbol{f}. \tag{2.23}$$

The vector $\boldsymbol{f} \triangleq [T_u, T_q, T_r]^T$ is the control input vector, containing the surge thrust (T_u), the pitch rudder angle (T_q) and the yaw rudder angle (T_r). The dimension of the control input vector $\boldsymbol{f}$ is two less than the DOFs of the vessel, therefore the model (2.22-2.23) is underactuated in its configuration space. The term $\boldsymbol{J}(\boldsymbol{\eta})$ is the velocity transformation matrix defined as:

$$\boldsymbol{J}(\boldsymbol{\eta}) \triangleq \begin{bmatrix} \boldsymbol{R}(\theta,\psi) & \boldsymbol{0} \\ \boldsymbol{0} & \boldsymbol{T}(\theta) \end{bmatrix}, \tag{2.24}$$

where $\boldsymbol{T}(\theta) \triangleq \mathrm{diag}(1, 1/\cos(\theta)), |\theta| \neq \frac{\pi}{2}$. The matrix $\boldsymbol{M} = \boldsymbol{M}^T > 0$ is the mass and inertia matrix, and includes hydrodynamic added mass. The matrix $\boldsymbol{C}$ is the Coriolis and centripetal matrix, $\boldsymbol{D}(\boldsymbol{\nu}_r)$ is the hydrodynamic damping matrix and $\boldsymbol{B} \in \mathbb{R}^{5\times 3}$ is the actuator configuration matrix. Following Assumption 2.7, the gravity vector in CG can be written as $\boldsymbol{g}(\boldsymbol{\eta}) \triangleq [0, 0, 0, BG_z W \sin(\theta), 0]^T$, where BG_z is the vertical distance between CG and CB, and W is the weight of the vehicle. For maneuvering control purposes, the matrices $\boldsymbol{R}(\theta, \psi)$, $\boldsymbol{M}$ and $\boldsymbol{B}$ are:

$$\begin{gathered} \boldsymbol{R}(\theta,\psi) \triangleq \begin{bmatrix} \cos(\psi)\cos(\theta) & -\sin(\psi) & \cos(\psi)\sin(\theta) \\ \sin(\psi)\cos(\theta) & \cos(\psi) & \sin(\psi)\sin(\theta) \\ -\sin(\theta) & 0 & \cos(\theta) \end{bmatrix}, \\ \boldsymbol{M} \triangleq \begin{bmatrix} m_{11} & 0 & 0 & 0 & 0 \\ 0 & m_{22} & 0 & 0 & m_{25} \\ 0 & 0 & m_{33} & m_{34} & 0 \\ 0 & 0 & m_{34} & m_{44} & 0 \\ 0 & m_{25} & 0 & 0 & m_{55} \end{bmatrix}, \quad \boldsymbol{B} \triangleq \begin{bmatrix} b_{11} & 0 & 0 \\ 0 & 0 & b_{23} \\ 0 & b_{32} & 0 \\ 0 & b_{42} & 0 \\ 0 & 0 & b_{53} \end{bmatrix}. \end{gathered} \tag{2.25}$$

The particular structure of $\boldsymbol{M}$ is justified by Assumptions 2.5-2.8. The actuator configuration matrix $\boldsymbol{B}$ has full column rank and maps the control inputs T_u, T_q and T_r into forces and moments acting on the vessel. The Coriolis and centripetal matrix $\boldsymbol{C}$ can be parametrized as described in [52]:

$$\boldsymbol{C}(\boldsymbol{\nu}_r) \triangleq \begin{bmatrix} 0 & 0 & 0 & m_{33}w_r + m_{34}q & -m_{22}v_r - m_{25}r \\ 0 & 0 & 0 & 0 & m_{11}u_r \\ 0 & 0 & 0 & -m_{11}u_r & 0 \\ -m_{33}w_r - m_{34}q & 0 & m_{11}u_r & 0 & 0 \\ m_{22}v_r + m_{25}r & -m_{11}u_r & 0 & 0 & 0 \end{bmatrix}. \tag{2.26}$$

The damping term $\boldsymbol{D}(\boldsymbol{\nu}_r)$ is here left undefined and its specification is considered case by case in the following chapters of the dissertation.

Remark 2.4. In the model (2.22-2.23) the environmental load vector $\boldsymbol{w}$ is not present. The dynamic disturbance $\boldsymbol{w}$ is neglected since the model describes the motion of underwater vehicles under the sea surface, below the wave affected zone where heading dependent dynamic disturbances are not significant for the path following control purposes addressed in this dissertation. Therefore, the effects of the disturbances are assumed to be modeled by the constant and irrotational ocean current $\boldsymbol{V}_c$ [52, 51].

2.4.3. Translation of the Equations of Motion

In the model (2.22-2.23) the pitch and yaw controls, T_q and T_r, influence not only the pitch and yaw dynamics but also the underactuated heave and sway dynamics. This complicates the controller design and the subsequent stability analysis. To overcome the problem, it is useful to transform the model into a cascaded form using coordinate transformations as done in [25] for a similar 3D case and in [59] for a surface vessel. In this paper the transformation is redefined as a translation of the equations of motion.

In [25] it is shown that the following transformation removes the effect of the yaw and pitch controls on the heave and sway motion:

$$\bar{u}_r = u_r,\ \bar{v}_r = v_r + \epsilon_1 r,\ \bar{w}_r = w_r + \epsilon_2 q,\ \bar{q} = q,\ \bar{r} = r. \tag{2.27}$$

The transformed velocity vector is $\bar{\boldsymbol{\nu}} \triangleq [\bar{u}_r, \bar{v}_r, \bar{w}_r, \bar{q}, \bar{r}]^T$ while ϵ_1 and ϵ_2 are constants given by:

$$\epsilon_1 \triangleq -\frac{m_{55}b_{23} - m_{25}b_{53}}{m_{22}b_{53} - m_{25}b_{23}}, \quad \epsilon_2 \triangleq -\frac{m_{44}b_{32} - m_{34}b_{42}}{m_{33}b_{42} - m_{34}b_{32}}. \tag{2.28}$$

Notice that ϵ_1 and ϵ_2 are well defined as long as the system is controllable in pitch and yaw. It is straightforward to define the corresponding transformation matrix $\boldsymbol{H}_{5\text{DOF}}$ such that $\boldsymbol{\nu}_r = \boldsymbol{H}_{5\text{DOF}}\bar{\boldsymbol{\nu}}_r$:

$$\boldsymbol{H}_{5\text{DOF}} \triangleq \begin{bmatrix} 1 & 0 & 0 & 0 & 0 \\ 0 & 1 & 0 & 0 & -\epsilon_1 \\ 0 & 0 & 1 & -\epsilon_2 & 0 \\ 0 & 0 & 0 & 1 & 0 \\ 0 & 0 & 0 & 0 & 1 \end{bmatrix}. \tag{2.29}$$

The linear transformation is invertible since all the diagonal elements of $\boldsymbol{H}_{5\mathrm{DOF}}$ are nonzero. It is interesting to notice that, if $\epsilon_1 = -\epsilon_2$ the transformation corresponds to a physical translation of the equations of motion (2.22-2.23) along the center line of the ship for a distance $\epsilon \triangleq \epsilon_1$ (see [52]). From (2.28) it is straightforward to verify that if $m_{22} = m_{33}$, $m_{44} = m_{55}$, $m_{25} = -m_{34}$, $b_{23} = -b_{32}$ and $b_{42} = b_{53}$ then $\epsilon_1 = -\epsilon_2$. These conditions are easily fulfilled by AUVs of cylindrical shape which employ similar types of steering and diving control surfaces. In fact, it can be seen that both the maneuvering models of the HUGIN, LAUV and ISiMI vehicles have $\epsilon_1 = -\epsilon_2$ (see [23] and [80]). In particular, the LAUV described by the model given in Appendix B has $\epsilon \cong 0.14$ [m]. Therefore, without any loss of generality, the vehicle model (2.22-2.23) is transformed to describe the motion of a point $\boldsymbol{P}$ located $\boldsymbol{r}_P \triangleq [\epsilon, 0, 0]^T$ from the original one. Notice that $\boldsymbol{r}_P$ is given in b and represents a translation along the center line of the vessel. The translation of the origin of the body fixed frame b to $\boldsymbol{P}$ is done as described in [52] and (2.22-2.23) becomes:

$$\dot{\boldsymbol{\eta}} = \boldsymbol{J}(\boldsymbol{\eta})\boldsymbol{\nu}_r + [\boldsymbol{V}_c^T, 0, 0]^T, \tag{2.30}$$

$$\boldsymbol{M}^P\dot{\boldsymbol{\nu}}_r + \boldsymbol{C}^P(\boldsymbol{\nu}_r)\boldsymbol{\nu}_r + \boldsymbol{D}^P(\boldsymbol{\nu}_r)\boldsymbol{\nu}_r + \boldsymbol{g}^P(\boldsymbol{\eta}) = \boldsymbol{B}^P\boldsymbol{f}. \tag{2.31}$$

where $\boldsymbol{M}^P = \boldsymbol{H}_{5\mathrm{DOF}}^T\boldsymbol{M}\boldsymbol{H}_{5\mathrm{DOF}}$, $\boldsymbol{D}^P(\boldsymbol{\nu}_r) = \boldsymbol{H}_{5\mathrm{DOF}}^T\boldsymbol{D}(\boldsymbol{\nu}_r)\boldsymbol{H}_{5\mathrm{DOF}}$, $\boldsymbol{g}^P(\boldsymbol{\eta}) = \boldsymbol{H}_{5\mathrm{DOF}}^T\boldsymbol{g}(\boldsymbol{\eta})$ and $\boldsymbol{B}^P = \boldsymbol{H}_{5\mathrm{DOF}}^T\boldsymbol{B}$. The vectors $\boldsymbol{\eta}$ and $\boldsymbol{\nu}_r$ in (2.30-2.31) now describe the motion of the point $\boldsymbol{P}$. This convention will be used in the following sections and chapters unless diversely specified. Furthermore, the translation does not change the structure nor the properties of the inertia, damping and actuator configuration matrices. It is straightforward to show that $\boldsymbol{M}^P$ and $\boldsymbol{B}^P$ are such that:

$$(\boldsymbol{M}^P)^{-1}\boldsymbol{B}^P\boldsymbol{f} = \begin{bmatrix} \frac{b_{11}}{m_{11}}T_u \\ 0 \\ 0 \\ \frac{m_{33}b_{42} - m_{34}b_{32}}{m_{33}m_{44} - m_{34}^2}T_q \\ \frac{m_{22}b_{53} - m_{25}b_{23}}{m_{22}m_{55} - m_{25}^2}T_r \end{bmatrix}. \tag{2.32}$$

Therefore, the influence of the pitch and yaw control inputs T_q and T_r has been removed from the heave and sway dynamics. This makes the model (2.30-2.31) suitable for several control design purposes and in the following chapters, whenever referring to single matrix elements, they are from the model in $\boldsymbol{P}$. Finally, since it is often necessary to expand the transformed model into its components, the component form control inputs

τ_u, τ_q and τ_r are defined and related to T_u, T_q and T_r through the following well-defined transformation:

$$\begin{bmatrix} \tau_u \\ \tau_q \\ \tau_r \end{bmatrix} \triangleq \begin{bmatrix} \frac{b_{11}}{m_{11}} & 0 & 0 \\ 0 & \frac{m_{33}b_{42}-m_{34}b_{32}}{m_{33}m_{44}-m_{34}^2} & 0 \\ 0 & 0 & \frac{m_{22}b_{53}-m_{25}b_{23}}{m_{22}m_{55}-m_{25}^2} \end{bmatrix} \begin{bmatrix} T_u \\ T_q \\ T_r \end{bmatrix}. \tag{2.33}$$

Chapter 3.

A Kinematic Approach to the ILOS Guidance for Surface Vessels

"Fear is the master only to those who do not dare."
— Franc Knez, Alpinist

In this chapter the Integral Line-of-Sight (ILOS) guidance is presented and applied to a simple kinematic model of a surface vessels. In particular, the ILOS guidance for planar motion is introduced and it is shown, using simple and intuitive mathematical tools, that current compensation for underactuated surface vessels reduces to a pure vectorial sum and has one possible solution that identifies the only heading the ship can hold to compensate for the drift. As done in [10], the relative velocity of the vessel is kept constant and compensation is achieved through side-slipping. It is proved that path following of straight lines is obtained. It is furthermore shown that the integral LOS guidance law executes the sum needed to compensate for the drift, between the relative velocity vector of the vehicle and the unknown ocean current velocity vector. This provides a useful practical explanation of the role that the integral term plays in the guidance law. Moreover, given the underactuated nature of the vehicles, the LOS guidance law is interpreted as a decoupling tool between the actuated dynamics and the underactuated dynamics. Therefore, as a first approximation, the control problem can be considered at the kinematic level only. This approach is similar to [3, 71] where the well known unicycle model is used, or to [100] where steering of miniature air vehicles is considered. This procedure, despite its simplicity, represents a valuable first step design tool for integral LOS guidance schemes applied to underactuated marine vehicles. Finally, stability of the closed loop kinematic system is analyzed and simulation results using a mathematical model of an offshore supply vessel are presented.

The objective of this chapter is to give practical and intuitive insights of the LOS/ILOS guidance law, and at the same time it introduces elements of mathematical analysis that are used and extended throughout this dissertation. This chapter is organized as follows: in Section 3.1 the current compensation problem for underactuated surface vessels is formulated and discussed, in Section 3.2 the integral LOS guidance law is introduced and in Section 3.3 the stability of the closed loop kinematic system is addressed. Finally, data from simulations are presented in Section 3.4 and conclusions are given in Section 3.5. The results presented in this chapter are based on [35, 36, 14].

3.1. Sea Current Compensation

In this section the current compensation problem for underactuated surface vessels is formulated. Some basic assumptions are first introduced, followed by the description of the notation used in this chapter. The path following control task is then defined and finally the description of the current compensation problem as a vectorial sum is given.

3.1.1. Basic Assumptions and Notation

Assumption 3.1. The motion of the vessel is described of 3 degrees of freedom (DOF): surge, sway and yaw.

Remark 3.1. Assumption 3.1 is a common assumption in manoeuvring control of surface vessels [52].

Assumption 3.2. The vessel is underactuated in its configuration space: there is no actuation in sway while control inputs are available in surge and yaw.

Remark 3.2. Assumption 3.2 is justified by the fact that most of surface vessels are equipped with a propeller and aft rudders only, making them underactuated in sway.

Assumption 3.3. The ocean current is defined in the inertial frame i and assumed constant, unknown, irrotational and bounded. Hence $\boldsymbol{V}_c \triangleq [V_x, V_y]^T$ and there exists $V_{\max} > 0$ such that $V_{\max} \geq \sqrt{V_x^2 + V_y^2}$.

Following Assumption 3.1, the system state is given by the vector $\boldsymbol{\eta} \triangleq [x, y, \psi]^T$ and describes the position and the orientation of the vessel with respect to the inertial frame i. In particular ψ is the yaw angle of the vessel. The vector $\boldsymbol{\nu} \triangleq [u, v, r]^T$ contains the linear and angular velocities defined in the body-fixed frame b, where u is the surge velocity, v is the sway velocity and r is the yaw rate. The ocean current linear velocity in the body frame b, $\boldsymbol{\nu}_c \triangleq [u_c, v_c, 0]^T$, is obtained from $\boldsymbol{\nu}_c = \boldsymbol{R}^T(\psi)[\boldsymbol{V}_c^T, 0]^T$ where $\boldsymbol{R}(\psi)$ is the rotation matrix from b to i:

$$\boldsymbol{R}(\psi) \triangleq \begin{bmatrix} \cos(\psi) & -\sin(\psi) & 0 \\ \sin(\psi) & \cos(\psi) & 0 \\ 0 & 0 & 1 \end{bmatrix}. \tag{3.1}$$

According to Assumption 3.3 the ocean current is constant and irrotational in i, i.e. $\dot{\boldsymbol{V}}_c = \boldsymbol{0}$, therefore $\dot{\boldsymbol{\nu}}_c = [rv_c, -ru_c, 0]^T$. In navigation problems involving ocean currents it is useful to introduce the relative velocity and [52] defines the relative velocity as the velocity of the vessel with respect to the flow. Given the vector:

$$\boldsymbol{U} \triangleq \begin{bmatrix} \dot{x} \\ \dot{y} \end{bmatrix} = \begin{bmatrix} \cos(\psi) & -\sin(\psi) \\ \sin(\psi) & \cos(\psi) \end{bmatrix} \begin{bmatrix} u \\ v \end{bmatrix}, \tag{3.2}$$

representing the linear velocity of the vessel in the inertial frame i, the linear relative velocity $\boldsymbol{U}_r$ in i is:

$$\boldsymbol{U}_r \triangleq \boldsymbol{U} - \boldsymbol{V}_c. \tag{3.3}$$

Following (3.3), $\boldsymbol{\nu}_r \triangleq \boldsymbol{\nu} - \boldsymbol{\nu}_c = [u_r, v_r, r]^T$ is the relative velocity of the vessel in b. Therefore, $\boldsymbol{U}_r$ can be expressed as:

$$\boldsymbol{U}_r = \begin{bmatrix} \cos(\psi) & -\sin(\psi) \\ \sin(\psi) & \cos(\psi) \end{bmatrix} \begin{bmatrix} u_r \\ v_r \end{bmatrix}. \tag{3.4}$$

After introducing the concept of relative velocity, it is possible to add the following assumption:

Assumption 3.4. To prevent the vessel from drifting away, the desired constant relative surge velocity U_{rd} has to be strictly greater than the ocean current intensity: $U_{rd} > V_{\max}$.

3.1.2. The Path Following Control Problem

The control system should make the vessel follow a given straight line $\mathcal{P}$ and maintain a desired constant surge relative velocity $U_{rd} > 0$. This should also hold in the presence of an unknown and constant ocean currents. To simplify the problem without any loss of generality since coordinates can always be rotated given a desired direction in the plane, the inertial reference frame i is placed such that the x-axis is aligned with the desired path $\mathcal{P} \triangleq \{(x, y) \in \mathbb{R}^2 : y = 0\}$ as shown in Figures 3.1. The y coordinate then corresponds to the cross-track error and the goals the control system should pursue are formalized as follows:

$$\lim_{t\to\infty} y(t) = 0, \tag{3.5}$$

$$\lim_{t\to\infty} \psi(t) = \psi_{ss}, \quad \psi_{ss} \in \left(-\frac{\pi}{2}, \frac{\pi}{2}\right), \tag{3.6}$$

$$\lim_{t\to\infty} u_r(t) = U_{rd}, \tag{3.7}$$

where $u_r(t)$ is the surge relative speed of the vessel and ψ_{ss} is a constant. Note that the $\psi(t)$ is not required to converge to zero but rather to a steady-state constant value bounded within $-\frac{\pi}{2}$ and $\frac{\pi}{2}$. This allows the ship to hold a non-zero yaw angle at equilibrium, and compensate for the ocean current as shown in Figure 3.1. This is necessary because the vessel is underactuated and no control forces are available in sway to counteract the drift. The value of ψ_{ss} will be specified later.

3.1.3. Relative Velocity and Current Compensation

In the following paragraphs it is shown how simple mathematical considerations conclude that there is only one possible angle ψ_{ss} the vehicle can hold to achieve current compensation.

Since there is no actuation in sway, it is not possible to have at the same time zero cross track errors as well as zero yaw angle. A non-zero ψ_{ss} angles is needed to use part of the vessel surge thrust for current compensation. Therefore, the control system has to find the constant steady state angle ψ_{ss} necessary to compensate and make ψ converge to this. To find the value of ψ_{ss} consider the desired equilibrium condition shown in Figure 3.1 and Figure 3.2. Notice that at equilibrium the control objective (3.7) is considered achieved and $v_r \to 0$. Hence, applying (3.4) concludes that

$$\lim_{t\to\infty} \boldsymbol{U}_r(t) = \boldsymbol{U}_{rd} \triangleq \begin{bmatrix} U_{rd}\cos(\psi_{ss}) \\ U_{rd}\sin(\psi_{ss}) \end{bmatrix}, \tag{3.8}$$

and $|\boldsymbol{U}_{rd}| = U_{rd}$. In order to make the vessel compensate for the drift and follow the desired course, the velocity $\boldsymbol{U}$ at equilibrium has to be oriented along the x axis (see

Figure 3.1):

$$\lim_{t\to\infty} \boldsymbol{U}(t) = \boldsymbol{U}_{ss} \triangleq [U_{ss}, 0]^T, \tag{3.9}$$

where $U_{ss} > 0$. According to (3.3), $\boldsymbol{U}_{ss}$ is the result of the following vectorial sum:

$$\boldsymbol{U}_{ss} = \boldsymbol{U}_{rd} + \boldsymbol{V}_c. \tag{3.10}$$

The ocean current vector $\boldsymbol{V}_c$, despite being unknown, has a well defined magnitude and direction. The vector $\boldsymbol{U}_{rd}$ is defined only in magnitude since ψ_{ss} is to be determined while the vector $\boldsymbol{U}_{ss}$ is defined in direction only. In principle, if the current $\boldsymbol{V}_c$ is known, it is possible to solve the vectorial equation and calculate the direction ψ_{ss} of $\boldsymbol{U}_{rd}$ and $U_{ss} > 0$. Geometrically, this corresponds at finding the intersections between the x axis and the circle having radius U_{rd} and center in $\boldsymbol{V}_c$. The intersection having a positive U_{ss} is chosen. A real positive solution exists as long as $U_{rd} > |\boldsymbol{V}_c|$ which is guaranteed by Assumption 3.4. This is shown in Figure 3.2. To conclude the analysis, it is possible to affirm that there exists only one possible heading ψ_{ss} that guarantees current compensation as long as Assumption 3.3 is valid. Applying (3.10) leads to the following relation between U_{rd} and U_{ss}:

$$U_{ss} = \sqrt{U_{rd}^2 - V_y^2} + V_x. \tag{3.11}$$

Furthermore, from (3.10) or, alternatively, from simple geometrical considerations shown in Figure 3.1 it follows that:

$$\psi_{ss} = -\tan^{-1}\left(\frac{V_y}{\sqrt{U_{rd}^2 - V_y^2}}\right). \tag{3.12}$$

The value (3.12) defines the heading the vehicle has to hold in order to follow the path $\mathcal{P}$ in presence of currents.

Remark 3.3. Notice that in this discussion the current is considered known, therefore as long as the vessel is underactuated, the heading defined by (3.12) represents the only possible solution for the controller to solve the current compensation problem, independently of the implemented technique (adaptive laws, current observers or integral action). In this case integral action inserted in the LOS guidance law is used to register the presence of ocean current and correctly set the heading of the vessel.

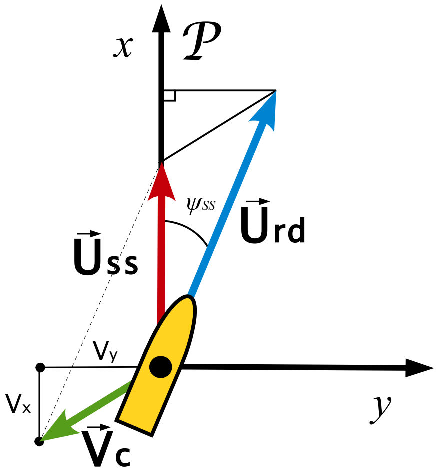

Figure 3.1.: Steady state: the vessel side-slips with a constant angle ψ_{ss} and follows the path.

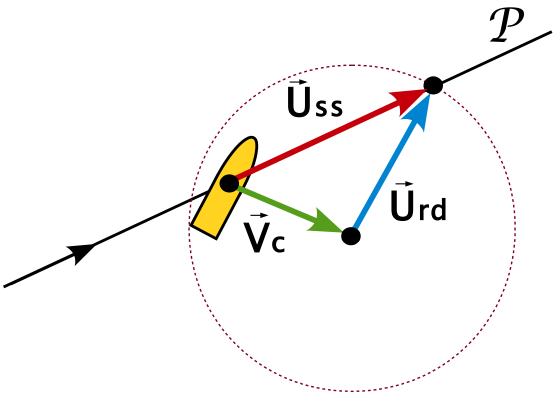

Figure 3.2.: Graphical solution of the current compensation problem for underactuated surface vessels.

3.2. The ILOS Reference Generator

In this section the ILOS guidance law from [26, 28] is presented. It is used to set the desired heading angle and make the vessel follow the x-axis. Furthermore, the ILOS guidance is interpreted as a decoupling tool between the kinematics and the kinetics of the system.

3.2.1. The Path Following Strategy

In order to solve the objective (3.5) of the the path following control problem, the marine vehicle has to converge to and follow the x-axis of the inertial frame i. To achieve the goal, the traditional LOS guidance reference generator used by [24] (see Figure 3.3) would set the vessel heading to:

$$\psi_{LOS} \triangleq -\tan^{-1}\left(\frac{y}{\Delta}\right). \tag{3.13}$$

The design parameter $\Delta > 0$ is the look-ahead distance. Convergence is however not guaranteed if there are ocean currents acting on the vessel since (3.13) does not allow the vessel to side-slip once it has converged to $\mathcal{P}$. To solve the problem, integral action is introduced in the heading reference. Hence, the integral LOS guidance law is defined as (see Figure 3.4):

$$\psi_{ILOS} \triangleq -\tan^{-1}\left(\frac{y + \sigma y_{\text{int}}}{\Delta}\right), \tag{3.14a}$$

$$\dot{y}_{\text{int}} = \frac{\Delta y}{(y + \sigma y_{\text{int}})^2 + \Delta^2}. \tag{3.14b}$$

The gains $\Delta > 0$ and $\sigma > 0$ are design parameters. The integral effects give nonzero LOS angle (3.14a), allowing the vessel to side-slip while staying on the desired path, so part of its relative forward velocity can counteract the effect of the ocean current. The integration law (3.14b) was first introduced by [26] and is chosen to give less integral action when the vessel is far from the desired path and thereby reduce the risk of integrator wind-up effects.

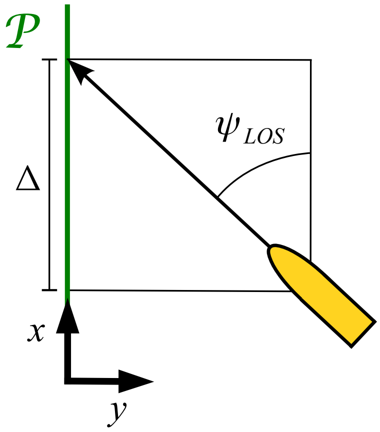

Figure 3.3.: Line of sight guidance for an underactuated surface vessel.

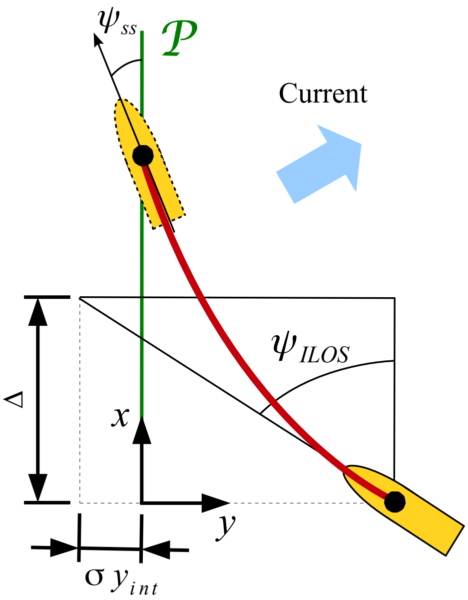

Figure 3.4.: Integral line of sight guidance for an underactuated surface vessel. At steady state the nonzero angle ψ_{ss} allows the underactuated vessel to counteract the disturbances.

3.2.2. Line-of-Sight and Underactuation

In this subsection the LOS guidance is revisited and interpreted as a decoupling element between the actuated surge and yaw dynamics and the underactuated sway dynamics, yielding a pure kinematic problem.

The line of sight guidance is simple and intuitive: it imitates a helmsman steering the vessel toward a point lying at a constant distance ahead of the ship along the desired path. It is a method that has been used in practice for a long time and is part of everyone daily life since it is implicitly used for instance when driving a car or riding a bicycle. The important feature that ships, cars and bicycles have in common and which makes this a good strategy, is that they are all underactuated systems. For most of the tasks these systems are requested to perform (such as path following) it is important to have as small as possible sway movements. The Line-of-Sight guidance is meant to avoid sway motion: the further ahead the helmsman looks, the smoother the turn and the less the not actuated sway dynamics are affected.

This intuitive argument can be explained mathematically by analyzing the work done in [24] where the traditional LOS guidance is used for straight line path following of surface vessels. The underactuated sway dynamics of the ship in [24, Equation (27)] are given by:

$$\dot{\bar{v}} = \frac{X(u_c)u_c\Delta}{(e^2+\Delta^2)^{3/2}}e + \left(Y(u_c) - \frac{X(u_c)\Delta^2}{(e^2+\Delta^2)^{3/2}}\right)\bar{v} + \left[\frac{-X(u_c+\tilde{u})\Delta}{e^2+\Delta^2}\boldsymbol{h}_e^T + \boldsymbol{h}_{\bar{v}}^T\right]\boldsymbol{\xi}, \quad (3.15)$$

where the functions $X(\cdot)$ and $Y(\cdot)$ are bounded for bounded arguments and u_c is the desired surge velocity. The function $Y(\cdot)$ is assumed to be negative for all the values of u_c. The vector $\boldsymbol{\xi}$ converges to zero exponentially and represents the dynamics of the speed and heading controllers. The state variables e and $\bar{v}$ are the cross track error and the sway velocity of the ship respectively. Finally, notice that Δ is the look-ahead distance of the two-dimensional LOS algorithm. Two facts can be noticed by carefully analyzing (3.15): first, the faster the speed and heading controllers, the faster the term proportional to $\boldsymbol{\xi}$ vanishes. Second, the longer the look-ahead distance Δ, the less the coupling terms in (3.15) count. This is justified by the fact that the coupling coefficients dependent on e tend to zero if Δ approaches infinity. Thus, setting a large Δ and having fast speed and heading controllers, ideally decouples the sway dynamics from the rest and the fact that $Y(\cdot)$ is negative guarantees $\bar{v} \to 0$. In other words, as explained before, the further ahead the LOS guidance law looks, the smoother the turn. Similar arguments can be easily generalized to [26] and [25] where the LOS algorithm is applied to AUVs. Therefore, the following key assumptions can be introduced:

Assumption 3.5. The underactuated vessel has internal controllers setting the desired relative surge velocity and the desired yaw angle.

Assumption 3.6. The internal controllers are assumed to be fast compared to the guidance law: the delay between the time the references are given by the guidance law and the time they are actually set by the controllers is small enough not to affect significantly the guidance dynamics.

Remark 3.4. Note that Assumptions 3.5 and 3.6 are often used implicitly when designing guidance laws for unmanned vehicles [20].

Assumption 3.7. The look-ahead distance Δ is assumed big enough so that the control surfaces do not affect significantly the sway dynamics. Therefore $v_r \approx 0$.

Remark 3.5. Applying Assumptions 3.5-3.7 leads to a pure kinematic problem: Assumptions 3.5 and 3.6 guarantee that the reference ILOS angle (3.14a) is followed and that the relative surge velocity u_r is set to U_{rd} while Assumption 3.7 states that the unactuated sway dynamics can be neglected.

Remark 3.6. In [3, 71, 100] several two dimensional underactuated control problems are addressed as kinematic problems and the control laws are derived from the closed loop Lyapunov analysis.

Remark 3.7. It is hard to tell quantitatively how fast the internal speed and attitude controllers must be and how long the look-ahead distance Δ must be so that Assumptions 3.5-3.7 are realistic. This depends on the vessel physical characteristics. Therefore, a good model of the vessel and careful simulations play a key role in this approach.

Following Assumption 3.3, Assumptions 3.5-3.7 and (3.3-3.4) the kinematic system can be written as:

$$\dot{x} = U_{rd} \cos(\psi_d) + V_x, \tag{3.16}$$

$$\dot{y} = U_{rd} \sin(\psi_d) + V_y. \tag{3.17}$$

where $\psi_d \triangleq \psi_{ILOS}$ is control input and hence the integral LOS (3.14) closes the loop.

Remark 3.8. Notice that this procedure is applicable in principle to any underactuated vessel since no dynamic model is needed.

3.3. Stability of the Closed Loop Kinematic System

Theorem 3.1. *Given a USV whose kinematics are defined by (3.16-3.17), if Assumptions 3.3-3.4 hold and if the gain σ satisfies:*

$$0 < \sigma < U_{rd} - V_{\max}, \tag{3.18}$$

then the guidance law (3.14) *achieves (3.5-3.6). The reference signal ψ_d is defined by* (3.14) *and the control objective* (3.6) *is fulfilled with ψ_{ss} given in* (3.12).

Proof. The dynamics of the cross track error y are analyzed first. The y subsystem is obtained from (3.17) and (3.14b):

$$\dot{y}_{\text{int}} = \frac{\Delta y}{(y + \sigma_{\text{int}})^2 + \Delta^2}, \tag{3.19}$$

$$\dot{y} = U_{rd} \sin(\psi_d) + V_y. \tag{3.20}$$

Substituting (3.14a) for ψ_d gives $\sin(\psi_d) = -(y + \sigma y_{\text{int}})/\sqrt{(y+\sigma_{\text{int}})^2 + \Delta^2}$ and leads (3.19-3.20) to the following expression of the $y_{\text{int}} - y$ dynamics:

$$\dot{y}_{\text{int}} = \frac{\Delta y}{\left(y + \sigma y_{\text{int}}\right)^2 + \Delta^2}, \tag{3.21}$$

$$\dot{y} = -U_{rd} \frac{y + \sigma y_{\text{int}}}{\sqrt{(y + \sigma y_{\text{int}})^2 + \Delta^2}} + V_y. \tag{3.22}$$

The equilibrium point of the system (3.20-3.19) is given by:

$$y_{\text{int}}^{\text{eq}} = \frac{\Delta}{\sigma} \frac{V_y}{\sqrt{U_{rd}^2 - V_y^2}}, \quad y^{\text{eq}} = 0. \tag{3.23}$$

A new set of variables is introduced to move the equilibrium point to the origin:

$$e_1 \triangleq y_{\text{int}} - y_{\text{int}}^{\text{eq}}, \quad e_2 \triangleq y + \sigma e_1. \tag{3.24}$$

The transformed y dynamics become:

$$\dot{e}_1 = -\frac{\Delta \sigma e_1}{\left(e_2 + \sigma y_{\text{int}}^{\text{eq}}\right)^2 + \Delta^2} + \frac{\Delta e_2}{\left(e_2 + \sigma y_{\text{int}}^{\text{eq}}\right)^2 + \Delta^2}, \tag{3.25}$$

$$\begin{aligned} \dot{e}_2 = &-\left[U_{rd}\sqrt{(e_2 + \sigma y_{\text{int}}^{\text{eq}})^2 + \Delta^2} - \sigma\Delta\right] \frac{e_2}{\left(e_2 + \sigma y_{\text{int}}^{\text{eq}}\right)^2 + \Delta^2} \\ &- \frac{\Delta \sigma^2 e_1}{\left(e_2 + \sigma y_{\text{int}}^{\text{eq}}\right)^2 + \Delta^2} + V_y f(e_2), \end{aligned} \tag{3.26}$$

where:

$$f(e_2) = 1 - \frac{\sqrt{(\sigma y_{\text{int}}^{\text{eq}})^2 + \Delta^2}}{\sqrt{(e_2 + \sigma y_{\text{int}}^{\text{eq}})^2 + \Delta^2}}. \tag{3.27}$$

The following bound holds for $f(e_2)$:

$$|f(e_2)| \leq \frac{|e_2|}{\sqrt{(e_2 + \sigma y_{\text{int}}^{\text{eq}})^2 + \Delta^2}}. \tag{3.28}$$

One can prove that (3.28) holds by squaring both sides of the inequality two consecutive times. Consider the quadratic Lyapunov function candidate:

$$V = \frac{\sigma^2}{2} e_1^2 + \frac{1}{2} e_2^2. \tag{3.29}$$

The time-derivative of V is:

$$\begin{aligned}\dot{V} = &-\left[-\sigma\Delta + U_{rd}\sqrt{(e_2 + \sigma y_{\text{int}}^{\text{eq}})^2 + \Delta^2}\right] \frac{e_2^2}{(e_2 + \sigma y_{\text{int}}^{\text{eq}})^2 + \Delta^2} \\ &- \frac{\sigma^3 \Delta}{(e_2 + \sigma y_{\text{int}}^{\text{eq}})^2 + \Delta^2} e_1^2 + V_y f(e_2) e_2.\end{aligned} \tag{3.30}$$

The variables $\bar{e}_1 \triangleq e_1/\sqrt{(e_2 + \sigma y_{\text{int}}^{\text{eq}})^2 + \Delta^2}$ and $\bar{e}_2 \triangleq e_2/\sqrt{(e_2 + \sigma y_{\text{int}}^{\text{eq}})^2 + \Delta^2}$ are defined to simplify the expression (3.30). This notation together with Assumption 3.3, $\min\{\sqrt{(e_2 + \sigma y_{\text{int}}^{\text{eq}})^2 + \Delta^2}\} = \Delta$ and the inequality (3.28) yields the following bound:

$$\dot{V} \leq -\sigma^3 \Delta |\bar{e}_1|^2 - \Delta(U_{rd} - V_{\max} - \sigma)|\bar{e}_2|^2 \triangleq -W. \tag{3.31}$$

It is straight forward to show that Assumption 3.4 and (3.18) guarantee positive definiteness of W. Hence, according to standard Lyapunov arguments, the system (3.20-3.19) is uniformly globally asymptotically stable (UGAS). Yet, the inequality $W \geq \bar{\lambda}_1|\bar{e}_1|^2 + \bar{\lambda}_2|\bar{e}_2|^2$ holds in a neighborhood of the origin for some constants $\bar{\lambda}_1, \bar{\lambda}_2 > 0$ and thus in any ball $\mathcal{B}_r \triangleq \{|e_2| \leq r\}, r > 0$ the function W can be estimated as $W \geq \lambda_1 |e_1|^2 + \lambda_2 |e_2|^2$ where $\lambda_i = \bar{\lambda}_i/((r + \sigma y_{\text{int}}^{\text{eq}})^2 + \Delta^2)$, $i = 1, 2$. This, together with the fact that V is a quadratic function of e_1, and e_2, concludes that (3.20-3.19) is also uniformly exponentially stable, ULES [82].

To conclude, under the conditions of Theorem 3.1 the equilibrium point $(y, y_{\text{int}}) = (0, y_{\text{int}}^{\text{eq}})$ of the system (3.20-3.19) is UGAS and ULES. Therefore, the control objectives (3.5-3.6 with exponential converging properties in any ball of initial conditions. ☐

Remark 3.9. Notice that the value $y_{\text{int}}^{\text{eq}}$ makes sure that at equilibrium the vessel holds the heading ψ_{ss} defined in (3.12)) which is, as explained in Section 3.1, the only possible heading that guarantees successful current compensation for underactuated surface vessels.

Remark 3.10. The analysis above gives well defined bounds upon the integral gain σ but it does not provide any criteria for how to choose the look-ahead distance Δ.

3.4. Simulations

In this section results from numerical simulation are presented. In particular, the developed control strategy is applied to an offshore supply vessel. The model of the vessel is given in Section B.1 of Appendix B. The objective is to make the vessel follow the path $\mathcal{P}$ with a desired surge relative speed $U_{rd} = 4$ [m/s]. The maximum intensity of the unknown current is $V_{\max} = 1$ [m/s] (the true value is $V_x = 0.28$ [m/s], $V_y = -0.86$ [m/s]). Thus, Assumptions 3.3 and 3.4 are fulfilled. The chosen values for the guidance law integral gain is $\sigma = 1$ [m/s] and satisfies (3.18). The internal speed and yaw controllers employed are of the feedback linearization type but other strategies can be used, such as PID or sliding mode. They make the vessel follow the desired references. The ship is given an initial cross track error of 1500 [m] and it has initially zero relative velocity, with the surge axis parallel to the desired path.

The length of the supply vessel has been set as a reference to choose the look-ahead distance Δ (the ship is approximately 80 [m] long). As shown in Figures 3.5a-3.5c, if look-ahead distances close to the the vessels length are chosen, the behavior of the ship becomes unstable and path convergence is hardly achieved. Clearly, in this situation Assumptions 3.5-3.7 are not valid anymore. However, higher values of Δ make the vessel converge smoothly. Figures 3.5d-3.5e show that the speed and heading controllers make sure that the references U_{rd} and ψ_d are followed fast enough so that Assumption 3.5 is satisfied. Finally, notice how the angle $\psi(t)$ converges smoothly to the expected value $\psi_{ss} \approx 12.3$ [deg], confirming what argued in Section 3.1.

3.5. Conclusions

In this chapter the ILOS guidance approach has been presented and applied to a simple kinematic model of surface vessels. An intuitive approach has been followed to make the reader understand the problem of disturbance compensation for underactuated marine vessels. In particular, constant irrotational ocean currents have been considered and it has been shown that the problem has one possible solution only. The integral LOS guidance is used to achieve side-slipping and compensate for the current where the closed loop system has been analyzed as a pure nonlinear kinematic problem. The analysis reveals UGAS as well as ULES stability properties and explicit conditions upon the choice of the integral gain σ are derived. Furthermore, it should be clear at this point that the choosing criteria upon the look-ahead distance Δ that are derived in the following chapters of this dissertation, will be inevitably affected by the properties of the underactuated sway dynamics of the vessel. This is suggested by the discussion of Section 3.2 and the simulation results of Section 3.4.

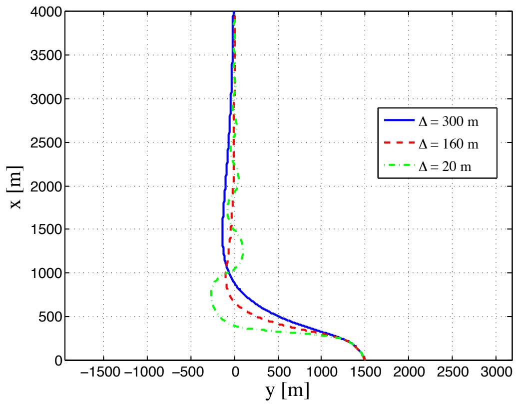

(a) Simulation of path following for different values of Δ.

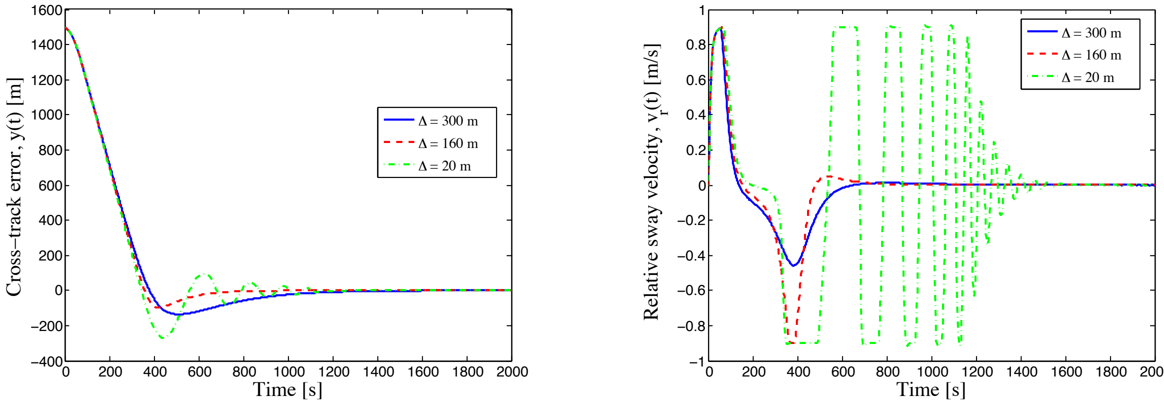

(b) Cross track error $y(t)$ for different values of Δ.

(c) Relative sway velocity $v_r(t)$ for different values of Δ.

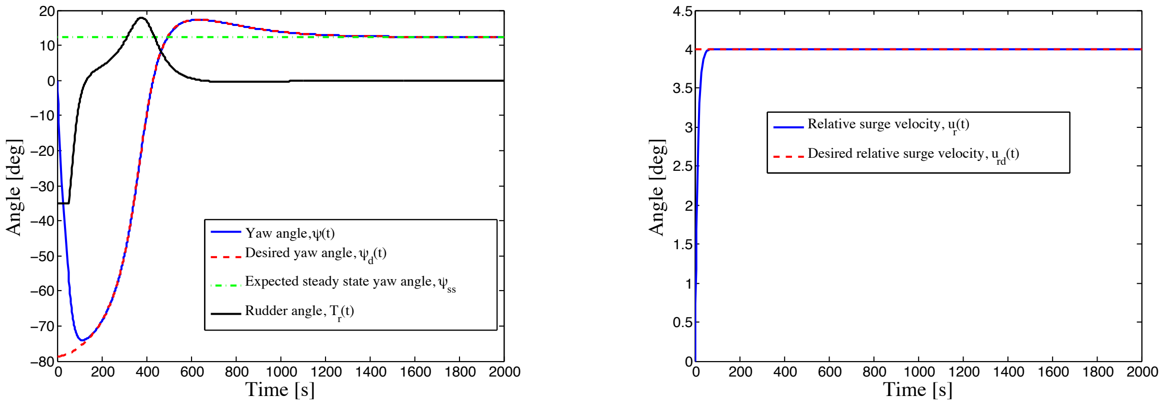

(d) Yaw $\psi(t)$ and rudder $T_r(t)$ angles for $\Delta = 300$ [m].

(e) Relative surge velocity $u_r(t)$ for $\Delta = 300$ [m].

Figure 3.5.: Simulation results.

Chapter 4.

A Kinematic Approach to the ILOS Guidance for Underwater Vehicles

"There is only one way to avoid criticism: do nothing, say nothing, and be nothing."
— Aristotle, Philosopher

In Chapter 3 a two dimensional Integral Line-of-Sight (ILOS) guidance law was applied to a simple kinematic model of a surface vessel. A discussion involving intuitive as well as practical aspects of the ILOS law was also given. In this chapter a three dimensional version of the same ILOS guidance system is presented and applied to a kinematic model of underactuated underwater vehicles. Path following of straight lines is considered and the explanation follows along the lines of Chapter 3. In particular, it is shown that current compensation for underactuated underwater vehicle reduces to a three dimensional vectorial sum that has exactly one possible solution. This solution identifies the only attitude the vehicle can hold to compensate for the drift, thus extending to 3D the concepts developed the in previous chapter for the planar motion case. Again, the relative velocity of the vessel is kept constant and compensation is achieved using the control surfaces only. The decoupling properties between the actuated dynamics and the underactuated dynamics of the LOS guidance scheme described in Chapter 3 are repeated and extended to the underactuated heave dynamics as well. Therefore, as a first approximation, the control problem is addressed at the kinematic level only. Similar kinematic approaches to solve guidance, control and ranging problems of underactuated underwater vehicles are found in [5, 73, 8], while autonomous aircraft are described with

3D kinematic models in [120] to develop collision avoidance strategies. Hence, a kinematic analysis represents a valuable design tool for integral LOS guidance schemes applied to underactuated marine vehicles as well. Finally, stability of the closed loop kinematic system is successfully analyzed and simulation results using a mathematical model of the HUGIN underactuated autonomous underwater vehicle (AUV) are presented.

The closed loop system analyzed in this chapter is the first example of a cascaded control problem solved in this thesis. It therefore represents a significant case despite its simplicity since the same concepts will be applied in far more complex cases addressed in this dissertation. This chapter is organized as follows: in Section 4.1 the current compensation problem for underactuated underwater vehicles is formulated and discussed, in Section 4.2 the 3D integral LOS guidance law is introduced and in Section 4.3 stability of the closed loop kinematic system is addressed. Finally, data from simulations are presented in Section 4.4 and conclusions are given in Section 4.5. The results presented in this chapter are based on [35].

4.1. Sea Current Compensation for Underwater Vehicles

In this section the path following control task is defined and the current compensation problem is described as a vectorial sum.

4.1.1. Basic Assumptions and Notation

Assumption 4.1. The roll motion of the vessel is assumed passively stabilized through fins or by gravity and therefore can be neglected limiting the analysis to a configuration space of 5 degrees of freedom: surge, sway, heave, pitch and yaw.

Remark 4.1. Assumption 4.1 is a common assumption in manoeuvring control of slender body underwater vehicles, see [52].

Assumption 4.2. The vehicle is underactuated in its configuration space: there is no actuation in sway and heave while control inputs are available in surge, pitch and yaw.

Remark 4.2. Most of underwater vehicles are equipped with a propeller as well as pitch and yaw rudders only, making them underactuated in sway and heave.

Assumption 4.3. The ocean current in the inertial frame i, $\boldsymbol{V}_c \triangleq [V_x, V_y, V_z]^T$ is constant, irrotational and bounded. Hence there exists $V_{\max} > 0$ such that $V_{\max} \geq \sqrt{V_x^2 + V_y^2 + V_z^2}$.

Since roll motion is neglected (see Assumption 4.1), the system state is given by the vector $\boldsymbol{\eta} \triangleq [x, y, z, \theta, \psi]^T$ and describes the position and the orientation of the vehicle with respect to the inertial frame i. In particular, θ is the vehicle pitch angle and ψ is the vehicle yaw angle. The vector $\boldsymbol{\nu} \triangleq [u, v, w, q, r]^T$ contains the linear and angular velocities defined in the body-fixed frame b, where u is the surge velocity, v is the sway velocity, w is the heave velocity, q is the pitch rate and r is the yaw rate. The ocean current linear velocity in the body frame b, $\boldsymbol{v}_c \triangleq [u_c, v_c, w_c]^T$, is obtained from $\boldsymbol{v}_c = \boldsymbol{R}^T(\theta, \psi)\boldsymbol{V}_c$ where $\boldsymbol{R}(\theta, \psi)$ is the rotation matrix from b to i:

$$\boldsymbol{R}(\theta, \psi) \triangleq \begin{bmatrix} \cos(\psi)\cos(\theta) & -\sin(\psi) & \cos(\psi)\sin(\theta) \\ \sin(\psi)\cos(\theta) & \cos(\psi) & \sin(\psi)\sin(\theta) \\ -\sin(\theta) & 0 & \cos(\theta) \end{bmatrix}. \tag{4.1}$$

According to Assumption 4.3 the ocean current is constant and irrotational in i, i.e. $\dot{\boldsymbol{V}}_c = \boldsymbol{0}$, therefore the current velocity in b becomes $\boldsymbol{\nu}_c \triangleq [u_c, v_c, w_c, 0, 0]^T$ and thus $\dot{\boldsymbol{\nu}}_c = [rv_c - qw_c, -ru_c, qu_c, 0, 0]^T$. In navigation problems involving ocean currents it is useful to introduce the relative velocity and [52] defines the relative velocity as the velocity of the vehicle with respect to the flow. Given the vector:

$$\boldsymbol{U} \triangleq \begin{bmatrix} \dot{x} \\ \dot{y} \\ \dot{z} \end{bmatrix} = \boldsymbol{R}(\theta, \psi) \begin{bmatrix} u \\ v \\ w \end{bmatrix}, \tag{4.2}$$

representing the linear velocity of the vehicle in the inertial frame i, the linear relative velocity $\boldsymbol{U}_r$ in i is:

$$\boldsymbol{U}_r \triangleq \boldsymbol{U} - \boldsymbol{V}_c. \tag{4.3}$$

Following (4.3), $\boldsymbol{\nu}_r \triangleq \boldsymbol{\nu} - \boldsymbol{\nu}_c = [u_r, v_r, w_r, q, r]^T$ is the relative velocity of the vessel in b. Therefore, $\boldsymbol{U}_r$ can be expressed as:

$$\boldsymbol{U}_r = \boldsymbol{R}(\theta, \psi)[u_r, v_r, w_r]^T. \tag{4.4}$$

To prevent the vehicle from drifting away, the relative surge velocity has to satisfy the following assumption:

Assumption 4.4. $U_{rd} > 2V_{\max}$.

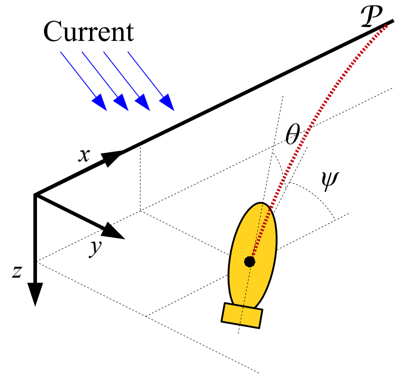

Figure 4.1.: The underactuated vehicle has to converge and follow the x axis.

4.1.2. The Path Following Control Problem

The control system should make the vehicle follow a given straight line $\mathcal{P}$ in space and maintain a desired constant surge relative velocity $U_{rd} > 0$. This should also hold in the presence of an unknown and constant ocean current $\boldsymbol{V}_c = [V_x, V_y, V_z]^T$. To simplify the problem without any loss of generality since coordinates can always be rotated given a desired direction in space, the inertial reference frame i is placed such that the z-axis points down and the x-axis is aligned with the desired path $\mathcal{P}$ (see Figure 4.1), giving $\mathcal{P} \triangleq \{(x, y, z) \in \mathbb{R}^3 : y = 0, z = 0\}$. The y and z coordinates then correspond to the horizontal and vertical cross-track errors and the goals of the control system become:

$$\lim_{t\to\infty} y(t) = 0, \tag{4.5}$$

$$\lim_{t\to\infty} z(t) = 0, \tag{4.6}$$

$$\lim_{t\to\infty} \psi(t) = \psi_{ss}, \quad \psi_{ss} \in \left(-\frac{\pi}{2}, \frac{\pi}{2}\right), \tag{4.7}$$

$$\lim_{t\to\infty} \theta(t) = \theta_{ss}, \quad \theta_{ss} \in \left(-\frac{\pi}{2}, \frac{\pi}{2}\right), \tag{4.8}$$

$$\lim_{t\to\infty} u_r(t) = U_{rd}, \tag{4.9}$$

where $u_r(t)$ is the surge relative speed of the vehicle and θ_{ss} as well as ψ_{ss} are constants. Notice that the angles $\psi(t)$ and $\theta(t)$ are not required to converge to zero but rather to steady-state constant values bounded within $-\frac{\pi}{2}$ and $\frac{\pi}{2}$. This allows the vehicle to hold non-zero yaw and pitch angles at equilibrium, and compensate for the ocean current as shown in Figure 4.2. This is necessary because the vehicle is underactuated and no control forces are available in sway and heave to counteract the drift. The values of ψ_{ss} and θ_{ss} will be specified later.

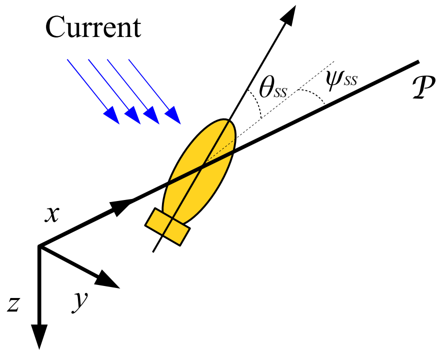

Figure 4.2.: Steady state condition: the vehicle side-slips and pitches with constant ψ_{ss} and θ_{ss} angles to compensate for the current.

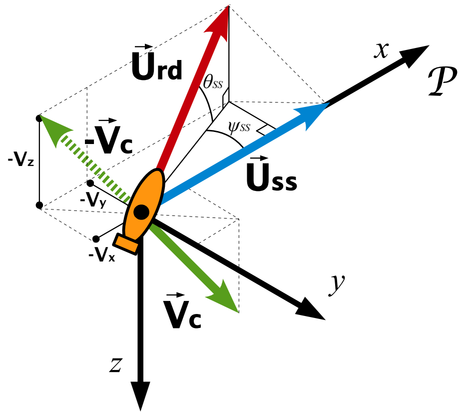

Figure 4.3.: Graphical solution of the current compensation problem for underactuated marine vehicles in 3D. The angles θ_{ss} and ψ_{ss} are given by (4.14) and (4.15).

4.1.3. Relative Velocity and Current Compensation

In the following paragraphs it is shown how simple mathematical considerations conclude that there is only one possible attitude (θ_{ss}, ψ_{ss}) the vehicle can hold to achieve current compensation. Since there is no actuation in sway and heave, it is not possible to have at the same time zero cross track errors as well as zero pitch and yaw angles. Non-zero ψ_{ss} and θ_{ss} angles are needed to use part of the vehicle's surge thrust for current compensation. Therefore, the control system has to find the constant steady state angles ψ_{ss} and θ_{ss} necessary to compensate and make θ and ψ converge to these. To find the values of ψ_{ss} and θ_{ss} consider the desired equilibrium condition shown in Figure 4.2 and Figure 4.3. Notice that at equilibrium the control objective (4.9) is considered achieved and $v_r \to 0$ as well as $w_r \to 0$. Hence, applying (4.4) concludes that $|\boldsymbol{U}_{rd}| = U_{rd}$ and that:

$$\lim_{t\to\infty} \boldsymbol{U}_r(t) = \boldsymbol{U}_{rd} \triangleq \boldsymbol{R}(\theta_{ss}, \psi_{ss})[U_{rd}, 0, 0]^T, \tag{4.10}$$

In order to make the vessel compensate for the drift and follow the desired course, the velocity $\boldsymbol{U}$ at equilibrium has to be oriented along the x axis (see Figure 4.3):

$$\lim_{t\to\infty} \boldsymbol{U}(t) = \boldsymbol{U}_{ss} \triangleq [U_{ss}, 0, 0]^T, \tag{4.11}$$

where $U_{ss} > 0$. According to (4.3), $\boldsymbol{U}_{ss}$ is the result of the following vectorial sum:

$$\boldsymbol{U}_{ss} = \boldsymbol{U}_{rd} + \boldsymbol{V}_c. \tag{4.12}$$

The ocean current vector $\boldsymbol{V}_c$, despite being unknown, is fully defined in magnitude and direction. The vector $\boldsymbol{U}_{rd}$ is defined in magnitude only since (θ_{ss}, ψ_{ss}) is to be determined, while the vector $\boldsymbol{U}_{ss}$ is defined in direction only. In principle, if the current $\boldsymbol{V}_c$ is known, it is possible to solve the vectorial equation and calculate the direction of $\boldsymbol{U}_{rd}$ and $U_{ss} > 0$. Geometrically, this corresponds at finding the intersections between the x axis and the sphere having radius U_{rd} and center in $\boldsymbol{V}_c$. The intersection having a positive U_{ss} is chosen. A real positive solution exists as long as $U_{rd} > |\boldsymbol{V}_c|$ which is guaranteed by Assumption 4.4. This is shown in two dimensions in Figure 4.4, where the space (see Figure 4.3) is cut along the plane defined by the x axis and $\boldsymbol{V}_c$. To conclude the analysis, it is possible to affirm that there exists only one possible vehicle attitude (θ_{ss}, ψ_{ss}) that satisfies (4.11) and guarantees current compensation as long as Assumption 4.4 is valid. Applying (4.12) leads to the following relation between U_{rd} and U_{ss}:

$$U_{ss} = \sqrt{U_{rd}^2 - V_y^2 - V_z^2} + V_x. \tag{4.13}$$

From simple geometrical considerations shown in Figure 4.3 it follows that:

$$\theta_{ss} = \tan^{-1}\left(\frac{V_z}{\sqrt{U_{rd}^2 - V_z^2}}\right), \tag{4.14}$$

$$\psi_{ss} = -\tan^{-1}\left(\frac{V_y}{\sqrt{U_{rd}^2 - V_z^2 - V_y^2}}\right). \tag{4.15}$$

The values (4.14) and (4.15) define the attitude the vehicle has to hold in order to follow the path $\mathcal{P}$ in presence of currents. From (4.14) it follows that Assumption 4.4 guarantees also robustness with respect to singularities at $\frac{\pi}{2}$ and $-\frac{\pi}{2}$ in pitch.

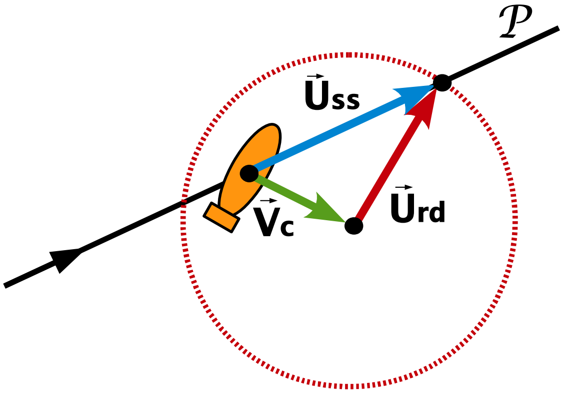

Figure 4.4.: Graphical solution of the current compensation problem for underactuated marine vehicles on the $x - \boldsymbol{V}_c$ plane.

Remark 4.3. Notice that in this discussion the current is considered known, therefore as long as the vehicle is underactuated, the attitude defined by (4.14) and (4.15) represents the only possible solution for the controller to solve the current compensation problem, independently of the implemented technique (adaptive laws, current observers or integral action). In this paper integral action inserted in the LOS guidance law is used to register the presence of ocean current and choose the attitude of the vehicle to precisely compensate for this.

4.2. The Integral LOS Guidance Law

This section presents the guidance strategy applied to solve the path following problem defined in Section 4.1. The ILOS guidance from Chapter 4 is extended to 3D and is interpreted as a decoupling tool between the kinematics and the kinetics of the system as a consequence of the arguments given in Section 3.2.

4.2.1. The Path Following Strategy

In order to solve the objectives (4.5-4.6) of the the path following control problem, the underwater vehicle has to converge to and follow the x-axis of the inertial frame i. To achieve the goal, the traditional LOS guidance reference generator used by [25] (see

Figure 4.5) would set the vessel heading and pitch angles to:

$$\theta_{LOS} \triangleq \tan^{-1}\left(\frac{z}{\Delta_z}\right), \quad \Delta_z > 0, \tag{4.16a}$$

$$\psi_{LOS} \triangleq -\tan^{-1}\left(\frac{y}{\Delta_y}\right), \quad \Delta_y > 0. \tag{4.16b}$$

The design parameters Δ_z and Δ_y are the look-ahead distances in the vertical plane and horizontal plane, respectively. Convergence is however not guaranteed if there are ocean currents acting on the vehicle since (4.16a) and (4.16b) do not allow the vessel to side-slip and pitch once it has converged to $\mathcal{P}$. To solve the problem, integral action is introduced in both the heading and pitch references, defining the integral LOS guidance:

$$\theta_{ILOS} \triangleq \tan^{-1}\left(\frac{z + \sigma_z z_{\text{int}}}{\Delta_z}\right), \tag{4.17a}$$

$$\dot{z}_{\text{int}} = \frac{\Delta_z z}{(z + \sigma_z z_{\text{int}})^2 + \Delta_z^2}, \tag{4.17b}$$

$$\psi_{ILOS} \triangleq -\tan^{-1}\left(\frac{y + \sigma_y y_{\text{int}}}{\Delta_y}\right), \tag{4.17c}$$

$$\dot{y}_{\text{int}} = \frac{\Delta_y y}{(y + \sigma_y y_{\text{int}})^2 + \Delta_y^2}. \tag{4.17d}$$

The look-ahead distances $\Delta_y, \Delta_z > 0$ and the gains $\sigma_y, \sigma_z > 0$ are design parameters. The integral effects give nonzero LOS angles (4.17a) and (4.17c), allowing the vessel to side-slip and pitch while staying on the desired path, so part of its relative forward velocity can counteract the effect of the ocean current. The integration laws (4.17b) and

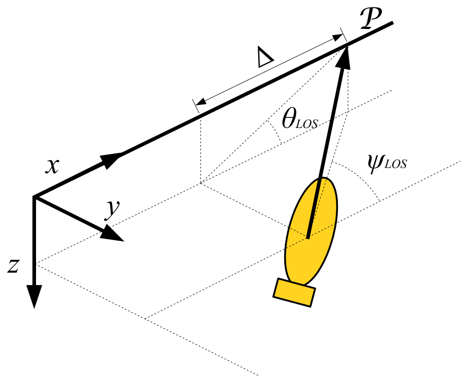

Figure 4.5.: Line of sight guidance for an underactuated underwater vehicle with $\Delta_y = \Delta_z = \Delta$.

(4.17d) were first introduced by [26] and are chosen to give less integral action when the vehicle is far from the desired path and thereby reduce the risk of wind-up effects.

4.2.2. 3D Line-of-Sight and Underactuation

The decoupling properties of the LOS guidance law between the actuated and underactuated dynamics of the vehicle are discussed in Section 3.2 for surface vessels. The same arguments applies to the 3D LOS introduced in [25]. This can be shown by analyzing the closed loop underactuated heave and sway dynamics of the AUV vehicle given in [25, Equation (34)] and [25, Equation (47)], respectively. The heave dynamics are considered first:

$$\begin{aligned}\dot{\bar{w}} = {} & \left(\frac{-X_{\bar{w}}(u_c)u_c\Delta_z}{(e_z^2+\Delta_z^2)^{3/2}} + \frac{Z_{\bar{w}}}{\sqrt{e_z^2+\Delta_z^2}}\right)e_z + \left(Y_{\bar{w}}(u_c) + \frac{X_{\bar{w}}(u_c)\Delta_z^2}{(e_z^2+\Delta_z^2)^{3/2}}\right)\bar{w} \\ & + \left[X_{\bar{w}}(u_c+\tilde{u})\frac{\Delta_z}{e_z^2+\Delta_z^2}\boldsymbol{h}_{e_z}^T + \boldsymbol{h}_{\bar{w}}^T\right]\boldsymbol{\xi},\end{aligned} \tag{4.18}$$

where the functions $X_{\bar{w}}(\cdot)$ and $Y_{\bar{w}}(\cdot)$ are bounded for bounded arguments and u_c is the desired surge velocity. The function $Y_{\bar{w}}(\cdot)$ is assumed to be negative for all the values of u_c. The vector $\boldsymbol{\xi}$ converges to zero exponentially and represents the dynamics of the speed and pitch controllers. The state variables e_z and $\bar{w}$ are the cross track error in the vertical plane and the heave velocity of the vehicle respectively. Finally, notice that Δ_z is the look-ahead distance in the vertical plane.

Two facts can be noticed by carefully analyzing (4.18): first, the faster the speed and pitch controllers, the faster the term proportional to $\boldsymbol{\xi}$ vanishes. Second, the longer the look-ahead distance Δ_z, the less the coupling terms in (4.18) count. Thus, setting a large Δ_z and having fast speed and heading controllers, ideally decouples the heave dynamics from the rest and the fact that $Y_{\bar{w}}(\cdot)$ is negative guarantees $\bar{w} \to 0$. In other words the further ahead the LOS guidance law looks, the smoother the turn. Similar arguments apply to the sway dynamics:

$$\begin{aligned}\dot{\bar{v}} = {} & \frac{X_{\bar{v}}(u_c)u_c\Delta}{(e_y^2+\Delta_y^2)^{3/2}}e_y + \left(Y_{\bar{v}}(u_c) - \frac{X_{\bar{v}}(u_c)\Delta_y^2}{(e_y^2+\Delta_y^2)^{3/2}}\right)\bar{v} \\ & + \left[-X_{\bar{v}}(u_c+\tilde{u})\frac{\Delta_y\cos(\theta)}{e_y^2+\Delta_y^2}\boldsymbol{h}_{e_y}^T + \boldsymbol{h}_{\bar{v}}^T\right]\boldsymbol{\zeta}.\end{aligned} \tag{4.19}$$

Again the functions $X_{\bar{v}}(\cdot)$ and $Y_{\bar{v}}(\cdot)$ are bounded for bounded arguments. The function $Y_{\bar{v}}(\cdot)$ is assumed to be negative for all the values of u_c while the vector $\boldsymbol{\zeta}$ converges to zero exponentially and represents the dynamics of the speed, pitch and yaw controllers. The coupling of the UGAS and ULES heave dynamics is also included in $\boldsymbol{\zeta}$ and the longer Δ_z the weaker the coupling. The state variables e_y and $\bar{v}$ are the cross track error in the horizontal plane and the sway velocity of the vehicle respectively. Δ_y is the look-ahead distance in the horizontal plane.

Equation (4.18) shows that the faster the speed, pitch and yaw controllers and the longer Δ_z, the faster the term proportional to $\boldsymbol{\zeta}$ vanishes. Furthermore, the longer the horizontal look-ahead distance Δ_y, the less the coupling terms in (4.19) are significant. Thus, setting large Δ_z and Δ_y and having fast speed, pitch and heading controllers, ideally decouples the heave dynamics from the rest and the fact that $Y_{\bar{w}}(\cdot)$ is negative guarantees that $\bar{v} \to 0$. Therefore, the following assumptions are introduced:

Assumption 4.5. The underactuated underwater vehicle has internal controllers setting the desired relative surge velocity and the desired pitch and yaw angles.

Assumption 4.6. The internal controllers are assumed to be fast compared to the guidance law: the delay between the time the references are given by the guidance law and the time they are actually set by the controllers is small enough not to affect significantly the guidance dynamics.

Assumption 4.7. The look-ahead distances Δ_y and Δ_z are assumed big enough so that the control surfaces do not affect significantly the sway and heave dynamics. Therefore it is possible to consider $v_r \approx 0$ and $w_r \approx 0$.

Remark 4.4. Applying Assumptions 4.5-4.7 to the issue addressed in this paper leads to a pure kinematic problem: Assumptions 4.5 and 4.6 guarantee that the reference LOS angles (4.17a) and (4.17c) are followed and that the relative surge velocity u_r is set to U_{rd} while Assumption 4.7 states that the unactuated sway and heave dynamics can be neglected.

Remark 4.5. [5, 120] solved underactuated control problems as kinematic problems using control laws derived from the Lyapunov analysis. Here the problem is similar but the kinematic control law has been chosen before testing any stability.

Remark 4.6. It is hard to tell quantitatively how fast the internal speed and attitude controllers must be and how long the look-ahead distances Δ_y and Δ_z must be so that Assumptions 4.5-4.7 are realistic. This depends on physical characteristics of the vehicle.

Therefore, a good model of the vessel and simulations play a key role in this approach (see Section 4.4).

Following Assumption 4.3, Assumptions 4.5-4.7 and (4.3-4.4) the kinematic system is:

$$\dot{x} = U_{rd}\cos(\psi_d)\cos(\theta_d) + V_x, \tag{4.20}$$

$$\dot{y} = U_{rd}\sin(\psi_d)\cos(\theta_d) + V_y, \tag{4.21}$$

$$\dot{z} = -U_{rd}\sin(\theta_d) + V_z, \tag{4.22}$$

where $\theta_d \triangleq \theta_{ILOS}$ and $\psi_d \triangleq \psi_{ILOS}$ are the control inputs, with (4.17) closing the loop.

4.3. Stability of the Closed Loop Kinematic System

In this section the conditions under which the proposed guidance law achieves the goals (4.5-4.8) are given.

Theorem 4.1. *Given an underactuated underwater vehicle whose kinematics are described by (4.20-4.22), if Assumptions 4.1-4.7 hold and if the integral gains σ_y, σ_z satisfy the conditions:*

$$0 < \sigma_y < U_{rd} - 2V_{\max}, \tag{4.23}$$

$$0 < \sigma_z < U_{rd} - V_{\max}, \tag{4.24}$$

then the guidance law (4.17) *guarantees achievement of the control objectives (4.5-4.8). Notice that the reference signals θ_d and ψ_d are defined by* (4.17a) *and* (4.17c)*. The control objectives (4.7-4.8) are fulfilled with ψ_{ss} and θ_{ss} given in* (4.15) *and* (4.14)*, respectively.*

Proof. The dynamics of the cross track error z are analyzed first. The z subsystem is obtained from (4.22) and (4.17b):

$$\dot{z}_{\text{int}} = \frac{\Delta_z z}{(z + \sigma_z z_{\text{int}})^2 + \Delta_z^2}, \tag{4.25}$$

$$\dot{z} = -U_{rd}\sin(\theta_d) + V_z. \tag{4.26}$$

Substituting (4.17a) for θ_d gives $\sin(\theta_d) = (z + \sigma_z z_{\text{int}})/\sqrt{(z + \sigma_z z_{\text{int}})^2 + \Delta_z^2})$ and leads (4.26-4.25) to:

$$\dot{z}_{\text{int}} = \frac{\Delta_z z}{(z + \sigma_z z_{\text{int}})^2 + \Delta_z^2}, \tag{4.27}$$

$$\dot{z} = -U_{rd} \frac{z + \sigma_z z_{\text{int}}}{\sqrt{(z + \sigma_z z_{\text{int}})^2 + \Delta_z^2}} + V_z. \tag{4.28}$$

The equilibrium point of the system (4.28-4.27) is given by:

$$z_{\text{int}}^{\text{eq}} = \frac{\Delta_z}{\sigma_z} \frac{V_z}{\sqrt{U_{rd}^2 - V_z^2}}, \quad z^{\text{eq}} = 0. \tag{4.29}$$

A new set of variables is introduced to move the equilibrium point to the origin:

$$e_{z1} \triangleq z_{\text{int}} - z_{\text{int}}^{\text{eq}}, \quad e_{z2} \triangleq z + \sigma_z e_{z1}. \tag{4.30}$$

The transformed z dynamics become:

$$\dot{e}_{z1} = -\frac{\Delta_z \sigma_z e_{z1}}{(e_{z2} + \sigma_z z_{\text{int}}^{\text{eq}})^2 + \Delta_z^2} + \frac{\Delta_z e_{z2}}{(e_{z2} + \sigma_z z_{\text{int}}^{\text{eq}})^2 + \Delta_z^2}, \tag{4.31}$$

$$\begin{aligned} \dot{e}_{z2} = &- \left[U_{rd} \sqrt{(e_{z2} + \sigma_z z_{\text{int}}^{\text{eq}})^2 + \Delta_z^2} - \sigma_z \Delta_z \right] \frac{e_{z2}}{(e_{z2} + \sigma_z z_{\text{int}}^{\text{eq}})^2 + \Delta_z^2} \\ &- \frac{\Delta_z \sigma_z^2 e_{z1}}{(e_{z2} + \sigma_z z_{\text{int}}^{\text{eq}})^2 + \Delta_z^2} + V_z f(e_{z2}), \end{aligned} \tag{4.32}$$

where:

$$f(e_{z2}) = 1 - \frac{\sqrt{(\sigma_z z_{\text{int}}^{\text{eq}})^2 + \Delta_z^2}}{\sqrt{(e_{z2} + \sigma_z z_{\text{int}}^{\text{eq}})^2 + \Delta_z^2}}, \tag{4.33}$$

and the following bound holds for $f(e_{z2})$:

$$|f(e_{z2})| \leq \frac{|e_{z2}|}{\sqrt{(e_{z2} + \sigma_z z_{\text{int}}^{\text{eq}})^2 + \Delta_z^2}}. \tag{4.34}$$

The system (4.31-4.32) is equivalent to the system (3.25-3.26) analyzed in Chapter 3. Therefore, Theorem 3.1 can be applied and it is hence possible to conclude UGAS and ULES for the system (4.31-4.32).

The dynamics of the horizontal cross track error y are analyzed next. The y subsystem is obtained from (4.21) and (4.17d):

$$\dot{y}_{\text{int}} = \frac{\Delta_y y}{(y + \sigma_y y_{\text{int}})^2 + \Delta_y^2}, \tag{4.35}$$

$$\dot{y} = U_{rd} \sin(\psi_d) \cos(\theta_d) + V_y. \tag{4.36}$$

Substituting (4.17c) for θ_d and (4.17a) for ψ_d gives $\cos(\theta_d) = \Delta_z / \sqrt{(z + \sigma_z z_{\text{int}})^2 + \Delta_z^2}$ and $\sin(\psi_d) = -(y + \sigma_y y_{\text{int}}) / \sqrt{(y + \sigma_y y_{\text{int}})^2 + \Delta_y^2}$. Factorizing the result with respect to e_{z2}, leads (4.36) to the following expression for the y dynamics:

$$\dot{y}_{\text{int}} = \frac{\Delta_y y}{(y + \sigma_y y_{\text{int}})^2 + \Delta_y^2}, \tag{4.37}$$

$$\dot{y} = -\sqrt{U_{rd}^2 - V_z^2} \frac{y + \sigma_y y_{\text{int}}}{\sqrt{(y + \sigma_y y_{\text{int}})^2 + \Delta_y^2}} + V_y + h(y, y_{\text{int}}, e_{z2}) e_{z2}, \tag{4.38}$$

where the perturbation term is:

$$h(y, y_{\text{int}}, e_{z2}) = \frac{U_{rd} \sin(\psi_d)}{e_{z2}} \left[\frac{\Delta_z}{\sqrt{(e_{z2} + \sigma_z z_{\text{int}}^{\text{eq}})^2 + \Delta_z^2}} - \frac{\sqrt{U_{rd}^2 - V_z^2}}{U_{rd}} \right]. \tag{4.39}$$

Notice that the limit of $h(y, y_{\text{int}}, e_{z2})$ for $e_{z2} \to 0$ exists and is finite and that the heave dynamics (4.31-4.32) perturb the y dynamics (4.37-4.38). Consider the nominal system defined on the manifold $e_{z2} = 0$:

$$\dot{y}_{\text{int}} = \frac{\Delta_y y}{(y + \sigma_y y_{\text{int}})^2 + \Delta_y^2}, \tag{4.40}$$

$$\dot{y} = -\sqrt{U_{rd}^2 - V_z^2} \frac{y + \sigma_y y_{\text{int}}}{\sqrt{(y + \sigma_y y_{\text{int}})^2 + \Delta_y^2}} + V_y. \tag{4.41}$$

Its equilibrium point is given by:

$$y_{\text{int}}^{\text{eq}} = \frac{\Delta_y}{\sigma_y} \frac{V_y}{\sqrt{U_{rd}^2 - V_z^2 - V_y^2}}, \quad y^{\text{eq}} = 0. \tag{4.42}$$

The following variables are introduced to move the equilibrium point to the origin:

$$e_{y1} \triangleq y_{\text{int}} - y_{\text{int}}^{\text{eq}}, \quad e_{y2} \triangleq y + \sigma_z e_{y1}, \tag{4.43}$$

The transformed nominal system becomes:

$$\dot{e}_{y1} = -\frac{\Delta_y \sigma_y e_{y1}}{\left(e_{y2} + \sigma_y y_{\text{int}}^{\text{eq}}\right)^2 + \Delta_y^2} + \frac{\Delta_y e_{y2}}{\left(e_{y2} + \sigma_y y_{\text{int}}^{\text{eq}}\right)^2 + \Delta_y^2}, \tag{4.44}$$

$$\begin{aligned} \dot{e}_{y2} = &-\left[\sqrt{U_{rd}^2 - V_z^2}\sqrt{(e_{y2} + \sigma_y y_{\text{int}}^{\text{eq}})^2 + \Delta_y^2} - \sigma_y \Delta_y\right] \frac{e_{y2}}{\left(e_{y2} + \sigma_y y_{\text{int}}^{\text{eq}}\right)^2 + \Delta_y^2} \\ &- \frac{\Delta_y \sigma_y^2 e_{y1}}{\left(e_{y2} + \sigma_y y_{\text{int}}^{\text{eq}}\right)^2 + \Delta_y^2} + V_y g(e_{y2}), \end{aligned} \tag{4.45}$$

where:

$$g(e_{y2}) = 1 - \frac{\sqrt{(\sigma_y y_{\text{int}}^{\text{eq}})^2 + \Delta_y^2}}{\sqrt{(e_{y2} + \sigma_y y_{\text{int}}^{\text{eq}})^2 + \Delta_y^2}}, \tag{4.46}$$

and the following bound holds for $g(e_{y2})$:

$$|g(e_{y2})| \leq \frac{|e_{y2}|}{\sqrt{(e_{y2} + \sigma_y y_{\text{int}}^{\text{eq}})^2 + \Delta_y^2}}. \tag{4.47}$$

The nominal system (4.44-4.45) is equivalent to the system (3.25-3.26) analyzed in Section 3.3. Therefore, Theorem 3.1 can be applied and it is thus possible to conclude UGAS and ULES for the system (4.44-4.45). Finally, the interconnected y and z dynamics obtained from (4.31-4.32), (4.39) and (4.44-4.45) are considered:

$$\dot{\boldsymbol{e}}_y = \boldsymbol{A}_2(e_{y2})\boldsymbol{e}_y + \boldsymbol{B}_2(e_{y2}) + \boldsymbol{H}(y, y_{\text{int}}, e_{z2})\boldsymbol{e}_z, \tag{4.48a}$$

$$\dot{\boldsymbol{e}}_z = \boldsymbol{A}_1(e_{z2})\boldsymbol{e}_z + \boldsymbol{B}_1(e_{z2}), \tag{4.48b}$$

where $\boldsymbol{e}_y \triangleq [e_{y1}, e_{y2}]^T$, $\boldsymbol{e}_z \triangleq [e_{z1}, e_{z2}]^T$ and:

$$\boldsymbol{A}_1(e_{z2}) \triangleq \begin{bmatrix} \frac{-\Delta_z \sigma_z}{\left(e_{z2}+\sigma_z z_{\text{int}}^{\text{eq}}\right)^2+\Delta_z^2} & \frac{\Delta_z}{\left(e_{z2}+\sigma z_{\text{int}}^{\text{eq}}\right)^2+\Delta_z^2} \\ \frac{-U_{rd}\sqrt{(e_{z2}+\sigma_z z_{\text{int}}^{\text{eq}})^2+\Delta_z^2}+\sigma_z \Delta_z}{\left(e_{z2}+\sigma_z z_{\text{int}}^{\text{eq}}\right)^2+\Delta_z^2} & \frac{-\Delta_z \sigma_z^2}{\left(e_{z2}+\sigma_z z_{\text{int}}^{\text{eq}}\right)^2+\Delta_z^2} \end{bmatrix}, \tag{4.49}$$

$$\boldsymbol{A}_2(e_{y2}) \triangleq \begin{bmatrix} \frac{-\Delta_y \sigma_y}{\left(e_{y2}+\sigma_y y_{\text{int}}^{\text{eq}}\right)^2+\Delta_y^2} & \frac{\Delta_y}{\left(e_{y2}+\sigma y_{\text{int}}^{\text{eq}}\right)^2+\Delta_y^2} \\ \frac{-\sqrt{U_{rd}^2-V_z^2}\sqrt{(e_{y2}+\sigma_y y_{\text{int}}^{\text{eq}})^2+\Delta_y^2}+\sigma_y \Delta_y}{\left(e_{y2}+\sigma_y y_{\text{int}}^{\text{eq}}\right)^2+\Delta_y^2} & \frac{-\Delta_y \sigma_y^2}{\left(e_{y2}+\sigma_y y_{\text{int}}^{\text{eq}}\right)^2+\Delta_y^2} \end{bmatrix}, \tag{4.50}$$

$$\boldsymbol{B}_1(e_{z2}) \triangleq \begin{bmatrix} 0 \\ V_z f(e_{z2}) \end{bmatrix}, \quad \boldsymbol{B}_2(e_{y2}) \triangleq \begin{bmatrix} 0 \\ V_y g(e_{y2}) \end{bmatrix}, \quad \boldsymbol{H}(y, y_{\text{int}}, e_{z2}) \triangleq \begin{bmatrix} 0 & 0 \\ 0 & h(y, y_{\text{int}}, e_{z2}) \end{bmatrix}. \tag{4.51}$$

The system (4.48) is a nonlinear cascaded system where the z dynamics (4.48b) perturb the y dynamics (4.48a) through the interconnection term $\boldsymbol{H}(y, y_{\text{int}}, e_{z2})$. In particular the perturbing system (4.48b) is UGAS and ULES while the system (4.48a) is UGAS and ULES on the manifold $\boldsymbol{e}_z = \mathbf{0}$. Furthermore, the interconnection term $\boldsymbol{H}(y, y_{\text{int}}, e_{z2})$ can be shown to satisfy $\| \boldsymbol{H} \| \leq \theta_1(\| \boldsymbol{e}_z \|)(|y| + |y_{\text{int}}|) + \theta_2(\| \boldsymbol{e}_z \|)$, where $\theta_1(\cdot)$, $\theta_2(\cdot)$ are some continuous non-negative functions. Therefore applying Theorem A.2 and Lemma A.2 shows UGAS and ULES for the cascaded system (4.48). $\square$

To conclude, under the conditions of Theorem 4.1, the origin of the system (4.48) is UGAS and ULES. Therefore, the control objectives (4.5-4.8) are achieved with exponential converging properties in any ball of initial conditions.

Remark 4.7. Notice that the values of $z_{\text{int}}^{\text{eq}}$ and $y_{\text{int}}^{\text{eq}}$ make sure that at equilibrium the vessel holds the attitude (θ_{ss}, ψ_{ss}) defined in (4.14-4.15) which is, as explained in Section 4.1, the only possible orientation that guarantees successful current compensation for underactuated underwater vehicles.

4.4. Simulations

In this section results from numerical simulation are presented. In particular, the developed control strategy is applied to the HUGIN AUV. The model of the AUV is given in Section B.4 of Appendix B. The objective is to make the vehicle follow the path $\mathcal{P}$ with a desired surge relative speed $U_{rd} = 1$ [m/s]. The maximum intensity of the current is $V_{\max} = 1/3$ [m/s] and its true value is $\boldsymbol{V}_c = [0.07, -0.16, 0.10]^T$ [m/s]. Thus, Assumptions 4.3 and 4.4 are fulfilled. The chosen values for the guidance law integral gains are $\sigma_y = \sigma_z = 0.3$ [m/s] and satisfy (4.23) and (4.24). The internal speed, pitch and yaw controllers employed are of the feedback linearization type but other strategies can be used, such as PID or sliding mode. They make the vehicle follow the desired references. The vehicle is given an initial cross track error of 25 [m] in the horizontal as well as vertical directions and initially has zero relative velocity. Its surge axis is parallel to the desired path.

To choose the look-ahead distances Δ_y and Δ_z, the AUV length has been set as a reference (the HUGIN AUV is approximately 5 [m] long). As shown in Figures 4.6a-4.6e, if look-ahead distances close to the the vessel's length are chosen, the behavior of the vehicle becomes unstable and path convergence is not achieved. Clearly, in this situation

Assumptions 4.5-4.7 are not valid anymore. However, higher values of Δ_y and Δ_z make the vehicle converge smoothly. A closer look to Figure 4.6d reveals that the heave relative velocity doesn't converge to zero but rather to a steady state small value. This is caused by gravity restoring forces. Figures 4.7a-4.7c show that the speed, pitch and yaw controllers make sure that the reference U_{rd}, ψ_d and θ_d are followed fast enough so that Assumptions 4.5 is satisfied. Finally, notice in Figures 4.7b-4.7c how the angles $\theta(t)$ and $\psi(t)$ converge smoothly to the expected values $\theta_{ss} \approx 5.9$ [deg] and $\psi_{ss} \approx 9.1$ [deg], confirming the discussion given in Section 4.1. Again, the little discrepancy between $\theta(t)$ and θ_{ss} is due to gravity.

4.5. Conclusions

In this chapter a 3D version of the ILOS guidance introduced in Chapter 3 has been presented and applied to a simple kinematic model of underactuated underwater vehicles. The intuitive approach followed in Chapter 3 has been repeated and extended for underactuated underwater vehicles moving in a 3D space. In particular, 3D constant irrotational ocean currents have been considered and it has been shown that the problem has one possible solution only. The integral LOS guidance is used to hold non-zero pitch and yaw angles at equilibrium and thus compensate for the current. The closed loop system has been analyzed revealing a cascaded structure with UGAS and ULES stability properties. Explicit conditions upon the choice of the integral gains σ_y and σ_z are derived. Given the discussion of Section 4.2 and the simulation results of Section 4.4, one should expect that the stability conditions upon Δ_z and Δ_z that are derived in the following chapters of this dissertation, will be inevitably affected by the properties of the underactuated sway and heave dynamics of the vessel.

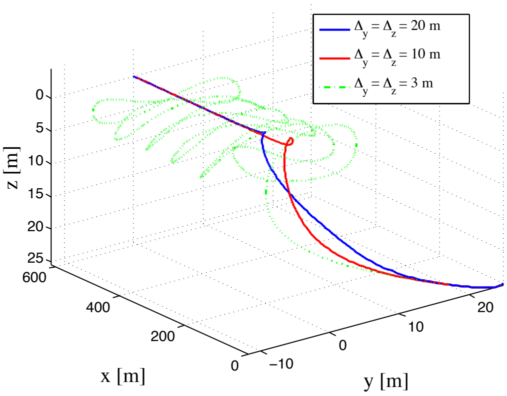

(a) Path following for different values of Δ_y and Δ_z.

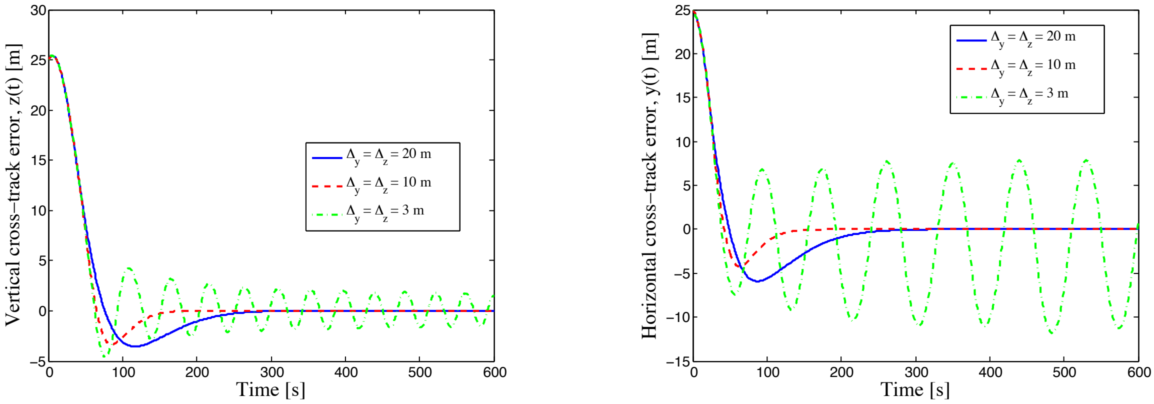

(b) Cross track error $y(t)$ for different values of Δ_y and Δ_z.

(c) Cross track error $z(t)$ for different values of Δ_y and Δ_z.

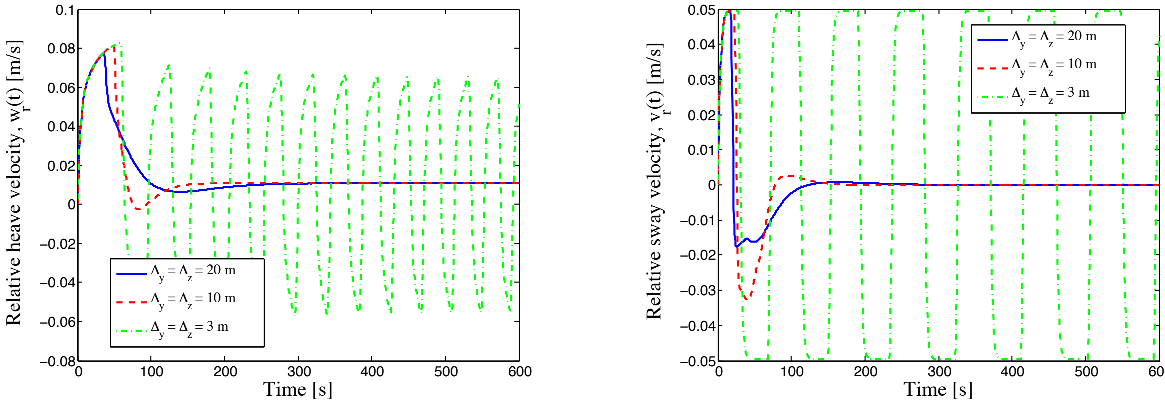

(d) Relative heave velocity $w_r(t)$ for different Δ_y and Δ_z.

(e) Relative sway velocity $v_r(t)$ for different Δ_y and Δ_z.

Figure 4.6.: Simulation results for different values of Δ_y and Δ_z.

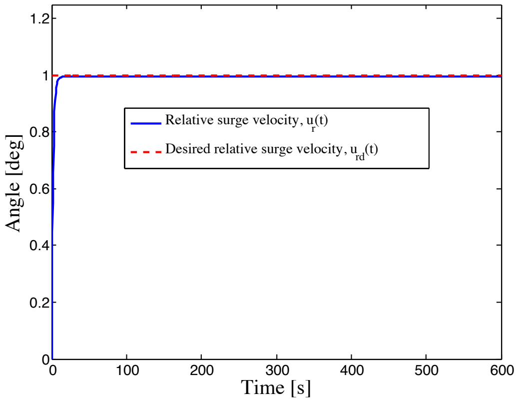

(a) Relative surge velocity $u_r(t)$ for $\Delta_y = \Delta_z = 20$ [m].

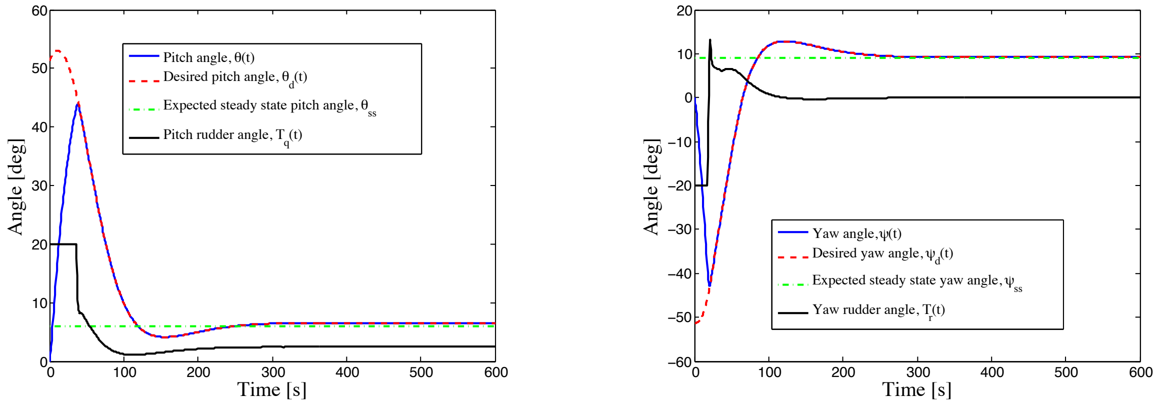

(b) Pitch $\theta(t)$ and rudder $T_q(t)$ angles for $\Delta_y = \Delta_z = 20$ [m].

(c) Yaw $\psi(t)$ and rudder $T_r(t)$ angles for $\Delta_y = \Delta_z = 20$ [m].

Figure 4.7.: Simulation results for $\Delta_y = \Delta_z = 20$[m].

Chapter 5.

The Underactuated Dynamics in ILOS Guidance Schemes

"Whatever you can do or dream you can, begin it. Boldness has genius, power and magic in it!"
— Johann Wolfgang von Goethe, Writer

In Chapters 3 and 4 the Integral Line-of-Sight (ILOS) guidance scheme was applied to simple kinematic models of surface vessels and underwater vehicles to achieve path following in the presence of unknown, constant and irrotational ocean currents. The kinematic models were obtained by not taking into account both the underactuated and the actuated dynamics, leading to an intuitive first step approach. The resulting analysis of the closed loop systems gave explicit bounds on the integral gains but did not give any guidelines on how to choose the look-ahead distances of the ILOS. It is argued in Sections 3.2 and 4.2 that the look-ahead distances should be 'long enough' to make the underactuated sway and heave dynamics insignificant and this argument is confirmed by the simulation results shown in Sections 3.4 and 4.4. In Sections 3.4 and 4.4 the rule of thumb to consider two times the physical length of the vehicle as the lower limit for the choice of the look-ahead distances is used.

In this chapter explicit bounds for the choice of the ILOS guidance look-ahead distance are derived. This is done by including the underactuated dynamics into the Lyapunov analysis. Disturbances in the form of constant irrotational ocean currents and constant dynamic, attitude dependent, forces are taken into account. Furthermore, more precise bounds upon the integral gains are obtained as well. A 3-DOFs planar motion scenario is considered with sway being the underactuated dynamics. The actuated dynamics are not taken into account under the assumption that there are a closed loop speed controller and a closed loop autopilot system setting the speed and the heading of the vessel. The mathematical complexity of the analysis increases significantly compared to Chapters 3 and 4 and it is shown that the properties of the underactuated dynamics determine the criteria for the choice of the look-ahead distance of the ILOS guidance. This confirms the intuitive arguments discussed in Sections 3.2 and 4.2.

This chapter is organized as follows: in Section 5.1 the model of the vessel that includes the sway dynamics is presented, in Section 5.2 the integral LOS guidance law is introduced and in Section 5.3 the stability properties of the closed loop system are given. The stability analysis is given in Section 5.4. Finally, conclusions are given in Section 5.5. The results presented in this chapter represent the generalization of some of the analysis methods used in the papers [28, 34, 31, 36, 29].

5.1. The Model of the Vessel and the Control Objective

In this section the model of the vessel that includes the sway dynamics is presented and the control objective is defined. The actuated surge and yaw dynamics are not taken into account. Some basic assumptions are first introduced, followed by the description of the notation used in this chapter.

5.1.1. Basic Assumptions and Notation

To clarify the forthcoming analysis some assumptions are introduced together with the symbols and physical quantities used in this chapter.

Assumption 5.1. The motion of the vessel is described of 3 degrees of freedom: surge, sway and yaw.

Assumption 5.2. The ocean current is defined in the inertial frame i and assumed constant, unknown, irrotational and bounded. Hence $\boldsymbol{V}_c \triangleq [V_x, V_y]^T$ and there exists $V_{\max} > 0$ such that $V_{\max} \geq \sqrt{V_x^2 + V_y^2}$.

Following Assumption 3.1, the system state is given by the vector $\boldsymbol{\eta} \triangleq [x, y, \psi]^T$ and describes the position and the orientation of the vessel with respect to the inertial frame i. In particular ψ is the yaw angle of the vessel. The vector $\boldsymbol{\nu} \triangleq [u, v, r]^T$ contains the linear and angular velocities defined in the body-fixed frame b, where u is the surge velocity, v is the sway velocity and r is the yaw rate. The ocean current linear velocity in the body frame b, $\boldsymbol{\nu}_c \triangleq [u_c, v_c, 0]^T$, is obtained from $\boldsymbol{\nu}_c = \boldsymbol{R}^T(\psi)[\boldsymbol{V}_c^T, 0]^T$ where $\boldsymbol{R}(\psi)$ is the rotation matrix from b to i:

$$\boldsymbol{R}(\psi) \triangleq \begin{bmatrix} \cos(\psi) & -\sin(\psi) & 0 \\ \sin(\psi) & \cos(\psi) & 0 \\ 0 & 0 & 1 \end{bmatrix}. \tag{5.1}$$

According to Assumption 3.3 the ocean current is constant and irrotational in i, i.e. $\dot{\boldsymbol{V}}_c = \boldsymbol{0}$, therefore $\dot{\boldsymbol{\nu}}_c = [rv_c, -ru_c, 0]^T$. In navigation problems involving ocean currents it is common to introduce the relative velocity. [52] defines the relative velocity as the velocity of the vessel with respect to the flow. Given the vector:

$$\boldsymbol{U} \triangleq \begin{bmatrix} \dot{x} \\ \dot{y} \end{bmatrix} = \begin{bmatrix} \cos(\psi) & -\sin(\psi) \\ \sin(\psi) & \cos(\psi) \end{bmatrix} \begin{bmatrix} u \\ v \end{bmatrix}, \tag{5.2}$$

representing the linear velocity of the vessel in the inertial frame i, the linear relative velocity $\boldsymbol{U}_r$ in i is:

$$\boldsymbol{U}_r \triangleq \boldsymbol{U} - \boldsymbol{V}_c. \tag{5.3}$$

Following (5.3), $\boldsymbol{\nu}_r \triangleq \boldsymbol{\nu} - \boldsymbol{\nu}_c = [u_r, v_r, r]^T$ is the relative velocity of the vessel in b. Therefore, $\boldsymbol{U}_r$ can be expressed as:

$$\boldsymbol{U}_r = \begin{bmatrix} \cos(\psi) & -\sin(\psi) \\ \sin(\psi) & \cos(\psi) \end{bmatrix} \begin{bmatrix} u_r \\ v_r \end{bmatrix}. \tag{5.4}$$

5.1.2. The Dynamics of the Relative Sway Velocity

The dynamics of the underactuated relative sway velocity v_r are modeled as:

$$\dot{v}_r = X(u_r)r + Y(u_r)v_r + w_v, \tag{5.5}$$

where $r = \dot{\psi}$ and the functions $X(u_r)$ and $Y(u_r)$ satisfy the following assumptions:

Assumption 5.3. The functions $X(u_r)$ and $Y(u_r)$ are continuous and bounded for bounded arguments.

Assumption 5.4. $Y(u_r)$ is such that $|Y(u_r)|$ is strictly increasing for $u_r > 0$ and satisfies $Y(u_r) \leq -Y^{\min} < 0, \quad \forall u_r \in [-V_{\max}, U_{rd}]$, where $Y^{\min}$ is a positive constant.

Remark 5.1. Assumption 5.4 is justified by a contradiction: $Y(u_r) \geq 0$ would imply a nominally unstable vehicle in sway which is not the case for commercial vessels by design. No bounds are implied on u_r and $U_{rd} > 0$ will be defined later.

The term w_v represents a bias term that embodies unmodeled dynamics and dynamic, heading dependent, disturbances caused by currents, winds and waves. In this context, the effects of constant wind disturbances acting in a constant direction $\beta_e \in [0, 2\pi]$ are considered in w_v. Hence the term w_v is defined as:

$$w_v \triangleq \kappa_v(\gamma_e)\sin(\beta_e - \psi), \tag{5.6}$$

where $\gamma_e = \psi - \beta_e - \pi$ is the angle of attack of the wind, and the function $\kappa_v(\gamma_e)$ satisfies the following assumptions:

Assumption 5.5. The function κ_v is bounded, periodic of class C^1 with bounded first derivative. Therefore, there exists $\kappa_v^{\max}, \kappa_v'^{\max}$ such that $\kappa_v(\cdot) \leq \kappa_v^{\max}, \frac{d\kappa_v(\cdot)}{d\cdot} \leq \kappa_v'^{\max}$.

Assumption 5.6. The function κ_v is such that, given any constants $k \in \mathbb{R}$ and $\beta_e \in [0, 2\pi]$, the following bound holds for all $s \in \mathbb{R}$:

$$\left| \kappa_v(\gamma_e^k) - \kappa_v(\gamma_e^{k+s}) \frac{\sqrt{k^2+1}}{\sqrt{(s+k)^2+1}} \right| \leq \kappa_v^{\max} \frac{|s|}{\sqrt{(s+k)^2+1}}, \tag{5.7}$$

where $\gamma_e^k \triangleq -\tan^{-1}(k) - \beta_e - \pi$ and $\gamma_e^{k+s} \triangleq -\tan^{-1}(k+s) - \beta_e - \pi$.

Remark 5.2. Notice that the wind load coefficients given in [76, 103, 15, 52] can be shown to satisfy Assumptions 5.5-5.6, or can be easily approximated with functions satisfying Assumptions 5.5-5.6.

Remark 5.3. Notice that there is no control input in (5.5) that can directly compensate for the sway drift v_c nor for the dynamic disturbance w_v.

5.1.3. The Actuated Surge and Yaw Dynamics

The surge and yaw dynamics are the actuated dynamics of the vessel. Their dynamics are neglected in this chapter in a similar way as done in Chapters 3 and 4:

Assumption 5.7. The underactuated vessel is assumed to have internal controllers setting the desired relative surge velocity and the desired yaw angle. The dynamics of these controller are neglected in this context, therefore $u_r \equiv u_{rd}$ and $\psi \equiv \psi_d$, where $u_r d$ is the desired relative surge velocity and ψ_d is the desired yaw angle.

5.1.4. The Model of the Vessel

Following Assumptions 5.2 and 5.7, the model of the vessel becomes:

$$\dot{x} = \cos(\psi_d)u_{rd} - \sin(\psi_d)v_r + V_x, \tag{5.8a}$$

$$\dot{y} = \sin(\psi_d)u_{rd} + \cos(\psi_d)v_r + V_y, \tag{5.8b}$$

$$\dot{v}_r = X(u_{rd})\dot{\psi}_d + Y(u_{rd})v_r + \kappa_v(\gamma_e)\sin(\beta_e - \psi_d), \tag{5.8c}$$

where (5.3-5.4) were used to derive (5.8a-5.8b). Notice that u_{rd}, ψ_d are the control inputs.

5.1.5. The Control Objective

The control system should make the vessel follow a given straight line $\mathcal{P}$ and maintain a desired constant surge relative velocity $U_{rd} > 0$. Hence, since the dynamics of u_r are neglected (Assumption 5.7), $u_r = u_{rd} = U_{rd}$. This should also hold in the presence of disturbances modeled as a combination of a constant and irrotational ocean current and a dynamic sway heading dependent force. To simplify the problem without any loss of generality since coordinates can always be rotated given a desired direction in the plane, the inertial reference frame i is placed such that the x-axis is aligned with the desired path $\mathcal{P} \triangleq \{(x, y) \in \mathbb{R}^2 : y = 0\}$. The y coordinate then corresponds to the cross-track error and the goals the control system should pursue are formalized as follows:

$$\lim_{t\to\infty} y(t) = 0, \tag{5.9}$$

$$\lim_{t\to\infty} \psi_d(t) = \psi_{ss}, \quad \psi_{ss} \in \left(-\frac{\pi}{2}, \frac{\pi}{2}\right), \tag{5.10}$$

where $u_r(t)$ is the surge relative speed of the vessel and ψ_{ss} is constant. Notice that the $\psi(t)$ is not required to converge to zero but rather to a steady-state constant value bounded within $-\frac{\pi}{2}$ and $\frac{\pi}{2}$. This allows the ship to hold a non-zero yaw angle at equilibrium, and compensate for the disturbances. This is necessary because the vessel is underactuated and no control forces are available in sway to counteract the drift. The value of ψ_{ss} will be specified later.

The relative velocity needs to be sufficiently large to guarantee ship maneuverability in presence of disturbances. In particular, it is shown in this paper that the following assumption guarantees path following in presence of kinematic and dynamic disturbances acting in any direction:

Assumption 5.8. The desired constant relative surge velocity U_{rd} satisfies the following condition:

$$U_{rd} > \max\left\{ V_{\max} + \frac{5}{2}\left|\frac{\kappa_v^{\max}}{Y(U_{rd})}\right|, 2V_{\max} + 2\left|\frac{\kappa_v^{\max} + \kappa_v'^{\max}}{Y(U_{rd})}\right| \right\},$$

Remark 5.4. It is always possible to find values of U_{rd} satisfying Assumption 5.8, since $|Y(u_r)|$ is strictly increasing for $u_r > 0$.

5.2. The Integral Line of Sight Guidance

The ILOS guidance is presented in this section. The surface vessel has to converge and follow the x-axis in presence of environmental disturbances. In this chapter explicit bounds for the choice of the look-ahead distance of the ILOS guidance presented in Chapter 3 are derived and this is done by including the underactuated sway dynamics into the Lyapunov analysis. This confirms the stabilizing effect of the ILOS guidance on the underactuated dynamics argued in Sections 3.2 and 4.2. Hence, the desired heading angle is:

$$\psi_{ILOS} \triangleq -\tan^{-1}\left(\frac{y + \sigma y_{\text{int}}}{\Delta}\right), \qquad \Delta, \sigma > 0, \tag{5.11a}$$

$$\dot{y}_{\text{int}} = \frac{\Delta y}{(y + \sigma y_{\text{int}})^2 + \Delta^2}, \tag{5.11b}$$

where Δ is the look-ahead distance and σ is the integral gain. Both are constant design parameters. The integral effect becomes significant when disturbances push the craft away from its path. This gives a nonzero angle (5.11a) and makes the vessel to side-slip while staying on the desired path, so part of its relative forward velocity can counteract the effect of the environmental disturbances. Notice that the law (5.11b) gives less integral action when the vehicle is far from $\mathcal{P}$, reducing the risk of wind-up effects.

5.3. Stability Conditions

This section presents the stability conditions under which the proposed ILOS guidance (5.11) achieves the objectives (5.9-5.10). The notation $X^{U_{rd}} \triangleq X(U_{rd})$ and $Y^{U_{rd}} \triangleq Y(U_{rd})$ is used.

Theorem 5.1. *Given an underactuated surface vessel described by the dynamical system* (5.8)*. If Assumptions 5.2-5.8 hold and, if the look-ahead distance* Δ *and the integral gain* σ *satisfy the conditions:*

$$\Delta > \frac{|X^{U_{rd}}|}{|Y^{U_{rd}}|}\Omega(\sigma)\left[\frac{5}{4}\frac{U_{rd}+V_{\max}+\sigma}{U_{rd}-V_{\max}-\sigma}+1\right], \tag{5.12}$$

$$0 < \sigma < U_{rd} - V_{\max} - \frac{5}{2}\left|\frac{\kappa_v^{\max}}{Y^{U_rd}}\right|, \tag{5.13}$$

where $\Omega(\sigma)$ *is defined as,*

$$\Omega(\sigma) \triangleq \frac{U_{rd}-V_{\max}-\sigma}{U_{rd}-V_{\max}-\sigma-\frac{5}{2}\left|\frac{\kappa_v^{\max}}{Y^{U_{rd}}}\right|}, \tag{5.14}$$

then the controller (5.11)*, where* $u_{rd} \triangleq U_{rd}$*, guarantee achievement of the control objectives (5.9-5.10).*

Remark 5.5. The lower bound (5.12) is expected and has a clear physical interpretation: a too short look-ahead distance $\Delta > 0$ makes the vessel overshoot the target and thus causes chattering as shown in Chapters 3-4.

Remark 5.6. Notice in (5.5) that the yaw rate $r = \dot{\psi}$ acts as a perturbation of the sway dynamics. In particular, if the sway motion is only lightly damped, i.e. if $X^{U_{rd}} \gg Y^{U_{rd}}$, then the yaw rate has a significant influence on the sway relative velocity v_r. Hence, the yaw rate must be limited to make sure that the sway dynamics behave properly. This is done by increasing the look-ahead distance Δ that makes the vessel turn slower, thus smoothing and limiting its yaw rate. The overall effect is a virtual increase in damping in sway. In the opposite case, when $X^{U_{rd}} \ll Y^{U_{rd}}$, damping is higher and hence the vessel can tolerate a higher yaw rate. In this case a shorter Δ can be used and the vessel is capable of more aggressive maneuvers. This confirms the analysis from Sections 3.2 and 4.2 where it is argued that longer look-ahead distances tend to decouple the underactuated dynamics from the actuated dynamics, thus avoiding sway motion (sway and heave motion in 3D).

Remark 5.7. The disturbances $\boldsymbol{V}_c$ and κ_v shrink the upper bound for $\sigma > 0$ and increase the lower bound for $\Delta > 0$. These changes can be compensated by increasing the relative velocity of the vessel U_{rd}.

5.4. Proof of Theorem 5.1

In this section the proof of Theorem 5.1 is given. The dynamics of the cross track error y and the relative sway velocity v_r have to be analyzed. The $y - v_r$ system is obtained combining (5.8b), (5.8c) and (5.11b):

$$\dot{y}_{\text{int}} = \frac{\Delta y}{(y + \sigma y_{\text{int}})^2 + \Delta^2}, \tag{5.15a}$$

$$\dot{y} = U_{rd} \sin(\psi_d) + v_r \cos(\psi_d) + V_y, \tag{5.15b}$$

$$\dot{v}_r = X(U_{rd})\dot{\psi}_d + Y(U_{rd})v_r + \kappa_v(\gamma_e)\sin(\beta_e - \psi_d). \tag{5.15c}$$

Substituting (5.11a) for ψ_d gives $\sin(\psi_d) = -(y+\sigma y_{\text{int}})/\sqrt{(y + \sigma y_{\text{int}}) + \Delta^2}$ and $\cos(\psi_d) = \Delta/\sqrt{(y + \sigma y_{\text{int}}) + \Delta^2}$, and leads 5.15 to:

$$\dot{y}_{\text{int}} = \frac{\Delta y}{(y + \sigma y_{\text{int}})^2 + \Delta^2}, \tag{5.16a}$$

$$\dot{y} = -U_{rd}\frac{y + \sigma y_{\text{int}}}{\sqrt{(y + \sigma y_{\text{int}})^2 + \Delta^2}} + \frac{\Delta}{\sqrt{(y + \sigma y_{\text{int}})^2 + \Delta^2}} v_r + V_y, \tag{5.16b}$$

$$\dot{v}_r = X(U_{rd})\dot{\psi}_d + Y(U_{rd})v_r + \kappa_v(\gamma_e)\sin(\beta_e - \psi_d). \tag{5.16c}$$

The calculation of the equilibrium point of the system (5.15) yields the following equation:

$$s\sqrt{s^2 + 1} = \frac{V_y}{U_{rd}} s^2 + \frac{\cos(\beta_e)s + \sin(\beta_e)}{U_{rd}|Y^{U_{rd}}|}\kappa_v^{\text{eq}}(s) + \frac{V_y}{U_{rd}}, \tag{5.17}$$

where $s \triangleq \sigma y_{\text{int}}^{\text{eq}}/\Delta$ and $y_{\text{int}}^{\text{eq}}$ is the value of y_{int} at equilibrium. The term $\kappa_v^{\text{eq}}(s)$ is defined as the value of $\kappa_v(\gamma_e)$ at equilibrium, i.e. when $\gamma_e = \gamma_e^{\text{eq}} \triangleq -\tan^{-1}(s) - \beta_e - \pi$. The equilibrium point equation (5.17) is a generalized case of similar equations found in [34, 36, 31, 32]. It has to be shown that (5.17) has a unique real solution to have a single equilibrium point. The following Lemma gives the sufficient conditions for (5.17) to have a unique real solution:

Lemma 5.1. *If Assumptions 5.5 and 5.8 hold, then* (5.17) *has exactly one real solution* $s = \sigma y_{\text{int}}^{\text{eq}}/\Delta$.

Proof. The proof of Lemma 5.1 is given in Appendix 5.A. □

At equilibrium $y^{\text{eq}} = 0$ while $y_{\text{int}}^{\text{eq}}$ and v_r^{eq} are constant values where $y_{\text{int}}^{\text{eq}}$ is the unique solution of (5.17) and v_r^{eq} relates to $y_{\text{int}}^{\text{eq}}$ as:

$$v_r^{\text{eq}} = U_{rd}\frac{\sigma y_{\text{int}}^{\text{eq}}}{\Delta} - V_y\sqrt{\left(\frac{\sigma y_{\text{int}}^{\text{eq}}}{\Delta}\right)^2 + 1} \tag{5.18}$$

The heading angle held by the vessel at steady-state is then $\psi_{ss} \triangleq -\tan^{-1}(\sigma y_{\text{int}}^{\text{eq}}/\Delta)$. A new set of variables is introduced to move the equilibrium point to the origin:

$$e_1 \triangleq y_{\text{int}} - y_{\text{int}}^{\text{eq}}, \quad (5.19) \qquad e_2 \triangleq y + \sigma e_1, \quad (5.20) \qquad e_3 \triangleq v_r - v_r^{\text{eq}}. \quad (5.21)$$

Taking the time derivatives of (5.19-5.21) and using (5.16), and (5.18) the transformed dynamics become:

$$\dot{e}_1 = \frac{\Delta(e_2 - \sigma e_1)}{(e_2 + \sigma y_{\text{int}}^{\text{eq}})^2 + \Delta^2}, \tag{5.22a}$$

$$\begin{aligned}\dot{e}_2 = &-\frac{\sigma^2\Delta e_1}{(e_2 + \sigma y_{\text{int}}^{\text{eq}})^2 + \Delta^2} + \frac{\Delta e_3}{\sqrt{(e_2 + \sigma y_{\text{int}}^{\text{eq}})^2 + \Delta^2}} + V_y f(e_2) \\ &- \left[U_{rd} - \frac{\sigma\Delta}{\sqrt{(e_2 + \sigma y_{\text{int}}^{\text{eq}})^2 + \Delta^2}}\right]\frac{e_2}{\sqrt{(e_2 + \sigma y_{\text{int}}^{\text{eq}})^2 + \Delta^2}},\end{aligned} \tag{5.22b}$$

$$\dot{e}_3 = X(U_{rd})\dot{\psi}_d + Y(U_{rd})e_3 + \frac{\kappa_v(\gamma_e)\cos(\beta_e)e_2}{\sqrt{(e_2 + \sigma y_{\text{int}}^{\text{eq}})^2 + \Delta^2}} + \sin(\psi_{ss} - \beta_e)g(e_2), \tag{5.22c}$$

where $f(e_2)$ is defined as:

$$f(e_2) \triangleq 1 - \frac{\sqrt{(\sigma y_{\text{int}}^{\text{eq}})^2 + \Delta^2}}{\sqrt{(e_2 + \sigma y_{\text{int}}^{\text{eq}})^2 + \Delta^2}}, \tag{5.23}$$

and $g(e_2)$ is defined as:

$$g(e_2) \triangleq \kappa_v^{\text{eq}} - \kappa_v(\gamma_e)\frac{\sqrt{(\sigma y_{\text{int}}^{\text{eq}})^2 + \Delta^2}}{\sqrt{(e_2 + \sigma y_{\text{int}}^{\text{eq}})^2 + \Delta^2}}. \tag{5.24}$$

Notice that the following bound holds for $f(e_2)$:

$$|f(e_2)| \leq \frac{|e_2|}{\sqrt{(e_2 + \sigma y_{\text{int}}^{\text{eq}})^2 + \Delta^2}}. \tag{5.25}$$

One can prove that (5.25) holds by squaring both sides of the inequality two consecutive times. Furthermore, as a direct consequence of Assumption 5.6, the following bound holds for $g(e_2)$:

$$|g(e_2)| \leq \kappa_v^{\max} \frac{|e_2|}{\sqrt{(e_2 + \sigma y_{\text{int}}^{\text{eq}})^2 + \Delta^2}}. \tag{5.26}$$

Now, substituting the expression:

$$\begin{aligned}
\dot{\psi}_d = \frac{d}{dt}\left[-\tan^{-1}\left(\frac{e_2 + \sigma y_{\text{int}}^{\text{eq}}}{\Delta}\right)\right] &= -\frac{\Delta}{(e_2 + \sigma y_{\text{int}}^{\text{eq}})^2 + \Delta^2}\dot{e}_2 = \\
= \frac{\sigma^2 \Delta^2 e_1}{((e_2 + \sigma y_{\text{int}}^{\text{eq}})^2 + \Delta^2)^2} &- \frac{\Delta^2 e_3}{((e_2 + \sigma y_{\text{int}}^{\text{eq}})^2 + \Delta^2)^{3/2}} - \frac{\Delta V_y f(e_2)}{(e_2 + \sigma y_{\text{int}}^{\text{eq}})^2 + \Delta^2} \\
+ \Delta \left[U_{rd} - \frac{\sigma \Delta}{\sqrt{(e_2 + \sigma y_{\text{int}}^{\text{eq}})^2 + \Delta^2}}\right] &\frac{e_2}{((e_2 + \sigma y_{\text{int}}^{\text{eq}})^2 + \Delta^2)^{3/2}},
\end{aligned} \tag{5.27}$$

in (5.22c) yields the following form for the system (5.22):

$$\begin{bmatrix} \dot{e}_1 \\ \dot{e}_2 \\ \dot{e}_3 \end{bmatrix} = \boldsymbol{A}(e_2)\begin{bmatrix} e_1 \\ e_2 \\ e_3 \end{bmatrix} + \boldsymbol{B}(e_2). \tag{5.28}$$

$\boldsymbol{A}(e_2)$ is given in (5.30) while $\boldsymbol{B}(e_2)$ is:

$$\boldsymbol{B}(e_2) \triangleq \begin{bmatrix} 0 \\ V_y f(e_2) \\ -\frac{\Delta X^{U_{rd}} V_y}{(e_2 + \sigma y_{\text{int}}^{\text{eq}})^2 + \Delta^2} f(e_2) + \sin(\psi_{ss} - \beta_e) g(e_2) \end{bmatrix}. \tag{5.29}$$

Lemma 5.2 states the stability properties of (5.28):

Lemma 5.2. *Under the conditions of Theorem 5.1, the system* (5.28) *is UGAS and ULES.*

Proof. The proof of Lemma 5.2 is given in Appendix 5.B. □

Lemma 5.2 concludes UGAS and ULES stability properties for the origin of (5.28) or alternatively global κ-exponential stability [129]. It is hence possible to conclude that the control objectives (5.9-5.10) are achieved with exponential converging properties in any ball of initial conditions.

Remark 5.8. Notice that the UGAS and ULES stability properties of (5.28) make this system very robust with respect to perturbations [82, Lemma 9.1]. This makes the ILOS guidance law (5.11) potentially very reliable under Assumptions 5.2-5.8. Such robustness with respect to perturbations is exploited in the following chapters where the actuated dynamics are added into the analysis yielding cascaded configurations.

Remark 5.9. The value $y_{\text{int}}^{\text{eq}}$ makes sure that, at equilibrium, the vessel holds the heading $\psi_{ss} = -\tan^{-1}(\sigma y_{\text{int}}^{\text{eq}}/\Delta)$ and is the only real solution of (5.17), i.e. ψ_{ss} is the only possible heading that guarantees path following and compensates for the disturbances.

5.5. Conclusions

In this chapter explicit bounds for the choice of the ILOS guidance look-ahead distance have been derived by including the underactuated dynamics into the Lyapunov analysis. These bounds confirm the analysis discussed in Sections 3.2 and 4.2. Furthermore, the bounds upon the ILOS integral gain have been refined. Disturbances in the form of constant irrotational ocean currents and constant dynamic, attitude dependent, forces have been also taken into account and their maximum ratings show up in the bounds derived for the guidance law parameters.

The actuated dynamics are not considered under the assumption that there are a closed loop speed controller and a closed loop autopilot system setting the speed and the heading of the vessel. The stability analysis reveals UGAS and ULES stability properties for the guidance closed loop system. This makes the guidance closed loop system very robust with respect to perturbations. Such robustness with respect to perturbations will be exploited in the following chapters were the actuated dynamics are added into the analysis in cascaded configurations.

$$\boldsymbol{A}(e_2) \triangleq \begin{bmatrix} -\frac{\sigma\Delta}{(e_2+\sigma y_{\text{int}}^{\text{eq}})^2+\Delta^2} & \frac{\Delta}{(e_2+\sigma y_{\text{int}}^{\text{eq}})^2+\Delta^2} & 0 \\ -\frac{\sigma^2\Delta}{(e_2+\sigma y_{\text{int}}^{\text{eq}})^2+\Delta^2} & -\frac{U_{rd}}{\sqrt{(e_2+\sigma y_{\text{int}}^{\text{eq}})^2+\Delta^2}} + \frac{\sigma\Delta}{(e_2+\sigma y_{\text{int}}^{\text{eq}})^2+\Delta^2} & \frac{\Delta}{\sqrt{(e_2+\sigma y_{\text{int}}^{\text{eq}})^2+\Delta^2}} \\ \frac{\sigma^2\Delta^2 X^{U_{rd}}}{((e_2+\sigma y_{\text{int}}^{\text{eq}})^2+\Delta^2)^2} & \frac{U_{rd}\Delta X^{U_{rd}}}{((e_2+\sigma y_{\text{int}}^{\text{eq}})^2+\Delta^2)^{3/2}} - \frac{\sigma\Delta^2 X^{U_{rd}}}{((e_2+\sigma y_{\text{int}}^{\text{eq}})^2+\Delta^2)^2} + \frac{\kappa_v(\gamma_e)\cos(\beta_e)}{\sqrt{(e_2+\sigma y_{\text{int}}^{\text{eq}})^2+\Delta^2}} & Y^{U_{rd}} - \frac{\Delta^2 X^{U_{rd}}}{((e_2+\sigma y_{\text{int}}^{\text{eq}})^2+\Delta^2)^{3/2}} \end{bmatrix} \tag{5.30}$$

5.A. Appendix: Proof of Lemma 5.1

Equation (5.17) is written again:

$$s\sqrt{s^2+1} = \frac{V_y}{U_{rd}}s^2 + \frac{\cos(\beta_e)s + \sin(\beta_e)}{U_{rd}|Y^{U_{rd}}|}\kappa_v^{\mathrm{eq}}(s) + \frac{V_y}{U_{rd}}. \tag{5.31}$$

Notice that $\kappa_v^{\mathrm{eq}}(s)$ is bounded and is defined as the value of $\kappa_v(\gamma_e)$ at equilibrium, i.e. when $\gamma_e = \gamma_e^{\mathrm{eq}} \triangleq -\tan^{-1}(s) - \beta_e - \pi$. This Lemma proves that there exists only one real solution to (5.31) if Assumptions 5.5 and 5.8 hold. First, it is shown that there exist real solutions to (5.31) and then uniqueness is argued. Squaring both sides of (5.31) gives:

$$\begin{aligned} p(s) \triangleq &(M^2 - U_{rd}^2)s^4 + 2MN_s s^3 + (2MP_s + N_s^2 - U_{rd}^2)s^2 \\ &+ 2N_s P_s s + P_s^2 = 0, \end{aligned} \tag{5.32}$$

where $M \triangleq V_y$, $N_s \triangleq \kappa_v^{\mathrm{eq}}(s)\cos(\beta_e)/|Y^{U_{rd}}|$ and $P_s \triangleq V_y + \kappa_v^{\mathrm{eq}}(s)\sin(\beta_e)/|Y^{U_{rd}}|$. Hence, $M^2 - U_{rd}^2 < 0$ as long as $U_{rd} > V_{\max}$ which is guaranteed by Assumption 5.8. This means that, if Assumption 5.8 holds and since N_s and P_s are bounded in s, the function $p(s) \to -\infty$ as $s \to \pm\infty$. Furthermore, since $P_s^2 \geq 0, \forall s$, then $p(0) \geq 0$. Therefore, $p(s)$ has at least one real zero, or at least two real zeros, one positive and one negative, if $P_s > 0, s = 0$. This proves the existence of real solutions to (5.31).

The intersections between the curves defined by the two sides of (5.31) are considered next to show uniqueness:

$$L_1(s^*) \triangleq s^*\sqrt{s^{*2}+1}, \tag{5.33}$$

$$L_2(s^*) \triangleq \frac{V_y}{U_{rd}}s^{*2} + \frac{\cos(\beta_e)s^* + \sin(\beta_e)}{U_{rd}|Y^{U_{rd}}|}\kappa_v^{\mathrm{eq}}(s^*) + \frac{V_y}{U_{rd}}. \tag{5.34}$$

The curve $L_1(s^*)$ is strictly increasing while $L_2(s^*)$ resembles a parabola since $\kappa_v^{\mathrm{eq}}(s^*)$ is bounded as shown in Figure 5.1. The first derivatives in s^* of $L_1(s^*)$ and $L_2(s^*)$ are analyzed:

$$\frac{dL_1}{ds^*} = \frac{2s^{*2}+1}{\sqrt{s^{*2}+1}}, \tag{5.35}$$

$$\frac{dL_2}{ds^*} = \frac{1}{U_{rd}}\left[2V_y - \frac{\frac{d\kappa_v^{\mathrm{eq}}}{d\gamma_e^{\mathrm{eq}}}\cos(\beta_e)}{|Y^{U_{rd}}|(1+s^{*2})}\right]s^* + \frac{\kappa_v^{\mathrm{eq}}(s^*)\cos(\beta_e)}{U_{rd}|Y^{U_{rd}}|} - \frac{\frac{d\kappa_v^{\mathrm{eq}}}{d\gamma_e^{\mathrm{eq}}}\sin(\beta_e)}{U_{rd}|Y^{U_{rd}}|(1+s^{*2})}, \tag{5.36}$$

where the property $\frac{d\kappa_v^{\text{eq}}}{ds^*} = \frac{d\kappa_v^{\text{eq}}}{d\gamma_e^{\text{eq}}}\frac{d\gamma_e^{\text{eq}}}{ds^*} = -\frac{d\kappa_v^{\text{eq}}}{d\gamma_e^{\text{eq}}}\frac{1}{1+s^{*2}}$ is used. The following bound holds:

$$\left[\frac{2V_{\max}}{U_{rd}} + \frac{\kappa_v'^{\max}}{U_{rd}|Y^{U_{rd}}|}\right]|s^*| + \frac{\kappa_v^{\max} + \kappa_v'^{\max}}{U_{rd}|Y^{U_{rd}}|} \geq \frac{dL_2}{ds^*}. \tag{5.37}$$

Notice that as long as $U_{rd} > 2V_{\max} + (\kappa_v'^{\max}/|Y^{U_{rd}}|)$ and $U_{rd} > (2/|Y^{U_{rd}}|)(\kappa_v^{\max} + \kappa_v'^{\max})$, which are both guaranteed by Assumption 5.8, the following inequality holds:

$$\frac{dL_1}{ds^*} > \left[\frac{2V_{\max}}{U_{rd}} + \frac{\kappa_v'^{\max}}{U_{rd}|Y^{U_{rd}}|}\right]|s^*| + \frac{\kappa_v^{\max} + \kappa_v'^{\max}}{U_{rd}|Y^{U_{rd}}|} \geq \frac{dL_2}{ds^*}, \quad \forall s^*. \tag{5.38}$$

This inequality has two important consequences: if there exist any intersections between L_1 and L_2, these intersections are transverse intersections. Yet, if there exists an intersection between L_1 and L_2, then this intersection is unique: since $dL_1/ds^* > dL_2/ds^*$, if the curves intersect in one point, they will never intersect again. The proven existence of real solutions to (5.31) guarantees that L_1 and L_2 intersect each other and hence it is possible to conclude that the intersection point is unique. To conclude, as long as Assumptions 5.5 and 5.8 are satisfied, there exists only one real solution s for (5.31).

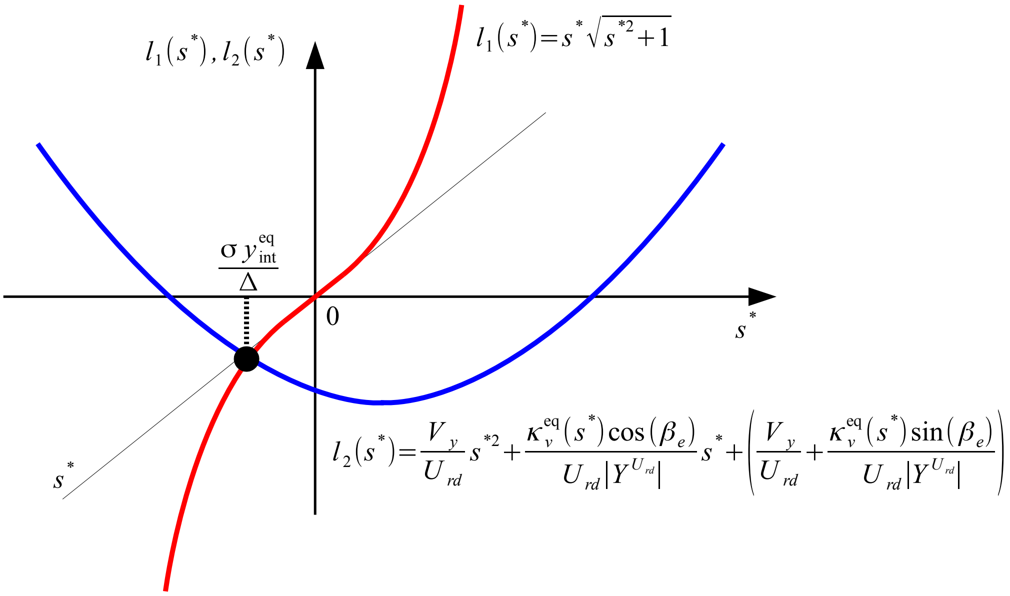

Figure 5.1.: Graphical solution of (5.31): $L_1(s^*)$ and $L_2(s^*)$ should intersect exclusively once to make sure that there exists a single equilibrium point. Notice that $L_1(s^*)$ is strictly increasing while $L_2(s^*)$ resembles a parabola since $\kappa_v^{\text{eq}}(s^*)$ is bounded.

5.B. Appendix: Proof of Lemma 5.2

The system (5.28) is written again:

$$\begin{bmatrix}\dot e_1\\ \dot e_2\\ \dot e_3\end{bmatrix} = \boldsymbol{A}(e_2)\begin{bmatrix}e_1\\ e_2\\ e_3\end{bmatrix} + \boldsymbol{B}(e_2). \tag{5.39}$$

Consider the quadratic Lyapunov function candidate (LFC):

$$V \triangleq \frac{1}{2}\sigma^2 e_1^2 + \frac{1}{2}e_2^2 + \frac{1}{2}\mu e_3^2, \quad \mu > 0. \tag{5.40}$$

The time-derivative of V is:

$$\begin{aligned}
\dot V = & -\frac{\sigma^3\Delta}{(e_2+\sigma y_{\text{int}}^{\text{eq}})^2+\Delta^2}e_1^2 \\
& + \left[\sigma\Delta - U_{rd}\sqrt{(e_2+\sigma y_{\text{int}}^{\text{eq}})^2+\Delta^2}\right]\frac{e_2^2}{(e_2+\sigma y_{\text{int}}^{\text{eq}})^2+\Delta^2} \\
& + \mu\sin(\psi_{ss}-\beta_e)g(e_2)e_3 + \frac{\Delta}{\sqrt{(e_2+\sigma y_{\text{int}}^{\text{eq}})^2+\Delta^2}}e_2e_3 \\
& + V_y f(e_2)e_2 - \mu\frac{\Delta X^{U_{rd}}V_y}{(e_2+\sigma y_{\text{int}}^{\text{eq}})^2+\Delta^2}f(e_2)e_3 \\
& - \mu\left[-Y^{U_{rd}} + \frac{\Delta^2 X^{U_{rd}}}{((e_2+\sigma y_{\text{int}}^{\text{eq}})^2+\Delta^2)^{3/2}}\right]e_3^2 \\
& + \mu\left[\frac{U_{rd}\Delta X^{U_{rd}}}{(e_2+\sigma y_{\text{int}}^{\text{eq}})^2+\Delta^2} - \frac{\sigma\Delta^2 X^{U_{rd}}}{((e_2+\sigma y_{\text{int}}^{\text{eq}})^2+\Delta^2)^{3/2}}\right] \\
& \cdot \frac{e_2e_3}{\sqrt{(e_2+\sigma y_{\text{int}}^{\text{eq}})^2+\Delta^2}} + \frac{\mu\sigma^2\Delta^2 X^{U_{rd}}}{((e_2+\sigma y_{\text{int}}^{\text{eq}})^2+\Delta^2)^2}e_1e_3 \\
& + \kappa_v(\gamma_e)\cos(\beta_e)\frac{e_2e_3}{\sqrt{(e_2+\sigma y_{\text{int}}^{\text{eq}})^2+\Delta^2}}.
\end{aligned} \tag{5.41}$$

Assumptions 5.2-5.8, inequalities (5.25-5.26) and the following properties:

$$\max\left\{\frac{\Delta}{(e_2+\sigma y_{\text{int}}^{\text{eq}})^2+\Delta^2}\right\} = \frac{1}{\Delta}, \tag{5.42}$$

$$\max\left\{\frac{\Delta^2}{((e_2+\sigma y_{\text{int}}^{\text{eq}})^2+\Delta^2)^{3/2}}\right\} = \frac{1}{\Delta}, \tag{5.43}$$

$$\min\left\{\sqrt{(e_2+\sigma y_{\text{int}}^{\text{eq}})^2+\Delta^2}\right\} = \Delta, \tag{5.44}$$

yield the following bound for $\dot{V}$:

$$\begin{aligned}\dot{V} \leq &- \frac{\sigma^3\Delta}{(e_2+\sigma y_{\text{int}}^{\text{eq}})^2+\Delta^2}e_1^2 \\ &- \Delta\left(U_{rd}-V_{\max}-\sigma\right)\frac{e_2^2}{(e_2+\sigma y_{\text{int}}^{\text{eq}})^2+\Delta^2} \\ &+ \frac{\Delta|e_2||e_3|}{\sqrt{(e_2+\sigma y_{\text{int}}^{\text{eq}})^2+\Delta^2}} + \frac{\mu\sigma^2|X^{U^{rd}}|}{\Delta}\frac{|e_1||e_3|}{\sqrt{(e_2+\sigma y_{\text{int}}^{\text{eq}})^2+\Delta^2}} \\ &+ \mu\left[\frac{|X^{U_{rd}}|}{\Delta}(U_{rd}+V_{\max}+\sigma)+2\kappa_v^{\max}\right]\frac{|e_2||e_3|}{\sqrt{(e_2+\sigma y_{\text{int}}^{\text{eq}})^2+\Delta^2}} \\ &- \mu\left(|Y^{U_{rd}}|-\frac{|X^{U_{rd}}|}{\Delta}\right)e_3^2.\end{aligned} \tag{5.45}$$

The notation $\bar{e}_1 \triangleq e_1/\sqrt{(e_2+\sigma y_{\text{int}}^{\text{eq}})^2+\Delta^2}$ and $\bar{e}_2 \triangleq e_2/\sqrt{(e_2+\sigma y_{\text{int}}^{\text{eq}})^2+\Delta^2}$ is introduced and the inequality (5.45) becomes:

$$\begin{aligned}\dot{V} \leq &- \sigma^3\Delta\bar{e}_1^2 - \Delta\left(U_{rd}-V_{\max}-\sigma\right)\bar{e}_2^2 - \mu\left(|Y^{U_{rd}}|-\frac{|X^{U_{rd}}|}{\Delta}\right)e_3^2 \\ &+ \Delta|\bar{e}_2||e_3| + \mu\left[\frac{|X^{U_{rd}}|}{\Delta}(U_{rd}+V_{\max}+\sigma)+2\kappa_v^{\max}\right]|\bar{e}_2||e_3| \\ &+ \frac{\mu\sigma^2|X^{U^{rd}}|}{\Delta}|\bar{e}_1||e_3|.\end{aligned} \tag{5.46}$$

It can be then rearranged as:

$$\dot{V} \leq -W_1(|\bar{e}_1|,|e_3|) - W_2(|\bar{e}_2|,|e_3|), \tag{5.47}$$

$$W_1 \triangleq \sigma^3\Delta|\bar{e}_1|^2 - \mu\frac{\sigma^2|X^{U_{rd}}|}{\Delta}|\bar{e}_1||e_3| + \mu\eta\left(|Y^{U_{rd}}|-\frac{|X^{U_{rd}}|}{\Delta}\right)|e_3|^2, \tag{5.48}$$

$$W_2 \triangleq \Delta\begin{bmatrix}|\bar{e}_2| & |e_3|\end{bmatrix}\begin{bmatrix}\beta & -\alpha \\ -\alpha & \frac{\alpha(2\alpha-1)}{\beta}\end{bmatrix}\begin{bmatrix}|\bar{e}_2| \\ |e_3|\end{bmatrix}, \tag{5.49}$$

where $0 < \eta < 1$, $\beta \triangleq U_{rd} - V_{\max} - \sigma$ and α is given by:

$$\alpha \triangleq (1-\eta)\frac{(U_{rd}-V_{\max}-\sigma)(\Delta|Y^{U_{rd}}|-|X^{U_{rd}}|)}{|X^{U_{rd}}|\left(U_{rd}+V_{\max}+\sigma\right)+2\Delta\kappa_v^{\max}}. \tag{5.50}$$

The parameter μ is chosen as:

$$\mu \triangleq \frac{\Delta^2(2\alpha - 1)}{|X^{U_{rd}}|(U_{rd} + V_{\max} + \sigma) + 2\Delta\kappa_v^{\max}}. \tag{5.51}$$

In (5.47) the term $\mu(|Y^{U_{rd}}| - |X^{U_{rd}}|/\Delta)|e_3|^2$ has been split in $\eta\mu(|Y^{U_{rd}}| - |X^{U_{rd}}|/\Delta)|e_3|^2$ and $(1-\eta)\mu(|Y^{U_{rd}}| - |X^{U_{rd}}|/\Delta)|e_3|^2$. This makes it possible to avoid splitting cross terms through Young's inequality as done for instance in [26] and hence shift the analysis on the two quadratic functions W_1 and W_2. In particular, if both W_1 and W_2 are definite positive then $\dot{V}$ is negative definite. Positive definiteness of W_1 is ensured if (5.52) and (5.53) are satisfied:

$$\Delta > \frac{|X^{U_{rd}}|}{|Y^{U_{rd}}|}, \tag{5.52}$$

$$\mu < \frac{4\eta\Delta^2\left[\Delta|Y^{U_{rd}}| - |X^{U_{rd}}|\right]}{\sigma|X^{U_{rd}}|^2}. \tag{5.53}$$

Notice that condition (5.52) is met as long as (5.12) holds. At this point, the choice of η becomes subject to constraints. In particular, it is necessary to show that there exist η such that $0 < \eta < 1$ and that (5.53) is satisfied. In particular, (5.53) and (5.50) lead to the following inequality:

$$\frac{(1-\eta)(U_{rd} - V_{\max} - \sigma)}{[|X^{U_{rd}}|(U_{rd} + V_{\max} + \sigma) + 2\Delta\kappa_v^{\max}]^2} < \frac{2\eta}{\sigma|X^{U_{rd}}|^2}. \tag{5.54}$$

It is straightforward to show that $\eta \geq 1/5$ is a sufficient condition for (5.54) to hold. Hence, if $\eta \geq 1/5$ then μ, defined in (5.51), satisfies (5.53). Therefore, without any loss of generality, η is set to 1/5. Both β and α must fulfill $\beta > 0$ and $\alpha > 1$ to guarantee positive definiteness of W_2. Assumption 5.8 and (5.13) make sure that $\beta > 0$ while it is easy to check that conditions (5.12) and (5.13) imply $\alpha > 1$. Furthermore, $\alpha > 1$ guarantees $\mu > 0$ and ensures positive definiteness of V. Therefore under the conditions stated in Theorem 5.1, V, W_1 and W_2 are positive definite and hence, following standard Lyapunov arguments, the system (5.39) is UGAS. Furthermore, the inequality $W \triangleq W_1 + W_2 \geq \bar{\lambda}_1|\bar{e}_1|^2 + \bar{\lambda}_2|\bar{e}_2|^2 + \lambda_3|e_3|^2$ holds in a neighbourhood of the origin for some constants $\bar{\lambda}_1, \bar{\lambda}_2, \lambda_3 > 0$ and thus in any ball $\mathcal{B}_r \triangleq \{|e_2| \leq r\}, r > 0$ the function W can be estimated as $W \geq \lambda_1|e_1|^2 + \lambda_2|e_2|^2 + \lambda_3|e_3|^2$ where $\lambda_i = \bar{\lambda}_i/((r + \sigma y_{\text{int}}^{\text{eq}})^2 + \Delta^2)$, $i = 1, 2$. This, together with the fact that V is a quadratic function of e_1, e_2 and e_3, concludes that (5.39) is also uniformly locally exponentially stable, ULES.

Chapter 6.

Relative Velocity Control for Path Following of Underactuated Surface Vessels in the Presence of Ocean Currents

"If you are going to do something, do it now. Tomorrow is too late."
— Pete Goss, Yachtsman

In Chapter 3 the Integral Line-of-Sight (ILOS) guidance for planar motion purposes was applied to a simple kinematic model of surface vessels and a discussion involving intuitive as well as practical aspects of the ILOS law was given. The resulting analysis of the closed loop system gave explicit bounds on the integral gain but did not give any guidelines on how to choose the look-ahead distance of the ILOS. Explicit bounds for the choice of the look-ahead distance were derived in Chapter 5. This was done by including the underactuated dynamics into the Lyapunov analysis where disturbances in the form of constant irrotational ocean currents and constant dynamic, heading dependent forces were also taken into account. More precise bounds upon the integral gain were obtained as well. However the actuated surge and yaw dynamics were not considered under the assumption that there are closed loop controllers setting the speed and the heading of the vessel.

In this chapter the complete kinematic and dynamic closed loop system of the ILOS guidance law for path following purposes of underactuated surface vessels is analyzed.

The actuated surge and yaw dynamics are included in the analysis and combined with the results from Chapter 5. It is shown that the resulting closed loop system forms a cascade where the actuated dynamics perturb the combined sway-guidance system analyzed in Chapter 5. The properties of Uniform Global Asymptotic Stability (UGAS) and Uniform Local Exponential Stability (ULES) (alternatively global κ-exponential stability [129]) are shown for the closed loop cascaded system. In this case disturbances in the form of irrotational ocean currents are taken into account, while dynamic heading dependent environmental disturbances are neglected. Path following of straight lines is considered and the dynamics of the vessel are expressed in terms of its relative velocity, where the relative velocity of the vessel is its velocity with respect to the water. This is possible since the current is assumed constant and irrotational in the inertial frame, as shown in [52]. Furthermore, it is shown that in steady state it is possible to estimate the unknown current by using the integral term of the ILOS guidance law as well as measurements of the absolute and relative speeds of the vessel. Results from simulations and field experiments are presented to verify and illustrate the theoretical results. The ILOS guidance is applied to the CART Unmanned Semi-Submersible Vehicle (USSV) for sea trials [22], while the model of an underactuated supply vessel is used for simulation purposes since a model of the CART USSV is not yet available. First, the model of the supply vessel is used to simulate the control system and to assess its robustness with respect to parameter uncertainties and process noise. Next, the model is scaled to match the dimensions of the CART USSV in order to have simulation results that can be directly compared with the experiments. Finally, experimental results from sea trials are presented and a back to back comparison between simulations and experimental results is given. Furthermore, different combinations of the guidance law parameters are tested for different speeds/thrust levels. The results show that the vehicle converges and follows the desired course despite the environmental disturbances. As expected, side-slipping is performed by the guidance law in order to compensate for the drift and thus hold the vehicle on the path.

The chapter is organized as follows: Section 6.1 presents the vessel model for control design purposes. The control problem is defined in Section 6.2 while Section 6.3 presents the ILOS guidance that solves the path following control problem in a cascaded configuration with feedback linearizing surge and yaw controllers. The stability properties of the closed loop system are given in Section 6.4 while the analysis is developed in Section 6.5. The current estimator is described in Section 6.6. Simulation results are given in Section 6.7 and results from field experiments with the CART USSV are shown in Section 6.8. Finally, conclusions are found in Section 6.9. The results presented in this chapter are based on the papers [28, 36, 14, 29].

6.1. The Control Plant Model

The control plant model is a simplified mathematical description of the surface vessel. It contains the physical properties that are significant for control design purposes [130].

6.1.1. Model Assumptions

Assumption 6.1. The motion of the vessel can be described by 3 degrees of freedom (DOF), that is surge, sway and yaw.

Assumption 6.2. The vessel is port-starboard symmetric.

Assumption 6.3. The body-fixed coordinate frame b is located on the center-line of the vessel at a distance x_g^* from the center of gravity (CG), where x_g^* is to be defined later.

Assumption 6.4. The hydrodynamic damping is linear.

Remark 6.1. Nonlinear damping is not considered in order to reduce the complexity of the controllers. However, the passive nature of the non-linear hydrodynamic damping forces should enhance the directional stability of the vessel [36].

Assumption 6.5. The ocean current is defined in the inertial frame i and is assumed constant, unknown, irrotational and bounded. Hence, $\boldsymbol{V}_c \triangleq [V_x, V_y, 0]^T$ and there exists a constant $V_{\max} > 0$ such that $V_{\max} \geq \sqrt{V_x^2 + V_y^2}$.

Remark 6.2. The constant and irrotational ocean current model is widely accepted to describe slowly varying disturbances and it represents a good approximation when closed loop control is implemented on-board of marine vehicles [51].

6.1.2. The Control Plant Model

The state of the surface vessel is given by the vector $[\boldsymbol{p}^T, \boldsymbol{\nu}_r^T]^T$ where $\boldsymbol{p} \triangleq [x, y, \psi]^T$ describes the position and the orientation of the vehicle with respect to the inertial frame

i. The vector $\boldsymbol{\nu} \triangleq [u, v, r]^T$ contains the linear and angular velocities of the ship defined in the body-fixed frame b, where u is the surge velocity, v is the sway velocity and r is the yaw rate. The ocean current velocity in the body frame b, $\boldsymbol{\nu}_c \triangleq [u_c, v_c, 0]^T$, is obtained from $\boldsymbol{\nu}_c = \boldsymbol{R}^T(\psi)\boldsymbol{V}_c$ where $\boldsymbol{R}(\psi)$ is the rotation matrix from b to i. According to Assumption 6.5 the ocean current is constant and irrotational in i and hence $\dot{\boldsymbol{V}}_c = \boldsymbol{0}$, and $\dot{\boldsymbol{\nu}}_c = [rv_c, -ru_c, 0]^T$. In navigation problems involving ocean currents it is useful to describe the state of the vessel with the relative velocity vector: $\boldsymbol{\nu}_r \triangleq \boldsymbol{\nu} - \boldsymbol{\nu}_c = [u_r, v_r, r]^T$. The vector $\boldsymbol{\nu}_r$ is defined in b, where u_r is the relative surge velocity and v_r is the relative sway velocity. This paper considers the class of marine vehicles described by the following 3-DOF maneuvering model [52]:

$$\dot{\boldsymbol{p}} = \boldsymbol{R}(\psi)\boldsymbol{\nu}_r + \boldsymbol{V}_c, \tag{6.1}$$

$$\boldsymbol{M}\dot{\boldsymbol{\nu}}_r + \boldsymbol{C}(\boldsymbol{\nu}_r)\boldsymbol{\nu}_r + \boldsymbol{D}\boldsymbol{\nu}_r = \boldsymbol{B}\boldsymbol{f}. \tag{6.2}$$

The model (6.1-6.2) describes the kinematics and dynamics of surface vessels as well as underwater vehicles moving in the horizontal plane.

Remark 6.3. It is shown in [52] that when the ocean current is constant and irrotational in i, as given in Assumption 6.5, the ship can be described by the 3-DOF maneuvering model (6.1-6.2).

The vector $\boldsymbol{f} \triangleq [T_u, T_r]^T$ is the control input vector, containing the surge thrust T_u and the rudder angle T_r.

Remark 6.4. Notice that the model (6.1-6.2) is underactuated in its configuration space since it has fewer control inputs than DOFs.

The matrix $\boldsymbol{M} = \boldsymbol{M}^T > 0$ is the mass and inertia matrix and includes hydrodynamic added mass. The matrix $\boldsymbol{C}$ is the Coriolis and centripetal matrix, $\boldsymbol{D} > 0$ is the hydrodynamic damping matrix and $\boldsymbol{B} \in \mathbb{R}^{3\times 2}$ is the actuator configuration matrix. For maneuvering control purposes, the matrices $\boldsymbol{R}(\psi)$, $\boldsymbol{M}$, $\boldsymbol{D}$, $\boldsymbol{B}$ are considered as [52]:

$$\boldsymbol{R}(\psi) \triangleq \begin{bmatrix} \cos(\psi) & -\sin(\psi) & 0 \\ \sin(\psi) & \cos(\psi) & 0 \\ 0 & 0 & 1 \end{bmatrix}, \quad \boldsymbol{M} \triangleq \begin{bmatrix} m_{11} & 0 & 0 \\ 0 & m_{22} & m_{23} \\ 0 & m_{23} & m_{33} \end{bmatrix}, \tag{6.3}$$

$$\boldsymbol{D} \triangleq \begin{bmatrix} d_{11} & 0 & 0 \\ 0 & d_{22} & d_{23} \\ 0 & d_{32} & d_{33} \end{bmatrix}, \quad \boldsymbol{B} \triangleq \begin{bmatrix} b_{11} & 0 \\ 0 & b_{22} \\ 0 & b_{32} \end{bmatrix}. \tag{6.4}$$

The particular structure of $\boldsymbol{M}$ and $\boldsymbol{D}$ is justified by Assumptions 6.1-6.4. The actuator configuration matrix $\boldsymbol{B}$ has full column rank and maps the control inputs T_u and T_r

into forces and moments acting on the vessel. The Coriolis and centripetal matrix $\boldsymbol{C}$ is obtained from $\boldsymbol{M}$ as [52]:

$$\boldsymbol{C}(\boldsymbol{\nu}_r) \triangleq \begin{bmatrix} 0 & 0 & -m_{22}v_r - m_{23}r \\ 0 & 0 & m_{11}u_r \\ m_{22}v_r + m_{23}r & -m_{11}u_r & 0 \end{bmatrix}. \tag{6.5}$$

Finally, x_g^* from Assumption 6.3 is chosen so that $\boldsymbol{M}^{-1}\boldsymbol{B}\boldsymbol{f} = [\tau_u, 0, \tau_r]^T$. The point $(x_g^*, 0)$ exists for all port-starboard symmetric vehicles [33]. Notice that in (6.1) the disturbance $\boldsymbol{V}_c$ represents a pure kinematic drift.

Remark 6.5. The model used in [26] contains both the velocity vector $\boldsymbol{\nu}$ as well as the relative velocity vector $\boldsymbol{\nu}_r$. This complicates the controller design and weakens the cascade configuration. The model (6.1-6.2) from [52] overcomes the problem and is suitable for several control design purposes.

6.1.3. The Model in Component Form

To solve nonlinear underactuated control design problems it is useful to expand the model (6.1-6.2) into a component form:

$$\dot{x} = u_r \cos(\psi) - v_r \sin(\psi) + V_x, \tag{6.6a}$$

$$\dot{y} = u_r \sin(\psi) + v_r \cos(\psi) + V_y, \tag{6.6b}$$

$$\dot{\psi} = r, \tag{6.6c}$$

$$\dot{u}_r = F_u(v_r, r) - \frac{d_{11}}{m_{11}} u_r + \tau_u, \tag{6.6d}$$

$$\dot{v}_r = X(u_r)r + Y(u_r)v_r, \tag{6.6e}$$

$$\dot{r} = F_r(u_r, v_r, r) + \tau_r. \tag{6.6f}$$

Notice the absence of any control inputs in sway (6.6e) to compensate for the environmental disturbances. The ship should therefore side-slip to counteract for currents, wind and waves. The expressions for $F_r(v_r, r)$, $F_u(v_r, r)$, $X(u_r)$ and $Y(u_r)$ are given in Appendix 6.A. Furthermore, the functions $Y(u_r)$ and $X(u_r)$ are bounded for bounded arguments and thus satisfy the following assumption:

Assumption 6.6. $Y(u_r)$ satisfies $Y(u_r) \leq -Y^{\min} < 0, \quad \forall u_r \in [-V_{\max}, U_{rd}]$, where $Y^{\min}$ is a positive constant.

Remark 6.6. Assumption 6.6 is justified by a contradiction: $Y(u_r) \geq 0$ would imply a nominally unstable vehicle in sway which is not the case for commercial vessels by design. No bounds are implied on u_r and $U_{rd} > 0$ will be defined later.

6.2. The Control Objective

This section formalises the control problem considered in this chapter: the control system should make the vessel follow a given straight line $\mathcal{P}$ and maintain a desired constant surge relative velocity $U_{rd} > 0$ in the presence of unknown and slowly varying (assumed to be constant in this context) ocean currents. To simplify the problem without any loss of generality, the inertial reference frame i is placed such that its x-axis is aligned with the desired path, giving $\mathcal{P} \triangleq \{(x, y) \in \mathbb{R}^2 : y = 0\}$. The vessel's y coordinate then corresponds to the cross-track error and the objectives the control system should pursue can be formalized as follows:

$$\lim_{t\to\infty} y(t) = 0, \qquad (6.7) \qquad \lim_{t\to\infty} \psi(t) = \psi_{ss}, \qquad (6.8) \qquad \lim_{t\to\infty} u_r(t) = U_{rd}, \qquad (6.9)$$

where ψ_{ss} is constant. The yaw angle $\psi(t)$ is not required to converge to zero but rather to a steady-state constant value, allowing the vehicle to hold a non-zero yaw angle at equilibrium and thus counteract the effect of the ocean current. This is necessary since the vehicle is underactuated, and no control force is available in sway to compensate for the drift. The value of the constant ψ_{ss} will be specified later.

Remark 6.7. In [26] the vessel is required to follow $\mathcal{P}$ with a constant total speed $U_d > 0$. In this paper the ship is required to hold a constant surge relative velocity U_{rd} as stated in (6.9). Therefore the path following speed is unconstrained and unknown. This is not ideal for speed profile planning/tracking scenarios. However, controlling the relative velocity of the vessel gives direct control over the energy consumption, as hydrodynamic damping depends on $\boldsymbol{\nu}_r$, and any lift forces due to transom stern effects. Furthermore, relative velocity control removes the unknown term $\boldsymbol{\nu}_c$ from the velocity feedback loop.

Remark 6.8. The relative velocity $\boldsymbol{\nu}_r$ is measurable and often relative velocity sensors are expected to give more reliable results than absolute velocity measurements.

Finally, the following assumption allows the vessel to achieve path following for sea currents acting in any directions of the plane:

Assumption 6.7. The propulsion system is rated with power and thrust capacity such that U_{rd} satisfies $U_{rd} > V_{\max}$.

Remark 6.9. For most surface vessels Assumption 6.7 is easy to meet since their propulsion systems are designed to give much more than 5 [m/s] of relative speed U_{rd}. In the North Atlantic ocean currents have usually an intensity of less than 1 [m/s].

6.3. The Control System

The control system that solves the path following task defined in Section 6.2 is presented. First the LOS guidance is introduced, and then the surge and yaw controllers are added in a cascaded configuration.

6.3.1. The Path Following Control Strategy

The surface vessel has to converge and follow the x-axis, therefore according to the integral LOS guidance method introduced in Chapter 3 the desired heading angle is:

$$\psi_{ILOS} \triangleq -\tan^{-1}\left(\frac{y + \sigma y_{\text{int}}}{\Delta}\right), \qquad \Delta, \sigma > 0, \tag{6.10a}$$

$$\dot{y}_{\text{int}} = \frac{\Delta y}{(y + \sigma y_{\text{int}})^2 + \Delta^2}, \tag{6.10b}$$

where Δ is the look-ahead distance and σ is the integral gain. Both are constant design parameters. The integral effect becomes significant when disturbances push the craft away from its path. This gives a nonzero angle (6.10a) and allows the vessel to side-slip while staying on the desired path, so part of its relative forward velocity can thus counteract the effect of the ocean current. The law (6.10b) gives less integral action when the vehicle is far from $\mathcal{P}$, reducing the risk of wind-up effects.

6.3.2. The Surge and Yaw Controllers

According to (6.9), $u_r(t)$ should follow the desired value $u_{rd}(t) \triangleq U_{rd} > 0$. Therefore, to track $u_{rd}(t)$ the following controller is used:

$$\tau_u = -F_{u_r}(v_r, r) + \frac{d_{11}}{m_{11}} u_{rd} + \dot{u}_{rd} - k_{u_r}(u_r - u_{rd}). \tag{6.11}$$

The gain $k_{u_r} > 0$ is constant. The controller (6.11) is a feedback linearising P-controller and guarantees exponential tracking of $u_{rd}(t)$. Part of the damping is not cancelled in order to guarantee some robustness with respect to model uncertainties.

The following controller can be used to track the desired yaw angle $\psi_d \triangleq \psi_{ILOS}$:

$$\tau_r = -F_r(u_r, v_r, r) + \ddot{\psi}_d - k_\psi(\psi - \psi_d) - k_r(\dot{\psi} - \dot{\psi}_d), \tag{6.12}$$

where $k_\psi, k_r > 0$ are constant gains. The controller (6.12) is a feedback linearising PD controller and makes sure that ψ and r exponentially track ψ_d and $\dot{\psi}_d$ respectively.

Remark 6.10. The controllers (6.11) and (6.12) are feedback linearizing controllers, hence if the model suffers from high uncertainty other approaches should be considered.

6.4. Stability Conditions

This section presents the stability conditions under which the proposed ILOS guidance (6.10) in a cascaded configuration with the feedback linearizing controllers (6.11-6.12) achieves the objectives (6.7-6.9). The notation $X^{U_{rd}} \triangleq X(U_{rd})$ and $Y^{U_{rd}} \triangleq Y(U_{rd})$ is used.

Theorem 6.1. *Given an underactuated surface vessel described by the dynamical system (6.6). If Assumptions 6.5-6.7 hold and, if the look-ahead distance* Δ *and the integral gain* σ *satisfy the conditions:*

$$\Delta > \frac{|X^{U_{rd}}|}{|Y^{U_{rd}}|}\left[\frac{5}{4}\frac{U_{rd} + V_{\max} + \sigma}{U_{rd} - V_{\max} - \sigma} + 1\right], \tag{6.13}$$

$$0 < \sigma < U_{rd} - V_{\max}, \tag{6.14}$$

then the controllers (6.11-6.12), where ψ_d *is given by* (6.10) *and* $u_{rd} \triangleq U_{rd}$*, guarantee achievement of the control objectives (6.7-6.9). The control objective* (6.8) *is fulfilled* *with:*

$$\psi_{ss} = -\tan^{-1}\left(\frac{V_y}{\sqrt{U_{rd}^2 - V_y^2}}\right). \tag{6.15}$$

6.5. Proof of Theorem 6.1

In this section the proof of Theorem 6.1 is presented. Given the vector $\boldsymbol{\zeta} \triangleq [\tilde{u}_r, \tilde{\psi}, \dot{\tilde{\psi}}]^T$ where $\tilde{u}_r \triangleq u_r - U_{rd}$, $\tilde{\psi}_r \triangleq \psi - \psi_d$ and $\dot{\tilde{\psi}}_r \triangleq \dot{\psi} - \dot{\psi}_d$, the dynamics of $\boldsymbol{\zeta}$ are obtained by combining the system equations (6.6c), (6.6d) and (6.6f) with the control laws (6.11) and (6.12):

$$\dot{\boldsymbol{\zeta}} = \begin{bmatrix} -k_{u_r} - \frac{d_{11}}{m_{11}} & 0 & 0 \\ 0 & 0 & 1 \\ 0 & -k_\psi & -k_r \end{bmatrix} \boldsymbol{\zeta} \triangleq \boldsymbol{\Sigma}\boldsymbol{\zeta}. \tag{6.16}$$

The system (6.16) is linear and time-invariant. Furthermore, since the gains k_{u_r}, k_ψ, k_r and the term d_{11}/m_{11} are all strictly positive, the system matrix $\boldsymbol{\Sigma}$ is Hurwitz and the origin $\boldsymbol{\zeta} = \mathbf{0}$ of (6.16) is UGES. Therefore the control goal (6.9) is achieved with exponential converging properties in any ball of initial conditions.

The dynamics of the cross track error y and the relative sway velocity v_r are analysed next. The $y - v_r$ subsystem is obtained combining (6.6b), (6.6e) and (6.10b):

$$\dot{y}_{\text{int}} = \frac{\Delta y}{(y + \sigma y_{\text{int}})^2 + \Delta^2}, \tag{6.17}$$

$$\dot{y} = (\tilde{u}_r + U_{rd})\sin(\tilde{\psi} + \psi_d) + v_r\cos(\tilde{\psi} + \psi_d) + V_y, \tag{6.18}$$

$$\dot{v}_r = X(\tilde{u}_r + U_{rd})(\dot{\tilde{\psi}} + \dot{\psi}_d) + Y(\tilde{u}_r + U_{rd})v_r. \tag{6.19}$$

The equilibrium point of the system (6.17-6.19) is given by:

$$y_{\text{int}}^{\text{eq}} = \frac{\Delta}{\sigma}\frac{V_y}{\sqrt{U_{rd}^2 - V_y^2}},\ y^{\text{eq}} = 0,\ v_r^{\text{eq}} = 0. \tag{6.20}$$

A new set of variables is introduced to move the equilibrium point to the origin: $e_1 \triangleq y_{\text{int}} - y_{\text{int}}^{\text{eq}}$ and $e_2 \triangleq y + \sigma e_1$. Substituting (6.10a) for ψ_d and factorizing the result with respect to $\boldsymbol{\zeta}$ leads (6.17-6.19) to the following expression of the interconnected dynamics:

$$\begin{bmatrix} \dot{e}_1 \\ \dot{e}_2 \\ \dot{v}_r \end{bmatrix} = \boldsymbol{A}(e_2) \begin{bmatrix} e_1 \\ e_2 \\ v_r \end{bmatrix} + \boldsymbol{B}(e_2) + \boldsymbol{H}(y, y_{\mathrm{int}}, \psi_d, v_r, \boldsymbol{\zeta})\boldsymbol{\zeta}, \tag{6.21a}$$

$$\dot{\boldsymbol{\zeta}} = \boldsymbol{\Sigma}\boldsymbol{\zeta}. \tag{6.21b}$$

The matrix $\boldsymbol{H}(y, y_{\mathrm{int}}, \psi_d, v_r, \boldsymbol{\zeta})$ contains all the terms vanishing at $\boldsymbol{\zeta} = \boldsymbol{0}$. $\boldsymbol{A}(e_2)$ is given in (6.38) of Appendix 6.A while $\boldsymbol{B}(e_2)$ and $\boldsymbol{H}(y, y_{\mathrm{int}}, \psi_d, v_r, \boldsymbol{\zeta})$ are:

$$\boldsymbol{B}(e_2) \triangleq \begin{bmatrix} 0 \\ V_y f(e_2) \\ -\frac{\Delta X^{U_{rd}} V_y}{(e_2 + \sigma y_{\mathrm{int}}^{\mathrm{eq}})^2 + \Delta^2} f(e_2) \end{bmatrix}, \tag{6.22}$$

$$\boldsymbol{H}(y, y_{\mathrm{int}}, \psi_d, v_r, \boldsymbol{\zeta}) \triangleq \begin{bmatrix} 0 & 0 \\ 1 & 0 \\ -\frac{\Delta X(\tilde{u}_r + U_{rd})}{(e_2 + \sigma y_{\mathrm{int}}^{\mathrm{eq}})^2 + \Delta^2} & 1 \end{bmatrix} \begin{bmatrix} \boldsymbol{h}_y^T \\ \boldsymbol{h}_{v_r}^T \end{bmatrix}, \tag{6.23}$$

where:

$$f(e_2) = 1 - \frac{\sqrt{(\sigma y_{\mathrm{int}}^{\mathrm{eq}})^2 + \Delta^2}}{\sqrt{(e_2 + \sigma y_{\mathrm{int}}^{\mathrm{eq}})^2 + \Delta^2}}. \tag{6.24}$$

Note that the following bound holds for $f(e_2)$:

$$|f(e_2)| \leq \frac{|e_2|}{\sqrt{(e_2 + \sigma y_{\mathrm{int}}^{\mathrm{eq}})^2 + \Delta^2}}. \tag{6.25}$$

The expressions of the vectors $\boldsymbol{h}_y$ and $\boldsymbol{h}_{v_r}$ are given in Appendix 6.A. Notice that the system (6.21) is a cascaded system, where the linear UGES system (6.21b) perturbs the dynamics (6.21a) through the interconnection matrix $\boldsymbol{H}(y, y_{\mathrm{int}}, \psi_d, v_r, \boldsymbol{\zeta})$. To analyze the stability properties of the cascade (6.21) consider the following nominal system defined on the manifold $\boldsymbol{\zeta} = \boldsymbol{0}$:

$$\begin{bmatrix} \dot{e}_1 \\ \dot{e}_2 \\ \dot{v}_r \end{bmatrix} = \boldsymbol{A}(e_2) \begin{bmatrix} e_1 \\ e_2 \\ v_r \end{bmatrix} + \boldsymbol{B}(e_2) f(e_2). \tag{6.26}$$

The following Lemma states the stability properties of the nominal system (6.26):

Lemma 6.1. *Under the conditions of Theorem 6.1, the system* (6.26) *is UGAS and ULES.*

Proof. The proof of Lemma 6.1 is given in Appendix 6.B. □

Next, the stability of the cascade (6.21) is analyzed. In particular, the perturbing system (6.21b) is UGES and the interconnection matrix $\boldsymbol{H}$ can be shown to satisfy:

$$\| \boldsymbol{H} \| \leq \theta_1(\| \boldsymbol{\zeta} \|)(|y| + |y_{\mathrm{int}}| + |v_r|) + \theta_2(\| \boldsymbol{\zeta} \|), \tag{6.27}$$

where $\theta_1(\cdot)$ and $\theta_2(\cdot)$ are some continuous non-negative functions. Therefore applying Theorem A.2 and Lemma A.2 concludes that under the conditions of Theorem 6.1 the origin $(e_1, e_2, v_r, \boldsymbol{\zeta}) = (0, 0, 0, \mathbf{0})$ of the system (6.21) is UGAS and ULES. Hence, the control objectives (6.7) and (6.8) are achieved with exponential converging properties with ψ_{ss} given in 6.15.

Remark 6.11. The value $y_{\mathrm{int}}^{\mathrm{eq}}$ guarantees that at equilibrium the vessel holds the heading ψ_{ss} defined in 6.15 which is, as explained in Section 3.1 of Chapter 3, the only possible yaw angle that guarantees successful current compensation for underactuated surface vessels.

Remark 6.12. The lower bound (6.13) is expected and has a clear physical interpretation: a too short look-ahead distance $\Delta > 0$ makes the vessel overshoot the target and thus causes chattering as shown in Chapters 3-4.

6.6. Measurement of the Ocean Current

In this section a short review of the instrumentation required to implement the control system (6.11-6.10) is given and it is shown how the ocean current can be estimated in steady state.

Relative velocity sensors as well as absolute position measurements are needed to implement the control system (6.10-6.12). Ships are usually equipped with a large variety of position, velocity and attitude sensors in order to reconstruct their state. The estimation of a system state variable is often the result of a certain sensor fusion algorithm [52]. For instance, to estimate the absolute position/velocity of the vessel, data from an Inertial Measurement Unit (IMU) and a GPS receiver can be combined to compensate for the drift affecting the IMU. When operating in shallow waters, the absolute velocity of the ship can also be measured using a Doppler Velocity Logs (DVL). The DVL compares the frequencies of a transmitted and received acoustic signal bounced to the sea bottom. To measure the relative velocity the following sensors are available: Acoustic Doppler Current Profilers (ADCP), Pitometer logs and Paddle meters. The ADCP is similar to the DVL: it samples repeatedly the return echo and produces a sea current profile over a range of depths. The Pitometer log compares the dynamic and static pressures of the fluid while the paddle meter measures the spin velocity of a paddle driven by the flow itself. Although relative velocity logs such as ADCPs or Pitometers can suffer from drift effects, they are expected to give reliable measurements. Therefore, having the state of the ship described by the relative velocity $\boldsymbol{\nu}_r$ decouples the controllers (6.11-6.12) from the guidance law (6.10) where absolute position measurements such as GPS data are required.

In general the relative velocity of the ship in i is defined as $\boldsymbol{U}_r(t) \triangleq \boldsymbol{U}(t) - \boldsymbol{V}_c$ where $\boldsymbol{U}(t) \triangleq [\dot{x}, \dot{y}]^T$ is the absolute velocity of the ship in i and $\boldsymbol{V}_c$ is the ocean current. The steady state condition is reached when the closed-loop system (6.21) has converged to its equilibrium point. In steady state the ship follows $\mathcal{P}$ and the relation between $\boldsymbol{U}_r(t)$ and $\boldsymbol{U}(t)$ becomes $\boldsymbol{U}_{rd} = \boldsymbol{U}_{ss} - \boldsymbol{V}_c$. The vectors $\boldsymbol{U}_{ss}$ and $\boldsymbol{U}_{rd}$ are defined as:

$$\boldsymbol{U}_{ss} \triangleq \lim_{t\to\infty} \boldsymbol{U}(t), \qquad (6.28) \qquad\qquad \boldsymbol{U}_{rd} \triangleq \lim_{t\to\infty} \boldsymbol{U}_r(t), \qquad (6.29)$$

where $\boldsymbol{U}_{ss} = [U_{ss}, 0]^T$ and the constant $U_{ss} > 0$. From the definition of $\boldsymbol{U}_r(t)$ the relation between the intensities U_{ss} and $U_{rd} \triangleq |\boldsymbol{U}_{rd}|$ is: $U_{rd} = \sqrt{(U_{ss} - V_x)^2 + V_y^2}$. This relation together with the value stored in the integrator at equilibrium $y_{\text{int}}^{\text{eq}}$ given in (6.20) yields:

$$V_y = \frac{y_{\text{int}}^{\text{eq}} U_{rd}}{\sqrt{(y_{\text{int}}^{\text{eq}})^2 + \frac{\Delta^2}{\sigma^2}}}, \quad V_x = U_{ss} - \sqrt{U_{rd}^2 - V_y^2}. \tag{6.30}$$

If measurements of $|\boldsymbol{U}|$ and $|\boldsymbol{U}_r|$ are available and if y_{int} is accessible, then the ocean current $\boldsymbol{V}_c$ can be estimated using (6.30) when the system is in steady state.

6.7. Simulations

Results from numerical simulations are presented in this section. First, the ILOS guidance (6.10) from Section 6.3 in a cascaded configuration with the feedback linearizing surge and yaw controllers (6.11-6.12), is applied to an underactuated supply vessel. In order to have simulation results that can be directly compared with the experiments on the CART USSV, the model is then scaled to the dimensions of the CART USSV. A scaled version of the supply ship model is used for simulation and tuning since an accurate model of the CART vehicle is not yet available. Disturbances in the form of an irrotational ocean current are taken into account since the CART vehicle operates semi-submersed. Therefore, disturbances from wind are also assumed to act as a current in the water layers close to the surface.

6.7.1. ILOS applied to an offshore supply vessel

The proposed control system (6.10-6.12) is applied to an underactuated supply vessel. The model of the ship is given in Section B.1 of Appendix B and the objective is to make the vessel follow the path $\mathcal{P}$ (north direction, 0 [deg]) with a desired surge relative speed $U_{rd} = 5$ [m/s]. The intensity of the current is $|\boldsymbol{V}_c| = \sqrt{2}$ [m/s] and its direction is unknown since it is randomly generated. In this case its components are $V_x = 0.60$ [m/s] and $V_y = -1.28$ [m/s]. Thus, Assumption 6.5 is fulfilled with $V_{\max} = 1.5$ [m/s] and it can be verified that Assumption 6.6 is satisfied with $Y_{\min} = 0.037$ [1/s]. The constants $|Y^{U_{rd}}|$ and $|X^{U_{rd}}|$ become $|Y^{U_{rd}}| = 0.07$ [1/s] and $|X^{U_{rd}}| = 4.34$ [m/s]. The chosen values for the integral gain and the look-ahead distance of the integral LOS guidance law are $\sigma = 1$ [m/s] and $\Delta = 300$ [m], and satisfy (6.13-6.14). The heading and speed controllers (6.11-6.12) are implemented with the following gains: $k_{u_r} = 0.1$ [1/s], $k_\psi = 0.04$ [1/s^2] and $k_r = 0.9$ [1/s]. Hence, the $\tilde{u}_r$ first order closed loop system has a time constant of 8.8 [s] while the $\tilde{\psi}$ second order closed loop system is overdamped with $\omega_0 = 0.2$ [rad/s]. Saturation is considered for both the rudder and the propeller. The maximum rudder angle is 35° and the maximum rudder turning rate is 10 [°/s]. The maximum available propeller force is 1600 [kN].

The ship is given an initial cross track error of 1500 meters and initially holds zero relative velocity. Its surge axis is parallel to the desired path and it is heading south (180 [deg]). Figures 6.1a, 6.1b and 6.1c show how the underactuated vessel successfully follows the path $\mathcal{P}$ with a constant side-slip angle $\psi_{ss} \approx 14.8$ [deg] to compensate for the current. It can be seen that choosing the guidance law parameters according to the criteria (6.13-6.14) gives smooth convergence and does not overload the controllers (6.11-6.12). The performance of the speed controller (6.11) is shown in Figure 6.1d, while the rudder angle is given in 6.1c. Finally, notice in Figure 6.1e how the unknown current can be estimated using (6.30). The signals y_{int}, $|\boldsymbol{U}_r|$ and $|\boldsymbol{U}|$ are available on-line. The quantity y_{int} is given in (6.10b) while $|\boldsymbol{U}_r|$ and $|\boldsymbol{U}|$ are calculated from: $|\boldsymbol{U}_r| = \sqrt{u_r^2 + v_r^2}$ and $|\boldsymbol{U}| = \sqrt{\dot{x}^2 + \dot{y}^2}$.

The guidance controller (6.10-6.12) is also simulated using the extended model of the same supply vessel to assess robustness with respect to model uncertainties. The extended model is given in Section B.1 of Appendix B and combines linear as well as nonlinear damping to give a more realistic picture of the vessel behavior at higher speeds. Linear damping is a fair approximation of the hydrodynamic drag forces in low-speed/station-keeping operating conditions (speed lower than 2 [m/s]) while nonlinear damping dominates at higher speeds [52]. Furthermore, process noise is added to the system. Figures 6.2a-6.2b show that the integral LOS guidance achieves convergence in presence of nonlinear drag as well as zero-mean Gaussian process noise having the following vector of standard deviations $[\sigma_x, \sigma_y, \sigma_\psi, \sigma_{u_r}, \sigma_{v_r}, \sigma_r]^T = 10^{-3}[1, 1, 1, 10, 100, 1]^T$. Yet, the integral LOS guidance is very robust with respect to the noise affecting the surge and sway velocities, while it is sensitive to noise affecting the position and yaw state variables. The speed controller (6.11) suffers from a significant offset caused by different hydrodynamic coefficients (see Figure 6.2c). However, this offset can be easily removed with integral action. The heading controller (6.12) does not seem to suffer significantly from model uncertainties but it does suffer from process noise (see Figure 6.2b). Finally, a Monte Carlo analysis is run on the model having linear damping only, where random uniformly distributed uncertainty is added to all the hydrodynamic coefficient of the dynamics (6.2). The model is generated and then held constant for each simulation run. Acceptable path following is achieved in 91% of 50000 simulation runs where the maximum uncertainties on the matrices $\boldsymbol{M}$, $\boldsymbol{D}$ and $\boldsymbol{B}$ are 40%, 70% and 50% respectively. These results further confirm the robustness of the ILOS guidance law with respect to model uncertainties.

6.7.2. Scaling the model to the CART vehicle dimensions

The CART USSV, presented in Section 6.8, is a 0.9 [m] long vehicle and its mass is approximately 50 [kg]. Since there is no accurate model of the CART vehicle available yet, the supply vessel model is scaled to the dimensions of the CART USSV through the *bis* normalization system [52]. The purpose is to analyze the behavior of a vehicle having the same dimensions of the CART in order to tune the gains Δ and σ for the experiments, and also to compare simulation results with experimental results. Since the vehicle operates semi-submersed, only constant irrotational ocean current disturbances are considered. The upper bound for the current intensity is selected as $V_{\max} = 0.3$ [m] and the vehicle is required to hold a relative surge velocity $U_{rd} = 0.7$ [m/s]. The desired U_{rd} satisfies Assumption 6.7. The chosen values for the guidance law integral gain and look-ahead distance are $\sigma = 0.1$ [m/s] and $\Delta = 5$ [m], and satisfy (6.13-6.14) with

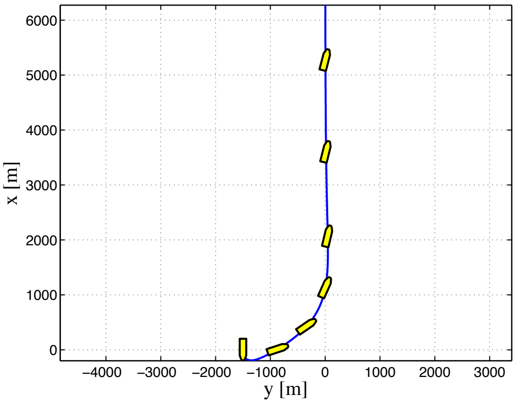

(a) Simulation of convergence and path following of the underactuated supply vessel in presence of currents. The time interval $0 - 1500$ [s] is considered in the figure.

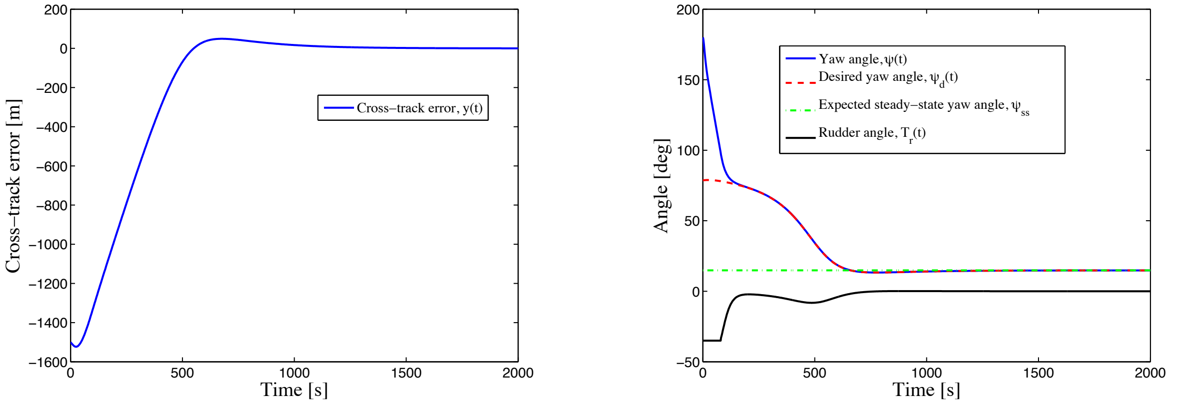

(b) Cross track error $y(t)$ of the vessel.

(c) Heading angle $\psi(t)$ and rudder angle $T_r(t)$ of the ship.

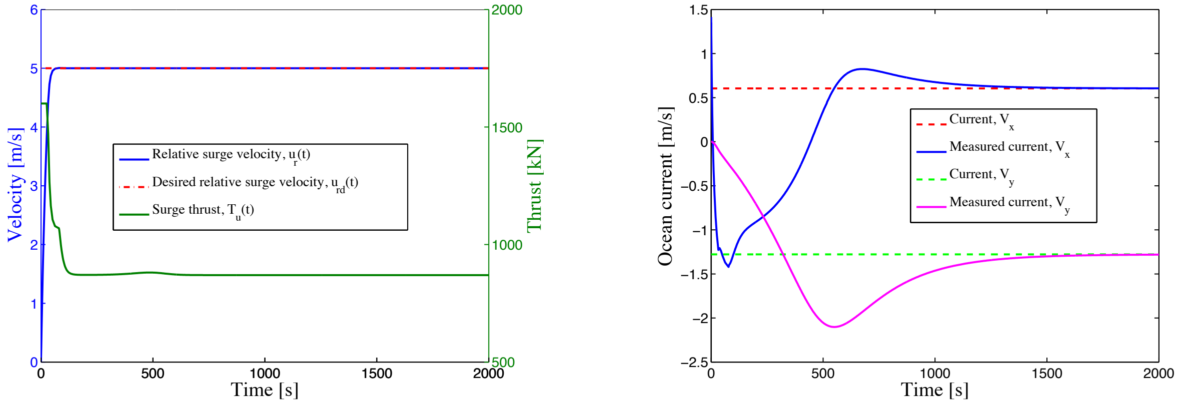

(d) Telative surge velocity $u_r(t)$ and surge thrust $T_u(t)$.

(e) Estimation of the current components V_x and V_y.

Figure 6.1.: Simulation results for $\Delta = 300$ [m] and $\sigma = 1$ [m/s].

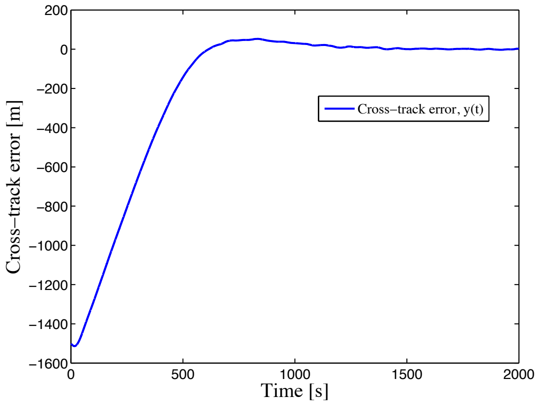

(a) Cross track error $y(t)$ of the vessel in presence of model uncertainties and process noise.

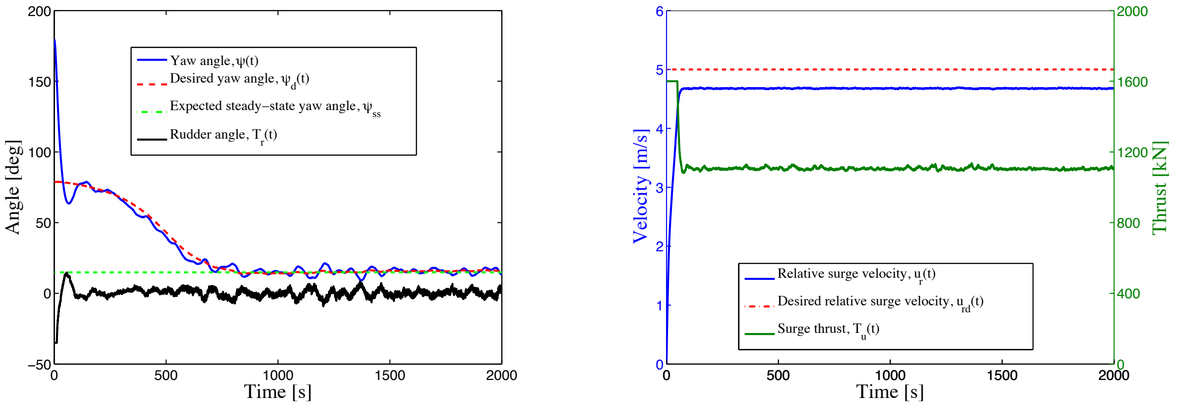

(b) Heading angle $\psi(t)$ of the ship in presence of model uncertainties as well as process noise.

(c) Relative surge velocity $u_r(t)$ of the vessel in presence of model uncertainty and process noise.

Figure 6.2.: Simulation results for $\Delta = 300$ [m] and $\sigma = 1$ [m/s] in presence of model uncertainties and process noise.

$\kappa_v^{\max} = 0$. The gains of the controllers (6.11-6.12) are set to: $k_{u_r} = 0.5$, $k_\psi = 1$, $k_r = 3$. Higher gains are used compared to the supply ship case since the CART USSV is a highly maneuverable vehicle [12]. In particular, the values for k_{u_r}, k_ψ and k_r are chosen to give a time constant of approximately 1.4 [s] for the $\tilde{u}_r$ first order closed loop system and to make the $\tilde{\psi}$ second order closed loop system overdamped with $\omega_0 = 1$ [rad/s]. The ocean current is set to $V_x = 0.02$ [m/s] and $V_y = -0.05$ [m/s], and equals the drift of the vehicle measured before the test runs shown in Section 6.8.

The simulation procedure resembles the test runs shown in Section 6.8 and requires the vehicle to move along two parallel straight lines in order to exhibit the transient response and the steady-state behavior of the ILOS guidance system. The reference paths are two parallel straight lines l_1 and l_2 defined by a point and an angular orientation in the $x - y$ plane:

- l_1: point (60 [m]; -50 [m]), orientation -130 [deg]
- l_2: point (70 [m]; -50 [m]), orientation 50 [deg]

At the beginning, the first reference line l_1 is fed to the ILOS. After a while, the vehicles is commanded to turn back and follow the second line l_2. Figures 6.4a, 6.4c and 6.4e show how the vehicle successfully follows the lines l_1 and l_2, with an average side-slip angle $\psi_{ss} \approx 4.6$ [deg] for l_1 and $\psi_{ss} \approx -4.6$ [deg] for l_2, to compensate for the disturbances. It can be seen that choosing the guidance law parameters according to the criteria (6.13-6.14) gives smooth convergence.

6.8. Experiments

In this section results from field experiments are presented. The CART USSV was used as a test platform and the sea trials were carried out off the coast of the Murter island in Croatia. First, a description of the CART USSV is given and then the results from the experiments are presented and commented. Weather conditions on the test day (28.09.2013) were good with a light breeze blowing from the South-East, sweeping along the coast of Dalmatia. This is in accordance with the estimated current of 0.02 [m/s] North and -0.05 [m/s] East. Notice that South-Eastern winds are common for the Adriatic sea.

6.8.1. Vehicle description

The CART USSV, shown in Figure 6.3, has been developed for emergency towing operations in Italy by CNR-ISSIA in cooperation with other international partners [22]. It is a 0.9 [m] long and 0.75 [m] wide robotic platform. Thrust is provided by four DC brushless motors coupled to 4-bladed propellers, capable of delivering a maximum bollard pull of about 150 [N]. A central cylindrical canister contains all the electronics and sensors. In particular, the USSV is equipped with a single board computer running a GNU/Linux based real-time control application, a GPS system providing absolute position measurements and an Attitude and Heading Reference System (AHRS). Another cylinder contains a set of lithium ions batteries. At full charge the vehicle can operate continuously for $5 - 6$ hours. The communication between the vehicle and the remote control station is provided by a 2.4 [Ghz] WiFi link.

For the purpose of exploiting the CART vehicle as a platform for the development of advanced navigation, guidance and control techniques, as well as payload carrier in different experimental campaigns, the software control architecture has been upgraded and an extensively tested and well known software system has been ported. In particular the control architecture of the CNR-ISSIA Charlie surface vehicle [12] has been customized and transferred on the CART USSV as well. The porting operation involved the development of a new *driver* layer, thus creating the connection between the hardware and the software architecture. No rearrangement of the higher levels of the architecture was required, due to the complete decoupling from hardware-related issues.

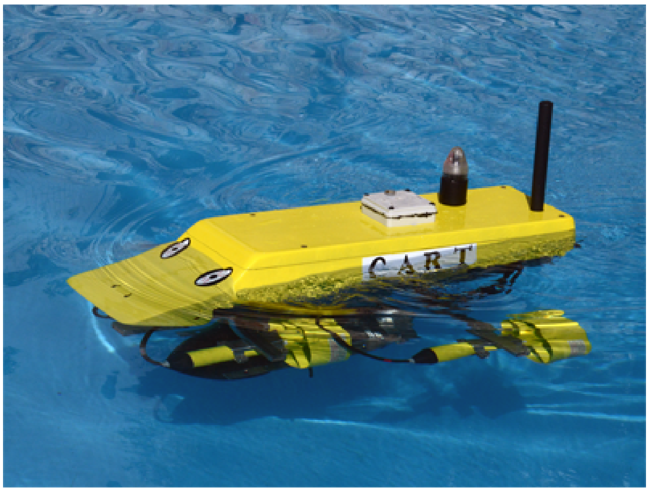

Figure 6.3.: The CART USSV during operations.

The CART USSV has a very high level of maneuverability. This, together with its high power-to-weight ratio and the smart placement of the motors, allows for choosing the thrust/torque mapping in such a way that all the engines deliver thrust, but only the two rear ones contribute to torque generation. This makes the motion of the vehicle smoother and less subjected to yaw jerks. Since a validated dynamic model of the employed vehicle is not yet available, a simple Proportional-Derivative (PD) control scheme has been implemented to provide the basic auto-heading feature. The controller parameters have been set through on the field tests, obtaining an overshoot-free response in normal sea conditions. More information about the CART vehicle is found in [12, 22, 14].

6.8.2. Sea Trials

An extensive set of sea trials has been carried out with the purpose of evaluating the performance of the ILOS guidance law. As explained in Section 6.7, the USSV is required to move along the two geo-referenced parallel straight lines l_1 and l_2 to exhibit both the transient response as well as the steady state behavior of the guidance law. This procedure has been repeated several times to test different combinations of the parameters Δ and σ for different thrust levels. However, focus is first put on comparing the ILOS on-the-field performances with the simulations from Section 6.7. In particular, the guidance law parameters Δ and σ are set to 5 [m] and 0.1 [m/s], respectively, as suggested by the simulations. The thrust level is set to 20%, which corresponds approximately to 0.7 [m/s] of relative velocity. Next, results from tests runs with different combinations of the guidance law parameters Δ and σ for different speeds/thrust levels are shown.

Remark 6.13. The control system on the CART USSV does not provide the option to directly control its relative velocity. However, the thrust level (RPMs) can be set. This is the closest available option to relative velocity control.

Figures 6.4b, 6.4d and 6.4f show that the experimental results are in good agreement with the simulations results in Figures 6.4a, 6.4c and 6.4e. The CART USSV successfully follows the lines l_1 and l_2, with an average side-slip angle $\psi_{ss} \approx 1$ [deg] for l_1 and $\psi_{ss} \approx -5$ [deg] for l_2, to compensate for the disturbances. The asymmetry in the two side-slip angles is probably caused by gyro-offsets (a magnetic declination of about 2 [deg] East is reported in the area) and dynamic, heading dependent disturbances caused by wind and waves.

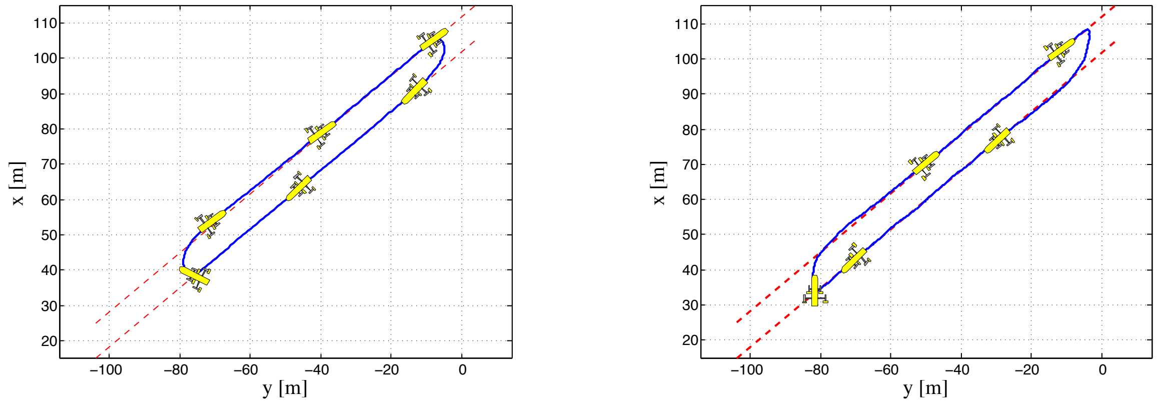

(a) Simulation of convergence and path following of the CART USSV in presence of constant irrotational ocean currents. The vehicle side-slips to compensate for the drift. In this case $\Delta = 5$[m] and $\sigma = 0.1$ [m/s].

(b) Experimental ILOS test run of the CART USSV off the coast of Murter, Croatia. Convergence and path following of the USSV is achieved. In this case $\Delta = 5$[m], $\sigma = 0.1$ [m/s] and the thrust is set to 20%.

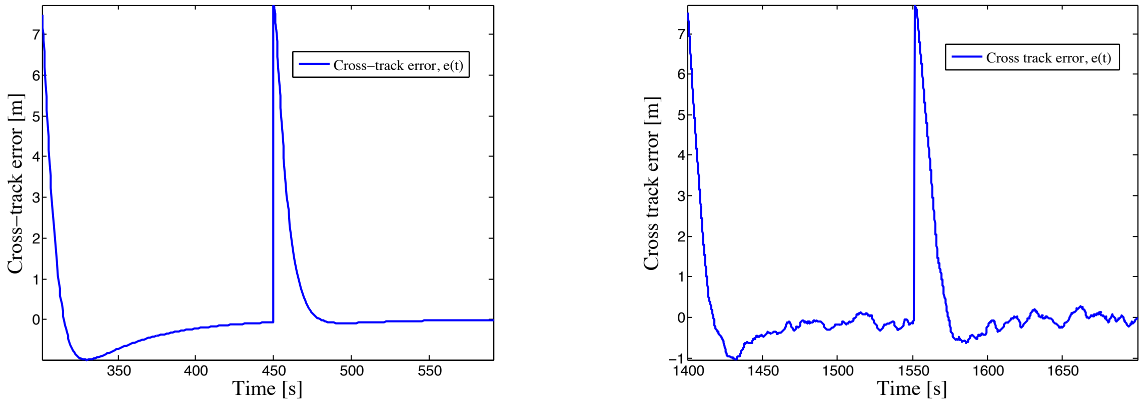

(c) Cross-track error of the CART USSV from simulations. Notice the overshoot caused by integral action. Afterwards, path following is achieved and the vehicles follows the line l_1 first and the line l_2 afterwords.

(d) Cross-track error of the CART USSV from sea trials. Notice the overshoot caused by integral action. Afterwards, path following is achieved for both the l_1 and l_2 lines. Disturbance from waves is present.

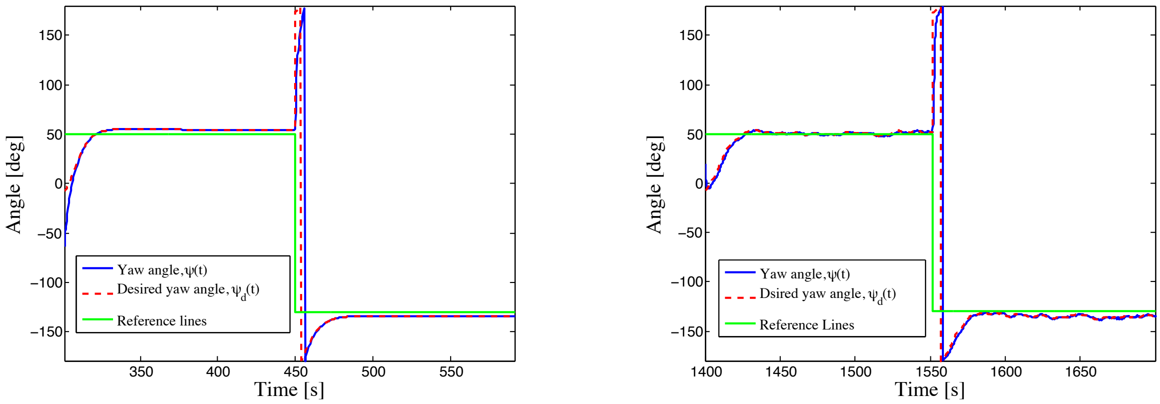

(e) Yaw angle $\psi(t)$ of the CART USSV from simulations. Notice the steady state side-slip angle $\psi_{ss} \approx 4.6$ [deg] for the l_1 line and $\psi_{ss} \approx -4.6$ [deg] for the l_2 line.

(f) Yaw angle $\psi(t)$ of the CART USSV from sea trials. Notice that while on path the vehicle holds an average side-slip angle of $\psi_{ss} \approx 1$ [deg] for the l_1 line and $\psi_{ss} \approx -5$ [deg] for the l_2 line.

Figure 6.4.: Back to back comparison between simulations and experimental results.

The next set of experiments focuses on the evaluation of the ILOS for different speeds held by the vehicle in motion. Figure 6.5 shows the comparison between different tests where the guidance system, characterized by the same parameter setting ($\Delta = 5.0$ [m] and $\sigma = 0.1$ [m/s]), is commanded to track the two reference lines at different surge thrust regimes. The commanded surge thrust values are 20%, 30%, 40% and 50% of the total available thrust provided by the motors. These values correspond to average steady state speeds of 0.7, 0.8, 0.9 and 1.0 [m/s], respectively. Notice that the values $\Delta = 5.0$ [m] and $\sigma = 0.1$ [m/s] were suggested by the simulations and are selected since they provide satisfactory path following performance. As shown in the plots of Figure 6.5, the vehicle converges and tracks the reference lines. Notice how every change of the reference line is followed by a peak in the cross track error. The ILOS guidance quickly reacts and takes the vehicle onto the new line. In particular, in the error plots of Figure 6.5 it can be noticed that during steady-state the cross-track error is always less than 1 m, with no significant difference with respect to the actual surge thrust setting. The statistical analysis reported in Table 6.1 supports this argument, indicating comparable standard deviation values during steady-state response. The steady-state mean values are in the order of $0.2 \div 0.3$ [m] thus indicating a practical rejection of external disturbances.

Table 6.1.: Speed dependency evaluation statistics.

thrust [%]	mean value [m]	standard deviation [m]
20	-0.1709	0.2762
30	-0.2193	0.3242
40	-0.2131	0.2546
50	-0.1847	0.3148

The second and third sets of test runs analyze the sensitivity of the guidance system with respect to the Δ and σ parameters. Figure 6.6 shows the motion of the vehicle where the parameter Δ is set to $2.0[m]$, $5.0[m]$ and 10.0 [m]. Interpreting the parameter Δ as the look-ahead distance, the effect of increasing its value induces a slower convergence onto the reference line, while Δ values approaching the size of the vehicle indeed reduce the convergence time, but introduce small oscillations during the on-path motion, caused by overshooting. This oscillating behavior at short Δ is simulated in Chapter 3 and is foreseen by the more detailed Lyapunov analysis of the complete kinematic-dynamic system in Section 6.5 where the lower bound (6.13) for Δ is analytically derived.

The results of the third experiment are shown in Figure 6.7. In Figure 6.7 the vehicle behavior is assessed with respect to different values of the integral gain σ. The guidance law is tested for the following values of σ: 0.05, 0.1 and 0.5 [m/s]. As it can be observed, with lower integral gains the guidance system loses its efficiency to reject constant disturbances, i.e. the side-slipping of the vehicle is not enough to completely compensate for the drift, while increasing the value of σ leads to overshoots in the transient response during the convergence phase. Notice that the condition (6.14), derived from the Lyapunov analysis of Section 6.5, gives an upper bound upon the choice of σ. The experimental results confirm what the theoretical analysis predicted: a high σ gain causes unstable behaviors.

6.9. Conclusions

In this chapter a solution for path following control of underactuated surface vessels has been presented and analyzed in details. It is based on the ILOS guidance law and path following of straight lines is considered. The complete kinematic and dynamic closed loop system of the ILOS guidance is analyzed where the actuated surge and yaw dynamics are considered as well. The resulting closed loop system forms a cascade where the actuated dynamics perturb the combined sway-guidance system analyzed in Chapter 5 and the UGAS and ULES stability properties are shown for the closed loop cascaded system. Disturbances in the form of irrotational ocean currents are taken into account and the dynamics of the vessel are expressed in terms of its relative velocity. This is possible since the current is assumed constant and irrotational in the inertial frame. Furthermore, it has been shown that in steady state it is possible to estimate the unknown current by using the integral term of the ILOS guidance law as well as measurements of the absolute and relative speeds of the vessel. The theoretical analysis is strongly supported by the results from simulations and field experiments where the ILOS guidance has been applied to the CART Unmanned Semi-Submersible Vehicle (USSV) for sea trials. Furthermore, different models of a supply ship are used to simulate the control system and to assess its robustness with respect to parameter uncertainties and process noise. This chapter relies significantly on the concepts developed in Chapter 3 and Chapter 5. Hence, the results from simulations and sea trials confirm the arguments and the theory presented in Chapter 3 and Chapter 5 as well.

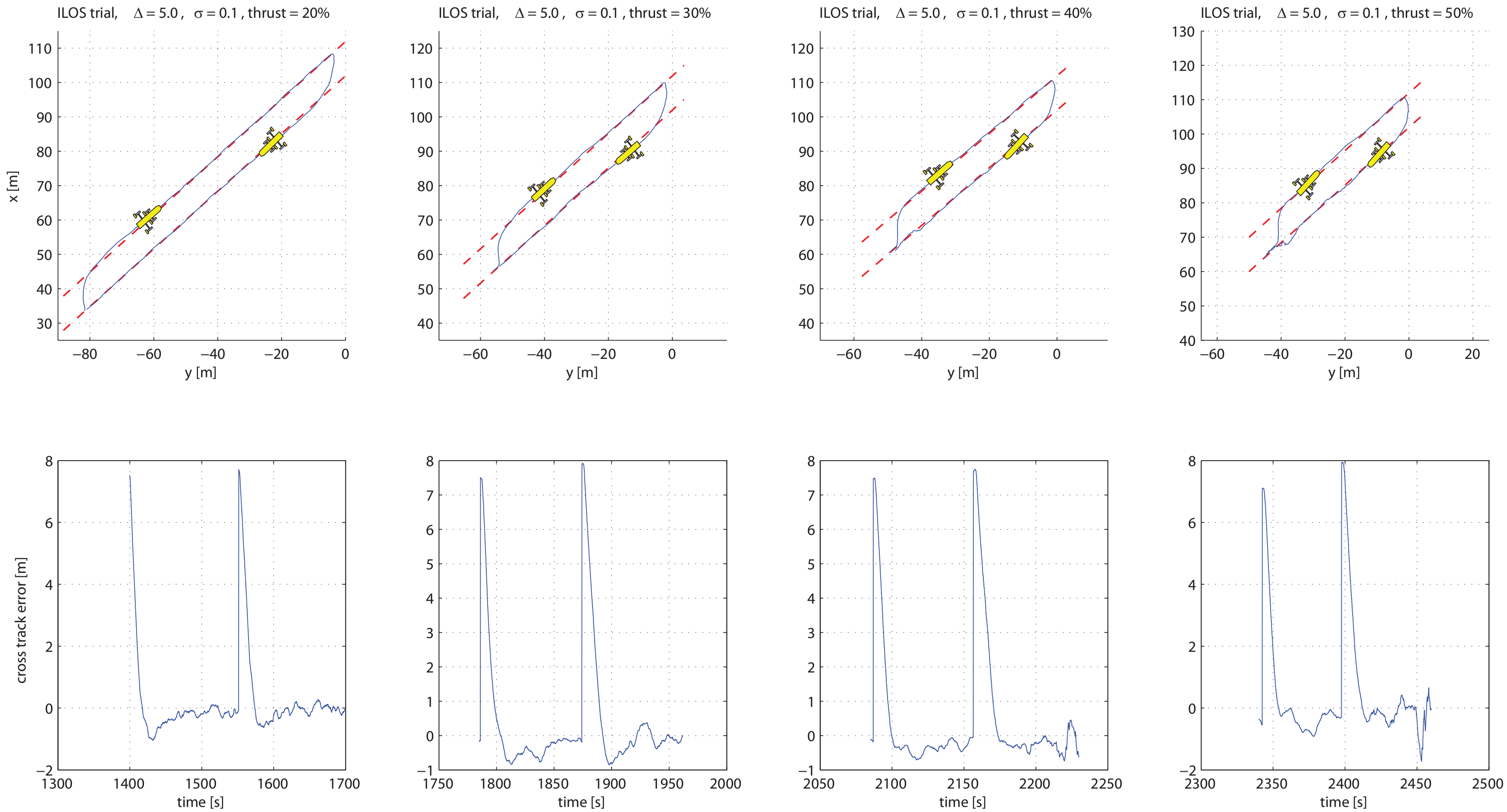

Figure 6.5.: Speed dependency evaluation - the upper plots show the motion of the vehicle (blue) along the reference lines (red); the lower plots show the cross track error variation in time.

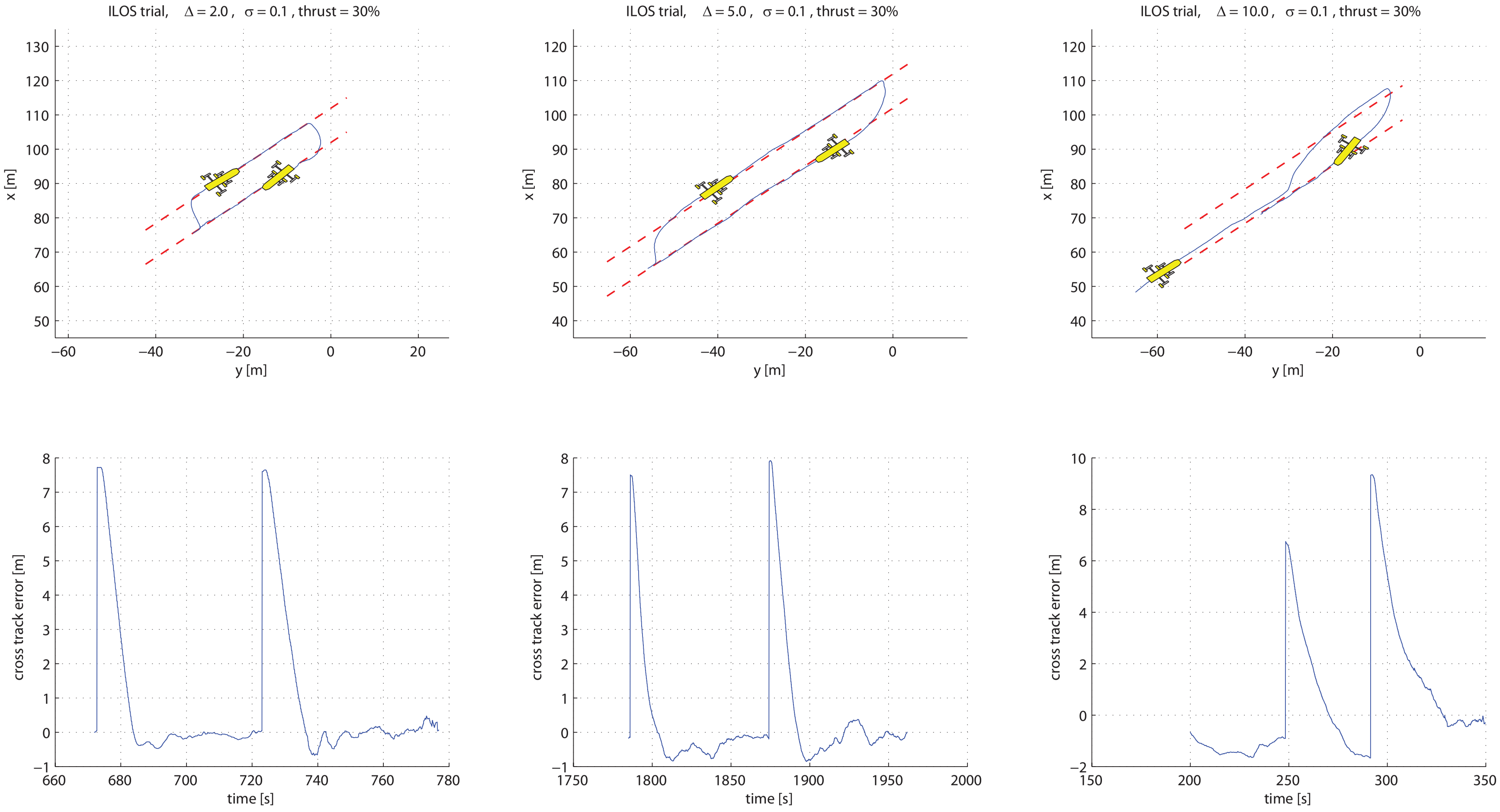

Figure 6.6.: Sensitivity of the ILOS guidance with respect to the look-ahead distance Δ - the upper plots show the motion of the vehicle (blue) along the reference lines (red); the lower plots show the cross track error variation in time.

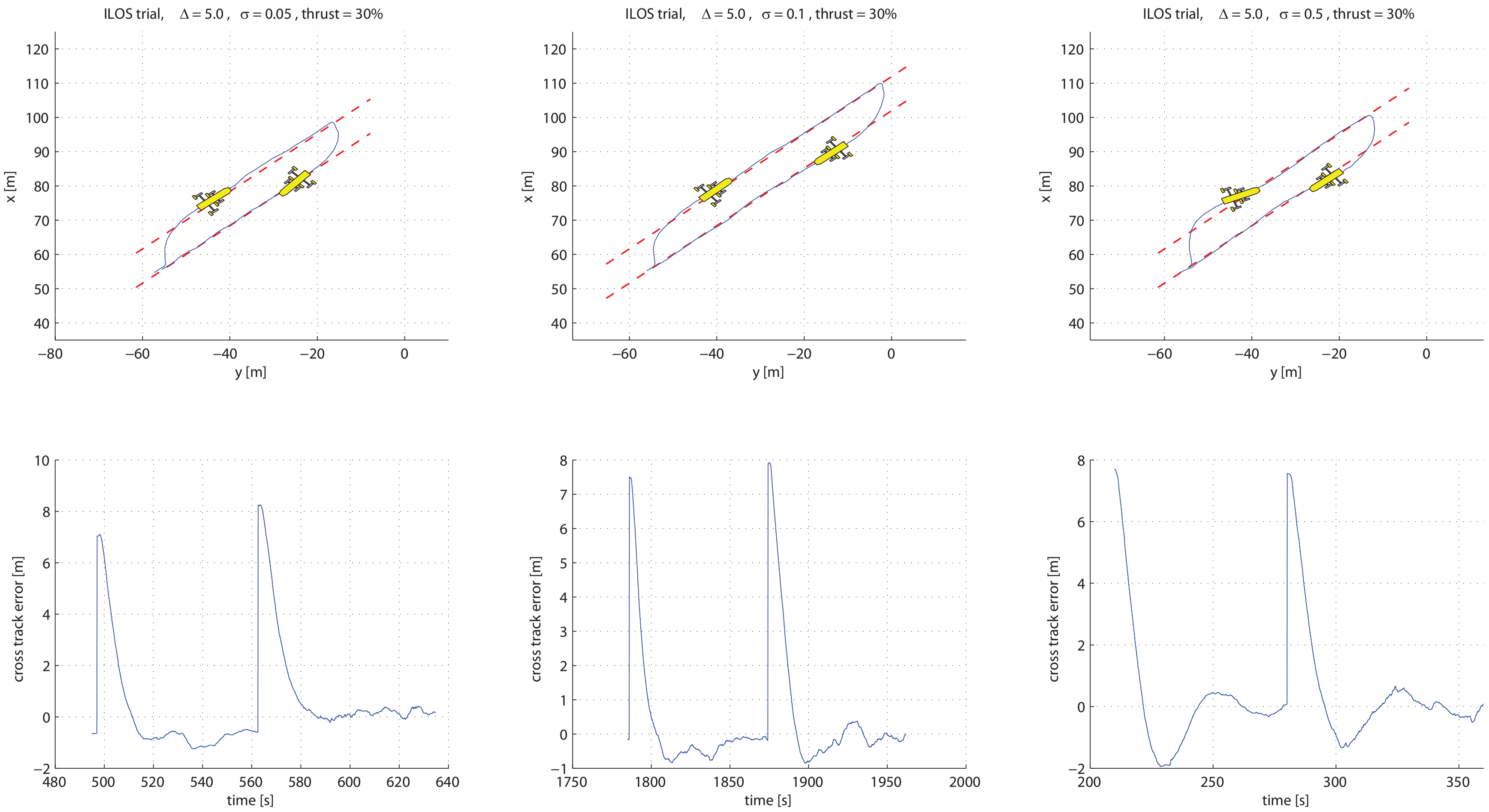

Figure 6.7.: Sensitivity of the ILOS guidance with respect to the integral gain σ - the upper plots show the motion of the vehicle (blue) along the reference lines (red); the lower plots show the cross track error variation in time.

6.A. Appendix: Functional Expressions

$$F_u(v_r, r) \triangleq \frac{1}{m_{11}}(m_{22}v_r + m_{23}r)r, \tag{6.31}$$

$$X(u_r) \triangleq \frac{m_{23}^2 - m_{11}m_{33}}{m_{22}m_{33} - m_{23}^2}u_r + \frac{d_{33}m_{23} - d_{23}m_{33}}{m_{22}m_{33} - m_{23}^2}, \tag{6.32}$$

$$Y(u_r) \triangleq \frac{(m_{22} - m_{11})m_{23}}{m_{22}m_{33} - m_{23}^2}u_r - \frac{d_{22}m_{33} - d_{32}m_{23}}{m_{22}m_{33} - m_{23}^2}, \tag{6.33}$$

$$\begin{aligned} F_r(u_r, v_r, r) &\triangleq \frac{m_{23}d_{22} - m_{22}(d_{32} + (m_{22} - m_{11})u_r)}{m_{22}m_{33} - m_{23}^2}v_r \\ &+ \frac{m_{23}(d_{23} + m_{11}u_r) - m_{22}(d_{33} + m_{23}u_r)}{m_{22}m_{33} - m_{23}^2}r. \end{aligned} \tag{6.34}$$

The functions $\boldsymbol{h}_y \triangleq [h_{y1}, h_{y2}, h_{y3}]^T$ and $\boldsymbol{h}_{v_r} \triangleq [h_{v_r1}, h_{v_r2}, h_{v_r3}]^T$ are:

$$\begin{aligned} h_{y3} = 0, \quad h_{y2} &= U_{rd}\left[\frac{\sin(\tilde{\psi})}{\tilde{\psi}}\cos(\psi_d) + \frac{\cos(\tilde{\psi}) - 1}{\tilde{\psi}}\sin(\psi_d)\right] + \\ &+ v_r\left[\frac{\cos(\tilde{\psi}) - 1}{\tilde{\psi}}\cos(\psi_d) - \frac{\sin(\tilde{\psi})}{\tilde{\psi}}\sin(\psi_d)\right], \quad h_{y1} = \sin(\tilde{\psi} + \psi_d), \end{aligned} \tag{6.35}$$

$$\begin{aligned} h_{v_r1} &= \frac{X(\tilde{u}_r + U_{rd}) - X^{U_{rd}}}{\tilde{u}_r}\gamma(y_{\text{int}}, y, v_r) + \\ &+ v_r\frac{Y(\tilde{u}_r + U_{rd}) - Y^{U_{rd}}}{\tilde{u}_r}, \quad h_{v_r2} = 0, \quad h_{v_r3} = X(\tilde{u}_r + U_{rd}), \end{aligned} \tag{6.36}$$

where the limits of h_{y2} for $\tilde{\psi} \to 0$ and h_{v_r1} for $\tilde{u}_r \to 0$ exist and are finite. The expression $\gamma(y_{\text{int}}, y, v_r)$ is defined as:

$$\begin{aligned} \gamma(y_{\text{int}}, y, v_r) &\triangleq \frac{\Delta U_{rd}(y + \sigma y_{\text{int}})}{((y + \sigma y_{\text{int}})^2 + \Delta^2)^{3/2}} - \frac{\Delta^2}{((y + \sigma y_{\text{int}})^2 + \Delta^2)^{3/2}}v_r \\ &- \frac{\sigma\Delta^2}{((y + \sigma y_{\text{int}})^2 + \Delta^2)^2}y - \frac{\Delta V_y}{(y + \sigma y_{\text{int}})^2 + \Delta^2}. \end{aligned} \tag{6.37}$$

$$\boldsymbol{A}(e_2) \triangleq \begin{bmatrix} -\frac{\sigma\Delta}{(e_2+\sigma y_{\text{int}}^{\text{eq}})^2+\Delta^2} & \frac{\Delta}{(e_2+\sigma y_{\text{int}}^{\text{eq}})^2+\Delta^2} & 0 \\ -\frac{\sigma^2\Delta}{(e_2+\sigma y_{\text{int}}^{\text{eq}})^2+\Delta^2} & -\frac{U_{rd}}{\sqrt{(e_2+\sigma y_{\text{int}}^{\text{eq}})^2+\Delta^2}} + \frac{\sigma\Delta}{(e_2+\sigma y_{\text{int}}^{\text{eq}})^2+\Delta^2} & \frac{\Delta}{\sqrt{(e_2+\sigma y_{\text{int}}^{\text{eq}})^2+\Delta^2}} \\ \frac{\sigma^2\Delta^2 X^{U_{rd}}}{((e_2+\sigma y_{\text{int}}^{\text{eq}})^2+\Delta^2)^2} & \frac{U_{rd}\Delta X^{U_{rd}}}{((e_2+\sigma y_{\text{int}}^{\text{eq}})^2+\Delta^2)^{3/2}} - \frac{\sigma\Delta^2 X^{U_{rd}}}{((e_2+\sigma y_{\text{int}}^{\text{eq}})^2+\Delta^2)^2} & Y^{U_{rd}} - \frac{\Delta^2 X^{U_{rd}}}{((e_2+\sigma y_{\text{int}}^{\text{eq}})^2+\Delta^2)^{3/2}} \end{bmatrix} \tag{6.38}$$

6.B. Appendix: Proof of Lemma 6.1

The system (6.26) is written again:

$$\begin{bmatrix} \dot{e}_1 \\ \dot{e}_2 \\ \dot{v}_r \end{bmatrix} = \boldsymbol{A}(e_2) \begin{bmatrix} e_1 \\ e_2 \\ v_r \end{bmatrix} + \boldsymbol{B}(e_2). \tag{6.39}$$

The nominal system (6.26) is equivalent to the system (5.28) analyzed in Chapter 5, with $g(e_2) = 0$, $\kappa_v(\gamma_e) = 0$ and $e_3 = v_r$. Hence, the proof follows along the lines of the proof of Lemma 5.2 given in Appendix 5.B of Chapter 5. Consider the quadratic Lyapunov function candidate (LFC):

$$V \triangleq \frac{1}{2}\sigma^2 e_1^2 + \frac{1}{2}e_2^2 + \frac{1}{2}\mu v_r^2, \quad \mu > 0. \tag{6.40}$$

Assumptions 6.5-6.7, inequality (6.25) and the notation $\bar{e}_1 \triangleq e_1/\sqrt{(e_2 + \sigma y_{\text{int}}^{\text{eq}})^2 + \Delta^2}$ and $\bar{e}_2 \triangleq e_2/\sqrt{(e_2 + \sigma y_{\text{int}}^{\text{eq}})^2 + \Delta^2}$ yield the following bound for the time derivative $\dot{V}$:

$$\dot{V} \leq -W_1(|\bar{e}_1|, |v_r|) - W_2(|\bar{e}_2|, |v_r|). \tag{6.41}$$

The quadratic functions $W_1(|\bar{e}_1|, |v_r|)$ and $W_2(|\bar{e}_2|, |v_r|)$ are defined as:

$$W_1 \triangleq \sigma^3\Delta|\bar{e}_1|^2 - \mu\frac{\sigma^2|X^{U_{rd}}|}{\Delta}|\bar{e}_1||v_r| + \mu\eta\left(|Y^{U_{rd}}| - \frac{|X^{U_{rd}}|}{\Delta}\right)|v_r|^2, \tag{6.42}$$

and:

$$W_2 \triangleq \Delta \begin{bmatrix} |\bar{e}_2| & |v_r| \end{bmatrix} \begin{bmatrix} \beta & -\alpha \\ -\alpha & \frac{\alpha(2\alpha-1)}{\beta} \end{bmatrix} \begin{bmatrix} |\bar{e}_2| \\ |v_r| \end{bmatrix}, \tag{6.43}$$

where $0 < \eta < 1$, $\beta \triangleq U_{rd} - V_{\max} - \sigma$ and α is given by:

$$\alpha \triangleq (1-\eta)\frac{(U_{rd} - V_{\max} - \sigma)(\Delta|Y^{U_{rd}}| - |X^{U_{rd}}|)}{|X^{U_{rd}}|\,(U_{rd} + V_{\max} + \sigma)}. \tag{6.44}$$

The parameter μ is chosen as:

$$\mu \triangleq \frac{\Delta^2(2\alpha - 1)}{|X^{U_{rd}}|(U_{rd} + V_{\max} + \sigma)}. \tag{6.45}$$

If both W_1 and W_2 are definite positive then $\dot{V}$ is negative definite. Positive definiteness of W_1 is ensured if (6.46) and (6.47) are satisfied:

$$\Delta > \frac{|X^{U_{rd}}|}{|Y^{U_{rd}}|}, \qquad (6.46) \qquad\qquad \mu < \frac{4\eta\Delta^2\left[\Delta|Y^{U_{rd}}| - |X^{U_{rd}}|\right]}{\sigma|X^{U_{rd}}|^2}. \qquad (6.47)$$

Notice that condition (6.46) is met as long as (6.13) holds. It is straightforward to show that $\eta \geq 1/5$ is a sufficient condition for μ, defined in (6.45), to satisfy (6.47). Therefore, without any loss of generality, η is set to $1/5$. Both β and α must fulfill $\beta > 0$ and $\alpha > 1$ to guarantee positive definiteness of W_2. Assumption 6.7 and (6.14) make sure that $\beta > 0$ while it is easy to check that conditions (6.13) and (6.14) imply $\alpha > 1$. Furthermore, $\alpha > 1$ guarantees $\mu > 0$ and ensures positive definiteness of V. Therefore under the conditions stated in Theorem 6.1, V, W_1 and W_2 are positive definite and hence, following standard Lyapunov arguments, the system (6.39) is UGAS. Furthermore, the inequality $W \triangleq W_1 + W_2 \geq \bar{\lambda}_1|\bar{e}_1|^2 + \bar{\lambda}_2|\bar{e}_2|^2 + \lambda_3|v_r|^2$ holds in a neighbourhood of the origin for some constants $\bar{\lambda}_1, \bar{\lambda}_2, \lambda_3 > 0$ and thus in any ball $\mathcal{B}_r \triangleq \{|e_2| \leq r\}, r > 0$ the function W can be estimated as $W \geq \lambda_1|e_1|^2 + \lambda_2|e_2|^2 + \lambda_3|v_r|^2$ where $\lambda_i = \bar{\lambda}_i/((r + \sigma y_{\text{int}}^{\text{eq}})^2 + \Delta^2)$, $i = 1, 2$. This, together with the fact that V is a quadratic function of e_1, e_2 and v_r, concludes that (6.39) is also uniformly locally exponentially stable, ULES [82].

Chapter 7.

Path Following Control of Underactuated Surface Vessels with Saturated Transverse Actuators

"The wonderful things in life are the things you do, not the things you have."

— Reinhold Messner, Alpinist

The marine vehicles considered in Chapters 3, 5 and 6 are assumed underactuated since most of marine surface vessels are equipped with fixed stern propellers and steering rudders. However, modern ships are often equipped with several actuators. Devices providing thrust in the transverse direction such as tunnel thrusters or azimuth thrusters are installed in addition to the main propellers and the aft rudders to increase maneuverability and implement dynamic positioning (DP) capabilities. These vessels can be considered fully actuated in 3 degrees of freedom (DOF) when performing low speed maneuvering or station keeping. Nevertheless, the transverse thrusters are in general smaller propulsive devices compared to the main propellers. This is justified by the fact that ships and marine vehicles are usually built for transit operations to minimize water resistance in the forward direction of motion. Therefore, the transverse actuators are more susceptible to saturation phenomena and thus their effectiveness to guarantee path following in presence of heavy disturbances such as strong sea currents is questionable.

This chapter investigates the possibility of extending the Integral Line-of-Sight (ILOS) guidance law proposed for underactuated surface marine vehicles in Chapter 6 to fully actuated marine vehicles with saturated transverse actuators. Low-speed path following of straight lines is considered and the proposed control system is designed to compensate for constant and irrotational ocean currents acting in any direction of the inertial frame. The proposed solution is inspired by practical issues faced when operating remotely operated vehicles (ROVs) at sea. Field experience of ROV pilots suggests that a combined control strategy involving both sway thursters and side-slipping may successfully guarantee path following of a straight line. Intuitively one can think of saturating the sway thruster first, and then, if this is not sufficient to counteract the disturbances, making the ship side-slip thus exploiting the stronger main propellers to compensate for the current and follow the desired direction. As a result, a solution combining the ILOS guidance law with a nonlinear bounded sway feedback controller is designed. A fully actuated surface vessel described by a 3-DOFs maneuvering model is considered and the guidance law is derived from the underactuated case described in Chapter 6. Compared to Chapter 6, it is shown that the additional use of the transverse actuators for disturbance compensation reduces the side-slip angle the vessel has to hold. This increases mission flexibility when trade-offs between path following speed, power usage and energy consumption become critical. Furthermore, there is no need to change guidance law when shifting operation mode between fully-actuated and underactuated. The problem addressed in this paper is partially a bounded control problem since saturation is considered for the transverse actuators while the surge and yaw control inputs are considered unconstrained. The proposed bounded sway controller is derived from elements of underactuated control design for marine vehicles and relies on the Lyapunov-based design developed in Chapters 5 and 6. The proposed control system is based on relative velocities with direct control over the vehicle relative speed as done in Chapter 6. Uniform global asymptotic stability (UGAS) and uniform local exponential stability (ULES) of the closed loop system are proved. Both the kinematic and dynamic levels of the problem are addressed and explicit bounds on the guidance law parameters are given to guarantee stability. Results from simulations are presented to verify and illustrate the theoretical results.

The chapter is organized as follows: Section 7.1 presents the control plant model of the vessel, Section 7.2 identifies the control objective and Section 7.3 presents the strategy that solves the path following task. The stability conditions are given in Section 7.4 and proven in Section 7.5. Simulation results and conclusions are given in Section 7.6 and Section 7.7 respectively. The results presented in this chapter a based on [31].

7.1. The Control Plant Model of the Vessel

The control plant model is a simplified mathematical description of the vessel. It contains the physical properties that are significant for control design purposes [130].

7.1.1. Model Assumptions

Assumption 7.1. The motion of the ship is described in 3 degrees of freedom (DOF), that is surge, sway and yaw.

Assumption 7.2. The ship is port-starboard symmetric.

Assumption 7.3. The body-fixed coordinate frame b is considered located in a point $(x_g^*, 0)$ from the vehicle's center of gravity (CG) along the center-line of the ship, where x_g^* is to be defined later.

Assumption 7.4. Damping is considered linear.

Remark 7.1. Nonlinear damping is not considered in order to reduce the complexity of the controllers. However, the passive nature of the non-linear hydrodynamic damping forces should enhance the directional stability of the ship [36].

Assumption 7.5. The ocean current is defined in the inertial frame i and is assumed constant, unknown, irrotational and bounded. Hence, $\boldsymbol{V}_c \triangleq [V_x, V_y, 0]^T$ and there exists a constant $V_{\max} > 0$ such that $V_{\max} \geq \sqrt{V_x^2 + V_y^2}$.

7.1.2. The Vessel Model

The state of the surface vessel is given by the vector $[\boldsymbol{p}^T, \boldsymbol{\nu}^T]^T$ where $\boldsymbol{p} \triangleq [x, y, \psi]^T$ describes the position and the orientation of the vehicle with respect to the inertial frame i. The vector $\boldsymbol{\nu} \triangleq [u, v, r]^T$ contains the linear and angular velocities of the ship defined in the body-fixed frame b, where u is the surge velocity, v is the sway velocity and r is the yaw rate. The ocean current velocity in the body frame b, $\boldsymbol{\nu}_c \triangleq [u_c, v_c, 0]^T$, is obtained from $\boldsymbol{\nu}_c = \boldsymbol{R}^T(\psi)\boldsymbol{V}_c$ where $\boldsymbol{R}(\psi)$ is the rotation matrix from b to i.

The ocean current is constant and irrotational in i, i.e. $\dot{\boldsymbol{V}}_c = \boldsymbol{0}$ and therefore $\dot{\boldsymbol{\nu}}_c = [rv_c, -ru_c, 0]^T$. In navigation problems involving ocean currents it is useful to introduce the relative velocity: $\boldsymbol{\nu}_r \triangleq \boldsymbol{\nu} - \boldsymbol{\nu}_c = [u_r, v_r, r]^T$. The vector $\boldsymbol{\nu}_r$ is defined in b, where u_r is the relative surge velocity and v_r is the relative sway velocity. The surface vessels described by the following 3-DOF manoeuvring model are considered [52]:

$$\dot{\boldsymbol{p}} = \boldsymbol{R}(\psi)\boldsymbol{\nu}_r + \boldsymbol{V}_c, \tag{7.1}$$

$$\boldsymbol{M}\dot{\boldsymbol{\nu}}_r + \boldsymbol{C}(\boldsymbol{\nu}_r)\boldsymbol{\nu}_r + \boldsymbol{D}\boldsymbol{\nu}_r = \boldsymbol{B}\boldsymbol{f}. \tag{7.2}$$

The vector $\boldsymbol{f} \triangleq [T_u, T_v, T_r]^T$ is the control input vector, containing the surge thrust T_u, the sway thrust T_v and the rudder angle T_r. The matrix $\boldsymbol{M} = \boldsymbol{M}^T > 0$ is the mass and inertia matrix, and includes hydrodynamic added mass. The matrix $\boldsymbol{C}$ is the Coriolis and centripetal matrix, $\boldsymbol{D} > 0$ is the hydrodynamic damping matrix and $\boldsymbol{B} \in \mathbb{R}^{3\times 3}$ is the actuator configuration matrix. For manoeuvring control purposes, the matrices $R(\psi)$, $\boldsymbol{M}$, $\boldsymbol{D}$ and $\boldsymbol{B}$ can be considered as having the following structure:

$$\boldsymbol{R}(\psi) \triangleq \begin{bmatrix} \cos(\psi) & -\sin(\psi) & 0 \\ \sin(\psi) & \cos(\psi) & 0 \\ 0 & 0 & 1 \end{bmatrix}, \quad \boldsymbol{M} \triangleq \begin{bmatrix} m_{11} & 0 & 0 \\ 0 & m_{22} & m_{23} \\ 0 & m_{23} & m_{33} \end{bmatrix}, \tag{7.3}$$

$$\boldsymbol{D} \triangleq \begin{bmatrix} d_{11} & 0 & 0 \\ 0 & d_{22} & d_{23} \\ 0 & d_{32} & d_{33} \end{bmatrix}, \quad \boldsymbol{B} \triangleq \begin{bmatrix} b_{11} & 0 & 0 \\ 0 & b_{22} & b_{23} \\ 0 & b_{32} & b_{33} \end{bmatrix}. \tag{7.4}$$

The actuator configuration matrix $\boldsymbol{B}$ is invertible and maps the control inputs T_u, T_v and T_r into forces and moments acting on the vessel. The Coriolis and centripetal matrix $\boldsymbol{C}$ is obtained from $\boldsymbol{M}$ as [52]:

$$\boldsymbol{C}(\boldsymbol{\nu}_r) \triangleq \begin{bmatrix} 0 & 0 & -m_{22}v_r - m_{23}r \\ 0 & 0 & m_{11}u_r \\ m_{22}v_r + m_{23}r & -m_{11}u_r & 0 \end{bmatrix}. \tag{7.5}$$

The body-fixed coordinate frame b is considered located in a point $(x_g^*, 0)$ from the vehicle center of gravity (CG) along the center-line of the ship, where x_g^* is chosen so that $\boldsymbol{M}^{-1}\boldsymbol{B}\boldsymbol{f} = [\tau_u, \tau_v, \delta\tau_v + \tau_r]^T$. The point $(x_g^*, 0)$ exists for all port-starboard symmetric ships [33, 28].

Remark 7.2. The point $(x_g^*, 0)$ should not be confused with the pivotal point of the vessel [52]. The two points are not necessarily coincident.

Notice that moving the origin of the frame b to the point $(x_g^*, 0)$ along the center line of ship removes the direct effect of the rudder on the sway dynamics. This, however, does not remove the effect of the sway thruster on the yaw dynamics and therefore the following assumption is introduced:

Assumption 7.6. The configuration of the transverse actuators is such that their combined thrust does not produce any yaw momentum, i.e. $\delta = 0$.

Remark 7.3. Most of the modern ships and vehicles are equipped with several advanced transverse thrusters. This overactuation allows the control allocation system to satisfy different constraints [78]. Therefore, the sway actuators can be configured not to give any yaw momentum.

To solve nonlinear control design problems it is convenient to expand (7.1-7.2) into:

$$\dot{y} = u_r \sin(\psi) + v_r \cos(\psi) + V_y, \tag{7.6a}$$

$$\dot{\psi} = r, \tag{7.6b}$$

$$\dot{u}_r = F_u(v_r, r) - \frac{d_{11}}{m_{11}} u_r + \tau_u, \tag{7.6c}$$

$$\dot{v}_r = X(u_r) r + Y(u_r) v_r + \tau_v, \tag{7.6d}$$

$$\dot{r} = F_r(u_r, v_r, r) + \tau_r. \tag{7.6e}$$

The expressions for $F_u(v_r, r)$, $X(u_r)$, $Y(u_r)$ and $F_r(u_r, v_r, r)$ are given in Appendix 7.A. Notice that the functions $X(u_r)$ and $Y(u_r)$ are bounded for bounded arguments. The path following task addressed in this chapter is a cross-track error problem where y represents the error (see Section 7.2). Hence, the x dynamics are not included in (7.6). Finally, the following assumptions are introduced:

Assumption 7.7. The function $Y(u_r)$ satisfies:

$$Y(u_r) \leq -Y^{\min} < 0, \quad \forall u_r \in [-V_{max}, U_{rd}].$$

Remark 7.4. Assumption 7.7 is justified by a contradiction: $Y(u_r) \geq 0$ would imply a nominally unstable ship in sway which is not the case for commercial ships by design. Furthermore, notice that no bounds are implied on u_r. The constant design parameter $U_{rd} > 0$ is defined in Section 7.2.

Assumption 7.8. The sway actuators are saturated:

$$|\tau_v| \leq K_{\text{sat}}, \quad K_{\text{sat}} > 0.$$

Remark 7.5. Following Assumption 7.8, a bounded control solution for the sway control input τ_v has to be designed if the option of using thrusters for disturbance compensation is considered.

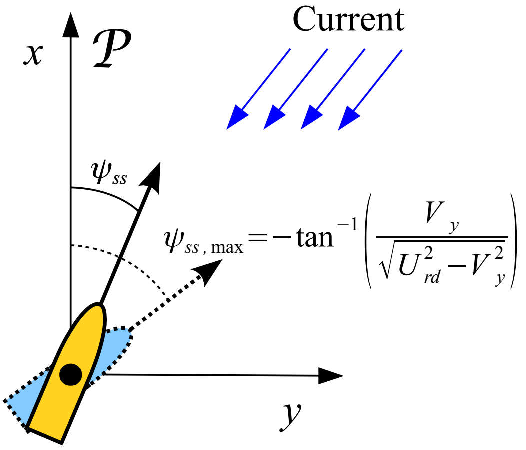

Figure 7.1.: At steady state the vessel combines side-slipping with the transverse actuators to compensate for the drift and reduce the ψ_{ss} angle. The largest side-slip angle $\psi_{ss,\max}$ is achieved in the underactuated case.

7.2. The Control Objective

This section formalizes the control problem solved in this chapter: the control system should make the vessel follow a given straight line $\mathcal{P}$ and maintain a desired constant surge relative velocity $U_{rd} > 0$ in the presence of unknown, constant and irrotational ocean currents. To simplify the control problem without any loss of generality, the inertial reference frame i is placed such that its x-axis is aligned with the desired path, giving $\mathcal{P} \triangleq \{(x, y) \in \mathbb{R}^2 : y = 0\}$ as shown in Figure 7.1. The y-coordinate of the vessel then corresponds to the cross-track error and the objectives the control system should pursue can be formalized as follows:

$$\lim_{t\to\infty} y(t) = 0, \tag{7.7}$$

$$\lim_{t\to\infty} \psi(t) = \psi_{ss}, \quad \psi_{ss} \in \left(-\frac{\pi}{2}, \frac{\pi}{2}\right), \tag{7.8}$$

$$\lim_{t\to\infty} u_r(t) = U_{rd}, \tag{7.9}$$

where ψ_{ss} is constant. The yaw angle $\psi(t)$ is not required to converge to zero but rather to a steady-state constant value, allowing the vehicle to hold a non-zero yaw angle at equilibrium and help the sway actuators to compensate for the drift (see Figure 7.1).

7.3. The Control system

The proposed control systems is based on two feedback linearizing controllers, a nonlinear bounded Proportional-Integral (PI) controller and the ILOS guidance law in a cascaded configuration.

7.3.1. The Integral LOS Guidance

The surface vessel has to converge and follow the x-axis, therefore according to the ILOS guidance method presented in Chapters 3, 5 and 6 the desired heading angle is:

$$\psi_{ILOS} \triangleq -\tan^{-1}\left(\frac{y+\sigma y_{\text{int}}}{\Delta}\right), \quad \Delta, \sigma > 0, \tag{7.10a}$$

$$\dot{y}_{\text{int}} = \frac{\Delta y}{(y+\sigma y_{\text{int}})^2 + \Delta^2}, \tag{7.10b}$$

where Δ is the look-ahead distance and σ is the integral gain. Both are constant design parameters.

7.3.2. The Surge and Yaw Controllers

According to (7.9), $u_r(t)$ should follow the desired value $u_{rd}(t) \triangleq U_{rd} > 0$. Therefore, to track $u_{rd}(t)$ the following controller is used:

$$\tau_u = -F_{u_r}(v_r, r) + \frac{d_{11}}{m_{11}} u_{rd} + \dot{u}_{rd} - k_{u_r}(u_r - u_{rd}). \tag{7.11}$$

The gain $k_{u_r} > 0$ is constant. The controller (7.11) is a feedback linearizing P-controller and guarantees exponential tracking of $u_{rd}(t)$. The following controller can be used to track the desired yaw angle $\psi_d \triangleq \psi_{ILOS}$:

$$\tau_r = -F_r(u_r, v_r, r) + \ddot{\psi}_d - k_\psi(\psi - \psi_d) - k_r(\dot{\psi} - \dot{\psi}_d), \tag{7.12}$$

where $k_\psi, k_r > 0$ are constant gains. The controller (7.12) is a feedback linearizing PD controller and makes sure that ψ and r exponentially track ψ_d and $\dot{\psi}_d$ respectively.

7.3.3. The Bounded Sway Controller

The following non linear PI controller is proposed to combine side-slipping with the sway thrusters and successfully compensate for the ocean current disturbance:

$$\tau_v = -k_{\text{sat}} \frac{k_p(y + \sigma y_{\text{int}})}{\sqrt{k_p^2(y + \sigma y_{\text{int}})^2 + \Delta^2}}, \quad k_{\text{sat}} \geq 0,\ k_p > 0. \tag{7.13}$$

Notice that the control input (7.13) is bounded: $|\tau_v| \leq k_{\text{sat}}$, $\forall\ (y + \sigma y_{\text{int}})$. The gain $k_{\text{sat}} \geq 0$ is constant and is chosen so that $k_{\text{sat}} \leq K_{\text{sat}}$, where K_{sat} is the maximum thrust available in sway. Hence, the controller (7.13) does not require higher control efforts than the sway thruster can provide. Notice that the controller (7.13) does not cancel any terms from the sway dynamics (7.6d). Furthermore, setting $k_{\text{sat}} = 0$ turns off the sway actuators and makes the vehicle underactuated. In this case the drift is compensated with side-slipping only. Finally, setting $k_{\text{sat}} = K_{\text{sat}}$ allows to exploit the sway thrusters to the limit and reduce the necessary side-slip angle. In addition to k_{sat}, the constant k_p is introduced to set the first derivative of the function (7.13) in the origin $y + \sigma y_{\text{int}} = 0$. The gain k_p is chosen according to the following assumption:

Assumption 7.9. The constant k_p has to satisfy $k_p \geq 1$.

Remark 7.6. In this chapter the vessel is required to hold a constant surge relative velocity U_{rd} as done in [28] and [34]. This simplifies the control problem and strengthens the stability properties of the closed loop system compared to [26] and [33] where the marine vehicle is required to follow $\mathcal{P}$ with a constant speed $U_d > 0$. Furthermore, controlling the relative velocity of the ship gives direct control over energy consumption since hydrodynamic damping depends on $\boldsymbol{\nu}_r$, but does not represent the ideal solution for speed profile planning/tracking scenarios. This chapter investigates the possibility of exploiting saturated sway actuators to increase flexibility of the relative velocity approach with respect to speed profile planning/tracking requirements. It is shown how the proposed bounded controller (7.13) shrinks the side-slip angle and therefore increases the path following speed compared to [28] if the same U_{rd} is used, at the expense of a higher power consumption. This represents an advantage when precise timing is critical. Moreover, the possibility of changing the side-slip angle is important in some operations such as installation of submarine pipelines and cables.

7.3.4. Constraints on U_{rd}

The following assumption allows the vessel to achieve path following for sea currents acting in any directions of the plane:

Assumption 7.10. The desired constant relative velocity U_{rd} satisfies the following condition:

$$U_{rd} > V_{\max} + \frac{5}{2}\left|\frac{k_p K_{\text{sat}}}{Y(U_{rd})}\right|.$$

Remark 7.7. It is always possible to find values of U_{rd} satisfying Assumption 7.10 since $|Y(u_r)|$ is strictly increasing for $u_r > 0$.

7.4. Stability Conditions

This section presents the stability conditions under which the proposed control law achieves (7.7-7.9). The notation $X^{U_{rd}} \triangleq X(U_{rd})$ and $Y^{U_{rd}} \triangleq Y(U_{rd})$ is used.

Theorem 7.1. *Given a fully actuated surface vessel described by the dynamical system (7.6). If Assumptions 7.7-7.10 hold and if the look-ahead distance* Δ *and the integral gain* σ *satisfy the conditions*

$$\Delta > \frac{|X^{U_{rd}}|}{|Y^{U_{rd}}|}\Omega(\sigma)\left[\frac{5}{4}\frac{U_{rd} + V_{\max} + \sigma}{U_{rd} - V_{\max} - \sigma} + 1\right], \tag{7.14}$$

$$0 < \sigma < U_{rd} - V_{\max} - \frac{5}{2}\left|\frac{k_p K_{\text{sat}}}{Y^{U_{rd}}}\right|, \tag{7.15}$$

where $\Omega(\sigma)$ *is defined as*

$$\Omega(\sigma) \triangleq \frac{U_{rd} - V_{\max} - \sigma}{U_{rd} - V_{\max} - \sigma - \frac{5}{2}\left|\frac{k_p K_{\text{sat}}}{Y^{U_{rd}}}\right|}, \tag{7.16}$$

then the controllers (7.11), (7.12) *and* (7.13) *where* ψ_d *is given by* (7.10) *and* $u_{rd} \triangleq U_{rd}$*, guarantee achievement of the control objectives (7.7-7.9). The control objective* (7.8) *is fulfilled with* $0 < |\psi_{ss}| \leq \left|\tan^{-1}\left(V_y/\sqrt{U_{rd}^2 - V_y^2}\right)\right|$.

Remark 7.8. it is shown in Chapter 5 that the ILOS guidance can effectively compensate for disturbances in sway and this property is here exploited to combine the ILOS with a bounded sway controller.

7.5. Proof of Theorem 7.1

In this section the proof of Theorem 7.1 is given. Focus is put on the determination of the equilibrium point of the system to show how the controllers and the guidance law exploit the integral action (7.10b) and use both side-slipping and the sway actuators to compensate for the current.

The actuated dynamics (7.6c) and (7.6e) of the ship in closed loop configuration with the controllers (7.11) and (7.12) are considered first. Given the vector $\boldsymbol{\zeta} \triangleq [\tilde{u}_r, \tilde{\psi}, \dot{\tilde{\psi}}]^T$ where $\tilde{u}_r \triangleq u_r - U_{rd}$, $\tilde{\psi} \triangleq \psi - \psi_d$ and $\dot{\tilde{\psi}} \triangleq \dot{\psi} - \dot{\psi}_d$, the dynamics of $\boldsymbol{\zeta}$ are obtained by combining the system equations (7.6b), (7.6c) and (7.6e) with the control laws (7.11) and (7.12):

$$\dot{\boldsymbol{\zeta}} = \begin{bmatrix} -k_{u_r} - \frac{d_{11}}{m_{11}} & 0 & 0 \\ 0 & 0 & 1 \\ 0 & -k_\psi & -k_r \end{bmatrix} \boldsymbol{\zeta} \triangleq \boldsymbol{\Sigma}\boldsymbol{\zeta}. \tag{7.17}$$

The system (7.17) is linear and time-invariant. Furthermore, since the gains k_{u_r}, k_ψ, k_r and the term d_{11}/m_{11} are all strictly positive, the system matrix $\boldsymbol{\Sigma}$ is Hurwitz and the origin $\boldsymbol{\zeta} = \mathbf{0}$ of (7.17) is UGES. Therefore the control goal (7.9) is achieved with exponential converging properties in any ball of initial conditions.

The dynamics of the cross track error y and the relative sway velocity v_r are analyzed next. The $y - v_r$ subsystem is obtained by combining (7.6a), (7.6d) and (7.10b):

$$\dot{y}_{\text{int}} = \frac{\Delta y}{(y + \sigma y_{\text{int}})^2 + \Delta^2}, \tag{7.18}$$

$$\dot{y} = (\tilde{u}_r + U_{rd}) \sin(\tilde{\psi} + \psi_d) + v_r \cos(\tilde{\psi} + \psi_d) + V_y, \tag{7.19}$$

$$\dot{v}_r = X(\tilde{u}_r + U_{rd})(\dot{\tilde{\psi}} + \dot{\psi}_d) + Y(\tilde{u}_r + U_{rd})v_r - k_{\text{sat}} \frac{k_p(y + \sigma y_{\text{int}})}{\sqrt{k_p^2 (y + \sigma y_{\text{int}})^2 + \Delta^2}}. \tag{7.20}$$

The calculation of the equilibrium point of the system (7.18-7.20) on the manifold $\boldsymbol{\zeta} = \mathbf{0}$ yields the following equation:

$$\rho \frac{k_p s}{\sqrt{k_p^2 s^2 + 1}} = V_y \sqrt{s^2 + 1} - U_{rd} s, \tag{7.21}$$

where $s \triangleq \sigma y_{\text{int}}^{\text{eq}} / \Delta$ and $y_{\text{int}}^{\text{eq}}$ is the value of y_{int} at equilibrium. The constant ρ is defined as $\rho \triangleq -k_{\text{sat}} / Y^{U_{rd}}$ and $\rho \geq 0$ since $k_{\text{sat}} \geq 0$ and $Y(U_{rd}) < 0$ from Assumption 7.7. The parameter s represents the only solution of (7.21). The Equation (7.21) has a unique

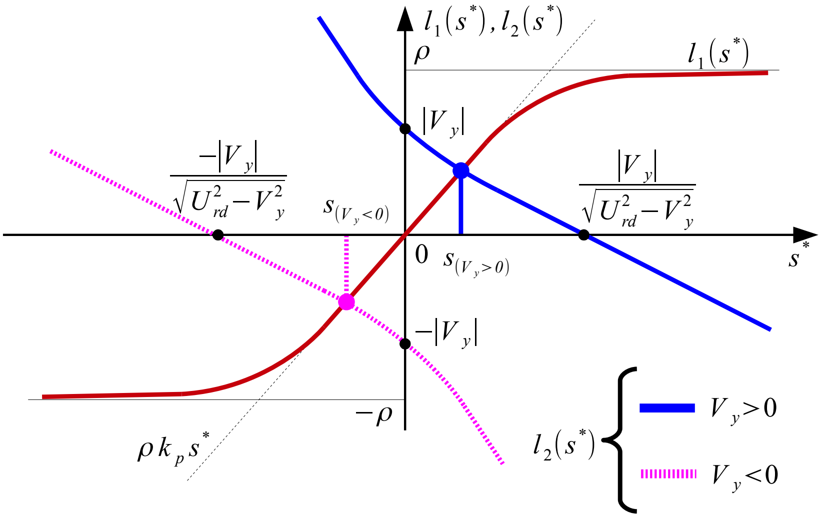

Figure 7.2.: Graphical solution of (7.21). Both cases $V_y > 0$ and $V_y < 0$ for $l_2(s)$ are considered since the sign of the constant V_y is unknown.

solution as long as Assumption 7.10 is satisfied since it guarantees $U_{rd} > V_{\max}$. This is shown in Figure 7.2 where the intersections between the curves defined by the two sides of Equation (7.21) are considered:

$$l_1(s^*) \triangleq \rho \frac{k_p s^*}{\sqrt{k_p^2 s^{*2} + 1}}, \quad l_2(s^*) \triangleq V_y \sqrt{s^{*2} + 1} - U_{rd} s^*. \tag{7.22}$$

The condition $U_{rd} > V_{\max}$ makes $l_2(s^*)$ strictly decreasing while $l_1(s^*)$ is strictly increasing. Therefore, there exists only one intersection point as long as Assumption 7.10 is satisfied. Furthermore, it is possible to conclude the following property:

$$|s| \leq |V_y| / \sqrt{U_{rd}^2 - V_y^2}. \tag{7.23}$$

Remark 7.9. The equality $|s| = |V_y| / \sqrt{U_{rd}^2 - V_y^2}$ holds when the sway thrusters are turned off ($k_{\text{sat}} = 0$) and the ship is underactuated. Figure 7.2 shows that as the sway thrusters are turned on and k_{sat} is gradually increased, s shrinks and the sideslip angle the ship has to hold at equilibrium to compensate for the current, becomes smaller. Notice that no matter which value is chosen for k_{sat}, the control system (7.10-7.13) will always set a non-zero side-slip angle as long as there is current acting in the sway direction of the ship, i.e. $V_y \neq 0$. Moreover, since Assumption 7.8 states that $k_{\text{sat}} \leq K_{\text{sat}}$, choosing $k_{\text{sat}} = K_{\text{sat}}$ allows the controller (7.13) to fully exploit the available sway thrust.

Remark 7.10. The gain $k_p \geq 1$ can be increased to further reduce the side-slip angle. This, however, tightens the stability margins (7.14-7.15) and forces the selection of a higher U_{rd}. The stricter margins are justified by the fact that a conservative classical Lyapunov approach is used to determine (7.14-7.15).

Remark 7.11. It is clear from Figure 7.2 that the control system (7.10-7.12) is not meant to perform current compensation with sway actuators only, unless a very large k_p is used. Nevertheless, this can be done by simply disconnecting the integrator y_{int} from the ILOS reference generator (7.10a). However, the saturated sway actuators alone might prove ineffective against stronger currents, while the proposed combined control solution achieves path following anyway.

The equilibrium point of the system (7.18-7.20) is $(y_{\text{int}}^{\text{eq}}, y^{\text{eq}}, v_r^{\text{eq}})$ where $y_{\text{int}}^{\text{eq}}$ is the only possible solution of (7.21), $y^{\text{eq}} = 0$ and v_r^{eq} is obtained from:

$$v_r^{\text{eq}} = U_{rd} \frac{\sigma y_{\text{int}}^{\text{eq}}}{\Delta} - \sqrt{\left(\frac{\sigma y_{\text{int}}^{\text{eq}}}{\Delta} \right)^2 + 1}. \tag{7.24}$$

Furthermore, the following relation follows from (7.21):

$$\frac{k_{\text{sat}}}{Y^{U_{rd}}} \frac{k_p \sigma y_{\text{int}}^{\text{eq}}}{\sqrt{(k_p \sigma y_{\text{int}}^{\text{eq}})^2 + \Delta^2}} = U_{rd} \frac{\sigma y_{\text{int}}^{\text{eq}}}{\Delta} - V_y \frac{\sqrt{(\sigma y_{\text{int}}^{\text{eq}})^2 + \Delta^2}}{\Delta} \tag{7.25}$$

A new set of variables is introduced to move the equilibrium point to the origin:

$$e_1 \triangleq y_{\text{int}} - y_{\text{int}}^{\text{eq}}, \quad e_2 \triangleq y + \sigma e_1, \quad e_3 \triangleq v_r - v_r^{\text{eq}}. \tag{7.26}$$

Substituting (7.10a) for ψ_d, factorizing the result with respect to $\boldsymbol{\zeta}$ and applying (7.24-7.26) leads to the following transformed interconnected dynamics:

$$\begin{bmatrix} \dot{e}_1 \\ \dot{e}_2 \\ \dot{e}_3 \end{bmatrix} = \boldsymbol{A}(e_2) \begin{bmatrix} e_1 \\ e_2 \\ e_3 \end{bmatrix} + \boldsymbol{B}(e_2) + \boldsymbol{H}(y, y_{\text{int}}, \psi_d, v_r, \boldsymbol{\zeta})\boldsymbol{\zeta}, \tag{7.27a}$$

$$\dot{\boldsymbol{\zeta}} = \boldsymbol{\Sigma}\boldsymbol{\zeta}. \tag{7.27b}$$

The matrix $\boldsymbol{H}(y, y_{\text{int}}, \psi_d, v_r, \boldsymbol{\zeta})$ contains all the terms vanishing at $\boldsymbol{\zeta} = \boldsymbol{0}$. $\boldsymbol{A}(e_2)$ is given in (7.43) of Appendix 7.A while $\boldsymbol{B}(e_2)$ and $\boldsymbol{H}(y, y_{\text{int}}, \psi_d, v_r, \boldsymbol{\zeta})$ are:

$$\boldsymbol{B}(e_2) \triangleq \begin{bmatrix} 0 \\ V_y f(e_2) \\ \frac{k_{\text{sat}} k_p \sigma y_{\text{int}}^{\text{eq}}}{\sqrt{(k_p \sigma y_{\text{int}}^{\text{eq}})^2 + \Delta^2}} g(e_2) - \frac{\Delta X^{U_{rd}} V_y}{(e_2 + \sigma y_{\text{int}}^{\text{eq}})^2 + \Delta^2} f(e_2) \end{bmatrix}, \tag{7.28}$$

$$\boldsymbol{H}(y, y_{\text{int}}, \psi_d, v_r, \boldsymbol{\zeta}) \triangleq \begin{bmatrix} 0 & 0 \\ 1 & 0 \\ \frac{-\Delta X(\tilde{u}_r + U_{rd})}{(e_2 + \sigma y_{\text{int}}^{\text{eq}})^2 + \Delta^2} & 1 \end{bmatrix} \begin{bmatrix} \boldsymbol{h}_y^T \\ \boldsymbol{h}_{v_r}^T \end{bmatrix}, \tag{7.29}$$

where:

$$f(e_2) = 1 - \frac{\sqrt{(\sigma y_{\text{int}}^{\text{eq}})^2 + \Delta^2}}{\sqrt{(e_2 + \sigma y_{\text{int}}^{\text{eq}})^2 + \Delta^2}}, \tag{7.30}$$

$$g(e_2) = 1 - \frac{\sqrt{(k_p \sigma y_{\text{int}}^{\text{eq}})^2 + \Delta^2}}{\sqrt{k_p^2 (e_2 + \sigma y_{\text{int}}^{\text{eq}})^2 + \Delta^2}}. \tag{7.31}$$

The vectors $\boldsymbol{h}_y(\psi_d, v_r, \boldsymbol{\zeta})$ and $\boldsymbol{h}_{y_r}(y, y_{\text{int}}, \psi_d, v_r, \boldsymbol{\zeta})$ are given in Appendix 7.A and the following bounds hold:

$$|f(e_2)| \leq \frac{|e_2|}{\sqrt{(e_2 + \sigma y_{\text{int}}^{\text{eq}})^2 + \Delta^2}}, \tag{7.32}$$

$$|g(e_2)| \leq \frac{k_p |e_2|}{\sqrt{k_p^2 (e_2 + \sigma y_{\text{int}}^{\text{eq}})^2 + \Delta^2}}, \tag{7.33}$$

$$\frac{k_p |e_2|}{\sqrt{k_p^2 (e_2 + \sigma y_{\text{int}}^{\text{eq}})^2 + \Delta^2}} \leq \frac{k_p |e_2|}{\sqrt{(e_2 + \sigma y_{\text{int}}^{\text{eq}})^2 + \Delta^2}}, \tag{7.34}$$

as long as $k_p \geq 1$. The system (7.27) is a cascaded system, where the linear UGES system (7.27b) perturbs the dynamics (7.27a) through the interconnection matrix $\boldsymbol{H}(y, y_{\text{int}}, \psi_d, v_r, \boldsymbol{\zeta})$. To analyze the stability properties of the cascade (7.27) consider the following nominal system defined on the manifold $\boldsymbol{\zeta} = \boldsymbol{0}$:

$$\begin{bmatrix} \dot{e}_1 \\ \dot{e}_2 \\ \dot{e}_2 \end{bmatrix} = \boldsymbol{A}(e_2) \begin{bmatrix} e_1 \\ e_2 \\ e_3 \end{bmatrix} + \boldsymbol{B}(e_2). \tag{7.35}$$

The following Lemma states the stability properties of the nominal system (7.35):

Lemma 7.1. *Under the conditions of Theorem 6.1, the system* (7.35) *is UGAS and ULES.*

Proof. The proof of Lemma 7.1 is given in Appendix 7.B. □

Next, the stability of the cascade (7.27) is analyzed. In particular, since the perturbing system (7.27b) is UGES and the interconnection matrix $\boldsymbol{H}(y, y_{\text{int}}, \psi_d, v_r, \boldsymbol{\zeta})$ can be shown to satisfy $\| \boldsymbol{H} \| \leq \theta_1(\| \boldsymbol{\zeta} \|)(|y| + |y_{\text{int}}| + |v_r|) + \theta_2(\| \boldsymbol{\zeta} \|)$, where $\theta_1(\cdot)$ and $\theta_2(\cdot)$ are some continuous non-negative functions, applying Theorem A.2 and Lemma A.2 shows UGAS and ULES for the cascaded system (7.27). To conclude, under the conditions of Theorem

7.1, the origin $(e_1, e_2, e_3, \boldsymbol{\zeta}) = (0, 0, 0, \mathbf{0})$ of the system (7.27) is UGAS and ULES. Hence, the control objectives (7.7) and (7.8) are achieved with exponential converging properties in and ball of initial conditions.

7.6. Simulations

Results from numerical simulations are presented in this section. The proposed control system (7.10-7.13) is applied to the scaled vessel model Cybership II. The Cybership II is a $1:70$ model of a supply vessel. It is fully actuated since it is equipped with stern rudders, aft propellers and sway thrusters. The model of the ship is given in Section B.2 of Appendix B and the objective is to make the vessel follow the path $\mathcal{P}$ with a desired surge relative velocity $U_{rd} = 0.6$ [m/s]. The intensity of the current is $|\boldsymbol{V}_c| = 0.15$ [m/s] and its direction is randomly generated. In this case its components are $V_x = -0.05$ [m/s] and $V_y = -0.14$ [m/s]. Thus, Assumption 7.5 is fulfilled with $V_{\max} = 0.15$ [m/s] and it can be verified that Assumption 7.7 is satisfied with $Y\min = 0.04$ [s^{-1}] and $Y(U_{rd}) = -0.80$ [m/s]. The Cybership is assumed to have 2 [N] and 1 [N] of maximum available thrust in surge and sway, respectively, while the maximum available yaw moment is 1.5 [Nm]. Therefore, expanding (7.1-7.2) into (7.6) gives $|\tau_u| \leq 0.078$ [m/s^2] and $|\tau_v| \leq K_{\text{sat}} = 0.030$ [m/s^2]. This difference suggests that the sway actuators are more susceptible to saturation phenomena than the surge ones. A $k_{\text{sat}} = K_{\text{sat}}$ is chosen, allowing the control system to fully exploit the sway thrusters. The gain k_p is set to $k_p = 2$ and hence Assumptions 7.9 and 7.10 are satisfied. The chosen values for the guidance law integral gain and look-ahead distance are $\sigma = 0.15$ [m/s] and $\Delta = 4$ [m], and satisfy (7.14-7.15). The internal controllers (7.11-7.12) are implemented with the following gains: $k_{u_r} = 1$, $k_\psi = 1$ and $k_r = 2.5$. Hence, the $\tilde{u}_r$ first order closed loop system has a time constant of 0.93 [s] while the $\tilde{\psi}$ second order closed loop system is slightly overdamped with $\omega_0 = 1$ [rad/s]. The ship is given an initial cross track error of 50 meters and initially holds zero relative velocity. Its surge axis is parallel to the desired path $\mathcal{P}$. Figures 7.3a and 7.3c show how path following is successfully achieved with a constant side-slip angle $\psi_{ss} \approx 11.8$ [deg]. This is smaller than the steady state side-slip angle in the underactuated case $\psi_{ss,\max} \approx 13.2$ [deg]. The performance of the speed controller (6.11) is shown in Figure 7.3d. The yaw moment is given in Figure 7.3c where the offset in steady state is due to $v_r^{eq} \neq 0$. This gives a nonzero $F_r(u_r, v_r, r)$ in the yaw controller (7.12) at equilibrium.

Holding $k_{\text{sat}} = K_{\text{sat}}$, the parameter k_p can be increased to further exploit the sway thrusters and reduce the side-slip angle at steady state (see Remark 7.10). This is shown in Figure 7.3e where $U_{rd} = 0.6$ [m/s], $\Delta = 4$ [m] and $\sigma = 0.15$ [m/s] are kept constant while k_p is gradually increased. The system is then eventually forced to operate out of the stability criteria (7.14-7.15). Nevertheless, convergence is achieved. This should not come as a surprise, since the Lyapunov approach yielding (7.14-7.15) is very conservative. Furthermore, Figure 7.3e shows that the side-slip angle at steady state cannot be reduced to less then 9.6 [deg]. At that point the sway thrusters are exploited to the limit, suggesting that a compensation solution based on transverse actuators only would not succeed to compensate for the current considered in this example. This confirms the importance of side-slipping solutions for path following applications in the presence of environmental disturbances. Finally, notice that the nonlinear bounded sway controller does not push the thrusters deep into saturation and at the same time uses the maximum available transverse thrust to converge to the path $\mathcal{P}$ (Figure 7.3e). The thrust then decreases unless a very high k_p is used. This reduces the wear and tear of the actuators.

7.7. Conclusions

In this chapter a combined control strategy for path following of fully actuated surface marine vehicles in presence of constant irrotational ocean currents has been developed. Saturation of the sway actuators is analytically taken into account yielding a partially bounded control problem. The guidance system is based on the ILOS guidance law developed in Chapter 6 and a sway nonlinear bounded PI controller. In particular, it is shown in Chapter 5 that the ILOS guidance can effectively compensate for disturbances in sway and this property is here exploited to combine the ILOS with a bounded sway controller. The control system compensates for the current and guarantees path following even when the sway thrusters are saturated, by making the ship side-slip. The analysis of the closed loop system through Lyapunov techniques and nonlinear cascaded systems theory gives explicit conditions to guarantee exponential stability. Numerical simulations support the theoretical results.

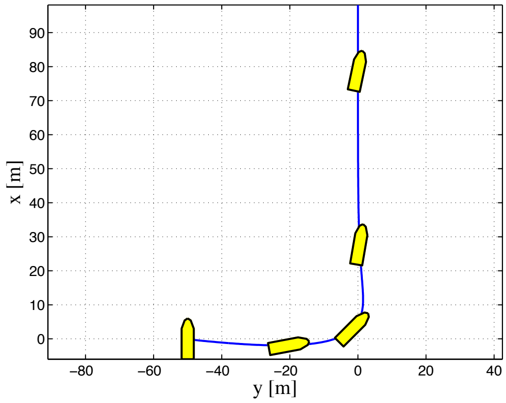

(a) Simulation of convergence and path following of Cybership II. The vessel combines side-slipping and the sway thrust to compensate for the drift. In this case $k_p = 2$, $k_{\text{sat}} = K_{\text{sat}} = 0.030$ [m/s^2], $\Delta = 4$ [m], $\sigma = 0.15$ [m/s]. in presence of currents.

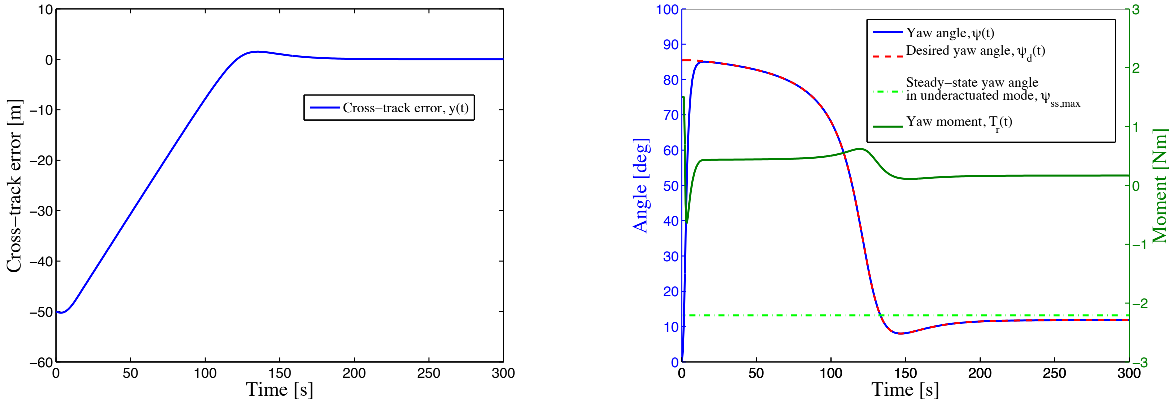

(b) Cross track error $y(t)$ of the vessel.

(c) Heading angle $\psi(t)$ of the Cybership II.

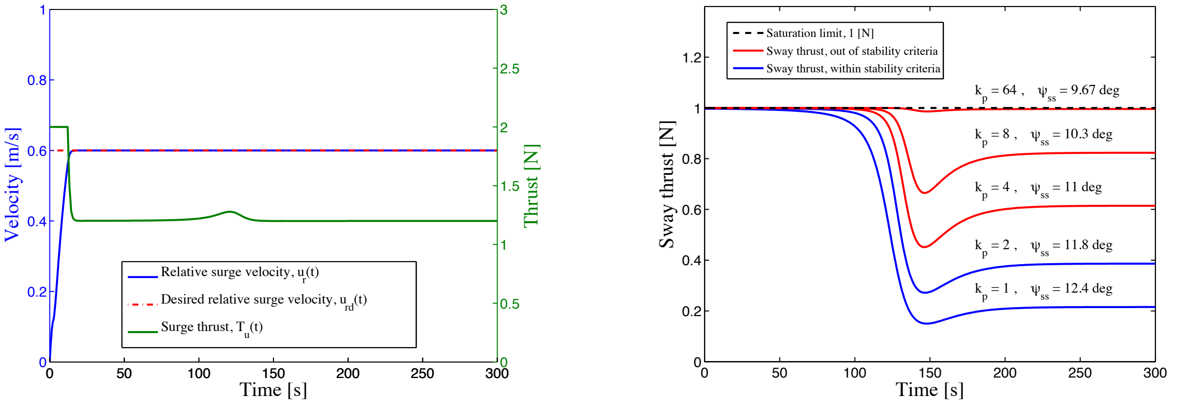

(d) Relative surge velocity $u_r(t)$ and surge thrust $T_u(t)$.

(e) Sway thrust over time for different k_p gains when $k_{\text{sat}} = K_{\text{sat}} = 0.030$ [m/s^2].

Figure 7.3.: Simulation results for $\Delta = 4$ [m] and $\sigma = 0.15$ [m/s].

7.A. Appendix: Functional Expressions

$$F_u(v_r, r) \triangleq \frac{1}{m_{11}}(m_{22}v_r + m_{23}r)r, \tag{7.36}$$

$$X(u_r) \triangleq \frac{m_{23}^2 - m_{11}m_{33}}{m_{22}m_{33} - m_{23}^2}u_r + \frac{d_{33}m_{23} - d_{23}m_{33}}{m_{22}m_{33} - m_{23}^2}, \tag{7.37}$$

$$Y(u_r) \triangleq \frac{(m_{22} - m_{11})m_{23}}{m_{22}m_{33} - m_{23}^2}u_r - \frac{d_{22}m_{33} - d_{32}m_{23}}{m_{22}m_{33} - m_{23}^2}, \tag{7.38}$$

$$\begin{aligned} F_r(u_r, v_r, r) \triangleq{} & \frac{m_{23}d_{22} - m_{22}(d_{32} + (m_{22} - m_{11})u_r)}{m_{22}m_{33} - m_{23}^2}v_r \\ & + \frac{m_{23}(d_{23} + m_{11}u_r) - m_{22}(d_{33} + m_{23}u_r)}{m_{22}m_{33} - m_{23}^2}r. \end{aligned} \tag{7.39}$$

The functions $\boldsymbol{h}_y \triangleq [h_{y1}, h_{y2}, h_{y3}]^T$ and $\boldsymbol{h}_{v_r} \triangleq [h_{v_r1}, h_{v_r2}, h_{v_r3}]^T$ are:

$$\begin{aligned} h_{y3} = 0, \quad h_{y2} = U_{rd} & \left[\frac{\sin(\tilde{\psi})}{\tilde{\psi}}\cos(\psi_d) + \frac{\cos(\tilde{\psi}) - 1}{\tilde{\psi}}\sin(\psi_d)\right] + \\ + v_r & \left[\frac{\cos(\tilde{\psi}) - 1}{\tilde{\psi}}\cos(\psi_d) - \frac{\sin(\tilde{\psi})}{\tilde{\psi}}\sin(\psi_d)\right], \quad h_{y1} = \sin(\tilde{\psi} + \psi_d), \end{aligned} \tag{7.40}$$

$$\begin{aligned} h_{v_r1} = {} & \frac{X(\tilde{u}_r + U_{rd}) - X^{U_{rd}}}{\tilde{u}_r}\gamma(y_{\text{int}}, y, v_r) + \\ & + v_r\frac{Y(\tilde{u}_r + U_{rd}) - Y^{U_{rd}}}{\tilde{u}_r}, \quad h_{v_r2} = 0, \quad h_{v_r3} = X(\tilde{u}_r + U_{rd}), \end{aligned} \tag{7.41}$$

where the limits of h_{y2} for $\tilde{\psi} \to 0$ and h_{v_r1} for $\tilde{u}_r \to 0$ exist and are finite. The expression $\gamma(y_{\text{int}}, y, v_r)$ is defined as:

$$\begin{aligned} \gamma(y_{\text{int}}, y, v_r) \triangleq{} & \frac{\Delta U_{rd}(y + \sigma y_{\text{int}})}{((y + \sigma y_{\text{int}})^2 + \Delta^2)^{3/2}} - \frac{\Delta^2}{((y + \sigma y_{\text{int}})^2 + \Delta^2)^{3/2}}v_r \\ & - \frac{\sigma\Delta^2}{((y + \sigma y_{\text{int}})^2 + \Delta^2)^2}y - \frac{\Delta V_y}{(y + \sigma y_{\text{int}})^2 + \Delta^2}. \end{aligned} \tag{7.42}$$

$$\boldsymbol{A}(e_2) \triangleq \begin{bmatrix} -\frac{\sigma\Delta}{(e_2+\sigma y_{\mathrm{int}}^{\mathrm{eq}})^2+\Delta^2} & \frac{\Delta}{(e_2+\sigma y_{\mathrm{int}}^{\mathrm{eq}})^2+\Delta^2} & 0 \\ -\frac{\sigma^2\Delta}{(e_2+\sigma y_{\mathrm{int}}^{\mathrm{eq}})^2+\Delta^2} & -\frac{U_{rd}}{\sqrt{(e_2+\sigma y_{\mathrm{int}}^{\mathrm{eq}})^2+\Delta^2}} + \frac{\sigma\Delta}{(e_2+\sigma y_{\mathrm{int}}^{\mathrm{eq}})^2+\Delta^2} & \frac{\Delta}{\sqrt{(e_2+\sigma y_{\mathrm{int}}^{\mathrm{eq}})^2+\Delta^2}} \\ \frac{\sigma^2\Delta^2 X^{U_{rd}}}{((e_2+\sigma y_{\mathrm{int}}^{\mathrm{eq}})^2+\Delta^2)^2} & \frac{U_{rd}\Delta X^{U_{rd}}}{((e_2+\sigma y_{\mathrm{int}}^{\mathrm{eq}})^2+\Delta^2)^{3/2}} - \frac{\sigma\Delta^2 X^{U_{rd}}}{((e_2+\sigma y_{\mathrm{int}}^{\mathrm{eq}})^2+\Delta^2)^2} - \frac{k_{\mathrm{sat}}k_p}{\sqrt{k_p^2(e_2+\sigma y_{\mathrm{int}}^{\mathrm{eq}})^2+\Delta^2}} & Y^{U_{rd}} - \frac{\Delta^2 X^{U_{rd}}}{((e_2+\sigma y_{\mathrm{int}}^{\mathrm{eq}})^2+\Delta^2)^{3/2}} \end{bmatrix} \tag{7.43}$$

7.B. Appendix: Proof of Lemma 7.1

The system (7.35) is written again:

$$\begin{bmatrix} \dot{e}_1 \\ \dot{e}_2 \\ \dot{e}_3 \end{bmatrix} = \boldsymbol{A}(e_2) \begin{bmatrix} e_1 \\ e_2 \\ e_3 \end{bmatrix} + \boldsymbol{B}(e_2). \tag{7.44}$$

The nominal system (7.35) is equivalent to the system (5.28) analyzed in Chapter 5, with:

$$\boldsymbol{B}(e_2)_{\{31\}} = \frac{k_{\text{sat}} k_p \sigma y_{\text{int}}^{\text{eq}}}{\sqrt{(k_p \sigma y_{\text{int}}^{\text{eq}})^2 + \Delta^2}} g(e_2) - \frac{\Delta X^{U_{rd}} V_y}{(e_2 + \sigma y_{\text{int}}^{\text{eq}})^2 + \Delta^2} f(e_2), \tag{7.45}$$

$$\begin{aligned} \boldsymbol{A}(e_2)_{\{32\}} = {} & \frac{U_{rd} \Delta X^{U_{rd}}}{((e_2 + \sigma y_{\text{int}}^{\text{eq}})^2 + \Delta^2)^{3/2}} - \frac{\sigma \Delta^2 X^{U_{rd}}}{((e_2 + \sigma y_{\text{int}}^{\text{eq}})^2 + \Delta^2)^2} \\ & - \frac{k_{\text{sat}} k_p}{\sqrt{k_p^2 (e_2 + \sigma y_{\text{int}}^{\text{eq}})^2 + \Delta^2}}, \end{aligned} \tag{7.46}$$

where:

$$f(e_2) = 1 - \frac{\sqrt{(\sigma y_{\text{int}}^{\text{eq}})^2 + \Delta^2}}{\sqrt{(e_2 + \sigma y_{\text{int}}^{\text{eq}})^2 + \Delta^2}}, \qquad g(e_2) = 1 - \frac{\sqrt{(k_p \sigma y_{\text{int}}^{\text{eq}})^2 + \Delta^2}}{\sqrt{k_p^2 (e_2 + \sigma y_{\text{int}}^{\text{eq}})^2 + \Delta^2}}. \tag{7.47}$$

Hence, the proof follows along the lines of the proof of Lemma 5.2 given in Appendix 5.B of Chapter 5. Consider the quadratic Lyapunov function candidate:

$$V \triangleq \frac{1}{2} \sigma^2 e_1^2 + \frac{1}{2} e_2^2 + \frac{1}{2} \mu e_3^2, \quad \mu > 0. \tag{7.48}$$

The notation $\bar{e}_1 \triangleq e_1 / \sqrt{(e_2 + \sigma y_{\text{int}}^{\text{eq}})^2 + \Delta^2}$, $\bar{e}_2 \triangleq e_2 / \sqrt{(e_2 + \sigma y_{\text{int}}^{\text{eq}})^2 + \Delta^2}$, Assumptions 7.5-7.10, and inequalities (7.32-7.34) yield the following bound for the time derivative $\dot{V}$:

$$\dot{V} \leq -W_1(|\bar{e}_1|, |e_3|) - W_2(|\bar{e}_2|, |e_3|). \tag{7.49}$$

The quadratic functions $W_1(|\bar{e}_1|, |e_3|)$ and $W_2(|\bar{e}_2|, |e_3|)$ are defined as:

$$W_1 \triangleq \sigma^3 \Delta |\bar{e}_1|^2 - \mu \frac{\sigma^2 |X^{U_{rd}}|}{\Delta} |\bar{e}_1||e_3| + \mu \eta \left(|Y^{U_{rd}}| - \frac{|X^{U_{rd}}|}{\Delta} \right) |e_3|^2, \tag{7.50}$$

$$W_2 \triangleq \Delta \begin{bmatrix} |\bar{e}_2| & |e_3| \end{bmatrix} \begin{bmatrix} \beta & -\alpha \\ -\alpha & \frac{\alpha(2\alpha - 1)}{\beta} \end{bmatrix} \begin{bmatrix} |\bar{e}_2| \\ |e_3| \end{bmatrix}, \tag{7.51}$$

where $0 < \eta < 1$, $\beta \triangleq U_{rd} - V_{\max} - \sigma$ and α is given by:

$$\alpha \triangleq (1-\eta)\frac{(U_{rd} - V_{\max} - \sigma)(\Delta|Y^{U_{rd}}| - |X^{U_{rd}}|)}{|X^{U_{rd}}|\left(U_{rd} + V_{\max} + \sigma + 2\Delta\frac{k_p K_{\text{sat}}}{|X^{U_{rd}}|}\right)}. \tag{7.52}$$

The parameter μ is chosen as:

$$\mu \triangleq \frac{2\alpha - 1}{\frac{|X^{U_{rd}}|}{\Delta^2}(U_{rd} + V_{\max} + \sigma) + 2\frac{k_p K_{\text{sat}}}{\Delta}}. \tag{7.53}$$

If both W_1 and W_2 are definite positive then $\dot{V}$ is negative definite. Positive definiteness of W_1 is ensured if (7.54) and (7.55) are satisfied:

$$\Delta > \frac{|X^{U_{rd}}|}{|Y^{U_{rd}}|}, \tag{7.54}$$

$$\mu < \frac{4\eta\Delta^2\left[\Delta|Y^{U_{rd}}| - |X^{U_{rd}}|\right]}{\sigma|X^{U_{rd}}|^2}. \tag{7.55}$$

Notice that condition (7.54) is met as long as (7.14) holds. It is straightforward to show that $\eta \geq 1/5$ is a sufficient condition for μ, defined in (7.53), to satisfy (7.55). Therefore, without any loss of generality, η is set to $1/5$. To guarantee positive definiteness of W_2, β and α must fulfill the inequalities $\beta > 0$ and $\alpha > 1$. Assumption 7.10 and (7.15) make sure that $\beta > 0$ while through some simple manipulation it is easy to check that conditions (7.14) and (7.15) imply $\alpha > 1$. Furthermore, $\alpha > 1$ guarantees $\mu > 0$ as required for V to be positive definite. Therefore, under the conditions stated in Theorem 7.1, V, W_1 and W_2 are positive definite and hence, according to standard Lyapunov arguments, the nominal system (7.44) is UGAS. Moreover, the inequality $W \triangleq W_1 + W_2 \geq \bar{\lambda}_1|\bar{e}_1|^2 + \bar{\lambda}_2|\bar{e}_2|^2 + \lambda_3|e_3|^2$ holds in a neighbourhood of the origin for some constants $\bar{\lambda}_1, \bar{\lambda}_2, \lambda_3 > 0$ and thus in any ball $\mathcal{B}_r \triangleq \{|e_2| \leq r\}, r > 0$ the function W can be bounded from below by $W \geq \lambda_1|e_1|^2 + \lambda_2|e_2|^2 + \lambda_3|e_3|^2$ where $\lambda_i = \bar{\lambda}_i/((r + \sigma y_{\text{int}}^{\text{eq}})^2 + \Delta^2)$, $i = 1, 2$. This, together with the fact that V is a quadratic function of e_1, e_2 and e_3, concludes that (7.44) is also uniformly exponentially stable, ULES [82].

Chapter 8.

Path Following Control of Underactuated Surface Vessels in the Presence of Multiple Disturbances

"If in normal conditions it is skill, which counts, in extreme situations,
it is the spirit, which saves."
— Walter Bonatti, Alpinist

An integral version of the Line-of-Sight (LOS) guidance for planar motion purposes in presence of ocean currents was applied to a simple kinematic model of surface vessels in Chapter 3. Explicit bounds for the choice of the integral gain of the guidance law were derived but the look-ahead distance of the integral LOS was left unconstrained. The underactuated sway dynamics were included into the Lyapunov analysis in Chapter 5 to calculate the mathematical conditions for the selection of the look-ahead distance in presence of disturbances. More precise bounds upon the integral gain were obtained as well. However the actuated surge and yaw dynamics were not considered under the assumption that there are closed loop controllers setting the speed and the heading of the vessel. This assumption was removed in Chapter 6 where the complete kinematic and dynamic closed loop system of the Integral Line-of-Sight (ILOS) guidance law for planar path following purposes was analyzed. However, in the case analyzed in Chapter 6, only disturbances in the form of constant irrotational ocean currents were taken into account, while dynamic heading dependent environmental disturbances were not taken into account.

In this chapter it is shown that the ILOS guidance law successfully compensates for combined kinematic and dynamic disturbances, thus further extending the results of Chapter 6. To this end and motivated by [52] and [15], the 3 Degrees-of-Freedom (DOFs) maneuvering model presented in Chapter 2 is used for control design. This includes both the kinematic and dynamic disturbance effects of currents, wind and waves. As discussed in Chapter 2 the model separates the disturbances into an unknown irrotational current (kinematic drift/bias) and an environmental load vector (dynamic bias). Such a distinction is proposed to capture the different effects of the otherwise combined disturbances [50]. The kinematic bias takes into account currents, tidal drifts, low frequency swells and second order wave-induced forces while the environmental load vector embodies the heading dependent dynamic effects of the disturbances. In this context wind forces are assumed to dominate in the load vector and are modeled as an unknown pressure acting in a certain direction. The two disturbances generally act in different directions and are assumed constant in this chapter. The first order wave-induced forces and the effects of wind gusts are neglected since they cause zero mean oscillatory motions that are usually removed through wave filtering.

The ILOS guidance method developed in Chapters 3, 5 and 6 is extended with adaptation and it is analytically shown that the resulting control scheme successfully compensates for both kinds of disturbances and hence guarantees path following of underactuated surface vessels in different sea conditions. Path following of straight lines is considered and the underactuated vessel is made to side-slip in order to compensate for the drift since no actuation is available in sway to counteract for the components of the disturbances acting in the transverse direction. The integral effect serves as a memory element that assesses the disturbing effects and sets the correct side-slip angle to follow the desired course. The integration law, first presented in [26], is chosen to reduce the risk of wind-up effects. The control approach in [26] includes both absolute and relative velocities, while here it is based on relative velocities only with direct control over the ship relative speed. It is hence not necessary to use adaptive techniques to estimate the unknown kinematic drift in the ship surge and yaw controllers, whereas adaptation is still required to estimate and compensate for the dynamic disturbances. The combined effect of kinematic and dynamic disturbances is analyzed assuming that the dynamic disturbance is known in direction but unknown in magnitude. It is shown that the ILOS guidance in a cascaded configuration with an adaptive speed-heading controller guarantees uniform global asymptotic stability (UGAS) and uniform local exponential stability (ULES) (alternatively, global κ-exponential stability) for the closed loop system. Notice that stability is here analyzed for the complete kinematic-dynamic closed loop system, including the underactuated sway dynamics. Finally, results from simulations are presented to verify and illustrate the theoretical results.

The chapter is organized as follows: Section 8.1 presents the vessel model for control design purposes that includes kinematic as well as dynamic disturbances. The control problem is defined in Section 8.2 while Section 8.3 presents the ILOS guidance. Section 8.4 presents the adaptive surge-yaw controller that solves the path following control problem in a cascaded configuration with the ILOS guidance. The stability properties of the closed loop system are given in Section 8.5 while the analysis is developed in Section 8.6. Simulation results are given in Section 8.7. Finally, conclusions are found in Section 8.8. The results presented in this chapter are based on the paper [29].

8.1. The Control Plant Model

The class of marine vehicles described by the 3-DOF maneuvering model presented in Section 2.3 of Chapter 2 are considered:

$$\dot{\boldsymbol{p}} = \boldsymbol{R}(\psi)\boldsymbol{\nu}_r + \boldsymbol{V}_c, \tag{8.1}$$

$$\boldsymbol{M}\dot{\boldsymbol{\nu}}_r + \boldsymbol{C}(\boldsymbol{\nu}_r)\boldsymbol{\nu}_r + \boldsymbol{D}\boldsymbol{\nu}_r = \boldsymbol{B}\boldsymbol{f} + \boldsymbol{w}. \tag{8.2}$$

The state of the surface vessel is given by the vector $[\boldsymbol{p}^T, \boldsymbol{\nu}_r^T]^T$ where $\boldsymbol{p} \triangleq [x, y, \psi]^T$ describes the position and the orientation of the vehicle with respect to the inertial frame i. As shown in Chapter 2, in navigation problems involving irrotational ocean currents it is useful to describe the state of the vessel with the relative velocity vector: $\boldsymbol{\nu}_r = [u_r, v_r, r]^T$. The vector $\boldsymbol{\nu}_r$ is defined in the body frame b, where u_r is the relative surge velocity, v_r is the relative sway velocity and r is the yaw rate. The model (8.1-8.2) describes the kinematics and dynamics of surface vessels as well as underwater vehicles moving in the horizontal plane.

Remark 8.1. Notice that the ocean current $\boldsymbol{V}_c$ does not depend on the heading of the vessel and represents a kinematic bias in (8.1). It defines in fact a constant and irrotational velocity drift and hence it does not capture the heading dependent disturbing effects of currents, wind and waves. In this chapter the vector $\boldsymbol{w}$ is used in (8.2) to take into account these disturbances as well. In particular, the significant effect of wind is analyzed in this context.

The vector $\boldsymbol{f} \triangleq [T_u, T_r]^T$ is the control input vector, containing the surge thrust T_u and the rudder angle T_r. Notice that the model (8.1-8.2) is underactuated in its configuration space since it has fewer control inputs than DOFs. The vector $\boldsymbol{w} \triangleq [w_u, w_v, w_r]^T$ is the body-fixed dynamic environmental load vector. The vector $\boldsymbol{w}$ is defined and discussed in details in Section 8.1.2. The matrix $\boldsymbol{M} = \boldsymbol{M}^T > 0$ is the mass and inertia matrix and includes hydrodynamic added mass. The matrix $\boldsymbol{C}(\boldsymbol{\nu}_r)$ is the Coriolis and centripetal matrix, $\boldsymbol{D} > 0$ is the hydrodynamic damping matrix and $\boldsymbol{B} \in \mathbb{R}^{3\times 2}$ is the actuator configuration matrix. The structure of the matrices $\boldsymbol{R}(\psi)$, $\boldsymbol{M}$, $\boldsymbol{C}(\boldsymbol{\nu}_r)$ and $\boldsymbol{B}$ is given in Chapter 2. The following assumption defines the properties of the damping matrix $\boldsymbol{D}$:

Assumption 8.1. The hydrodynamic damping is linear.

Remark 8.2. Nonlinear damping is not considered in order to reduce the complexity of the controllers. However, the passive nature of the non-linear hydrodynamic damping forces should enhance the directional stability of the vessel [36].

The hydrodynamic damping matrix $\boldsymbol{D}$ is therefore considered to have the following structure [52]:

$$\boldsymbol{D} \triangleq \begin{bmatrix} d_{11} & 0 & 0 \\ 0 & d_{22} & d_{23} \\ 0 & d_{32} & d_{33} \end{bmatrix}. \tag{8.3}$$

The particular structure of $\boldsymbol{D}$ is justified by symmetry arguments (see Section 2.3 of Chapter 2) and Assumption 8.1. Finally, the following assumption is introduced:

Assumption 8.2. The body-fixed coordinate frame b is located on the center-line of the vessel at a distance x_g^* from the center of gravity (CG), where x_g^* is chosen so that $\boldsymbol{M}^{-1}\boldsymbol{B}\boldsymbol{f} = [\tau_u, 0, \tau_r]^T$.

The point $(x_g^*, 0)$ exists for all port-starboard symmetric vehicles (see Section 2.3 of Chapter 2). Notice that in (8.1-8.2) there are two terms describing environmental disturbances: the current $\boldsymbol{V}_c$ in (8.1), representing a pure kinematic drift, and the vector $\boldsymbol{w}$ in (8.2), representing heading dependent disturbances that show up at the dynamic level. The vectors $\boldsymbol{V}_c$ and $\boldsymbol{w}$ are defined and discussed in the following sections.

8.1.1. The Ocean Current

The drifting effect of currents, tides, low frequency swells and second order wave-induced forces is embodied into the ocean current vector $\boldsymbol{V}_c$:

Assumption 8.3. The ocean current is defined in the inertial frame i and is assumed constant, unknown, irrotational and bounded. Hence, $\boldsymbol{V}_c \triangleq [V_x, V_y, 0]^T$ and there exists a constant $V_{\max} > 0$ such that $V_{\max} \geq \sqrt{V_x^2 + V_y^2}$.

Remark 8.3. The constant and irrotational ocean current model is widely accepted to describe slowly varying disturbances and it represents a good approximation when closed loop control is implemented on-board of marine vehicles [51].

Remark 8.4. The first order wave-induced forces are neglected in this context since they cause zero mean oscillatory motions that are usually removed through wave filtering [52].

8.1.2. The Environmental Load Vector $\boldsymbol{w}$

The vector $\boldsymbol{w}$ represents a bias term that embodies unmodeled dynamics and dynamic, heading dependent disturbances caused by currents, winds and waves. In this context, the significant effect of constant wind disturbances is assumed to dominate in $\boldsymbol{w}$. Inspired by [15] and [52], the overall effect of wind is modeled as a constant pressure P_e acting on the vessel in a constant direction β_e:

Assumption 8.4. The pressure $P_e > 0$ in considered constant, unknown, and acting in a constant and known direction β_e of the inertial frame. Therefore, there exists a constant $P_e^{\max} > 0$ such that $P_e^{\max} > P_e$.

Remark 8.5. The mean and slowly varying drifting effect caused by wind is considered, while highly oscillating zero mean effects due to wind gusts are not taken into account since they are often removed through wave filtering. Furthermore, the vessel inertia has low pass filtering effects as well. β_e is assumed known since the tools to measure and estimate the wind direction are often available [118, 52].

The forces and moments generated by the wind pressure P_e on the ship are proportional to the frontal and lateral projected areas above the waterline of the ship, and to some well defined load coefficients. The areas above the waterline are considered since the effect of wind is mostly limited to the surface and the very upper layers of the sea. The loading coefficients depend on the geometry of the ship hull and superstructure, and are functions of the disturbance angle of attack. They are usually obtained through interpolation of data from simulations and wind tunnel tests for different types of ships [76, 103, 15]. The environmental load vector $\boldsymbol{w}$ is then defined as:

$$\boldsymbol{w} \triangleq \begin{bmatrix} P_e A_{Fw} C_X(\gamma_e) \\ P_e A_{Lw} C_Y(\gamma_e) \\ P_e A_{Lw} L_{oa} C_N(\gamma_e) \end{bmatrix}, \tag{8.4}$$

where A_{Fw} is the frontal projected area above the waterline, A_{Lw} is the lateral projected area above the waterline and L_{oa} is the length overall of the vessel (maximum length of the vessel hull). The term $\gamma_e \triangleq \psi - \beta_e - \pi$ is the angle of attack of the wind. The terms $C_X(\gamma_e)$, $C_Y(\gamma_e)$ and $C_N(\gamma_e)$ are the load coefficients. The following assumption is introduced:

Assumption 8.5. There are no dynamic disturbances in sway and yaw in presence of head/following sea ($\gamma_e = k\pi$) and no dynamic disturbances in surge in presence of beam sea ($\gamma_e = \pi/2 \pm k\pi$).

The load coefficients can be then redefined as: $C_X(\gamma_e) \triangleq C_X^*(\gamma_e)\cos(\gamma_e)$, $C_Y(\gamma_e) \triangleq C_Y^*(\gamma_e)\sin(\gamma_e)$ and $C_N(\gamma_e) \triangleq C_N^*(\gamma_e)\sin(\gamma_e)$. The vector $\boldsymbol{w}$ is rewritten as:

$$\boldsymbol{w} = \begin{bmatrix} -P_e A_{Fw} C_X^*(\gamma_e)\cos(\beta_e - \psi) \\ P_e A_{Lw} C_Y^*(\gamma_e)\sin(\beta_e - \psi) \\ P_e A_{Lw} L_{oa} C_N^*(\gamma_e)\sin(\beta_e - \psi) \end{bmatrix}. \tag{8.5}$$

Furthermore, the functions $C_X^*(\gamma_e)$, $C_Y^*(\gamma_e)$ and $C_N^*(\gamma_e)$ are required to satisfy:

Assumption 8.6. $C_X^*(\gamma_e)$, $C_Y^*(\gamma_e)$, $C_N^*(\gamma_e)$ are bounded, periodic, class C^1 functions with bounded first derivatives and satisfy:

- $C_X^*(\gamma_e) < 0, \quad \forall\ \gamma_e,$
- $C_Y^*(\gamma_e) > 0, \quad \forall\ \gamma_e,$
- $-m_{23}C_Y^*(\gamma_e) + m_{22}L_{oa}C_N^*(\gamma_e) \neq 0$ for $\gamma_e = \pi/2 \pm k\pi$.

Finally, the following function is considered:

$$\kappa_v(\cdot) \triangleq \frac{P_e A_{Lw}}{m_{22}m_{33} - m_{23}^2}\left[m_{33}C_Y^*(\cdot) - m_{23}L_{oa}C_N^*(\cdot)\right]. \tag{8.6}$$

Since $C_Y^*(\cdot)$ and $C_N^*(\cdot)$ are bounded, have bounded first derivatives and P_e is bounded, then there exists $\kappa_v^{\max}$, $\kappa_v'^{\max}$ such that $\kappa_v(\cdot) < \kappa_v^{\max}$, $\frac{d\kappa_v(\cdot)}{d\cdot} < \kappa_v'^{\max}$.

Assumption 8.7. $C_Y^*(\cdot)$ and $C_N^*(\cdot)$ are such that, given any constants $k \in \mathbb{R}$ and $\beta_e \in [0, 2\pi]$, the following bound holds for all $s \in \mathbb{R}$:

$$\left|\kappa_v(\gamma_e^k) - \kappa_v(\gamma_e^{k+s})\frac{\sqrt{k^2+1}}{\sqrt{(s+k)^2+1}}\right| \leq \kappa_v^{\max}\frac{|s|}{\sqrt{(s+k)^2+1}}, \tag{8.7}$$

where $\gamma_e^k \triangleq -\tan^{-1}(k) - \beta_e - \pi$ and $\gamma_e^{k+s} \triangleq -\tan^{-1}(k+s) - \beta_e - \pi$.

Remark 8.6. Notice that the wind load coefficients given in [76, 103, 15, 52] trivially satisfy Assumptions 8.5-8.7, or can be easily approximated with functions satisfying Assumptions 8.5-8.7.

Remark 8.7. Given the model (8.1-8.2) one can choose to consider both the proposed disturbances, $[V_x, V_y, 0]^T$ and $\boldsymbol{w}$, or only one, depending on the application, type of vessel and the environmental conditions.

8.1.3. The Model in Component Form

To solve nonlinear underactuated control design problems it is useful to expand the model (8.1-8.2) into a component form:

$$\dot{x} = u_r \cos(\psi) - v_r \sin(\psi) + V_x, \tag{8.8a}$$

$$\dot{y} = u_r \sin(\psi) + v_r \cos(\psi) + V_y, \tag{8.8b}$$

$$\dot{\psi} = r, \tag{8.8c}$$

$$\dot{u}_r = F_u(u_r, v_r, r) + P_e \kappa_u^*(\gamma_e) \cos(\beta_e - \psi) + \tau_u, \tag{8.8d}$$

$$\dot{v}_r = X(u_r)r + Y(u_r)v_r + \kappa_v(\gamma_e) \sin(\beta_e - \psi), \tag{8.8e}$$

$$\dot{r} = F_r(u_r, v_r, r) + P_e \kappa_r^*(\gamma_e) \sin(\beta_e - \psi) + \tau_r. \tag{8.8f}$$

Notice the absence of any control inputs in sway (8.8e) to compensate for the environmental disturbances. The ship should therefore side-slip to counteract for currents, wind and waves. The expressions for $\kappa_u^*(\gamma_e)$, $\kappa_r^*(\gamma_e)$, $F_r(u_r, v_r, r)$, $F_u(v_r, r)$, $X(u_r)$ and $Y(u_r)$ are given in Appendix 8.A. Furthermore, the functions $Y(u_r)$ and $X(u_r)$ are bounded for bounded arguments and thus satisfy the following assumption:

Assumption 8.8. $Y(u_r)$ satisfies $Y(u_r) \leq -Y^{\min} < 0, \quad \forall u_r \in [-V_{\max}, U_{rd}]$, where $Y^{\min}$ is a positive constant.

Remark 8.8. Assumption 8.8 is justified by a contradiction: $Y(u_r) \geq 0$ would imply a nominally unstable vehicle in sway which is not the case for commercial vessels by design. No bounds are implied on u_r and $U_{rd} > 0$ will be defined later.

8.2. The Control Objective

This section formalizes the control problem solved in this chapter. The control system should make the vessel follow a given straight line $\mathcal{P}$ and maintain a desired constant surge relative velocity $U_{rd} > 0$ in the presence of environmental disturbances, modeled as a combination of the ocean ocean current $\boldsymbol{V}_c$ and the wind pressure P_e. The inertial reference frame i is placed such that x-axis is aligned with the desired path $\mathcal{P}$ as shown in Figure 8.1. This simplifies the control problem without any loss of generality, giving $\mathcal{P} \triangleq \{(x, y) \in \mathbb{R}^2 : y = 0\}$. The vehicle y coordinate then corresponds to the horizontal cross-track error and the control objectives become:

$$\lim_{t\to\infty} y(t) = 0, \qquad (8.9) \qquad \lim_{t\to\infty} \psi(t) = \psi_{ss}, \qquad (8.10) \qquad \lim_{t\to\infty} u_r(t) = U_{rd}, \qquad (8.11)$$

where $\psi_{ss} \in (-\pi/2, \pi/2)$ is constant. The yaw angle $\psi(t)$ is not required to converge to zero but rather to a steady-state constant value to make the vessel side-slip at equilibrium and thus counteract the environmental disturbances. This is necessary since the ship is underactuated and no control forces are available in sway to compensate for the drift. The value of ψ_{ss} will be specified later.

Remark 8.9. A control approach based on relative velocities is used. As done in Chapters 3, 5 and 6, the vessel is required to hold a constant surge relative velocity U_{rd} as stated in (8.11). Therefore the path following speed is unconstrained and unknown. This is not ideal for speed profile planning/tracking scenarios. However, controlling the relative velocity of the ship gives direct control over energy consumption as hydrodynamic damping depends on $\boldsymbol{\nu}_r$, and removes the unknown term $\boldsymbol{\nu}_c$ from the velocity feedback loop. Furthermore, relative velocity is measurable and relative velocity sensors such as Doppler Velocity Logs (DVLs) are available.

The relative velocity needs to be sufficiently large to guarantee ship maneuverability in presence of disturbances. In particular, it is shown in this chapter that the following assumption guarantees path following in presence of kinematic and dynamic disturbances acting in any direction:

Assumption 8.9. The desired constant relative surge velocity U_{rd} satisfies the following condition:

$$U_{rd} > \max\left\{ V_{\max} + \frac{5}{2}\left|\frac{\kappa_v^{\max}}{Y(U_{rd})}\right|, 2V_{\max} + 2\left|\frac{\kappa_v^{\max} + \kappa_v'^{\max}}{Y(U_{rd})}\right| \right\}.$$

Remark 8.10. It is always possible to find values of U_{rd} satisfying Assumption 8.9, since $|Y(u_r)|$ is strictly increasing for $u_r > 0$.

8.3. The Integral Line of Sight Guidance

The ILOS guidance is presented in this section. The ILOS guidance is introduced in a cascaded configuration with adaptive surge and yaw controllers to solve the path following problem described in Section 8.2. The surface vessel has to converge and follow the

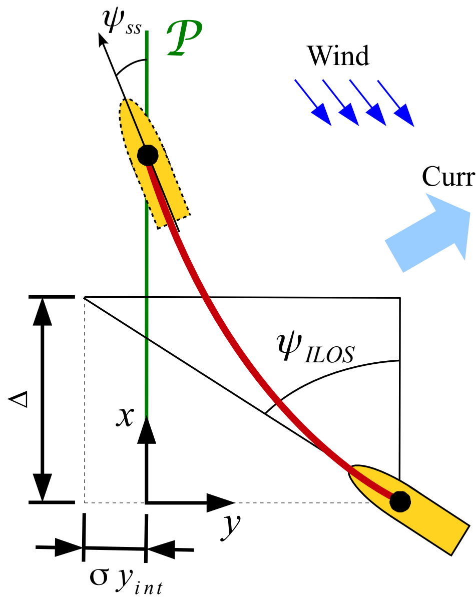

Figure 8.1.: Integral line of sight guidance for an underactuated surface vessel. At steady state the nonzero angle ψ_{ss} allows the underactuated vehicle to counteract the disturbances.

x-axis in presence of environmental disturbances. In this chapter it is shown that the ILOS guidance method introduced in Chapter 3 compensates for both kinematic as well as dynamic disturbances, further extending the results. Hence, the desired heading angle is defined as:

$$\psi_{ILOS} \triangleq -\tan^{-1}\left(\frac{y+\sigma y_{\text{int}}}{\Delta}\right), \qquad \Delta, \sigma > 0, \tag{8.12a}$$

$$\dot{y}_{\text{int}} = \frac{\Delta y}{(y+\sigma y_{\text{int}})^2 + \Delta^2}, \tag{8.12b}$$

where Δ is the look-ahead distance and σ is the integral gain. Both are constant design parameters. The integral effect becomes significant when disturbances push the craft away from its path. This gives a nonzero angle (8.12a) and makes the vessel to side-slip while staying on the desired path, so part of its relative forward velocity can counteract the effect of the disturbances as shown in Figure 8.1. Notice that the law (8.12b) gives less integral action when the vehicle is far from $\mathcal{P}$, reducing the risk of wind-up effects.

8.4. The Surge and Yaw Controllers

This section presents the adaptive surge-yaw controller that, added in a cascaded configuration with the ILOS guidance from Section 8.3, solves the tasks defined in Section 8.2 when the wind pressure P_e is unknown.

Remark 8.11. An adaptive version for the surge and yaw controllers is presented to add robustness with respect to the unknown dynamic disturbance P_e. It is common to have both feed-forward and integral action in modern autopilots and speed controllers [52].

The following combined surge-yaw controller is proposed:

$$\begin{aligned}\tau_u =& -F_{u_r}(u_r, v_r, r) + \dot{u}_{rd} - k_{u_r}(u_r - u_{rd}) \\ & - \hat{P}_e \kappa_u^*(\gamma_e) \cos(\beta_e - \psi),\end{aligned} \tag{8.13a}$$

$$\begin{aligned}\tau_r =& -F_r(u_r, v_r, r) + \ddot{\psi}_d - (k_\psi + \lambda k_r)(\psi - \psi_d) \\ & - (k_r + \lambda)(\dot{\psi} - \dot{\psi}_d) - \hat{P}_e \kappa_r^*(\gamma_e) \sin(\beta_e - \psi),\end{aligned} \tag{8.13b}$$

$$\dot{\hat{P}}_e = \gamma_1 \boldsymbol{G}^T(\psi) \begin{bmatrix} u_r - u_{rd} \\ \gamma_2(\psi - \psi_d) \\ \gamma_2[(\dot{\psi} - \dot{\psi}_d) + \lambda(\psi - \psi_d)] \end{bmatrix}, \tag{8.13c}$$

where $\boldsymbol{G}(\psi) \triangleq [\kappa_u^*(\gamma_e) \cos(\beta_e - \psi) \quad 0 \quad \kappa_r^*(\gamma_e) \sin(\beta_e - \psi)]^T$ is the regressor, $k_{u_r}, k_\psi, k_r, \lambda > 0$ are constant controller gains and $\gamma_1, \gamma_2 > 0$ are constant adaption gains. The controller (8.13) is an adaptive feedback linearizing controller and, as later shown in Section 8.6, it makes sure that u_r, ψ and r exponentially track u_{rd}, ψ_d and $\dot{\psi}_d$. Furthermore, $\hat{P}_e$ exponentially estimates the magnitude of the unknown disturbance P_e.

8.5. Stability Conditions

This section presents the stability conditions under which the proposed ILOS guidance (8.12) in a cascaded configuration with the adaptive controller (8.13) achieves the objectives (8.9-8.11). The notation $X^{U_{rd}} \triangleq X(U_{rd})$ and $Y^{U_{rd}} \triangleq Y(U_{rd})$ is used.

Theorem 8.1. *Given an underactuated surface vessel described by the dynamical system (8.8). If Assumptions 8.3-8.9 hold and, if the look-ahead distance* Δ *and the integral gain*

σ satisfy the conditions:

$$\Delta > \frac{|X^{U_{rd}}|}{|Y^{U_{rd}}|}\Omega(\sigma)\left[\frac{5}{4}\frac{U_{rd}+V_{\max}+\sigma}{U_{rd}-V_{\max}-\sigma}+1\right], \tag{8.14}$$

$$0 < \sigma < U_{rd} - V_{\max} - \frac{5}{2}\left|\frac{\kappa_v^{\max}}{Y^{U_{rd}}}\right|, \tag{8.15}$$

where $\Omega(\sigma)$ is defined as,

$$\Omega(\sigma) \triangleq \frac{U_{rd}-V_{\max}-\sigma}{U_{rd}-V_{\max}-\sigma-\frac{5}{2}\left|\frac{\kappa_v^{\max}}{Y^{U_{rd}}}\right|}, \tag{8.16}$$

then the controller (8.13)*, where ψ_d is given by* (8.12) *and $u_{rd} \triangleq U_{rd}$, guarantees achievement of the control objectives (8.9-8.11).*

8.6. Proof of Theorem 8.1

In this section the proof of Theorem 8.1 is given. The dynamics of the cross track error y and the relative sway velocity v_r are analyzed first. Given the error signals $\tilde{u}_r \triangleq u_r - U_{rd}$, $\tilde{\psi} \triangleq \psi - \psi_d$, $\dot{\tilde{\psi}} \triangleq r - \dot{\psi}_d$, the vector $\boldsymbol{\zeta} \triangleq [\tilde{u}_r, \tilde{\psi}, \dot{\tilde{\psi}}]^T$ is defined. The $y - v_r$ subsystem is obtained combining (8.8b), (8.8e) and (8.12b):

$$\dot{y}_{\text{int}} = \frac{\Delta y}{(y+\sigma y_{\text{int}})^2+\Delta^2}, \tag{8.17a}$$

$$\dot{y} = (\tilde{u}_r + U_{rd})\sin(\tilde{\psi}+\psi_d) + v_r\cos(\tilde{\psi}+\psi_d) + V_y, \tag{8.17b}$$

$$\begin{aligned}\dot{v}_r = &X(\tilde{u}_r+U_{rd})(\dot{\tilde{\psi}}+\dot{\psi}_d) + Y(\tilde{u}_r+U_{rd})v_r \\ &+ \kappa_v(\gamma_e)\sin(\beta_e - \tilde{\psi} - \psi_d).\end{aligned} \tag{8.17c}$$

The calculation of the equilibrium point of the system (8.17) on the manifold $\boldsymbol{\zeta} = [\tilde{u}_r, \tilde{\psi}, \dot{\tilde{\psi}}]^T = \mathbf{0}$ yields the following equation:

$$s\sqrt{s^2+1} = \frac{V_y}{U_{rd}}s^2 + \frac{\cos(\beta_e)s+\sin(\beta_e)}{U_{rd}|Y^{U_{rd}}|}\kappa_v^{\text{eq}}(s) + \frac{V_y}{U_{rd}}, \tag{8.18}$$

where $s \triangleq \sigma y_{\text{int}}^{\text{eq}}/\Delta$ and $y_{\text{int}}^{\text{eq}}$ is the value of y_{int} at equilibrium. The term $\kappa_v^{\text{eq}}(s)$ is defined as the value of $\kappa_v(\gamma_e)$ at equilibrium, i.e. when $\gamma_e = \gamma_e^{\text{eq}} \triangleq -\tan^{-1}(s) - \beta_e - \pi$. It has to be shown that (8.18) has a unique real solution to have a single equilibrium point. The equilibrium point equation (8.18) is similar to Equation (7.21) in Section 7.5 and is of the same kind of Equation (5.17) in Section 7.5. Therefore, it is straightforward to apply Lemma 5.1 from Chapter 5 and conclude that if Assumptions 8.6 and 8.9 hold, then (8.18) has exactly one real solution $s = \sigma y_{\text{int}}^{\text{eq}}/\Delta$.

At equilibrium $y^{\text{eq}} = 0$ while $y_{\text{int}}^{\text{eq}}$ and v_r^{eq} are constant values where $y_{\text{int}}^{\text{eq}}$ is the unique solution of (8.18) and v_r^{eq} relates to $y_{\text{int}}^{\text{eq}}$ as $v_r^{\text{eq}} = U_{rd}\sigma y_{\text{int}}^{\text{eq}}/\Delta - V_y\sqrt{(\sigma y_{\text{int}}^{\text{eq}}/\Delta)^2 + 1)}$. The heading angle held by the vessel at steady-state is then $\psi_{ss} \triangleq -\tan^{-1}(\sigma y_{\text{int}}^{\text{eq}}/\Delta)$. A new set of variables is introduced to move the equilibrium point to the origin: $e_1 \triangleq y_{\text{int}} - y_{\text{int}}^{\text{eq}}$, $e_2 \triangleq y + \sigma e_1$ and $e_3 \triangleq v_r - v_r^{\text{eq}}$. Substituting (8.12a) for ψ_d and factorizing the result with respect to $\boldsymbol{\zeta}$ leads (8.17) to the following expression:

$$\begin{bmatrix} \dot{e}_1 \\ \dot{e}_2 \\ \dot{e}_3 \end{bmatrix} = \boldsymbol{A}(e_2)\begin{bmatrix} e_1 \\ e_2 \\ e_3 \end{bmatrix} + \boldsymbol{B}(e_2) + \boldsymbol{H}(y, y_{\text{int}}, \psi_d, v_r, \boldsymbol{\zeta})\boldsymbol{\zeta}. \tag{8.19}$$

The term $\boldsymbol{H}$ contains all the terms vanishing at $\boldsymbol{\zeta} = \mathbf{0}$. $\boldsymbol{A}(e_2)$ is given in (8.41) of Appendix 8.A while $\boldsymbol{B}(e_2)$ and $\boldsymbol{H}(y, y_{\text{int}}, \psi_d, v_r, \boldsymbol{\zeta})$ are:

$$\boldsymbol{B}(e_2) \triangleq \begin{bmatrix} 0 \\ V_y f(e_2) \\ -\frac{\Delta X^{U_{rd}} V_y}{(e_2+\sigma y_{\text{int}}^{\text{eq}})^2+\Delta^2} f(e_2) + \sin(\psi_{ss} - \beta_e) g(e_2) \end{bmatrix}, \tag{8.20}$$

$$\boldsymbol{H}(y, y_{\text{int}}, \psi_d, v_r, \boldsymbol{\zeta}) \triangleq \begin{bmatrix} 0 & 0 \\ 1 & 0 \\ -\frac{\Delta X(\tilde{u}_r + U_{rd})}{(e_2+\sigma y_{\text{int}}^{\text{eq}})^2+\Delta^2} & 1 \end{bmatrix} \begin{bmatrix} \boldsymbol{h}_y^T \\ \boldsymbol{h}_{v_r}^T \end{bmatrix}, \tag{8.21}$$

and

$$f(e_2) \triangleq 1 - \frac{\sqrt{(\sigma y_{\text{int}}^{\text{eq}})^2 + \Delta^2}}{\sqrt{(e_2 + \sigma y_{\text{int}}^{\text{eq}})^2 + \Delta^2}}, \tag{8.22}$$

$$g(e_2) \triangleq \kappa_v^{\text{eq}} - \frac{\kappa_v(\gamma_e)\sqrt{(\sigma y_{\text{int}}^{\text{eq}})^2 + \Delta^2}}{\sqrt{(e_2 + \sigma y_{\text{int}}^{\text{eq}})^2 + \Delta^2}}. \tag{8.23}$$

Notice that the following bound holds for $f(e_2)$:

$$|f(e_2)| \leq \frac{|e_2|}{\sqrt{(e_2 + \sigma y_{\text{int}}^{\text{eq}})^2 + \Delta^2}}. \tag{8.24}$$

One can prove that (8.24) holds by squaring both sides of the inequality two consecutive times. Furthermore, as a direct consequence of Assumption 8.7, the following bound holds for $g(e_2)$:

$$|g(e_2)| \leq \kappa_v^{\max} \frac{|e_2|}{\sqrt{(e_2 + \sigma y_{\text{int}}^{\text{eq}})^2 + \Delta^2}}. \tag{8.25}$$

The vectors $\boldsymbol{h}_y$ and $\boldsymbol{h}_{v_r}$ are given in Appendix 8.A. The system (8.19) on the manifold $\boldsymbol{\zeta} = \mathbf{0}$ is equivalent to the following nominal system:

$$\begin{bmatrix} \dot{e_1} \\ \dot{e_2} \\ \dot{e_3} \end{bmatrix} = \boldsymbol{A}(e_2) \begin{bmatrix} e_1 \\ e_2 \\ e_3 \end{bmatrix} + \boldsymbol{B}(e_2). \tag{8.26}$$

Lemma 8.1 states the stability properties of (8.26):

Lemma 8.1. *Under the conditions of Theorem 5.1, the nominal system* (8.26) *is UGAS and ULES.*

Proof. The proof of Lemma 8.1 is given in Appendix 8.B. □

The actuated dynamics (8.8d) and (8.8f) of the ship in closed loop configuration with the controller (8.13) are considered next. Given the error signals $\tilde{u}_r$, $\tilde{\psi}$, $\epsilon \triangleq \dot{\tilde{\psi}} + \lambda\tilde{\psi}$ and the estimation error $\tilde{P}_e \triangleq P_e - \hat{P}_e$, the vector $\boldsymbol{\xi} \triangleq [\tilde{u}_r, \tilde{\psi}, \epsilon]^T$ is defined. The dynamics of $\boldsymbol{\xi}$ and $\tilde{P}_e$ are obtained by combining the system equations (8.8c), (8.8d) and (8.8f) with (8.13):

$$\dot{\boldsymbol{\xi}} = \chi(\boldsymbol{\xi}) + \boldsymbol{G}(\tilde{\psi} + \psi_d(\boldsymbol{\xi}, t))\tilde{P}_e, \tag{8.27a}$$

$$\dot{\tilde{P}}_e = -\gamma_1 \boldsymbol{G}^T(\tilde{\psi} + \psi_d(\boldsymbol{\xi}, t)) \left[\frac{\partial W_1(\boldsymbol{\xi})}{\partial \boldsymbol{\xi}}\right]^T, \tag{8.27b}$$

where:

$$\chi(\boldsymbol{\xi}) \triangleq \begin{bmatrix} -k_{u_r} & 0 & 0 \\ 0 & -\lambda & 1 \\ 0 & -k_\psi & -k_r \end{bmatrix} \boldsymbol{\xi}, \tag{8.28}$$

$$W_1(\boldsymbol{\xi}) \triangleq \frac{1}{2}\tilde{u}_r^2 + \frac{\gamma_2 k_\psi}{2}\tilde{\psi}^2 + \frac{\gamma_2}{2}\epsilon^2. \tag{8.29}$$

The stability properties of the origin $(\mathbf{0}, 0)$ of (8.27) are assessed using Theorem A.3. Assumption (A2) of Theorem A.3 is considered first. In particular, notice that it is trivial to find three constants $c_1, c_2, c_3 > 0$ such that $c_1 \parallel \boldsymbol{\xi} \parallel \leq W_1(\boldsymbol{\xi}) \leq c_2 \parallel \boldsymbol{\xi} \parallel$ and $[\partial W_1(\boldsymbol{\xi})/\partial \boldsymbol{\xi}]\ \chi(\boldsymbol{\xi}) \leq -c_3 \parallel \boldsymbol{\xi} \parallel$. This satisfies Assumption (A2) of Theorem A.3.

Assumption (A1) of Theorem A.3 is considered next. To this end notice that the regressor $\boldsymbol{G}(\tilde{\psi} + \psi_d(\boldsymbol{\xi}, t))$ relies on the error signal $\tilde{\psi}$ and the reference $\psi_d(\boldsymbol{\xi}, t)$ to estimate the unknown P_e, where the reference $\psi_d(\boldsymbol{\xi}, t)$ is allowed to depend upon $\boldsymbol{\xi}$ as well. According to Theorem A.3 the regressor $\boldsymbol{G}(\tilde{\psi} + \psi_d(\boldsymbol{\xi}, t))$ has to be analyzed on the manifold $\boldsymbol{\xi} = \mathbf{0}$ (notice that $\boldsymbol{\xi} = \mathbf{0}$ implies $\boldsymbol{\zeta} = \mathbf{0}$). The notation $\psi_d^0 \triangleq \psi_d(\mathbf{0}, t)$ and $\boldsymbol{G}_0(\psi_d^0(t)) \triangleq \boldsymbol{G}(\tilde{\psi} + \psi_d(\boldsymbol{\xi}, t))|_{\boldsymbol{\xi} \equiv \mathbf{0}}$ is introduced for this purpose. Furthermore, some preliminary analysis of ψ_d^0 and its time derivative $\dot{\psi}_d^0 = \rho(y_{\mathrm{int}}(t), y(t), v_r(t))|_{\boldsymbol{\xi} \equiv \mathbf{0}}$, where $\rho(y_{\mathrm{int}}, y, v_r)$ is given in Appendix 8.A, is necessary:

Corollary 8.1. *The signals ψ_d^0 and $\dot{\psi}_d^0$ are bounded and continuous.*

Proof. The signal $\psi_d(t) = -\tan^{-1}[(y(t) + \sigma y_{\mathrm{int}}(t))/\Delta]$ is function of the time trajectories $[e_1(t), e_2(t), e_3(t), \boldsymbol{\xi}^T(t), \tilde{P}_e(t)]^T$ as suggested by (8.19). However, the condition $\boldsymbol{\xi} = \mathbf{0}$ required by Theorem A.3 and that defines ψ_d^0, opens the loop. In fact, $\psi_d^0 = -\tan^{-1}[(y(t) + \sigma y_{\mathrm{int}}(t))/\Delta]|_{\boldsymbol{\xi} \equiv \mathbf{0}}$ is function of the time trajectories $[e_1(t), e_2(t), e_3(t)]^T|_{\boldsymbol{\xi} \equiv \mathbf{0}}$ generated by the nominal system (8.26). Following Lemma 8.1, the nominal system (8.26) is UGAS and ULES, and therefore, the signals ψ_d^0 and $\dot{\psi}_d^0$ are always bounded and continuous. □

It is now possible to check that all the conditions of Assumption (A1) in Theorem A.3 are satisfied. First, notice that it is trivial to find a continuous non-decreasing function $\theta_1(\cdot)$ such that $\max\{\| \chi(\boldsymbol{\xi}) \|, \| \partial W_1(\boldsymbol{\xi})/\partial \boldsymbol{\xi} \|\} \leq \theta_1(\| \boldsymbol{\xi} \|) \| \boldsymbol{\xi} \|$. Next, since $\boldsymbol{G}(\cdot)$ is globally bounded, it is straightforward to find a continuous non-decreasing function $\theta_2(\cdot)$ satisfying the inequality $\max\{\| \boldsymbol{G}(\tilde{\psi} + \psi_d(\boldsymbol{\xi}, t)) \|, \| \boldsymbol{G}_0(\psi_d^0(t)) \|\} \leq \theta_2(\| [\boldsymbol{\xi}^T, \tilde{P}_e]^T \|)$. Furthermore, Assumption 8.6 guarantees that there exists a constant $b_m > 0$ such that $\boldsymbol{G}(\cdot)^T \boldsymbol{G}(\cdot) \geq b_m$, regardless of the argument. Therefore, conditions (A.18), (A.19) and (A.21) in Assumption (A1) of Theorem A.3 are satisfied. This last condition is often referred to as the persistence of excitation (PE) condition.

Finally, the partial derivative $\partial \boldsymbol{G}_0(\psi_d^0)/\partial \tilde{P}_e$ and the time derivative $\partial \boldsymbol{G}_0(\psi_d^0)/\partial t$ are analyzed to show that condition (A.20) in Theorem A.3 is fulfilled. In particular, $\partial \boldsymbol{G}_0(\psi_d^0)/\partial \tilde{P}_e = 0$, while the term $\partial \boldsymbol{G}_0(\psi_d^0)/\partial t$ can be rewritten as $\partial \boldsymbol{G}_0(\psi_d^0)/\partial t = (\partial \boldsymbol{G}_0(\psi_d^0)/\partial \psi_d^0)\dot{\psi}_d^0$. Assumption 8.6 makes sure that $\partial \boldsymbol{G}_0(\psi_d^0)/\partial \psi_d^0$ is well defined and bounded, while continuity and boundedness of $\dot{\psi}_d^0$ is shown by Corollary 8.1. Thus, the time derivative $\partial \boldsymbol{G}_0(\psi_d^0)/\partial t$ is bounded and there exists a non-decreasing function $\theta_3(\cdot)$ such that $\max\{\| \partial W_1(\boldsymbol{\xi})/\partial \tilde{P}_e \|, \| \partial \boldsymbol{G}_0(\psi_d^0(t))/\partial t \|\} \leq \theta_3(|\tilde{P}_e|)$. This fulfills condition (A.20) in Assumption (A1) of Theorem A.3.

All the assumptions of Theorem A.3 are thus satisfied and it is therefore possible to conclude UGAS and ULES for the origin of the system (8.27). Therefore the control goal (8.11) is achieved with exponential converging properties in any ball of initial conditions.

Remark 8.12. The nominal system (8.26) represents the closed loop dynamics of ILOS guidance when the actuated surge and yaw dynamics are neglected ($\boldsymbol{\zeta} = \mathbf{0}$). It can be considered as an ideal unperturbed case since (8.26) has very strong stability properties. Notice that the time trajectories of (8.26) play a role in determining the stability properties of (8.27).

Finally, the interconnected dynamics of (8.17) and (8.27) are considered. The complete cascaded system of (8.17) and (8.27) is given by:

$$\begin{bmatrix} \dot{e}_1 \\ \dot{e}_2 \\ \dot{e}_3 \end{bmatrix} = \boldsymbol{A}(e_2) \begin{bmatrix} e_1 \\ e_2 \\ e_3 \end{bmatrix} + \boldsymbol{B}(e_2) + \boldsymbol{H}(y, y_{\text{int}}, \psi_d, v_r, \boldsymbol{\Lambda\xi})\boldsymbol{\Lambda\xi}, \tag{8.30a}$$

$$\dot{\boldsymbol{\xi}} = \chi(\boldsymbol{\xi}) + \boldsymbol{G}(\tilde{\psi} + \psi_d)\tilde{P}_e, \tag{8.30b}$$

$$\dot{\tilde{P}}_e = -\gamma_1 \boldsymbol{G}^T(\tilde{\psi} + \psi_d) \left[\frac{\partial W_1(\boldsymbol{\xi})}{\partial \boldsymbol{\xi}}\right]^T, \quad \boldsymbol{\Lambda} \triangleq \begin{bmatrix} 1 & 0 & 0 \\ 0 & 1 & 0 \\ 0 & -\lambda & 1 \end{bmatrix}, \tag{8.30c}$$

where $\boldsymbol{\zeta} = \boldsymbol{\Lambda\xi}$, with $\boldsymbol{\Lambda} > 0$ non-singular. Notice that the system (8.30) is a cascaded system, where the subsystem (8.30b-8.30c) perturbs the dynamics (8.30a) through the interconnection matrix $\boldsymbol{H}$. The perturbing system (8.30b-8.30c) is UGAS and ULES and the interconnection matrix $\boldsymbol{H}$ can be shown to satisfy:

$$\| \boldsymbol{H} \| \leq \theta_4(\| \boldsymbol{\zeta} \|)(|y| + |y_{\text{int}}| + |v_r|) + \theta_5(\| \boldsymbol{\zeta} \|), \tag{8.31}$$

where $\theta_4(\cdot)$ and $\theta_5(\cdot)$ are some continuous non-negative functions. Therefore, applying Theorem A.2 and Lemma A.2 concludes that under the conditions of Theorem 5.1 the origin $(e_1, e_2, e_3, \boldsymbol{\xi}, \tilde{P}_e) = (0, 0, 0, \mathbf{0}, 0)$ of the system (8.30) is UGAS and ULES, or alternatively, globally κ-exponentially stable. Hence, the objectives (8.9-8.10) are achieved with exponential converging properties in any ball of initial conditions and $\psi_{ss} = -\tan^{-1}(\sigma y_{\text{int}}^{\text{eq}}/\Delta)$.

Remark 8.13. The value $y_{\text{int}}^{\text{eq}}$ makes sure that, at equilibrium, the vessel holds the heading $\psi_{ss} = -\tan^{-1}(\sigma y_{\text{int}}^{\text{eq}}/\Delta)$ and is the only real solution of (8.18), i.e. ψ_{ss} is the only possible heading that guarantees path following and compensates for the two disturbances.

Remark 8.14. The lower bound (8.14) is expected and has a clear physical interpretation: a too short look-ahead distance $\Delta > 0$ makes the vessel overshoot the target and thus causes chattering [35].

8.7. Simulations

Results from numerical simulations are presented in this section. The ILOS guidance (8.12) from Section 8.3 in a cascaded configuration with the adaptive surge-yaw controller (8.13) presented in Section 8.4, is applied to an underactuated supply vessel where both the kinematic and the dynamic disturbances are considered. The supply ship model from Section B.1 of Appendix B is used. The objective is to make the vessel follow the path $\mathcal{P}$ with a desired surge relative velocity $U_{rd} = 6$ [m/s] in presence of both ocean currents and wind disturbances. The intensity of the current is $|\boldsymbol{V}_c| = 0.9$ [m/s] and its direction is randomly generated. In this case its components are $V_x = -0.17$ [m/s] and $V_y = 0.88$ [m/s], having a direction of 100.7 [deg]. Thus, Assumption 8.3 is fulfilled with $V_{\max} = 1$ [m/s] and it can be verified that Assumption 8.8 is satisfied with $Y_{\min} = 0.039$ [s^{-1}]. The upper limit for the wind pressure P_e is set to $P_e^{\max} = 570$ [N/m^2]. It corresponds approximately to the dynamic pressure generated by wind having 30 [m/s] of speed at the temperature of 10 [C°]. This is a reasonable upper limit since most offshore operations will not be carried out in such harsh conditions. The pressure P_e and its direction β_e are also randomly generated and in this case their values are $P_e = 139.25$ [N/m^2] and $\beta_e = 196.9$ [deg]. Notice that the two disturbances act in different directions.

The wind load coefficients for the offshore supply vessel case from [15] and given in Appendix B satisfy Assumption 8.5 and are chosen to define $C_X^*(\gamma_e), C_Y^*(\gamma_e), C_N^*(\gamma_e)$. Notice that $C_X^*(\gamma_e), C_Y^*(\gamma_e), C_N^*(\gamma_e)$ are smoothened as shown in Appendix B to become class C^1 functions with bounded first derivatives. Hence, it is possible to verify that Assumptions 8.6-8.7 are verified with $\kappa_v^{\max} = 0.036$ [m/s^2] and $\kappa_v'^{\max} = 0.02$ [m/s^2]. Furthermore, the frontal and lateral projected areas above the waterline of the supply vessel in Appendix C are estimated as $A_{Fw} = 282.00$ [m^2] and $A_{Lw} = 554.90$ [m^2], and its length overall is $L_{oa} = 82.45$ [m]. Notice that, given the bounds $V_{\max} = 1$ [m/s], $\kappa_v^{\max} = 0.036$ [m/s^2] and $\kappa_v'^{\max} = 0.02$ [m/s^2], the desired relative velocity $U_{rd} = 6$ [m/s] satisfies Assumption 8.9.

Remark 8.15. The coefficients from [15] are chosen to define the environmental load vector $\boldsymbol{w}$ in consideration of their wide use to assess wind loads on ships.

The values for the guidance law integral gain and look-ahead distance are chosen to satisfy (8.14-8.15) and are $\sigma = 1$ [m/s] and $\Delta = 340$ [m]. The adaptive controller (8.13) is implemented with the following gains: $k_{u_r} = 0.1$, $k_\psi = 0.04$, $k_r = 0.9$ and $\lambda = 0.05$. The values for k_{u_r}, k_ψ and k_r are chosen to give a time constant of 10 [s] for the $\tilde{u}_r$ first order closed loop system and to make the $\tilde{\psi}$ second order closed loop system overdamped with $\omega_0 = 0.2$ [rad/s] when the adaption law (8.13c) is turned off ($P_e = 0$). The adaptation gains are set to $\gamma_1 = 10^6$ and $\gamma_2 = 10^3$. Such high values for γ_1 and γ_2 are necessary to guarantee fast convergence since the quantities $1/m_{11}$ and $1/(m_{22}m_{33} - m_{23}^2)$ render $\kappa_u(\gamma_e)^*$ and $\kappa_r(\gamma_e)^*$ very small (see Appendix 8.A). Finally, the supply vessel has 1600 [kN] of maximum available thrust in surge, while the maximum rudder angle is 35 [deg] and the maximum turning rate is 10 [deg/s].

The ship is given an initial cross track error of 1500 [m] and initially holds zero relative velocity. Its surge axis is parallel to the desired path $\mathcal{P}$. Figures 8.2a-8.2d show how the underactuated vessel successfully follows the path $\mathcal{P}$ with a constant side-slip angle $\psi_{ss} \approx -8.0°$ to compensate for the disturbances. Hence, choosing the guidance law parameters according to the criteria (8.14-8.15) gives smooth convergence and does not overload the ship surge-yaw controller (8.13). The relative surge velocity is shown in Figure 8.2d while the rudder angle is given in Figure 8.2b. Furthermore, Figure 8.2e shows the performance of the adaption law (8.13c). As expected, the estimate $\hat{P}_e$ converges to the real value. Notice that for angles of attack that at equilibrium are close to $\gamma_e^{\text{eq}} \approx \pm\pi/2$ convergence is slower as shown in Figure 8.2f. When $\gamma_e \approx \pm\pi/2$ the product $\boldsymbol{G}(\gamma_e)^T\boldsymbol{G}(\gamma_e) > 0$ is at its minimum and therefore the convergence of the persistently exciting (PE) regressor $\boldsymbol{G}(\gamma_e)$ is slower.

8.8. Conclusions

In this chapter it has been shown that the ILOS guidance law developed in Chapters 5 and 6 for path following purposes of underactuated surface vehicles effectively compensates for kinematic as well as dynamic disturbances. Theoretical results and simulations have been presented in a unified manner for this purpose. The disturbances are modeled as a combination of a constant irrotational ocean current and constant heading dependent wind forces. It has been shown that the ILOS guidance guarantees path following with global κ-exponential stability properties in closed loop configuration with an adaptive surge-yaw controller, in presence of both the disturbances. The full kinematic-dynamic closed loop system has been considered and explicit conditions to guarantee stability have been derived. The theoretical results are supported by numerical simulations.

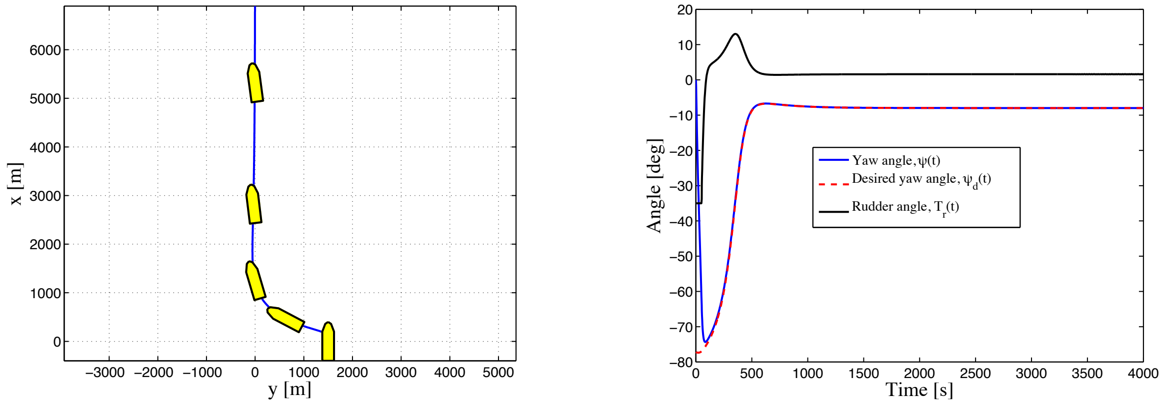

(a) Simulation of convergence and path following of the supply vessel in presence of multiple disturbances. The time interval $0 - 1400$ [s] is considered.

(b) Yaw angle $\psi(t)$ and rudder angle $T_r(t)$ of the supply ship from simulations. Notice the side-slip angle $\psi_{ss} \approx -7.9$ [deg] in steady state.

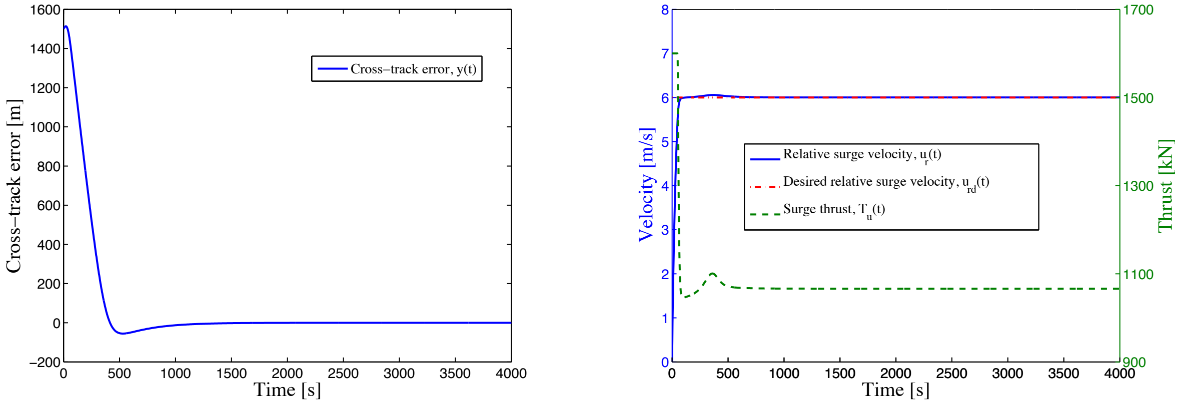

(c) Cross track error $y(t)$ of the vessel.

(d) Relative surge velocity $u_r(t)$ and surge thrust $T_u(t)$.

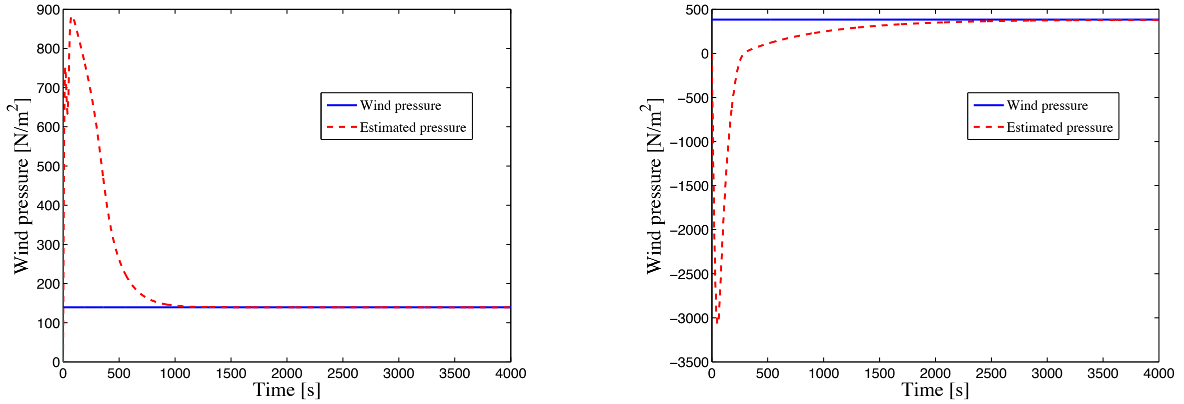

(e) Adaptive surge-yaw controller estimate $\hat{P}_e(t)$ from simulations. In this case $V_x = -0.17$ [m/s], $V_y = 0.88$ [m/s], $P_e = 139.25$ [N/m^2] and $\beta_e = 196.9$ [deg]. The steady state attack angle is $\gamma_e^{\text{eq}} \approx -24.8$ [deg].

(f) Adaptive surge-yaw controller estimate $\hat{P}_e(t)$ from simulations. In this case $V_x = -0.41$ [m/s], $V_y = -0.80$ [m/s], $P_e = 382.76$ [N/m^2] and $\beta_e = 286.3$ [deg]. The steady state attack angle is $\gamma_e^{\text{eq}} \approx -96.2$ [deg].

Figure 8.2.: Simulation results for $\Delta = 340$ [m] and $\sigma = 1$ [m/s].

8.A. Appendix: Functional Expressions

$$\kappa_u(\gamma_e)^* = -\frac{1}{m_{11}} A_{Fw} C_X^*(\gamma_e), \tag{8.32}$$

$$\kappa_r(\gamma_e)^* = -\frac{m_{23} A_{Lw} C_Y^*(\gamma_e)}{m_{22}m_{33} - m_{23}^2} + \frac{m_{22} L_{oa} A_{Lw} C_N^*(\gamma_e)}{m_{22}m_{33} - m_{23}^2}, \tag{8.33}$$

$$F_{u_r}(u_r, v_r, r) \triangleq \frac{1}{m_{11}}(m_{22}v_r + m_{23}r)r - \frac{d_{11}}{m_{11}}u_r, \tag{8.34}$$

$$X(u_r) \triangleq \frac{m_{23}^2 - m_{11}m_{33}}{m_{22}m_{33} - m_{23}^2}u_r + \frac{d_{33}m_{23} - d_{23}m_{33}}{m_{22}m_{33} - m_{23}^2}, \tag{8.35}$$

$$Y(u_r) \triangleq \frac{(m_{22} - m_{11})m_{23}}{m_{22}m_{33} - m_{23}^2}u_r - \frac{d_{22}m_{33} - d_{32}m_{23}}{m_{22}m_{33} - m_{23}^2}, \tag{8.36}$$

$$\begin{aligned} F_r(u_r, v_r, r) &\triangleq \frac{m_{23}d_{22} - m_{22}(d_{32} + (m_{22} - m_{11})u_r)}{m_{22}m_{33} - m_{23}^2}v_r \\ &+ \frac{m_{23}(d_{23} + m_{11}u_r) - m_{22}(d_{33} + m_{23}u_r)}{m_{22}m_{33} - m_{23}^2}r. \end{aligned} \tag{8.37}$$

The vectors $\boldsymbol{h}_y \triangleq [h_{y1}, h_{y2}, h_{y3}]^T$, $\boldsymbol{h}_{v_r} \triangleq [h_{v_r1}, h_{v_r2}, h_{v_r3}]^T$ are:

$$\begin{aligned} h_{y1} &= \sin(\tilde{\psi} + \psi_d), \quad h_{y3} = 0, \\ h_{y2} &= U_{rd}\left[\frac{\sin(\tilde{\psi})}{\tilde{\psi}}\cos(\psi_d) + \frac{\cos(\tilde{\psi}) - 1}{\tilde{\psi}}\sin(\psi_d)\right] \\ &+ v_r\left[\frac{\cos(\tilde{\psi}) - 1}{\tilde{\psi}}\cos(\psi_d) - \frac{\sin(\tilde{\psi})}{\tilde{\psi}}\sin(\psi_d)\right], \end{aligned} \tag{8.38}$$

$$\begin{aligned} h_{v_r1} &= \frac{X(\tilde{u}_r + U_{rd}) - X^{U_{rd}}}{\tilde{u}_r}\rho(y_{\text{int}}, y, v_r) + v_r\frac{Y(\tilde{u}_r + U_{rd}) - Y^{U_{rd}}}{\tilde{u}_r}, \\ h_{v_r2} &= \kappa_v(\gamma_e)\left[\frac{\cos(\tilde{\psi}) - 1}{\tilde{\psi}}\sin(\beta_e - \psi_d) - \frac{\sin(\tilde{\psi})}{\tilde{\psi}}\cos(\beta_e - \psi_d)\right], \\ h_{v_r3} &= X(\tilde{u}_r + U_{rd}), \end{aligned} \tag{8.39}$$

where the limits of h_{y2} for $\tilde{\psi} \to 0$ and h_{v_r1} for $\tilde{u}_r \to 0$ exist and are finite. The expression $\rho(y_{\text{int}}, y, v_r)$ is defined as:

$$\rho(y_{\text{int}}, y, v_r) \triangleq \frac{\Delta U_{rd}(y + \sigma y_{\text{int}}) - \Delta^2 v_r}{((y + \sigma y_{\text{int}})^2 + \Delta^2)^{3/2}} - \frac{\sigma\Delta^2}{((y + \sigma y_{\text{int}})^2 + \Delta^2)^2}y - \frac{\Delta V_y}{(y + \sigma y_{\text{int}})^2 + \Delta^2}. \tag{8.40}$$

$$\boldsymbol{A}(e_2) \triangleq \begin{bmatrix} -\frac{\sigma\Delta}{(e_2+\sigma y_{\text{int}}^{\text{eq}})^2+\Delta^2} & \frac{\Delta}{(e_2+\sigma y_{\text{int}}^{\text{eq}})^2+\Delta^2} & 0 \\ -\frac{\sigma^2\Delta}{(e_2+\sigma y_{\text{int}}^{\text{eq}})^2+\Delta^2} & -\frac{U_{rd}}{\sqrt{(e_2+\sigma y_{\text{int}}^{\text{eq}})^2+\Delta^2}} + \frac{\sigma\Delta}{(e_2+\sigma y_{\text{int}}^{\text{eq}})^2+\Delta^2} & \frac{\Delta}{\sqrt{(e_2+\sigma y_{\text{int}}^{\text{eq}})^2+\Delta^2}} \\ \frac{\sigma^2\Delta^2 X^{U_{rd}}}{((e_2+\sigma y_{\text{int}}^{\text{eq}})^2+\Delta^2)^2} & \frac{U_{rd}\Delta X^{U_{rd}}}{((e_2+\sigma y_{\text{int}}^{\text{eq}})^2+\Delta^2)^{3/2}} - \frac{\sigma\Delta^2 X^{U_{rd}}}{((e_2+\sigma y_{\text{int}}^{\text{eq}})^2+\Delta^2)^2} + \frac{\kappa_v(\gamma_e)\cos(\beta_e)}{\sqrt{(e_2+\sigma y_{\text{int}}^{\text{eq}})^2+\Delta^2}} & Y^{U_{rd}} - \frac{\Delta^2 X^{U_{rd}}}{((e_2+\sigma y_{\text{int}}^{\text{eq}})^2+\Delta^2)^{3/2}} \end{bmatrix} \tag{8.41}$$

8.B. Appendix: Proof of Lemma 8.1

The nominal system (8.26) is written again:

$$\begin{bmatrix} \dot{e_1} \\ \dot{e_2} \\ \dot{e_3} \end{bmatrix} = \boldsymbol{A}(e_2) \begin{bmatrix} e_1 \\ e_2 \\ e_3 \end{bmatrix} + \boldsymbol{B}(e_2). \tag{8.42}$$

The nominal system (8.26) is equivalent to the system (5.28) analyzed in Chapter 5. Hence, the proof follows along the lines of the proof of Lemma 5.2 given in Appendix 5.B of Chapter 5. Consider the quadratic Lyapunov function candidate (LFC):

$$V \triangleq \frac{1}{2}\sigma^2 e_1^2 + \frac{1}{2}e_2^2 + \frac{1}{2}\mu e_3^2, \quad \mu > 0. \tag{8.43}$$

The notation $\bar{e}_1 \triangleq e_1/\sqrt{(e_2 + \sigma y_{\text{int}}^{\text{eq}})^2 + \Delta^2}$, $\bar{e}_2 \triangleq e_2/\sqrt{(e_2 + \sigma y_{\text{int}}^{\text{eq}})^2 + \Delta^2}$, Assumptions 8.3-8.9 and inequalities (8.24-8.25) yield the following bound for the time derivative $\dot{V}$:

$$\dot{V} \leq -W_2(|\bar{e}_1|, |e_3|) - W_3(|\bar{e}_2|, |e_3|). \tag{8.44}$$

The functions W_2 and W_3 are defined as:

$$W_2 \triangleq \sigma^3\Delta|\bar{e}_1|^2 - \mu\frac{\sigma^2|X^{U_{rd}}|}{\Delta}|\bar{e}_1||e_3| + \mu\eta\left(|Y^{U_{rd}}| - \frac{|X^{U_{rd}}|}{\Delta}\right)|e_3|^2, \tag{8.45}$$

$$W_3 \triangleq \Delta \begin{bmatrix} |\bar{e}_2| & |e_3| \end{bmatrix} \begin{bmatrix} \beta & -\alpha \\ -\alpha & \frac{\alpha(2\alpha-1)}{\beta} \end{bmatrix} \begin{bmatrix} |\bar{e}_2| \\ |e_3| \end{bmatrix}, \tag{8.46}$$

where $0 < \eta < 1$, $\beta \triangleq U_{rd} - V_{\max} - \sigma$ and α is given by:

$$\alpha \triangleq (1-\eta)\frac{(U_{rd} - V_{\max} - \sigma)(\Delta|Y^{U_{rd}}| - |X^{U_{rd}}|)}{|X^{U_{rd}}|\,(U_{rd} + V_{\max} + \sigma) + 2\Delta\kappa_v^{\max}}. \tag{8.47}$$

The parameter μ is chosen as:

$$\mu \triangleq \frac{\Delta^2(2\alpha - 1)}{|X^{U_{rd}}|(U_{rd} + V_{\max} + \sigma) + 2\Delta\kappa_v^{\max}}. \tag{8.48}$$

If both W_2 and W_3 are definite positive then $\dot{V}$ is negative definite. Positive definiteness of W_2 is ensured if (8.49) and (8.50) are satisfied:

$$\Delta > \frac{|X^{U_{rd}}|}{|Y^{U_{rd}}|}, \tag{8.49}$$

$$\mu < \frac{4\eta\Delta^2\left[\Delta|Y^{U_{rd}}| - |X^{U_{rd}}|\right]}{\sigma|X^{U_{rd}}|^2}. \tag{8.50}$$

Notice that condition (8.49) is met as long as (8.14) holds. It is straightforward to show that $\eta \geq 1/5$ is a sufficient condition for μ, defined in (8.48), to satisfy (8.50). Therefore, without any loss of generality, η is set to 1/5. Both β and α must fulfill $\beta > 0$ and $\alpha > 1$ to guarantee positive definiteness of W_3. Assumption 8.9 and (8.15) make sure that $\beta > 0$ while it is easy to check that conditions (8.14) and (8.15) imply $\alpha > 1$. Furthermore, $\alpha > 1$ guarantees $\mu > 0$ and ensures positive definiteness of V. Therefore under the conditions stated in Theorem 8.1, V, W_2 and W_3 are positive definite and hence, following standard Lyapunov arguments, the nominal system (8.42) is UGAS. Furthermore, the inequality $W \triangleq W_2 + W_3 \geq \bar{\lambda}_1|\bar{e}_1|^2 + \bar{\lambda}_2|\bar{e}_2|^2 + \lambda_3|e_3|^2$ holds in a neighbourhood of the origin for some constants $\bar{\lambda}_1, \bar{\lambda}_2, \lambda_3 > 0$ and thus in any ball $\mathcal{B}_r \triangleq \{|e_2| \leq r\}, r > 0$ the function W can be estimated as $W \geq \lambda_1|e_1|^2 + \lambda_2|e_2|^2 + \lambda_3|e_3|^2$ where $\lambda_i = \bar{\lambda}_i/((r + \sigma y_{\text{int}}^{\text{eq}})^2 + \Delta^2)$, $i = 1, 2$. This, together with the fact that V is a quadratic function of e_1, e_2 and v_r, concludes that (8.42) is also uniformly locally exponentially stable, ULES [82].

Chapter 9.

Path Following Control of Underactuated AUVs in the Presence of Ocean Currents

“And the sea will grant each man new hope, as sleep brings dreams of home.”

— Larry Ferguson, Screenwriter

In Chapter 4 a three dimensional (3D) Integral Line-of-Sight (ILOS) guidance law was presented and applied to a kinematic model of underactuated underwater vehicles. The actuated and underactuated dynamics were not considered and the guidance law was designed to make the vehicle follow 3D straight lines in the presence of constant and irrotational ocean currents. A discussion involving intuitive and practical aspects of the current compensation problem and the 3D ILOS control law was also given. The resulting analysis of the closed loop system gave explicit bounds on the integral gains but did not give any guidelines on how to choose the look-ahead distances of the ILOS. The underactuated sway dynamics were included in the analysis of the two dimensional (2D) ILOS in Chapter 5 while the complete kinematic and dynamic closed loop system of the 2D ILOS guidance law was analyzed in Chapter 6. In this way an explicit bound for the choice of the look-ahead distance was derived.

In this chapter the underactuated and the actuated dynamics are included in the analysis of the 3D ILOS guidance law from Chapter 4. The analysis developed in Chapters 5 and 6 for surface vessels is hence extended to underactuated AUVs for 3D straight-line path following applications in the presence of constant irrotational ocean currents acting in any direction of the inertial frame. The 3D ILOS guidance law from Chapter 4 with integral action in both the vertical and horizontal directions is shown to solve the task together with three feedback controllers in a cascaded configuration. The control approach is based on relative velocities with direct control over the AUV relative speed. It is shown that redefining the AUV dynamics in terms of relative velocities only, as explained in [52], makes it possible to prove the stability properties of uniform global asymptotic stability (UGAS) and uniform local exponential stability (ULES) for the origin of the closed loop system. Compared to Chapter 4, both the kinematic and dynamic levels of the problem are addressed and explicit bounds on all of the guidance law parameters are given to guarantee stability. The proposed 3D ILOS guidance control scheme is applied to the LAUV autonomous underwater vehicle [126]. First, simulations are run using a mathematical model of the LAUV vehicle to analyze the guidance law response and tune the ILOS controllers. The simulations include an example of a 3D underwater path following case and a 2D underwater way-point following case, analogous to the sea trial runs, for a back-to-back comparison. Next, experimental results from full scale underwater 2D way-point following tests are shown. Finally, the ILOS guidance law is compared to the vector field guidance law for path following purposes from [100]. The comparison is based on experimental results.

The chapter is organized as follows: Section 9.1 presents the model of the vehicle and Section 9.2 identifies the control objective. Section 9.3 presents the strategy that solves the path following task defined in Section 9.2. The stability conditions are given in Section 9.4 and proven in Section 9.5. The simulation results are shown in Section 9.6 and the results from field experiments with the LAUV are presented in Section 9.7. Finally, the ILOS guidance law is compared to the vector field guidance law in Section 9.8. Conclusions are given in Section 9.9. The results presented in this chapter are based on the papers [34, 30].

9.1. The Control Plant Model

The class of marine vehicles described by the 5-DOF maneuvering model presented in Section 2.4 of Chapter 2 are considered:

$$\dot{\boldsymbol{\eta}} = \boldsymbol{J}(\boldsymbol{\eta})\boldsymbol{\nu}_r + [\boldsymbol{V}_c^T, 0, 0]^T, \tag{9.1}$$

$$\boldsymbol{M}\dot{\boldsymbol{\nu}}_r + \boldsymbol{C}(\boldsymbol{\nu}_r)\boldsymbol{\nu}_r + \boldsymbol{D}\boldsymbol{\nu}_r + \boldsymbol{g}(\boldsymbol{\eta}) = \boldsymbol{B}\boldsymbol{f}. \tag{9.2}$$

The state of the underwater vehicle is given by the vector $\boldsymbol{\eta} \triangleq [x, y, z, \theta, \psi]^T$ which describes the position and the orientation of the AUV with respect to the inertial frame i. In particular, θ is the vehicle pitch angle and ψ is the vehicle yaw angle. As shown in Chapter 2, in navigation problems involving irrotational ocean currents it is useful to describe the state of the vessel with the relative velocity vector: $\boldsymbol{\nu}_r = [u_r, v_r, w_r, q, r]^T$. The vector $\boldsymbol{\nu}_r$ is defined in b where u_r is the relative surge velocity, v_r is the relative sway velocity, w_r is the relative heave velocity, q is pitch rate and r is the yaw rate.

Remark 9.1. The models used in [26, 33] contain the velocity vector $\boldsymbol{\nu}$ as well as the relative velocity vector $\boldsymbol{\nu}_r$. This complicates the controller design and weakens the cascade configuration. The model (9.1-9.2) overcomes the problem.

The vector $\boldsymbol{f} \triangleq [T_u, T_q, T_r]^T$ is the control input vector, containing the surge thrust (T_u), the pitch rudder angle (T_q) and the yaw rudder angle (T_r). The dimension of the control input vector $\boldsymbol{f}$ is two less than the DOF of the vessel, therefore the model (9.2) is underactuated in its configuration space. The term $\boldsymbol{J}(\boldsymbol{\eta})$ is the velocity transformation matrix defined as:

$$\boldsymbol{J}(\boldsymbol{\eta}) \triangleq \begin{bmatrix} \boldsymbol{R}(\theta,\psi) & \boldsymbol{0} \\ \boldsymbol{0} & \boldsymbol{T}(\theta) \end{bmatrix}, \tag{9.3}$$

where $\boldsymbol{T}(\theta) \triangleq \mathrm{diag}(1, 1/\cos(\theta)), |\theta| \neq \frac{\pi}{2}$.

Remark 9.2. The definition of $\boldsymbol{T}(\theta)$ implies a singularity in θ. However the global results refer to the analysis of the closed loop system given in Section 9.5, where no singularity is present.

The matrix $\boldsymbol{M} = \boldsymbol{M}^T > 0$ is the mass and inertia matrix, and includes hydrodynamic added mass. The matrix $\boldsymbol{C}(\boldsymbol{\nu}_r)$ is the Coriolis and centripetal matrix, $\boldsymbol{D} > 0$ is the hydrodynamic damping matrix, $\boldsymbol{g}(\boldsymbol{\eta})$ is the gravity vector and $\boldsymbol{B} \in \mathbb{R}^{5\times 3}$ is the actuator configuration matrix. The structure of the matrices $\boldsymbol{R}(\theta, \psi)$, $\boldsymbol{M}$, $\boldsymbol{C}(\boldsymbol{\nu}_r)$, $\boldsymbol{B}$ and of the vector $\boldsymbol{g}(\boldsymbol{\eta})$ is given in Chapter 2. The following assumption defines the properties of the damping matrix $\boldsymbol{D}$:

Assumption 9.1. Damping is considered linear.

Remark 9.3. For low speed maneuvering, Assumption 9.1 is a mild assumption as any non-linear damping should enhance the directional stability of the vehicle due to the passive nature of the hydrodynamic damping forces.

The hydrodynamic damping matrix $\boldsymbol{D}$ is therefore considered to have the following structure [52]:

$$\boldsymbol{D} \triangleq \begin{bmatrix} d_{11} & 0 & 0 & 0 & 0 \\ 0 & d_{22} & 0 & 0 & d_{25} \\ 0 & 0 & d_{33} & d_{34} & 0 \\ 0 & 0 & d_{43} & d_{44} & 0 \\ 0 & d_{52} & 0 & 0 & d_{55} \end{bmatrix}. \tag{9.4}$$

The particular structure of $\boldsymbol{D}$ is justified by symmetry arguments (see Section 2.4 of Chapter 2) and Assumption 9.1. Furthermore, the following assumption is introduced:

Assumption 9.2. The body-fixed coordinate frame b is located in a point $(x_g^*, 0, 0)$ from the vehicle's center of gravity (CG) along the center-line of the vessel, where x_g^* is chosen so that $\boldsymbol{M}^{-1}\boldsymbol{B}\boldsymbol{f} = [\tau_u, 0, 0, \tau_q, \tau_r]^T$.

The point $(x_g^*, 0, 0)$ exists for all AUVs of cylindrical shape employing symmetric steering and diving control surfaces, (see Section 2.4 of Chapter 2). Finally the following assumption is taken from Section 2.4 for clarity and completeness:

Assumption 9.3. The ocean current in the inertial frame i, $\boldsymbol{V}_c \triangleq [V_x, V_y, V_z]^T$, is constant, irrotational and bounded. Hence, there exists $V_{\max} > 0$ such that $V_{\max} \geq \sqrt{V_x^2 + V_y^2 + V_z^2}$.

9.1.1. The Model in Component Form

To solve nonlinear underactuated control design problems it is convenient to expand (9.1-9.2) into:

$$
\begin{aligned}
\dot{x} &= u_r \cos(\psi)\cos(\theta) - v_r \sin(\psi) + w_r \cos(\psi)\sin(\theta) + V_x, && \text{(9.5a)}\\
\dot{y} &= u_r \sin(\psi)\cos(\theta) + v_r \cos(\psi) + w_r \sin(\psi)\sin(\theta) + V_y, && \text{(9.5b)}\\
\dot{z} &= -u_r \sin(\theta) + w_r \cos(\theta) + V_z, && \text{(9.5c)}\\
\dot{\theta} &= q, && \text{(9.5d)}\\
\dot{\psi} &= \frac{r}{\cos(\theta)}, && \text{(9.5e)}\\
\dot{u}_r &= F_{u_r}(v_r, w_r, r, q) - \frac{d_{11}}{m_{11}} u_r + \tau_u, && \text{(9.5f)}\\
\dot{v}_r &= X_{v_r}(u_r) r + Y_{v_r}(u_r) v_r, && \text{(9.5g)}\\
\dot{w}_r &= X_{w_r}(u_r) q + Y_{w_r}(u_r) w_r + Z_{w_r} \sin(\theta), && \text{(9.5h)}\\
\dot{q} &= F_q(\theta, u_r, w_r, q) + \tau_q, && \text{(9.5i)}\\
\dot{r} &= F_r(u_r, v_r, r) + \tau_r. && \text{(9.5j)}
\end{aligned}
$$

The expressions F_{u_r}, X_{v_r}, Y_{v_r}, X_{w_r}, Y_{w_r}, Z_{w_r}, F_q and F_r are given in Appendix 9.A. Notice that the functions $X_{v_r}(u_r)$, $X_{w_r}(u_r)$, $Y_{v_r}(u_r)$ and $Y_{w_r}(u_r)$ are bounded for bounded arguments. An additional key assumption is introduced:

Assumption 9.4. The functions $Y_{v_r}(u_r)$ and $Y_{w_r}(u_r)$ satisfy: $Y_a(u_r) \leq -Y_a^{\min} < 0$, $\forall u_r \in [-V_{\max}, U_{rd}]$, $a \in \{v_r, w_r\}$.

Remark 9.4. Assumption 9.4 is justified by the following contradiction: $Y_{v_r}(u_r) \geq 0$ and $Y_{w_r}(u_r) \geq 0$ would imply an undamped or nominally unstable vehicle in sway and heave which is not the case in practice [25]. This assumption is thus linked to the straight-line stability properties the AUV. Notice that no bounds are implied on u_r while $U_{rd} > 0$ will be defined later.

9.2. The Control Objective

This section formalizes the control problem solved in this chapter. The control system should make the vehicle follow a given straight line $\mathcal{P}$ and maintain a desired constant surge relative velocity $U_{rd} > 0$ in the presence of unknown constant and irrotational ocean currents. The inertial reference frame i is placed such that the z-axis points down and the x-axis is aligned with the desired path $\mathcal{P}$ as shown in Figure 9.1. This simplifies the control problem without any loss of generality. The desired path $\mathcal{P}$ is then defined as $\mathcal{P} \triangleq \{(x, y, z) \in \mathbb{R}^3 : y = 0, z = 0\}$. Hence, the y and z coordinates of the vehicle correspond to the horizontal and vertical cross-track errors and the objectives the control system should pursue can be formalized as:

$$\lim_{t\to\infty} y(t) = 0, \tag{9.6}$$

$$\lim_{t\to\infty} z(t) = 0, \tag{9.7}$$

$$\lim_{t\to\infty} \psi(t) = \psi_{ss}, \quad \psi_{ss} \in \left(-\frac{\pi}{2}, \frac{\pi}{2}\right), \tag{9.8}$$

$$\lim_{t\to\infty} \theta(t) = \theta_{ss}, \quad \theta_{ss} \in \left(-\frac{\pi}{2}, \frac{\pi}{2}\right), \tag{9.9}$$

$$\lim_{t\to\infty} u_r(t) = U_{rd}, \tag{9.10}$$

where θ_{ss} as well as ψ_{ss} are constants. The yaw angle $\psi(t)$ and the pitch angle $\theta(t)$ are not required to converge to zero but rather to steady-state constant values to make the vehicle pitch and side-slip at equilibrium in order to counteract the ocean current. This is necessary when the ocean current has components in the transverse y and z directions of the path, since the vehicle is underactuated and no control forces are available in sway and heave to compensate. The AUV is thus required to side-slip in order not to drift away. The values of ψ_{ss} and θ_{ss} will be specified later.

Remark 9.5. Notice that non horizontal motion can also be considered. Non horizontal motion affects the the gravity vector $\boldsymbol{g}(\boldsymbol{\eta})$ where gravity is represented by the term $Z_{wr}\sin(\theta)$ in (9.5h). In particular, this term is seen as an additional bounded constant disturbance in heave that the guidance system compensates for as well (see Section 9.5).

Remark 9.6. In [26] and [33] the vehicle is required to follow $\mathcal{P}$ with a constant speed $U_d > 0$. In this chapter the AUV is required to hold a constant surge relative velocity U_{rd} as stated in (9.10). Therefore the constant path following speed is not directly controlled, but is instead results from the relative speed and the current velocity. This would not be ideal if speed profile planning/tracking scenarios were considered. However, controlling the relative velocity of the ship gives direct control over the energy consumption as hydrodynamic damping depends on $\boldsymbol{\nu}_r$, and also it removes the unknown term $\boldsymbol{\nu}_c$ from the velocity feedback loop. Furthermore, relative velocity can be measured or estimated using devices such as Doppler Velocity Logs or other sensor fusion techniques [99].

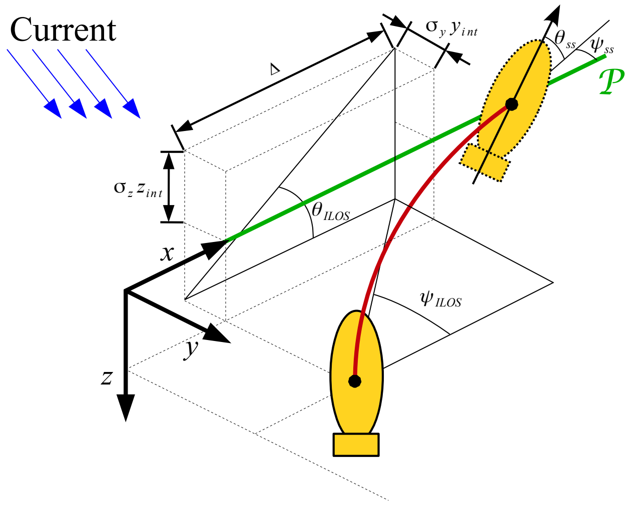

Figure 9.1.: Integral line of sight guidance for an underactuated underwater vehicle, in this case $\Delta_y = \Delta_z = \Delta$. At steady state the angles ψ_{ss} and θ_{ss} allow the underactuated AUV to counteract the current.

Finally, the desired relative surge velocity needs to be sufficiently large compared to the ocean current velocity in order to guarantee maneuverability of the AUV. It is later shown that the particular bound given in Assumption 9.5 allows the AUV to achieve path following for currents acting in any direction of the 3D space:

Assumption 9.5. The desired constant relative surge velocity U_{rd} satisfies the following condition:

$$U_{rd} > \max\left\{ V_{\max} + \frac{5}{2}\left|\frac{Z_{w_r}}{Y_{w_r}(U_{rd})}\right|, 2V_{\max} + 2\left|\frac{Z_{w_r}}{Y_{w_r}(U_{rd})}\right| \right\},$$

Remark 9.7. It is always possible to find values of U_{rd} satisfying Assumption 9.5, since $|Y_{w_r}(u_r)|$ is strictly increasing for $u_r > 0$.

9.3. The Control System

In this section a control strategy to solve the control problem defined in Section 9.2 is proposed. First, the LOS guidance is introduced and then the surge, pitch and yaw controllers are added in a cascaded configuration.

9.3.1. Path Following Control Strategy

The following integral LOS guidance law is chosen to set the heading and pitch angles, and make the AUV converge and follow the x-axis in presence of ocean currents:

$$\theta_{ILOS} \triangleq \tan^{-1}\left(\frac{z + \sigma_z z_{\text{int}}}{\Delta_z}\right), \quad \Delta_z > 0, \tag{9.11a}$$

$$\dot{z}_{\text{int}} = \frac{\Delta_z z}{(z + \sigma_z z_{\text{int}})^2 + \Delta_z^2}, \tag{9.11b}$$

$$\psi_{ILOS} \triangleq -\tan^{-1}\left(\frac{y + \sigma_y y_{\text{int}}}{\Delta_y}\right), \quad \Delta_y > 0, \tag{9.11c}$$

$$\dot{y}_{\text{int}} = \frac{\Delta_y y}{(y + \sigma_y y_{\text{int}})^2 + \Delta_y^2}, \tag{9.11d}$$

where the look-ahead distances in the vertical and horizontal planes Δ_z and Δ_y, as well as the integral gains $\sigma_y > 0$ and $\sigma_z > 0$, are constant design parameters. A graphical explanation of the integral LOS is given in Figure 9.1. The integral effects become significant when disturbances push the craft away from its path. This gives nonzero angles (9.11a), (9.11c) and makes the AUV side-slip and pitch while staying on the desired path, so part of its relative forward velocity can counteract the effect of the ocean current as shown in Figure 9.1. The laws (9.11b) and (9.11d) give less integral action when the vehicle is far from $\mathcal{P}$, reducing the risk of wind-up effects. The integral LOS guidance laws (9.11) were proposed in [26] and [33].

In this chapter it is shown how integral action in both the heading and pitch LOS angles generators in a cascaded configuration with three feedback controllers guarantees path following of underwater vessels in the presence of constant irrotational currents acting in any direction of the inertial frame.

9.3.2. The Surge, Pitch and Yaw Controllers

According to (9.10), the relative surge velocity of the vessel u_r should follow the desired value $u_{rd}(t) = U_{rd}$. Therefore, to track $u_{rd}(t)$ the following controller is used:

$$\tau_u = -F_{u_r}(v_r, w_r, r, q) + \frac{d_{11}}{m_{11}} u_{rd} + \dot{u}_{rd} - k_{u_r}(u_r - u_{rd}). \tag{9.12}$$

The gain $k_{u_r} > 0$ is constant. The controller (9.12) is a feedback linearizing P-controller that in a closed loop configuration with (9.5f) guarantees exponential tracking of $u_{rd}(t)$. Damping is not canceled to guarantee some robustness with respect to model uncertainties.

The following controller is used to track the desired pitch angle $\theta_d \triangleq \theta_{ILOS}$:

$$\tau_q = -F_q(\theta, u_r, w_r, q) + \ddot{\theta}_d - k_\theta(\theta - \theta_d) - k_q(\dot{\theta} - \dot{\theta}_d), \tag{9.13}$$

where $k_\theta, k_q > 0$ are constant gains. The controller (9.13) is a feedback linearizing PD controller that in a closed loop configuration with (9.5d)-(9.5i) makes sure that θ and q exponentially track θ_d and $\dot{\theta}_d$ respectively.

Finally, the following feedback linearizing PD-controller is used to track the desired yaw angle $\psi_d \triangleq \psi_{ILOS}$:

$$\tau_r = -F_r(u_r, v_r, r) - q\sin(\theta)\dot{\psi} + \cos(\theta)\Big[\ddot{\psi}_d - k_\psi(\psi - \psi_d) - k_r(\dot{\psi} - \dot{\psi}_d)\Big]. \tag{9.14}$$

The parameters $k_\psi, k_r > 0$ are constant gains and the yaw control law (9.14), in a closed loop configuration with (9.5e)-(9.5j), guarantees exponential convergence of ψ and $\dot{\psi}$ to ψ_d and $\dot{\psi}_d$ respectively.

Remark 9.8. The closed loop system given by the controller (9.14) in combination with (9.5e)-(9.5j) does not have singularities since the limits of $\cos(\theta)/\cos(\theta)$ and $\cos^2(\theta)/\cos^2(\theta)$ for $\theta \to \pi/2 + k\pi$ exist and equal 1 (see for instance [25]).

Remark 9.9. The controllers (9.12), (9.13) and (9.14) are feedback linearizing controllers, hence if the model suffers from high uncertainty other approaches should be considered. It can be seen in the following stability analysis that any control law that gives UGES or UGAS and ULES of the fully actuated dynamics will give the derived stability result.

9.4. Stability Conditions

This section presents the main result of this chapter, including the conditions under which the proposed control law achieves (9.6-9.10). The abbreviations $X_a^{U_{rd}} \triangleq X_a(U_{rd})$ and $Y_a^{U_{rd}} \triangleq Y_a(U_{rd})$ are used, where $a \in \{v_r, w_r\}$.

Theorem 9.1. *Given an underactuated underwater vehicle described by the dynamical system* (9.5)*. If Assumptions 9.3-9.5 hold and if the look-ahead distances* Δ_y*,* Δ_z *satisfy the conditions:*

$$\Delta_y > \frac{|X_{v_r}^{U_{rd}}|}{|Y_{v_r}^{U_{rd}}|}\left[\frac{5}{4}\frac{\Gamma_{\max} + V_{\max} + \sigma_y}{\Gamma_{\inf} - V_{\max} - \sigma_y} + 1\right], \tag{9.15}$$

$$\Delta_z > \frac{|X_{w_r}^{U_{rd}}|}{|Y_{w_r}^{U_{rd}}|}\rho(\sigma_z)\left[\frac{5}{4}\frac{U_{rd} + V_{\max} + \sigma_z}{U_{rd} - V_{\max} - \sigma_z} + 1\right], \tag{9.16}$$

where the integral gains σ_y*,* σ_z *satisfy:*

$$0 < \sigma_y < \Gamma_{\inf} - V_{\max}, \tag{9.17}$$

$$0 < \sigma_z < U_{rd} - V_{\max} - \frac{5}{2}\left|\frac{Z_{w_r}}{Y_{w_r}^{U_{rd}}}\right|, \tag{9.18}$$

then the controllers (9.12-9.14) and the guidance law (9.11) *with* $u_{rd}(t) = U_{rd}$ *guarantee achievement of the control objectives (9.6-9.10). The control objectives (9.8-9.9) are fulfilled with* $\psi_{ss} = -\tan^{-1}\left(V_y/\sqrt{\Gamma(s)^2 - V_y^2}\right)$ *and* $\theta_{ss} = \tan^{-1}(s)$*.*

Remark 9.10. The constant s is defined in Section 9.5. The constants $\Gamma_{\max}$, $\Gamma_{\inf}$ and the functions $\Gamma(s)$, $\rho(\sigma_z)$ are given in (9.19-9.21). It is shown in Section 9.5 that s is such that $\Gamma_{\inf} < \Gamma(s) \leq \Gamma_{\max}$. Notice that $\Gamma_{\inf} > 0$ as long as Assumption 9.5 is satisfied.

$$\Gamma(s) \triangleq U_{rd}\frac{1}{\sqrt{s^2 + 1}} - \frac{Z_{w_r}}{Y_{w_r}^{U_{rd}}}\frac{s^2}{s^2 + 1}, \tag{9.19}$$

$$\Gamma_{\inf} \triangleq \frac{3}{5}\left[U_{rd} - \left|\frac{Z_{w_r}}{Y_{w_r}^{U_{rd}}}\right|\right], \quad \Gamma_{\max} \triangleq U_{rd}, \tag{9.20}$$

$$\rho(\sigma_z) \triangleq \frac{U_{rd} - V_{\max} - \sigma_z}{U_{rd} - V_{\max} - \sigma_z - \frac{5}{2}\left|\frac{Z_{w_r}}{Y_{w_r}^{U_{rd}}}\right|}. \tag{9.21}$$

9.5. Proof of Theorem 9.1

The actuated dynamics (9.5f), (9.5i) and (9.5j) of the AUV in closed loop configuration with the controllers (9.12-9.14) are considered first. Given the vector $\boldsymbol{\zeta} \triangleq [\tilde{u}_r, \tilde{\theta}, \dot{\tilde{\theta}}, \tilde{\psi}, \dot{\tilde{\psi}}]^T$ where $\tilde{u}_r \triangleq u_r - U_{rd}$, $\tilde{\theta} \triangleq \theta - \theta_d$, $\dot{\tilde{\theta}} \triangleq \dot{\theta} - \dot{\theta}_d$, $\tilde{\psi} \triangleq \psi - \psi_d$ and $\dot{\tilde{\psi}} \triangleq \dot{\psi} - \dot{\psi}_d$, the dynamics of $\boldsymbol{\zeta}$ are obtained by combining the system equations (9.5d), (9.5e), (9.5f), (9.5i) and (9.5j) with the control laws (9.12-9.14):

$$\dot{\boldsymbol{\zeta}} = \begin{bmatrix} -k_{u_r} - \frac{d_{11}}{m_{11}} & 0 & 0 & 0 & 0 \\ 0 & 0 & 1 & 0 & 0 \\ 0 & -k_\theta & -k_q & 0 & 0 \\ 0 & 0 & 0 & 0 & 1 \\ 0 & 0 & 0 & -k_\psi & -k_r \end{bmatrix} \boldsymbol{\zeta} \triangleq \boldsymbol{\Sigma}\boldsymbol{\zeta}. \tag{9.22}$$

The system (9.22) is linear and time-invariant. Furthermore, the gains k_{u_r}, k_θ, k_q, k_ψ, k_r and the term $\frac{d_{11}}{m_{11}}$ are all strictly positive. Therefore the matrix $\boldsymbol{\Sigma}$ is Hurwitz and the origin $\boldsymbol{\zeta} = \mathbf{0}$ of (9.22) is UGES. Hence, $u(t) \to u_{rd}(t)$, $\theta(t) \to \theta_d(t)$ and $\psi(t) \to \psi_d(t)$ exponentially. As a result, the control goal (9.10) is achieved with exponential converging properties in any ball of initial conditions.

The dynamics of the cross track error z and the relative heave velocity w_r are analyzed next. The $z - w_r$ subsystem is obtained combining (9.5c), (9.5h) and (9.11b):

$$\dot{z}_{\text{int}} = \frac{\Delta_z z}{(z + \sigma_z z_{\text{int}})^2 + \Delta_z^2}. \tag{9.23}$$

$$\dot{z} = -u_r \sin(\tilde{\theta} + \theta_d) + w_r \cos(\tilde{\theta} + \theta_d) + V_z, \tag{9.24}$$

$$\dot{w}_r = X_{w_r}(\tilde{u}_r + U_{rd})(\dot{\tilde{\theta}} + \dot{\theta}_d) + Y_{w_r}(\tilde{u}_r + U_{rd})w_r + Z_{w_r}\sin(\tilde{\theta} + \theta_d). \tag{9.25}$$

The calculation of the equilibrium point of the system (9.23-9.25) on the manifold $\boldsymbol{\zeta} = \mathbf{0}$ yields the following equation:

$$s\sqrt{s^2+1} = \frac{V_z}{U_{rd}}s^2 - \frac{Z_{w_r}}{U_{rd}Y_{w_r}^{U_{rd}}}s + \frac{V_z}{U_{rd}}, \tag{9.26}$$

where $s \triangleq \sigma_z z_{\text{int}}^{\text{eq}}/\Delta_z$ and $z_{\text{int}}^{\text{eq}}$ is the value of z_{int} at equilibrium. It has to be shown that (9.26) has a unique real solution to have a single equilibrium point. The following Lemma gives the sufficient conditions for (9.26) to have a unique real solution:

Lemma 9.1. *If Assumption 9.5 holds then* (9.26) *has exactly one real solution* $s = \sigma_z z_{\text{int}}^{\text{eq}}/\Delta_z$.

Proof. The proof of Lemma 9.1 is given in Appendix 9.B. □

At equilibrium $z^{\text{eq}} = 0$ while $z_{\text{int}}^{\text{eq}}$ and w_r^{eq} are constant values where $z_{\text{int}}^{\text{eq}}$ is the unique solution of (9.26) and w_r^{eq} relates to $z_{\text{int}}^{\text{eq}}$ as:

$$w_r^{\text{eq}} = U_{rd}\frac{\sigma_z z_{\text{int}}^{\text{eq}}}{\Delta_z} - V_z\sqrt{\left(\frac{\sigma_z z_{\text{int}}^{\text{eq}}}{\Delta_z}\right)^2 + 1}. \tag{9.27}$$

The pitch angle held by the AUV at steady state is then $\theta_{ss} = \tan^{-1}(s) = \tan^{-1}(\sigma_z z_{\text{int}}^{\text{eq}}/\Delta_z)$.

Before proceeding with the analysis of the system (9.23-9.25) another consequence of Assumption 9.5 is considered: as long as Assumption 9.5 is satisfied, the following bound holds:

$$\left|\frac{V_z}{U_{rd}}s^2 - \frac{Z_{w_r}}{U_{rd}Y_{w_r}^{U_{rd}}}s + \frac{V_z}{U_{rd}}\right| < \frac{1}{2}\left(s^2 + |s| + 1\right). \tag{9.28}$$

The upper bound $s_{\text{sup}} > |s|$ can be then calculated by equalizing the bound (9.28) to $|s\sqrt{s^2+1}|$:

$$\left|s_{\text{sup}}\sqrt{{s_{\text{sup}}}^2 + 1}\right| = \frac{1}{2}\left({s_{\text{sup}}}^2 + |s_{\text{sup}}| + 1\right). \tag{9.29}$$

Solving (9.29) for $s_{\text{sup}} > 0$ gives the only accepted real positive solution $s_{\text{sup}} \approx 1.13$. Therefore, it is straightforward to verify that $\Gamma_{\text{inf}} < \Gamma(s_{\text{sup}}) \leq \Gamma(s)$, where Γ_{inf} and $\Gamma(s)$ were defined in (9.19-9.20).

At this point a new set of variables is introduced to move the equilibrium of (9.23-9.25) to the origin:

$$e_{z1} \triangleq z_{\text{int}} - z_{\text{int}}^{\text{eq}},\ e_{z2} \triangleq z + \sigma_z e_{z1},\ e_{z3} \triangleq w_r - w_r^{\text{eq}}. \tag{9.30}$$

Substituting (9.11a) for θ_d, factorizing the result with respect to $\boldsymbol{\zeta}$ and applying the transformation (9.30) leads to the following transformed interconnected dynamics:

$$\begin{bmatrix} \dot{e}_{z1} \\ \dot{e}_{z2} \\ \dot{e}_{z3} \end{bmatrix} = \boldsymbol{A}_1(e_{z2})\begin{bmatrix} e_{z1} \\ e_{z2} \\ e_{z3} \end{bmatrix} + \boldsymbol{B}_1(e_{z2})f(e_{z2}) + \boldsymbol{H}_1(z, z_{\text{int}}, \theta_d, w_r, \boldsymbol{\zeta})\boldsymbol{\zeta}, \tag{9.31a}$$

$$\dot{\boldsymbol{\zeta}} = \boldsymbol{\Sigma}\boldsymbol{\zeta}. \tag{9.31b}$$

The matrix $\boldsymbol{H}_1$ contains all the terms vanishing at $\boldsymbol{\zeta} = \boldsymbol{0}$. $\boldsymbol{A}_1(e_{z2})$ is given in (9.81) of Appendix 9.A while $\boldsymbol{B}_1(e_{z2})$, $\boldsymbol{H}_1(z, z_{\text{int}}, \theta_d, w_r, \boldsymbol{\zeta})$ and $f(e_{z2})$ are:

$$\boldsymbol{B}_1(e_{z2}) \triangleq \begin{bmatrix} 0 \\ V_z \\ \frac{\Delta_z X_{w_r}^{U_{rd}} V_z}{(e_{z2}+\sigma_z z_{\text{int}}^{\text{eq}})^2+\Delta_z^2} - Z_{w_r} \frac{s}{\sqrt{s^2+1}} \end{bmatrix}, \tag{9.32}$$

$$\boldsymbol{H}_1(z, z_{\text{int}}, \theta_d, w_r, \boldsymbol{\zeta}) \triangleq \begin{bmatrix} 0 & 0 \\ 1 & 0 \\ \frac{\Delta_z X_{w_r}(\tilde{u}_r+U_{rd})}{(e_{z2}+\sigma_z z_{\text{int}}^{\text{eq}})^2+\Delta_z^2} & 1 \end{bmatrix} \begin{bmatrix} \boldsymbol{h}_z^T \\ \boldsymbol{h}_{w_r}^T \end{bmatrix}, \tag{9.33}$$

$$f(e_{z2}) = 1 - \frac{\sqrt{(\sigma_z z_{\text{int}}^{\text{eq}})^2 + \Delta_z^2}}{\sqrt{(e_{z2} + \sigma_z z_{\text{int}}^{\text{eq}})^2 + \Delta_z^2}}. \tag{9.34}$$

The expression of $f(e_{z2})$ given in (9.34) has been obtained using (9.26) and (9.27). The vectors $\boldsymbol{h}_z(\theta_d, w_r, \boldsymbol{\zeta})$ and $\boldsymbol{h}_{w_r}(z, z_{\text{int}}, \theta_d, w_r, \boldsymbol{\zeta})$ are given in Appendix 9.A and the following bound holds for $f(e_{z2})$:

$$|f(e_{z2})| \leq \frac{|e_{z2}|}{\sqrt{(e_{z2} + \sigma_z z_{\text{int}}^{\text{eq}})^2 + \Delta_z^2}}. \tag{9.35}$$

One can prove that (9.35) holds by squaring both sides of the inequality two consecutive times.

The system (9.31) is a cascaded system, where the linear UGES system (9.31b) perturbs the dynamics (9.31a) through the interconnection matrix $\boldsymbol{H_1}$. The next lemma states the stability properties of the cascade (9.31).

Lemma 9.2. *Under the conditions of Theorem 9.1, the origin of the system* (9.31) *is UGAS and ULES.*

Proof. The proof follows along the line of the proof of Lemma 5.2 given in Appendix 5.B of Chapter 5. Consider the nominal system

$$\begin{bmatrix} \dot{e}_{z1} \\ \dot{e}_{z2} \\ \dot{e}_{z3} \end{bmatrix} = \boldsymbol{A}_1(e_{z2}) \begin{bmatrix} e_{z1} \\ e_{z2} \\ e_{z3} \end{bmatrix} + \boldsymbol{B}_1(e_{z2}) f(e_{z2}), \tag{9.36}$$

and the quadratic Lyapunov function candidate (LFC)

$$V = \frac{1}{2}\sigma_z^2 e_{z1}^2 + \frac{1}{2}e_{z2}^2 + \frac{1}{2}\mu e_{z3}^2, \quad \mu > 0. \tag{9.37}$$

The time-derivative of V is:

$$\begin{aligned}
\dot{V} = &-\frac{\sigma_z^3\Delta_z}{(e_{z2}+\sigma_z z_{\text{int}}^{\text{eq}})^2+\Delta_z^2}e_{z1}^2 - \Bigg[-\sigma_z\Delta_z \\
&+ U_{rd}\sqrt{(e_{z2}+\sigma_z z_{\text{int}}^{\text{eq}})^2+\Delta_z^2}\Bigg]\frac{e_{z2}^2}{(e_{z2}+\sigma_z z_{\text{int}}^{\text{eq}})^2+\Delta_z^2} \\
&+ \frac{\Delta_z}{\sqrt{(e_{z2}+\sigma_z z_{\text{int}}^{\text{eq}})^2+\Delta_z^2}}e_{z2}e_{z3} + V_z f(e_{z2})e_{z2} \\
&- \mu\Bigg[-Y_{w_r}^{U_{rd}} - \frac{\Delta_z^2 X_{w_r}^{U_{rd}}}{((e_{z2}+\sigma_z z_{\text{int}}^{\text{eq}})^2+\Delta_z^2)^{3/2}}\Bigg]e_{z3}^2 \\
&+ \mu\Bigg[-\frac{sZ_{w_r}}{\sqrt{s^2+1}} + \frac{\Delta_z X_{w_r}^{U_{rd}}V_z}{(e_{z2}+\sigma_z z_{\text{int}}^{\text{eq}})^2+\Delta_z^2}\Bigg]f(e_{z2})e_{z3} \\
&+ \mu\Bigg[-\frac{U_{rd}\Delta_z X_{w_r}^{U_{rd}}}{(e_{z2}+\sigma_z z_{\text{int}}^{\text{eq}})^2+\Delta_z^2} + Z_{w_r} \\
&+ \frac{\sigma_z\Delta_z^2 X_{w_r}^{U_{rd}}}{((e_{z2}+\sigma_z z_{\text{int}}^{\text{eq}})^2+\Delta_z^2)^{3/2}}\Bigg]\frac{e_{z2}e_{z3}}{\sqrt{(e_{z2}+\sigma_z z_{\text{int}}^{\text{eq}})^2+\Delta_z^2}} \\
&- \frac{\mu\sigma_z^2\Delta_z^2 X_{w_r}^{U_{rd}}}{((e_{z2}+\sigma_z z_{\text{int}}^{\text{eq}})^2+\Delta_z^2)^2}e_{z1}e_{z3}.
\end{aligned} \tag{9.38}$$

The variables $\bar{e}_{z1} \triangleq e_{z1}/\sqrt{(e_{z2}+\sigma_z z_{\text{int}}^{\text{eq}})^2+\Delta_z^2}$ and $\bar{e}_{z2} \triangleq e_{z2}/\sqrt{(e_{z2}+\sigma_z z_{\text{int}}^{\text{eq}})^2+\Delta_z^2}$ are defined to simplify the expression (9.38). This notation together with Assumptions 9.3-9.4 and (9.35) yields the following bound for $\dot{V}$:

$$\dot{V} \leq -W_1(|\bar{e}_{z1}|,|e_{z3}|) - W_2(|\bar{e}_{z2}|,|e_{z3}|), \tag{9.39}$$

$$\begin{aligned}
W_1 \triangleq\ &\sigma_z^3\Delta_z|\bar{e}_{z1}|^2 - \mu\frac{\sigma_z^2|X_{w_r}^{U_{rd}}|}{\Delta_z}|\bar{e}_{z1}||e_{z3}| \\
&+ \mu\eta\left(|Y_{w_r}^{U_{rd}}| - \frac{|X_{w_r}^{U_{rd}}|}{\Delta_z}\right)|e_{z3}|^2,
\end{aligned} \tag{9.40}$$

$$W_2 \triangleq \Delta_z \begin{bmatrix} |\bar{e}_{z2}| & |e_{z3}| \end{bmatrix} \begin{bmatrix} \beta & -\alpha \\ -\alpha & \frac{\alpha(2\alpha-1)}{\beta} \end{bmatrix} \begin{bmatrix} |\bar{e}_{z2}| \\ |e_{z3}| \end{bmatrix}, \tag{9.41}$$

where $0 < \eta < 1$, $\beta \triangleq U_{rd} - V_{\max} - \sigma_z$ and α is given by the expression:

$$\alpha \triangleq (1-\eta)\frac{(U_{rd}-V_{\max}-\sigma_z)(\Delta_z|Y_{w_r}^{U_{rd}}| - |X_{w_r}^{U_{rd}}|)}{|X_{w_r}^{U_{rd}}|\left(U_{rd}+V_{\max}+\sigma_z+2\Delta_z\frac{|Z_{w_r}|}{|X_{w_r}^{U_{rd}}|}\right)}. \tag{9.42}$$

The parameter μ is chosen as:

$$\mu \triangleq \frac{2\alpha - 1}{\frac{|X^{U_{rd}}_{w_r}|}{\Delta_z^2}(U_{rd} + V_{\max} + \sigma_z) + 2\frac{|Z_{w_r}|}{\Delta_z}}. \tag{9.43}$$

If both W_1 and W_2 are definite positive then $\dot{V}$ is negative definite. Positive definiteness of W_1 is ensured if (9.44) and (9.45) are satisfied:

$$\Delta_z > \frac{|X^{U_{rd}}_{w_r}|}{|Y^{U_{rd}}_{w_r}|}, \tag{9.44}$$

$$\mu < \frac{4\eta\Delta_z^2\left[\Delta_z|Y^{U_{rd}}_{w_r}| - |X^{U_{rd}}_{w_r}|\right]}{\sigma_z|X^{U_{rd}}_{w_r}|}. \tag{9.45}$$

Notice that condition (9.44) is met as long as (9.16) holds. It is straightforward to show that $\eta \geq 1/5$ is a sufficient condition for μ, defined in (9.43), to satisfy (9.45). Therefore, without any loss of generality, η is set to $1/5$.

To guarantee positive definiteness of W_2, β and α must fulfil the inequalities $\beta > 0$ and $\alpha > 1$. Assumption 9.5 and (9.18) make sure that $\beta > 0$ while through some simple manipulation it is easy to check that conditions (9.16) and (9.18) imply $\alpha > 1$. Furthermore, $\alpha > 1$ guarantees $\mu > 0$ as required for V to be positive definite. Therefore under the conditions stated in Theorem 9.1 V, W_1 and W_2 are positive definite and hence, according to standard Lyapunov theory, the origin of the nominal system (9.36) is UGAS. Moreover, the inequality $W \triangleq W_1 + W_2 \geq \bar{\lambda}_1|\bar{e}_{z1}|^2 + \bar{\lambda}_2|\bar{e}_{z2}|^2 + \lambda_3|e_{z3}|^2$ holds in a neighbourhood of the origin for some constants $\bar{\lambda}_1, \bar{\lambda}_2, \lambda_3 > 0$ and thus in any ball $\mathcal{B}_r \triangleq \{|e_{z2}| \leq r\}, r > 0$ the function W can be estimated as $W \geq \lambda_1|e_{z1}|^2 + \lambda_2|e_{z2}|^2 + \lambda_3|e_{z3}|^2$ where $\lambda_i = \bar{\lambda}_i/((r + \sigma_z z^{\text{eq}}_{\text{int}})^2 + \Delta_z^2)$, $i = 1, 2$. This, together with the fact that V is a quadratic function of e_{z1}, e_{z2} and e_{z3}, concludes that (9.36) is also uniformly locally exponentially stable, ULES [82]. Finally, since the perturbing system (9.31b) is UGES and the interconnection matrix $\boldsymbol{H}_1(z, z_{\text{int}}, \theta_d, w_r, \boldsymbol{\zeta})$ can be shown to satisfy $\| \boldsymbol{H}_1 \| \leq \delta_1(\| \boldsymbol{\zeta} \|)(|z| + |z_{\text{int}}| + |w_r|) + \delta_2(\| \boldsymbol{\zeta} \|)$, where $\delta_1(\cdot)$ and $\delta_2(\cdot)$ are some continuous non-negative functions, applying Theorem A.2 and Lemma A.2 it is possible to conclude UGAS and ULES for the cascaded system (9.31). $\square$

According to Lemma 9.2, under the conditions of Theorem 9.1, the origin of the system (9.31) given by $(e_{z1}, e_{z2}, e_{z3}, \boldsymbol{\zeta}) = (0, 0, 0, \mathbf{0})$ is UGAS and ULES. Hence, the control objectives (9.7) and (9.9) are achieved with exponential converging properties with $\theta_{ss} = \theta^*_{ss}$ and $\boldsymbol{\chi} \triangleq [e_{z1}, e_{z2}, e_{z3}, \boldsymbol{\zeta}^T]^T$ is a vector of exponentially converging signals.

Finally, the $y - v_r$ subsystem is considered. The AUV dynamics and kinematics form a cascaded system where (9.31) perturbs the y cross-track error. The $y - v_r$ subsystem is obtained from (9.5b), (9.5g) and (9.11d):

$$\dot{y}_{\text{int}} = \frac{\Delta_y y}{(y + \sigma_y y_{\text{int}})^2 + \Delta_y^2}, \tag{9.46}$$

$$\begin{aligned}\dot{y} = {} & u_r \cos(\tilde{\theta} + \theta_d) \sin(\tilde{\psi} + \psi_d) + v_r \cos(\tilde{\psi} + \psi_d) \\ & + w_r \sin(\tilde{\psi} + \psi_d) \sin(\tilde{\theta} + \theta_d) + V_y,\end{aligned} \tag{9.47}$$

$$\dot{v}_r = X_{v_r}(\tilde{u}_r + U_{rd})(\dot{\tilde{\psi}} + \dot{\psi}_d) \cos(\tilde{\theta} + \theta_d) + Y_{v_r}(\tilde{u}_r + U_{rd}) v_r. \tag{9.48}$$

The equilibrium point of the system (9.46-9.48) on the manifold $\boldsymbol{\chi} = \mathbf{0}$ is:

$$y_{\text{int}}^{\text{eq}} = \frac{\Delta_y}{\sigma_y} \frac{V_y}{\sqrt{\Gamma(s)^2 - V_y^2}}, \quad y^{\text{eq}} = 0, \quad v_r^{\text{eq}} = 0, \tag{9.49}$$

where $\Gamma(s)$ is defined in (9.19). Therefore, a new set of variables is introduced to move the equilibrium point to the origin:

$$e_{y1} \triangleq y_{\text{int}} - y_{\text{int}}^{\text{eq}}, \quad e_{y2} \triangleq y + \sigma_y e_{y1}. \tag{9.50}$$

Substituting (9.11a) and (9.11c) for θ_d and ψ_d, factorizing the result with respect to $\boldsymbol{\chi}$ and moving the equilibrium point to the origin yields the following interconnected dynamics:

$$\begin{bmatrix} \dot{e}_{y1} \\ \dot{e}_{y2} \\ \dot{v}_r \end{bmatrix} = \boldsymbol{A}_2(e_{y2}) \begin{bmatrix} e_{y1} \\ e_{y2} \\ v_r \end{bmatrix} + \boldsymbol{B}_2(e_{y2}) g(e_{y2}) + \boldsymbol{H}_2(y, y_{\text{int}}, \theta_d, \psi_d, v_r, \boldsymbol{\chi})\boldsymbol{\chi}, \tag{9.51a}$$

$$\dot{\boldsymbol{\chi}} = \begin{bmatrix} \boldsymbol{A}_1(e_{z2}) & \boldsymbol{H}_1(z, z_{\text{int}}, \theta_d, w_r, \boldsymbol{\zeta}) \\ \mathbf{0} & \boldsymbol{\Sigma} \end{bmatrix} \boldsymbol{\chi} + \begin{bmatrix} \boldsymbol{B}_1(e_{z2}) \\ \mathbf{0} \end{bmatrix} f(e_{z2}). \tag{9.51b}$$

The term $\boldsymbol{H}_2$ contains all the terms vanishing at $\boldsymbol{\chi} = \mathbf{0}$. $\boldsymbol{A}_2(e_{y2})$ is given in (9.82) of Appendix 9.A while $\boldsymbol{B}_2(e_{y2})$ and $\boldsymbol{H}_2(y, y_{\text{int}}, \theta_d, \psi_d, v_r, \boldsymbol{\chi})$ are defined as:

$$\boldsymbol{B}_2(e_{y2}) \triangleq \begin{bmatrix} 0 \\ V_y \\ -\frac{1}{\sqrt{s^2+1}} \frac{\Delta_y X_{v_r}^{U_{rd}} V_y}{(e_{y2} + \sigma_y y_{\text{int}}^{\text{eq}})^2 + \Delta_y^2} \end{bmatrix}, \tag{9.52}$$

$$\boldsymbol{H}_2(y, y_{\text{int}}, \theta_d, \psi_d, v_r, \boldsymbol{\chi}) \triangleq \begin{bmatrix} 0 & 0 \\ 1 & 0 \\ -\frac{\Delta_y X_{v_r}(\tilde{u}_r + U_{rd}) \cos(\tilde{\theta} + \theta_d)}{(e_{y2} + \sigma_y y_{\text{int}}^{\text{eq}})^2 + \Delta_y^2} & 1 \end{bmatrix} \begin{bmatrix} \boldsymbol{h}_y^T \\ \boldsymbol{h}_{v_r}^T \end{bmatrix}. \tag{9.53}$$

The function $g(e_{y2})$ is identical to $f(e_{z2})$, i.e. $g(\cdot) \equiv f(\cdot)$, and thus the same bound (9.35) applies. The vectors $\boldsymbol{h}_y(\theta_d, \psi_d, v_r, \boldsymbol{\chi})$ and $\boldsymbol{h}_{v_r}(y, y_{\text{int}}, \theta_d, \psi_d, v_r, \boldsymbol{\chi})$ are given in Appendix 9.A.

The system (9.51) is a cascaded system, where the UGAS and ULES system (9.51b) perturbs the dynamics (9.51a) through $\boldsymbol{H_2}$. The next lemma states the stability properties of (9.51).

Lemma 9.3. *Under the conditions of Theorem 9.1, the origin of the system* (9.51) *is UGAS and ULES.*

Proof. The nominal system:

$$\begin{bmatrix} \dot{e}_{y1} \\ \dot{e}_{y2} \\ \dot{v}_r \end{bmatrix} = \boldsymbol{A}_2(e_{y2}) \begin{bmatrix} e_{y1} \\ e_{y2} \\ v_r \end{bmatrix} + \boldsymbol{B}_2(e_{y2}) g(e_{y2}), \tag{9.54}$$

is equivalent to the system considered in Lemma 9.2. The conditions (9.15) and (9.17) on Δ_y and σ_y are equivalent to (9.16) and (9.18) on Δ_z and σ_z. However, there are two minor differences: the absence of the gravity term Z_{w_r} and the presence of the unknown constants $\Gamma(s)$ and s. Nevertheless, the bounds $0 < \Gamma_{\text{inf}} < \Gamma(s) \leq \Gamma_{\text{max}}$ from (9.19-9.20), $1/\sqrt{s^2+1} < 1$ and $|s|/\sqrt{s^2+1} < 1$ are available. Hence, by repeating the first part of the proof of Lemma 9.2 it follows that the nominal system (9.54) is UGAS and ULES.

The perturbing system (9.51b) is UGAS and ULES, as proved in Lemma 9.2. Furthermore the interconnection matrix $\boldsymbol{H}_2(y, y_{\text{int}}, \theta_d, \psi_d, v_r, \boldsymbol{\chi})$ can be shown to satisfy $\| \boldsymbol{H}_2 \| \leq \delta_3(\| \boldsymbol{\chi} \|)(|y| + |y_{\text{int}}| + |v_r|) + \delta_4(\| \boldsymbol{\chi} \|)$, where $\delta_3(\cdot)$ and $\delta_4(\cdot)$ are some continuous non-negative functions. Therefore, Theorem A.2 and Lemma A.2 conclude UGAS and ULES for the cascaded system (9.51). □

According to Lemma 9.3, under the conditions of Theorem 9.1, the origin of the system (9.51), given by $(e_{y1}, e_{y2}, v_r, \boldsymbol{\chi}) = (0, 0, 0, \boldsymbol{0})$, is UGAS and ULES. Therefore, the control objectives (9.6) and (9.8) are achieved with exponential converging properties and $\psi_{ss} = -\tan^{-1}\left(V_y / \sqrt{\Gamma(s)^2 - V_y^2}\right)$.

Remark 9.11. The values $y_{\text{int}}^{\text{eq}}$ and $z_{\text{int}}^{\text{eq}}$ make sure that, at equilibrium, the AUV holds $\theta_{ss} = \tan^{-1}(\sigma_z z_{\text{int}}^{\text{eq}} / \Delta_z)$ and $\psi_{ss} = -\tan^{-1}(\sigma_y y_{\text{int}}^{\text{eq}} / \Delta_y)$ which is the only possible attitude that guarantees path following and compensates for the ocean current disturbances.

Remark 9.12. The lower bounds (9.15) and (9.16) are expected and has a clear physical interpretation: short look-ahead distances $\Delta_y, \Delta_z > 0$ make the vessel overshoot the target and thus causes instability as shown in Chapter 4.

9.6. Simulations

In this section results from numerical simulations are presented. The ILOS guidance laws (9.11) in a cascaded configuration with the surge, pitch and yaw controllers (9.12-9.14) are applied to the underactuated LAUV vehicle [126]. A short description of the LAUV is given in Section 9.7. First, simulations are run to confirm that the ILOS guidance (9.11) makes the AUV follow a straight line in a 3D environment. Furthermore, in order to have simulation results that can be directly compared with the experiments and since most of underwater operations involve horizontal path following or constant altitude motion, results from planar way-point following simulations are shown as well. The model of the LAUV from Section B.3 of Appendix B is used. In particular, following the requirements of Section 9.1 and given the low speed motion of the AUV, only linear damping is considered and lift is not taken into account. The rudder coefficients of the $\boldsymbol{B}$ matrix are calculated as done in [85] for the desired constant surge relative velocity U_{rd} set in the simulation. The forward thrust $T_u \in [-T_u^{\max}(u_r), T_u^{\max}(u_r)]$ is dynamically saturated with saturation limits given by $T_u^{\max} = T_{nn} n_{\max}^2 - T_{un} n_{\max} u_r$. Here, $n_{\max} = 2500/60$ [rps], $T_{nn} = 0.0096$ and $T_{un} = 0.1260$ are taken from [85]. The maximum rudder angle is 25 [deg] and their maximum turning rate is set to 10 [deg/s].

9.6.1. ILOS for Straight Line Path Following in 3D

The objective is to make the AUV follow the path $\mathcal{P}$ with a desired surge relative velocity $U_{rd} = 1.9$ [m/s] in presence of ocean currents acting in any direction of the space. The intensity of the current is $|\boldsymbol{V}_c| = 0.2$ [m/s] and its direction is randomly generated. In this case its components are $V_x = 0.07$ [m/s], $V_y = -0.16$ [m/s] and $V_z = 0.10$ [m/s], having -66.7 [deg] of azimuth and 30.8 [deg] of elevation in the North-East-Down (NED) frame. Thus, Assumption 9.3 is fulfilled with $V_{\max} = 0.21$ [m/s] and it can be verified that Assumption 9.4 is satisfied with $Y_{v_r}^{\min} = 0.67$ [s^{-1}] and $Y_{w_r}^{\min} = 0.67$ [s^{-1}]. Notice that, given the bound $V_{\max} = 0.21$ [m/s], the desired relative velocity $U_{rd} = 1.9$ [m/s] satisfies Assumption 9.5.

The values for the guidance law look-ahead distances and integral gains are chosen to satisfy (9.15-9.16) and (9.17-9.18), and are $\Delta_y = 4$ [m], $\sigma_y = 0.2$ [m/s] for the horizontal plane and $\Delta_z = 8$ [m], $\sigma_z = 0.2$ [m/s] for the vertical plane. The controllers (9.12-9.14) are implemented with the following gains: $k_{u_r} = 1$, $k_\theta = 1$, $k_q = 2$, $k_\psi = 1$ and $k_r = 2$.

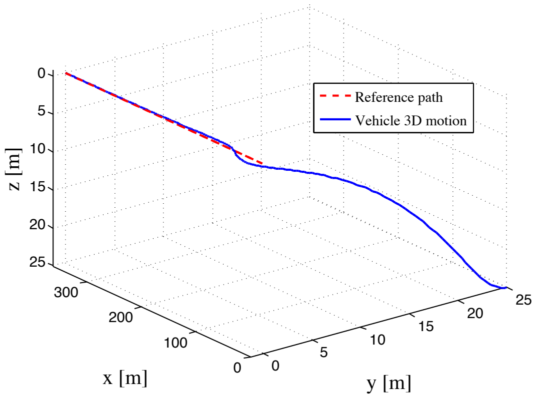

(a) Simulation of convergence and path following in 3D of the LAUV in presence of constant irrotational ocean currents.

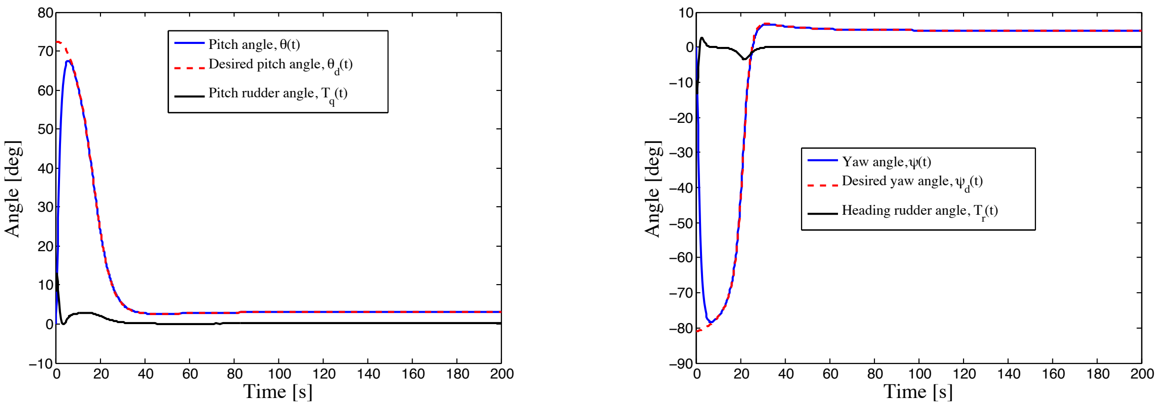

(b) Pitch angle $\theta(t)$ of the LAUV from simulations. Notice the vertical side-slip angle $\theta_{ss} \approx 3.2$ [deg] in steady state.

(c) Yaw angle $\psi(t)$ of the LAUV from simulations. Notice the horizontal side-slip angle $\psi_{ss} \approx 4.8$ [deg] in steady state.

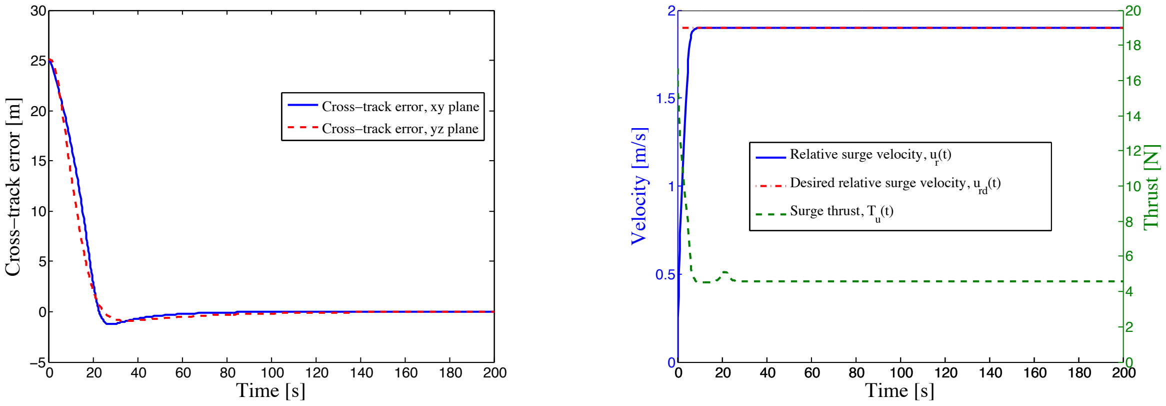

(d) Cross track errors $y(t)$ and $z(t)$ of the LAUV from simulations: convergence is faster in the horizontal plane since $\Delta_z > \Delta_y$.

(e) Relative surge velocity $u_r(t)$ and surge thrust $T_u(t)$ of the LAUV from simulations. Some dynamic thrust saturation is visible during the transient phase.

Figure 9.2.: Simulation results for $\Delta_y = 4$ [m], $\Delta_z = 8$ [m] and $\sigma_y = \sigma_z = 0.2$ [m/s].

The value for k_{u_r} is chosen to give a time constant of 1 [s] for the $\tilde{u}_r$ first order closed loop system. The values chosen for k_θ, k_q k_ψ and k_r make the $\tilde{\theta}$ and $\tilde{\psi}$ second order closed loop systems critically damped with $\omega_n = 1$ [rad/s] and $\zeta = 1$. The pitch and yaw closed loop systems are made critically damped to have the fastest possible response without overshoots.

The vehicle is given an initial cross track error of 25 [m] in both the horizontal and vertical directions, and initially holds zero relative velocity. Its surge axis is parallel to the desired path $\mathcal{P}$. Figures 9.2a and 9.2d show how the underactuated vehicle successfully converges to and follows the path $\mathcal{P}$ in the NED frame. The pitch and yaw angles of the AUV are given in Figures 9.2b and 9.2c where it is shown that the AUV holds non-zero pitch and yaw angles while on path to compensate for the ocean current acting in the horizontal and vertical planes. At steady state the pitch side-slip angle is $\theta_{ss} \approx 3.2$ [deg] while the yaw side-slip angle is $\psi_{ss} \approx 4.8$ [deg]. Figures 9.2b and 9.2c present the pitch and yaw rudder angles as well. The performance of the speed controller (9.12) is shown in Figure 9.2e, where the surge thrust $T_u(t)$ is also plotted. The plotted results show that choosing the guidance law parameters according to the criteria (9.15-9.18) gives smooth convergence and does not overload the controllers (9.12-9.14). Notice that a shorter look-ahead distance in the horizontal plane Δ_y compared to Δ_z makes convergence in the xy plane faster.

9.6.2. ILOS for Planar Way-Point Following

The way-point following simulations involve 2D planar motion only and given the shallow waters where the tests were carried out, the current is assumed horizontal, i.e. its vertical component is $V_z = 0$. Therefore, simulations are run with the vertical ILOS (9.11a-9.11b) acting as a depth controller with $\sigma_z = 0$, while the horizontal ILOS (9.11c-9.11d) makes the vehicle converge to the straight lines connecting the way-points. Therefore, the bounds (9.15-9.17) become:

$$\Delta_y > \frac{|X_{v_r}^{U_{rd}}|}{|Y_{v_r}^{U_{rd}}|}\left[\frac{5}{4}\frac{U_{rd}+V_{\max}+\sigma_y}{U_{rd}-V_{\max}-\sigma_y}+1\right], \tag{9.55}$$

$$\Delta_z > \frac{|X_{w_r}^{U_{rd}}|}{|Y_{w_r}^{U_{rd}}|}\frac{2U_{rd}}{U_{rd}-|Z_{w_r}/Y_{w_r}^{U_{rd}}|}, \tag{9.56}$$

$$0 < \sigma_y < U_{rd} - V_{\max}, \tag{9.57}$$

where Assumption 9.5 can be relaxed to $U_{rd} > \max\{V_{\max}, \, |Z_{w_r}/Y_{w_r}^{U_{rd}}|\}$. The values for the guidance law look-ahead distances and integral gain are in this case chosen to satisfy (9.55-9.57), and are $\Delta_y = 4$ [m], $\Delta_z = 4$ [m] and $\sigma_y = 0.5$ [m/s]. The velocity $U_{rd} = 1.2$ [m/s] and satisfies $U_{rd} > \max\{V_{\max}, |Z_{w_r}/Y_{w_r}^{U_{rd}}|\}$ with $V_{\max} = 0.2$ [m/s]. The controllers (9.12-9.14) are implemented with the same gains as in Section 9.6.1. A switching system that turns on the horizontal ILOS integrator exclusively when the AUV is located within a certain distance from the desired path is implemented to make the simulations resemble the tests even more. This is done not to have too much integral error and hence to avoid overshoots. The corridor in which the integral action is turned on is 3 [m] wide and is centered around the desired straight path. Moreover, the LOS used outside this corridor has a horizontal look-ahead distance $\Delta_y = 5.6$ [m]. A longer Δ_y is used compared to the in-corridor situation to make the tested ILOS guidance scheme comparable in its gains to the vector filed guidance law from [100] tested on the same day.

It is straightforward to show mathematically through Lemma 9.2 that a LOS guidance without integral action in presence of current will not make the vehicle converge to the path. It will instead make the vehicle hold a constant offset with respect to it and hence move along a parallel line if $U_{rd} > V_{\max}$. This steady state offset depends on the choice of the look-ahead distance, the magnitude of the current and the AUV surge relative velocity. Its maximum expected value is found from 9.5b to be:

$$E_{\text{eq}}^{\max} = \Delta_y \frac{V_{\max}}{\sqrt{U_{rd}^2 - V_{\max}^2}}. \tag{9.58}$$

This offset should be smaller then half of the corridor width to make sure that the vehicle does not enter the steady state condition before the integral action turns on. For the case above, with $U_{rd} = 1.2$ [m/s], $\Delta_y = 5.6$ [m] and $V_{\max} = 0.2$ [m/s], the maximum expected offset is 0.95 [m]. This is clearly below the 1.5 [m] distance from the path that triggers the integrator on. Therefore, the LOS guidance with $\Delta_y = 5.6$ [m] will make the AUV enter the 3 [m] wide corridor.

Finally, a way-point switching system based on a circle of acceptance algorithm is employed [52]. The radius of the way-point acceptance circle is set to 5 [m] as it was done in the experiments. The simulation procedure resembles the test runs shown in Section 9.7 and requires the vehicle to move along an 8 shaped path to exhibit the transient response and the steady-state behavior of the ILOS guidance system. An 8 shaped path is used since it contains a complete set of port/starboard maneuvers to test the AUV performance and is defined by 6 way-points. The way-points are located 40 [m] from each other with the longest legs measuring 80 [m] in length. They are placed as shown in Figures 9.4a and 9.4b. This configuration makes the vehicle hold 4 different courses: -170 [deg], 100 [deg], 10 [deg] and -80 [deg]. The desired depth is set to 3 [m] and the vehicle is initially at rest on the surface with a heading of 180 [deg]. The ocean current is set to $V_x = -0.15$ [m/s] and $V_y = 0.04$ [m/s], and equals the drift of the vehicle measured before the test runs shown in Section 9.7. Figures 9.4a, 9.4c and 9.4e show how the vehicle successfully converges to the paths defined by the way-points and side-slips to compensate for the disturbances.

9.7. Experiments

In this section results from field experiments are presented. The LAUV vehicle was used as a test platform and the sea trials were carried in the sheltered waters at the entrance of the Leixões seaport near the city of Porto in Portugal. First, a description of the LAUV is given and then the results from the experiments are presented and discussed. Weather conditions on the test day were good and a tidal change from high to law was reported at the time when the trials were carried out. The resulting tidal current is in accordance with the drift of the vehicle of -0.15 [m/s] North and 0.04 [m/s] East measured before the test run. Notice that tidal changes, fresh water from Rio Leça and the relatively small size of the bay suggest that the local current may vary in space and time.

Figure 9.3.: The LAUV vehicle.

9.7.1. Vehicle description

The Light Autonomous Underwater Vehicle (LAUV) system has been developed and designed by the Laboratório de Sistemas e Tecnologia Subaquática (LSTS) from the University of Porto in cooperation with OceanScan-MST Lda. The LAUV is shown in Figure 9.3 and is 1.1 [m] long and 0.30 [m] wide. It is classified as a 'One-man portable AUV' since it can be deployed and controlled by a single operator. The hull of the vehicle is made of different materials to make the AUV weight less then 20 [kg] and at the same time achieve 100 [m] of maximum rated depth. Thrust is provided by a brush-less DC motor magnetically coupled to a 3-bladed propeller capable of providing a maximum water speed of approximately 2 [m/s]. The permanent magnetic coupling physically separates the dry motor shaft from the wet rotor attached to the propeller. Steering is provided by four independent fins directly actuated by four high-torque DC servos. A set of 546 [Wh] rechargeable lithium-ion batteries guarantees $6-8$ [h] of continuous operations at a speed of 1.4 [m/s], depending on the vehicle configuration. The LAUV is equipped with on board electronics and sensors. In particular, the control and navigation computer has a low power PC104 CPU and a high speed solid state disk. A Linux based operative system runs the DUNE navigation software that operates the vehicle [85]. Different navigation solutions are employed depending on the payload, the environment and the required accuracy. For low accuracy navigation a Long Base Line (LBL) aided dead reckoning compass is used. The LBL aided Doppler Velocity Log (DVL) option adds robustness with respect to LBL faults while the DVL aided Inertial Navigation System (INS) configuration can be used for long range operations. All these solutions calibrate the estimated navigation state with GPS fixes every time the AUV surfaces. On the surface the vehicle communicates with the remote operators through a WiFi radio link or through the HSDPA/GSM radio network. Underwater, a low bandwidth acoustic communication is established. Given its low bitrate, it is mostly used to send telemetry data. Different payload configurations of the LAUV include a multibeam sonar, a sidescan sonar, a CTD sensor and a downwards looking camera. More information about the LAUV vehicle can be found in [40, 126].

9.7.2. Sea Trials

An extensive set of sea trials has been carried out with the purpose of evaluating the performance of the ILOS guidance law. As explained in Section 9.6, the AUV is required

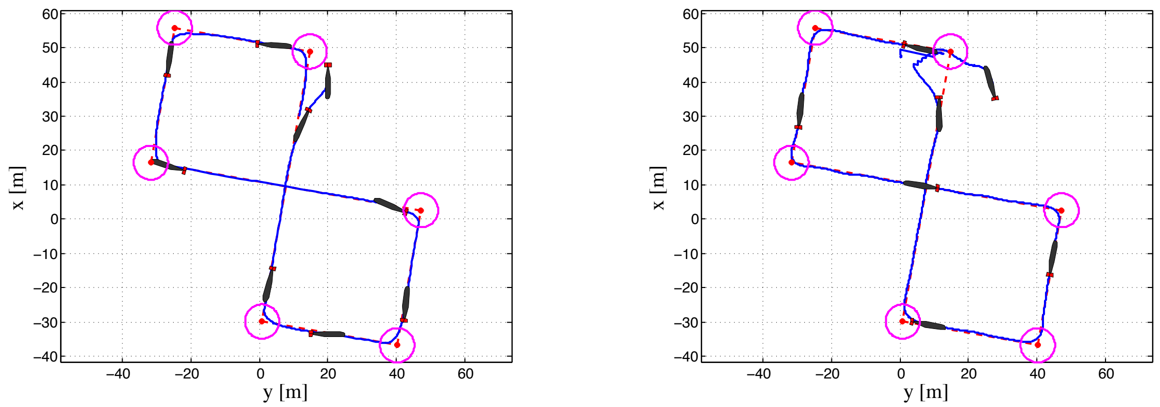

(a) Simulation of convergence and path following of the LAUV in presence of constant irrotational ocean currents.

(b) Experimental ILOS test run of the LAUV in Porto, Portugal.

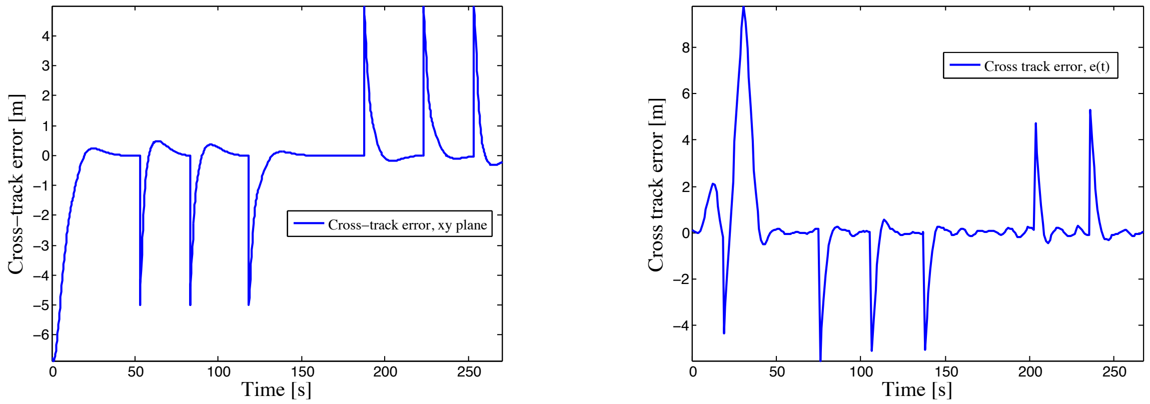

(c) Cross-track error of the LAUV from simulations. Notice the overshoots caused by integral action.

(d) Cross-track error of the LAUV from sea trials. Notice the overshoots caused by integral action.

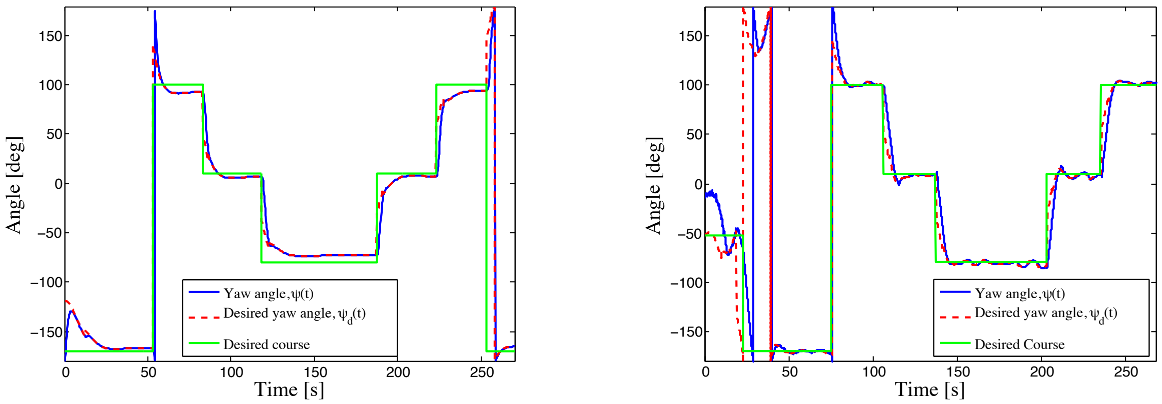

(e) Yaw angle $\psi(t)$ of the LAUV from simulations. The vehicle side-slips to compensate for the ocean current.

(f) Yaw angle $\psi(t)$ of the LAUV from sea trials. The side-slip angle varies in time since the sea current probably exhibits spatial variations.

Figure 9.4.: Back to back comparison between simulations and experimental results.

to move along a geo-referenced 8 shaped path identified by 6 way-points to exhibit both the transient response as well as the steady state behavior of the guidance law. Focus is put on comparing the ILOS performances with the simulations from Section 9.6. In particular, the guidance law parameters Δ_y and σ_y are set to 4 [m] and 0.5 [m/s], respectively, as suggested by the simulations. The ILOS guidance is used for underwater planar motion purposes because most of underwater operations involve horizontal path following or constant altitude motion. Constant depth is set by standard PID depth controller since the implementation of an ILOS-based depth controller such as the one from Section 9.6 would require a significant redesign of the DUNE software system governing the LAUV vehicle. The desired absolute/water speed of the vehicle is set to 1.2 [m/s] and the desired depth is set to 3 [m].

Remark 9.13. The DUNE control system of the LAUV does not provide the option to directly control its relative velocity. The speed controller automatically combines water speed measurements and absolute speed measurements and chooses the most reliable data.

Figures 9.4b, 9.4d and 9.4f show that the experimental results are in good agreement with the simulations results given in Figures 9.4a, 9.4c and 9.4e. The LAUV successfully follows the lines defined by the 6 way-points. Side-slipping is achieved to compensate for underwater currents. The side-slip angels are however often different compared to the simulation results and during the longest 80 [m] long legs the angle varies significantly. This is most probably due to the spatial variation of the current. Nevertheless, the vehicle stays on path as shown in Figure 9.4d, thus proving robustness of the ILOS guidance law with respect to varying current as well.

9.8. A Comparison between the ILOS Guidance and the Vector Field Guidance

In this section the experimental results of the ILOS guidance law shown in Section 9.7 are compared to similar test runs where a Vector Field (VF) guidance law is used instead. In particular, the VF guidance law presented in [100] for straight line path following purposes is implemented on the LAUV as well. Its implementation algorithm is given in [127] and [85]. First, rejection of time-varying disturbances at zero cross track error $y = 0$ of the two guidance laws is evaluated. Afterwards, the behavior of the ILOS and the VF guidance laws are analyzed away from the path. Finally, the data from the tests are analyzed and the performances of the two guidance laws are compared.

9.8.1. The VF Guidance and the ILOS Guidance at Equilibrium

The VF guidance from [100] performs course control rather then heading control and it hence requires an estimation of the side-slip angle to compensate for the current. Moreover, it is a sliding mode controller and its design is based on a kinematic model of the vehicle where the width of the corridor around the desired path represents an invariant set. The closed loop system of the vector field guidance law in steady state and on the sliding surface $S \triangleq \{(y,\chi), \chi = -\chi^{\infty}\frac{2}{\pi}\tan^{-1}(ky)\}$ is:

$$\dot{y} = -V_g \sin\left(\chi^{\infty}\frac{2}{\pi}\tan^{-1}(ky)\right), \tag{9.59}$$

where V_g is the absolute or ground speed of the vehicle, y is the cross track error, $\chi^{\infty} \in (0, \pi/2]$ is the approach course at $y \to \infty$, and $k > 0$ is a gain parameter. The system (9.59) is linearized about the equilibrium point $y = 0$ to assess the sensitivity of the VF guidance law with respect to small time-varying disturbances:

$$\dot{y} = -V_g\chi^{\infty}\frac{2}{\pi}ky + d_{V_y}(t). \tag{9.60}$$

The term $d_{V_y}(t)$ represents time-varying zero average current disturbances around the mean value V_y, which is, in this case, compensated for through direct course control. The disturbance transfer function in the frequency domain is given by:

$$T_{d,\mathrm{vf}}(j\omega) = \frac{1}{j\omega + k_{p,\mathrm{vf}}}, \tag{9.61}$$

where $k_{p,\mathrm{vf}} = V_g\chi^{\infty}\frac{2}{\pi}k$. Notice that (9.61) is a low pass filter where higher speeds make the VF guidance less sensitive to time-varying disturbances. At equilibrium the kinematic closed loop system of the 2D ILOS guidance law is approximated by (3.21-3.22) given in Chapter 3 since the underactuated and the actuated dynamics are not considered:

$$\dot{y}_{\mathrm{int}} = \frac{\Delta_y y}{(y + \sigma_y y_{\mathrm{int}})^2 + \Delta_y^2}, \tag{9.62}$$

$$\dot{y} = -U_{rd}\frac{y + \sigma_y y_{\mathrm{int}}}{\sqrt{(y + \sigma_y y_{\mathrm{int}})^2 + \Delta_y^2}} + V_y. \tag{9.63}$$

The system (9.62-9.63) is linearized about the equilibrium point $(\frac{\Delta_y}{\sigma_y} V_y / \sqrt{U_{rd}^2 - V_y^2}, 0)$ to assess the sensitivity of the ILOS guidance law with respect to small time-varying disturbances:

$$\dot{y}_{\text{int}} = \alpha y, \tag{9.64}$$

$$\dot{y} = -k_{i,\text{ilos}}\, y_{\text{int}} - k_{p,\text{ilos}}\, y + d_{V_y}(t), \tag{9.65}$$

where $k_{i,\text{ilos}} = \frac{U_{rd}\sigma_y}{\Delta_y} \left[1 - V_y^2/U_{rd}^2\right]^{3/2}$, $k_{p,\text{ilos}} = \frac{U_{rd}}{\Delta_y} \left[1 - V_y^2/U_{rd}^2\right]^{3/2}$, $\alpha = \frac{1}{\Delta_y} \left[1 - V_y^2/U_{rd}^2\right]$ and $d_{V_y}(t)$ again represents time-varying zero average current disturbances around the mean value V_y, which is, in this case, compensated through integral action. The disturbance transfer function in the frequency domain is:

$$T_{d,\text{ilos}}(j\omega) = \frac{j\omega}{-\omega^2 + j\omega k_{p,\text{ilos}} + \alpha k_{i,\text{ilos}}}, \tag{9.66}$$

Notice that (9.66) is a band pass filter. In particular, high U_{rd} values and low V_y values decrease its quality factor, hence rendering the ILOS system more robust to time-varying disturbances. Vice versa, lower speeds U_{rd} and higher currents V_y increase the quality factor of the filter and make the ILOS more sensitive to the disturbances. Given the values used in the tests $V_g = 1.2$ [m/s], $\chi^\infty = 15$ [deg], $k = 1$ [1/m], $U_{rd} = 1.2$ [m/s], $\Delta_y = 4$ [m], $\sigma_y = 0.5$ [m/s] and $V_y = V_{\max} = 0.2$ [m/s], the disturbance transfer functions $T_{d,\text{vf}}(j\omega)$ and $T_{d,\text{ilos}}(j\omega)$ are evaluated in the frequency domain in Figure 9.5. The two guidance laws exhibit similar responses with respect to disturbances at higher frequencies, while the band pass behavior of the ILOS guidance makes it more prone to time-varying disturbance rejection at lower frequencies respect to the VF guidance. Notice the peak at around 0.03 [Hz] of the frequency response of the ILOS guidance.

9.8.2. The VF Guidance and the ILOS Guidance Away from the Path

To make the VF guidance converge to the invariant set represented by the 3 [m] wide corridor, a course control guidance similar to a line-of-sight guidance is employed [85]. Its line-of-sight is approximately 5.6 [m]. Therefore the ILOS guidance is implemented with $\Delta_y = 5.6$ [m] outside the corridor to make the ILOS and the VF guidance laws comparable when the vehicle is away from the path. Notice that the ILOS integrator is turned on when the AUV is located within the 3 [m] corridor. This is done in order not

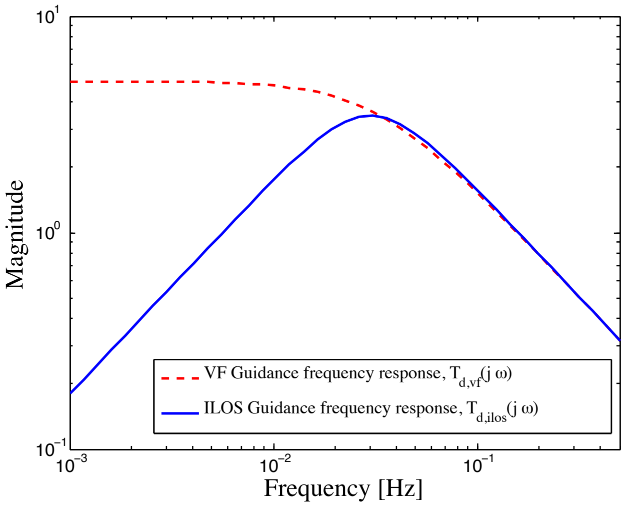

Figure 9.5.: Frequency response with respect to disturbances of the VF and ILOS guidance laws at equilibrium.

to have too much integral error and hence to avoid overshoots as explained in Section 9.6. In Section 9.6 it is furthermore shown that, despite the absence of integral action and the presence of current, the ILOS will make the vehicle enter the corridor. At that point the integrator is turned on and makes the vehicle converge on the path.

9.8.3. Comparison of Experimental Results

The same 8-shaped test runs described in Sections 9.6 and 9.7 are completed using the VF guidance law to make the system exhibit its transient response and its steady state behavior. Since the VF and the ILOS guidance laws show very similar behavior in transient condition (Figures 9.6a and 9.6b), focus is put on the steady state when the vehicle is on path. In particular, the cross track error data are analyzed to assess the path following performance of the guidance laws while the servo data are analyzed to assess the stress on the actuators. The steady state intervals are identified by checking the cross track error. Each steady state interval is then considered to represent a realization of a discrete periodic wide-sense stationary random process. Hence, the realization windows are autocorrelated and then averaged to estimate the autocorrelation function. The spectral density of the random process is then calculated. This procedure is followed to analyze and compare the cross track error data and the servo data. The results are shown in Figures 9.6 and 9.7. Moreover, the overall mean values and standard deviations for the selected data are calculated and are given in Table 9.1 and Table 9.2. The analysis of the cross track in Figure 9.6, and Tables 9.1-9.2 shows good path following properties for both the VF and the ILOS guidance laws, with the VF controller preforming slightly better since it exhibits lower mean cross track error and lower standard deviation. Notice that the spectra of Figures 9.6e and 9.6f resemble the expected disturbance responses of Figure 9.5, with a peak value at around 0.09 [Hz]. However the analysis of the servo data in Figure 9.7 and Tables 9.1-9.2 tells a different story: the VF guidance law suffers from significant chattering on the horizontal rudders (Servos 0 and 3) while the ILOS guidance law does not stress the actuators excessively giving smooth servo commands. The difference in magnitude between the spectral densities shown in Figures 9.7e and 9.7f reaches and often exceeds the factor 100 for the horizontal rudders (Servos 0 and 3). The chattering is probably caused by the switching nature of the sliding mode VF guidance law.

Table 9.1.: Evaluation statistics of the ILOS guidance law.

data type	mean value	standard deviation
Cross track error	-0.03 [m]	0.11 [m]
Servo 0	4.39 [deg]	3.03 [deg]
Servo 1	-5.68 [deg]	1.68 [deg]
Servo 2	0.99 [deg]	1.66 [deg]
Servo 3	-2.51 [deg]	3.59 [deg]

Table 9.2.: Evaluation statistics of the VF guidance law.

data type	mean value	standard deviation
Cross track error	-0.01 [m]	0.07 [m]
Servo 0	4.01 [deg]	6.93 [deg]
Servo 1	-5.66 [deg]	2.40 [deg]
Servo 2	0.84 [deg]	1.60 [deg]
Servo 3	-2.16 [deg]	6.74 [deg]

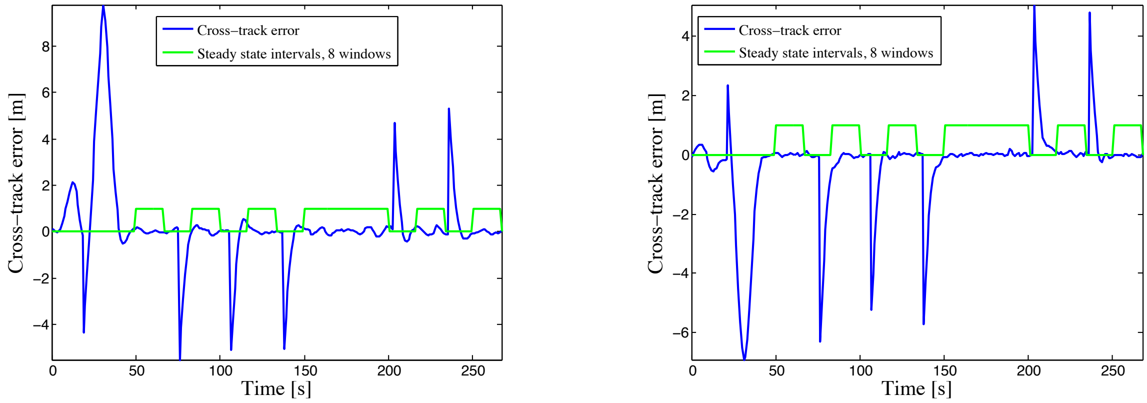

(a) Cross track error of the ILOS guidance law. The identified steady state intervals are highlighted.

(b) Cross track error of the VF guidance law. The identified steady state intervals are highlighted.

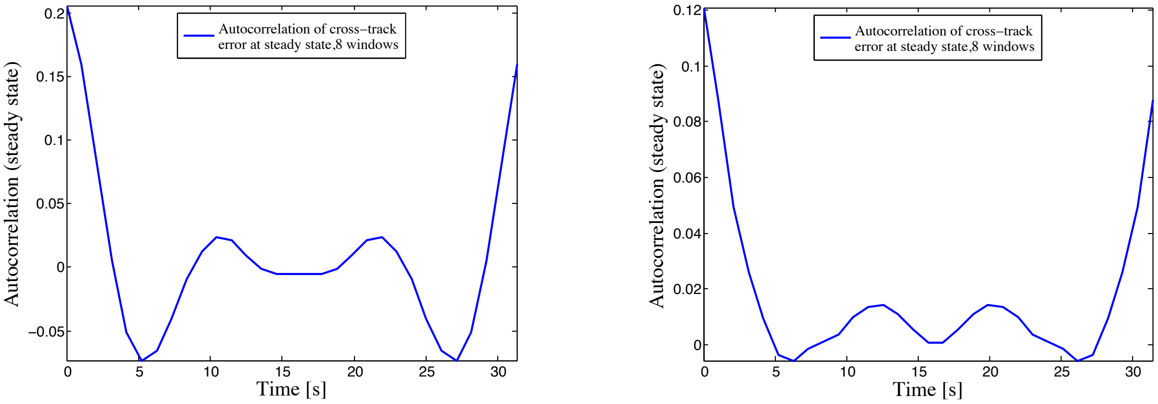

(c) Estimation of the autocorrelation function of the cross track error - ILOS guidance law.

(d) Estimation of the autocorrelation function of the cross track error - VF guidance law.

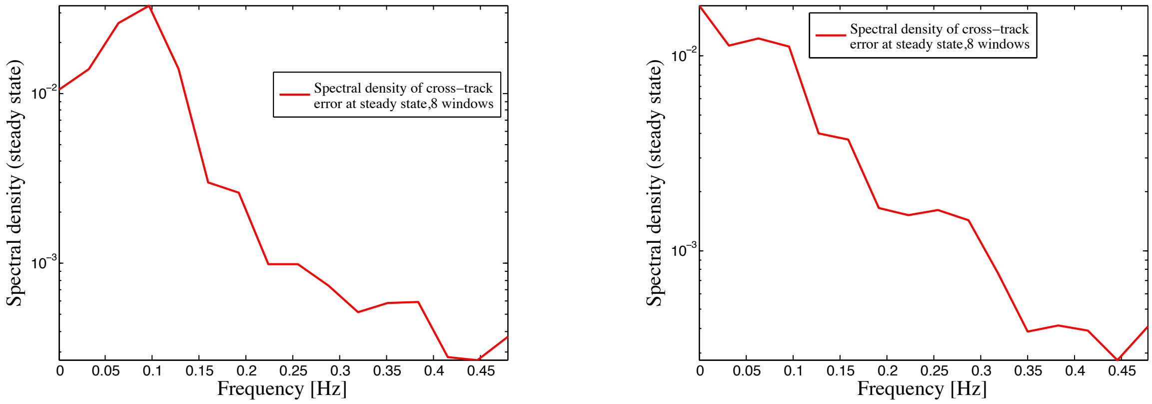

(e) Estimation of the spectral density of the cross track error - ILOS guidance law.

(f) Estimation of the spectral density of the cross track error - VF guidance law.

Figure 9.6.: Comparsion between the VF and the ILOS: the cross track error.

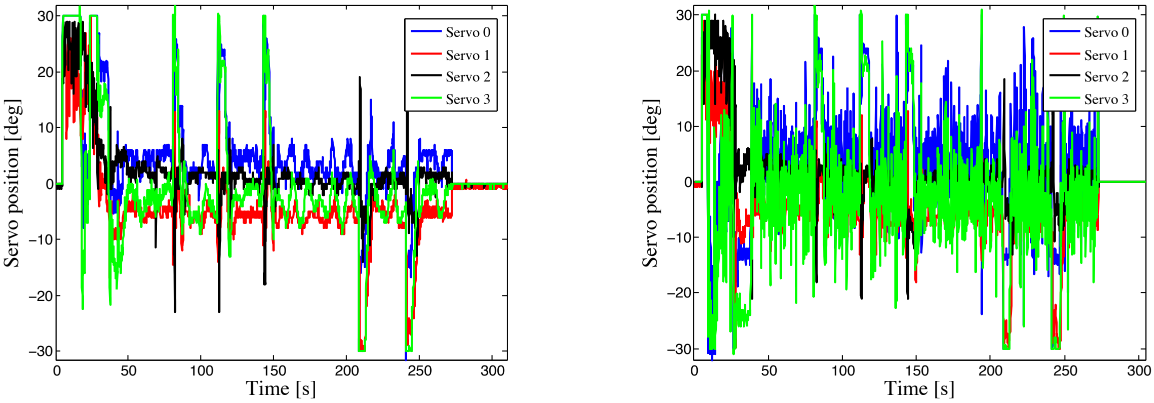

(a) Servo positions set by the ILOS guidance law.

(b) Servo positions set by the VF guidance law.

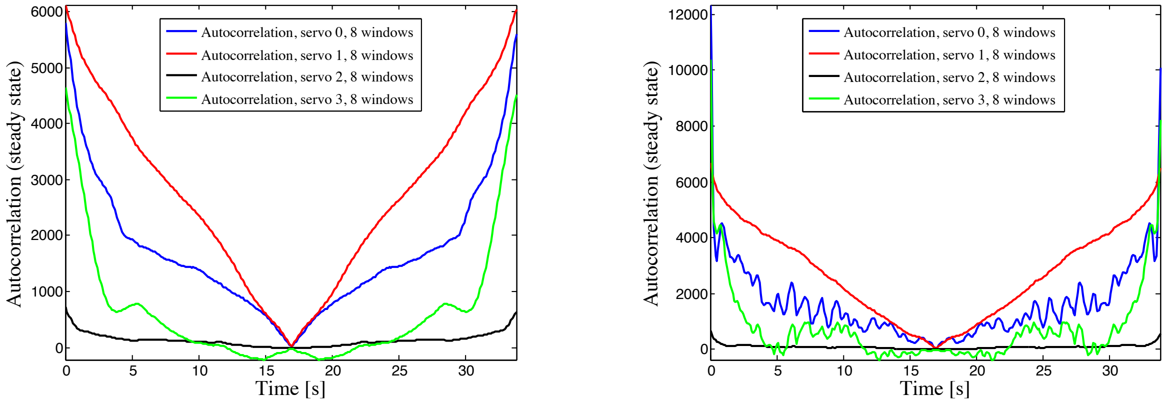

(c) Estimation of the autocorrelation functions of the servo data - ILOS guidance law.

(d) Estimation of the autocorrelation functions of the servo data - VF guidance law.

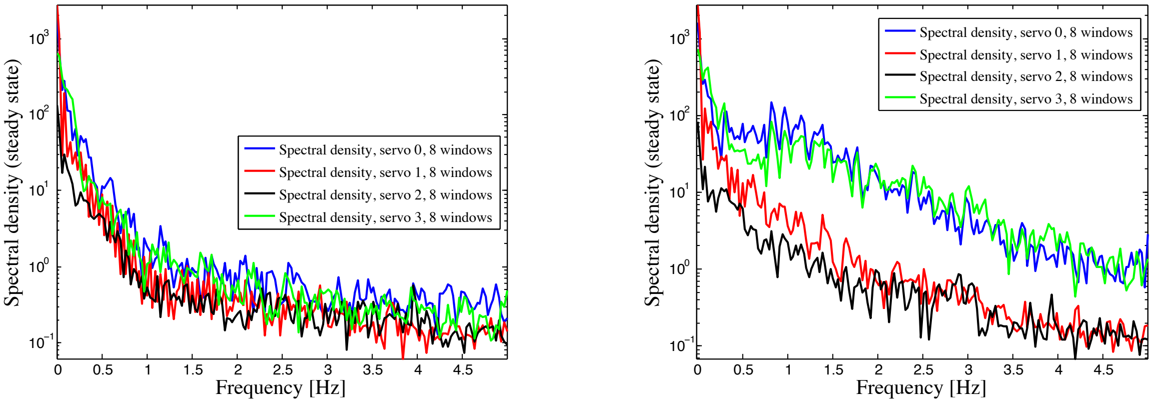

(e) Estimation of the spectral density of the servo data - ILOS guidance law.

(f) Estimation of the spectral density of the servo data - VF guidance law.

Figure 9.7.: Comparsion between the VF and the ILOS: the servo data.

9.9. Conclusions

In this chapter a control strategy for path following of underactuated AUVs in presence of constant irrotational ocean currents acting in any direction of the inertial frame has been developed. It is based on the modified LOS guidance law with integral action in both the vertical and horizontal directions that was first presented in Chapter 4. The three dimensional integral LOS is combined with three feedback controllers in a cascaded configuration and the full kinematic-dynamic closed loop system is analyzed using Lyapunov techniques and nonlinear cascaded systems theory. In particular, the analysis gives explicit conditions on the control design parameters to guarantee UGAS and ULES stability. The theoretical results are supported and completed with an extensive set of simulations and sea trials. In particular, the presented guidance law shows good path following performance, comparable to the vector field guidance law, it does not stress the actuators and it gives smooth servo signals.

9.A. Appendix: Functional Expressions

The expressions $F_{u_r}(v_r, w_r, r, q)$, $X_{v_r}(u_r)$, $Y_{v_r}(u_r)$, $X_{w_r}(u_r)$, $Y_{w_r}(u_r)$, Z_{w_r}, $F_q(\theta, u_r, w_r, q)$ and $F_r(u_r, v_r, r)$ are:

$$F_{u_r}(v_r, w_r, r, q) \triangleq \frac{1}{m_{11}}\big[(m_{22}v_r + m_{25}r)r - (m_{33}w_r + m_{34}q)q\big], \tag{9.67}$$

$$X_{v_r}(u_r) \triangleq \frac{m_{25}^2 - m_{11}m_{55}}{m_{22}m_{55} - m_{25}^2}u_r + \frac{d_{55}m_{25} - d_{25}m_{55}}{m_{22}m_{55} - m_{25}^2}, \tag{9.68}$$

$$Y_{v_r}(u_r) \triangleq \frac{(m_{22} - m_{11})m_{25}}{m_{22}m_{55} - m_{25}^2}u_r - \frac{d_{22}m_{55} - d_{52}m_{25}}{m_{22}m_{55} - m_{25}^2}, \tag{9.69}$$

$$X_{w_r}(u_r) \triangleq \frac{-m_{34}^2 + m_{11}m_{44}}{m_{33}m_{44} - m_{34}^2}u_r + \frac{d_{44}m_{34} - d_{34}m_{44}}{m_{33}m_{44} - m_{34}^2}, \tag{9.70}$$

$$Y_{w_r}(u_r) \triangleq \frac{(m_{11} - m_{33})m_{34}}{m_{33}m_{44} - m_{34}^2}u_r - \frac{d_{33}m_{44} - d_{43}m_{34}}{m_{33}m_{44} - m_{34}^2}, \tag{9.71}$$

$$Z_{w_r} \triangleq \frac{BG_zWm_{34}}{m_{33}m_{44} - m_{34}^2}, \tag{9.72}$$

$$\begin{aligned} F_q(\theta, u_r, w_r, q) \triangleq\ & \frac{m_{34}d_{33} - m_{33}(d_{43} - (m_{33} - m_{11})u_r)}{m_{33}m_{44} - m_{34}^2}w_r \\ & + \frac{m_{34}(d_{34} - m_{11}u_r) - m_{33}(d_{44} - m_{34}u_r)}{m_{33}m_{44} - m_{34}^2}q - \frac{BG_zWm_{33}}{m_{33}m_{44} - m_{34}^2}\sin(\theta), \end{aligned} \tag{9.73}$$

$$\begin{aligned} F_r(u_r, v_r, r) \triangleq\ & \frac{m_{25}d_{22} - m_{22}(d_{52} + (m_{22} - m_{11})u_r)}{m_{22}m_{55} - m_{25}^2}v_r \\ & + \frac{m_{25}(d_{25} + m_{11}u_r) - m_{22}(d_{55} + m_{25}u_r)}{m_{22}m_{55} - m_{25}^2}r. \end{aligned} \tag{9.74}$$

The vectors $\boldsymbol{h}_z \triangleq [h_{z1}, h_{z2}, h_{z3}, h_{z4}, h_{z5}]^T$ and $\boldsymbol{h}_{w_r} \triangleq [h_{w_r1}, h_{w_r2},\ h_{w_r3}, h_{w_r4}, h_{w_r5}]^T$ are defined as:

$$h_{z1} = -\sin(\tilde{\theta} + \theta_d), \tag{9.75a}$$

$$\begin{aligned} h_{z2} = & -U_{rd}\left[\frac{\sin(\tilde{\theta})}{\tilde{\theta}}\cos(\theta_d) + \frac{\cos(\tilde{\theta}) - 1}{\tilde{\theta}}\sin(\theta_d)\right] \\ & + w_r\left[\frac{\cos(\tilde{\theta}) - 1}{\tilde{\theta}}\cos(\theta_d) - \frac{\sin(\tilde{\theta})}{\tilde{\theta}}\sin(\theta_d)\right], \end{aligned} \tag{9.75b}$$

$$h_{z3} = h_{z4} = h_{z5} = 0, \tag{9.75c}$$

$$
\begin{aligned}
h_{w_r1} &= \frac{X_{w_r}(\tilde{u}_r + U_{rd}) - X_{w_r}^{U_{rd}}}{\tilde{u}_r}\gamma_{w_r}(z_{\text{int}}, z, w_r) \\
&\quad + w_r \frac{Y_{w_r}(\tilde{u}_r + U_{rd}) - Y_{w_r}^{U_{rd}}}{\tilde{u}_r},
\end{aligned} \tag{9.76a}
$$

$$
h_{w_r2} = Z_{w_r}\left[\frac{\sin(\tilde{\theta})}{\tilde{\theta}}\cos(\theta_d) + \frac{\cos(\tilde{\theta}) - 1}{\tilde{\theta}}\sin(\theta_d)\right], \tag{9.76b}
$$

$$
h_{w_r3} = X_{w_r}(\tilde{u}_r + U_{rd}), \tag{9.76c}
$$

$$
h_{w_r4} = h_{w_r5} = 0, \tag{9.76d}
$$

Notice that the limits of h_{z2} for $\tilde{\theta} \to 0$, h_{w_r1} for $\tilde{u}_r \to 0$ and h_{w_r2} for $\tilde{\theta} \to 0$ exist and are finite. The vectors $\boldsymbol{h}_y \triangleq [h_{y1}, h_{y2}, h_{y3}, h_{y4}, h_{y5}, h_{y6}, h_{y7}, h_{y8}]^T$ and $\boldsymbol{h}_{v_r} \triangleq [h_{v_r1}, h_{v_r2}, h_{v_r3}, h_{v_r4}, h_{v_r5}, h_{v_r6}, h_{v_r7}, h_{v_r8}]^T$ are defined as:

$$
\begin{aligned}
h_{y2} &= \frac{U_{rd}}{e_{z2}}\left[\frac{\Delta_z}{\sqrt{(e_{z2} + \sigma_z z_{\text{int}}^{\text{eq}})^2 + \Delta_z^2}} - \frac{1}{\sqrt{s^2+1}}\right] \\
&\quad - \frac{s}{\sqrt{s^2+1}}\frac{Z_{w_r}}{Y_{w_r}^{U_{rd}}}\frac{1}{e_{z2}}\left[\frac{e_{z2} + \sigma_z z_{\text{int}}^{\text{eq}}}{\sqrt{(e_{z2} + \sigma_z z_{\text{int}}^{\text{eq}})^2 + \Delta_z^2}} - \frac{s}{\sqrt{s^2+1}}\right],
\end{aligned} \tag{9.77a}
$$

$$
h_{y3} = \sin(\tilde{\theta} + \theta_d)\sin(\tilde{\psi} + \psi_d), \tag{9.77b}
$$

$$
h_{y4} = \cos(\tilde{\theta} + \theta_d)\sin(\tilde{\psi} + \psi_d), \tag{9.77c}
$$

$$
\begin{aligned}
h_{y5} &= U_{rd}\sin(\psi_d)\left[\frac{\cos(\tilde{\theta}) - 1}{\tilde{\theta}}\cos(\theta_d) - \frac{\sin(\tilde{\theta})}{\tilde{\theta}}\sin(\theta_d)\right] \\
&\quad - \frac{s}{\sqrt{s^2+1}}\frac{Z_{w_r}}{Y_{w_r}^{U_{rd}}}\sin(\psi_d)\left[\frac{\sin(\tilde{\theta})}{\tilde{\theta}}\cos(\theta_d) + \frac{\cos(\tilde{\theta}) - 1}{\tilde{\theta}}\sin(\theta_d)\right],
\end{aligned} \tag{9.77d}
$$

$$
\begin{aligned}
h_{y7} &= \left[U_{rd}\cos(\tilde{\theta} + \theta_d) - \frac{s}{\sqrt{s^2+1}}\frac{Z_{w_r}}{Y_{w_r}^{U_{rd}}}\sin(\tilde{\theta} + \theta_d)\right] \\
&\quad \cdot \left[\frac{\sin(\tilde{\psi})}{\tilde{\psi}}\cos(\psi_d) + \frac{\cos(\tilde{\psi}) - 1}{\tilde{\psi}}\sin(\psi_d)\right] \\
&\quad + v_r\left[\frac{\cos(\tilde{\psi}) - 1}{\tilde{\psi}}\cos(\psi_d) - \frac{\sin(\tilde{\psi})}{\tilde{\psi}}\sin(\psi_d)\right],
\end{aligned} \tag{9.77e}
$$

$$
h_{y1} = h_{y6} = h_{y8} = 0, \tag{9.77f}
$$

$$
\tag{9.77g}
$$

$$h_{v_r2} = \frac{X_{v_r}^{U_{rd}}}{e_{z2}} \left[\frac{\Delta_z}{\sqrt{(e_{z2} + \sigma_z z_{\text{int}}^{\text{eq}})^2 + \Delta_z^2}} - \frac{1}{\sqrt{s^2+1}} \right] \gamma_{v_r}(y_{\text{int}}, y, v_r), \tag{9.78a}$$

$$\begin{aligned} h_{v_r4} = {} & \frac{X_{v_r}(\tilde{u}_r + U_{rd}) - X_{v_r}^{U_{rd}}}{\tilde{u}_r} \cos(\tilde{\theta} + \theta_d) \gamma_{v_r}(y_{\text{int}}, y, v_r) \\ & + v_r \frac{Y_{v_r}(\tilde{u}_r + U_{rd}) - Y_{v_r}^{U_{rd}}}{\tilde{u}_r}, \end{aligned} \tag{9.78b}$$

$$h_{v_r5} = \left[\frac{\cos(\tilde{\theta}) - 1}{\tilde{\theta}} \cos(\theta_d) - \frac{\sin(\tilde{\theta})}{\tilde{\theta}} \sin(\theta_d) \right] X_{v_r}^{U_{rd}} \gamma_{v_r}(y_{\text{int}}, y, v_r), \tag{9.78c}$$

$$h_{v_r8} = X_{v_r}(\tilde{u}_r + U_{rd}) \cos(\tilde{\theta} + \theta_d), \tag{9.78d}$$

$$h_{v_r1} = h_{v_r3} = h_{v_r6} = h_{v_r7} = 0. \tag{9.78e}$$

$$\tag{9.78f}$$

Notice that the limits of h_{y2} for $e_{z2} \to 0$, h_{y5} for $\tilde{\theta} \to 0$, h_{y7} for $\tilde{\psi} \to 0$, h_{v_r2} for $e_{z2} \to 0$, h_{v_r4} for $\tilde{u}_r \to 0$ and h_{v_r5} for $\tilde{\theta} \to 0$ exist and are finite. The expressions $\gamma_{w_r}(z_{\text{int}}, z, w_r)$ and $\gamma_{v_r}(y_{\text{int}}, y, v_r)$ are defined as:

$$\begin{aligned} \gamma_{w_r} \triangleq {} & -\frac{\Delta_z U_{rd}(z + \sigma_z z_{\text{int}})}{((z + \sigma_z z_{\text{int}})^2 + \Delta_z^2)^{3/2}} + \frac{\Delta_z^2}{((z + \sigma_z z_{\text{int}})^2 + \Delta_z^2)^{3/2}} w_r \\ & + \frac{\sigma_z \Delta_z^2}{((z + \sigma_z z_{\text{int}})^2 + \Delta_z^2)^2} z + \frac{\Delta_z V_z}{(z + \sigma_z z_{\text{int}})^2 + \Delta_z^2}, \end{aligned} \tag{9.79}$$

$$\begin{aligned} \gamma_{v_r} \triangleq {} & \frac{\Delta_y \Gamma(s)(y + \sigma_y y_{\text{int}})}{((y + \sigma_y y_{\text{int}})^2 + \Delta_y^2)^{3/2}} - \frac{\Delta_y^2}{((y + \sigma_y y_{\text{int}})^2 + \Delta_y^2)^{3/2}} v_r \\ & - \frac{\sigma_y \Delta_y^2}{((y + \sigma_y y_{\text{int}})^2 + \Delta_y^2)^2} y - \frac{\Delta_y V_y}{(y + \sigma_y y_{\text{int}})^2 + \Delta_y^2}. \end{aligned} \tag{9.80}$$

$$\boldsymbol{A}_1(e_{z2}) \triangleq \begin{bmatrix} -\frac{\sigma_z\Delta_z}{(e_{z2}+\sigma_z z_{\text{int}}^{\text{eq}})^2+\Delta_z^2} & \frac{\Delta_z}{(e_{z2}+\sigma_z z_{\text{int}}^{\text{eq}})^2+\Delta_z^2} & 0 \\ -\frac{\sigma_z^2\Delta_z}{(e_{z2}+\sigma_z z_{\text{int}}^{\text{eq}})^2+\Delta_z^2} & \left(-\frac{U_{rd}}{\sqrt{(e_{z2}+\sigma_z z_{\text{int}}^{\text{eq}})^2+\Delta_z^2}} + \frac{\sigma_z\Delta_z}{(e_{z2}+\sigma_z z_{\text{int}}^{\text{eq}})^2+\Delta_z^2}\right) & \frac{\Delta_z}{\sqrt{(e_{z2}+\sigma_z z_{\text{int}}^{\text{eq}})^2+\Delta_z^2}} \\ \frac{-\sigma_z^2\Delta_z^2 X_{w_r}^{U_{rd}}}{((e_{z2}+\sigma_z z_{\text{int}}^{\text{eq}})^2+\Delta_z^2)^2} & \left(\frac{-U_{rd}\Delta_z X_{w_r}^{U_{rd}}}{((e_{z2}+\sigma_z z_{\text{int}}^{\text{eq}})^2+\Delta_z^2)^{3/2}} + \frac{\sigma_z\Delta_z^2 X_{w_r}^{U_{rd}}}{((e_{z2}+\sigma_z z_{\text{int}}^{\text{eq}})^2+\Delta_z^2)^2} + \frac{Z_{w_r}}{\sqrt{(e_{z2}+\sigma_z z_{\text{int}}^{\text{eq}})^2+\Delta_z^2}}\right) & \left(Y_{w_r}^{U_{rd}} + \frac{\Delta_z^2 X_{w_r}^{U_{rd}}}{((e_{z2}+\sigma_z z_{\text{int}}^{\text{eq}})^2+\Delta_z^2)^{3/2}}\right) \end{bmatrix} \tag{9.81}$$

$$\boldsymbol{A}_2(e_{y2}) \triangleq \begin{bmatrix} -\frac{\sigma_y\Delta_y}{(e_{y2}+\sigma_y y_{\text{int}}^{\text{eq}})^2+\Delta_y^2} & \frac{\Delta_y}{(e_{y2}+\sigma_y y_{\text{int}}^{\text{eq}})^2+\Delta_y^2} & 0 \\ -\frac{\sigma_y^2\Delta_y}{(e_{y2}+\sigma_y y_{\text{int}}^{\text{eq}})^2+\Delta_y^2} & \left(-\frac{\Gamma(s)}{\sqrt{(e_{y2}+\sigma_y y_{\text{int}}^{\text{eq}})^2+\Delta_y^2}} + \frac{\sigma_y\Delta_y}{(e_{y2}+\sigma_y y_{\text{int}}^{\text{eq}})^2+\Delta_y^2}\right) & \frac{\Delta_y}{\sqrt{(e_{y2}+\sigma_y y_{\text{int}}^{\text{eq}})^2+\Delta_y^2}} \\ \frac{1}{\sqrt{s^2+1}}\frac{\sigma_y^2\Delta_y^2 X_{v_r}^{U_{rd}}}{((e_{y2}+\sigma_y y_{\text{int}}^{\text{eq}})^2+\Delta_y^2)^2} & \frac{1}{\sqrt{s^2+1}}\left(\frac{\Gamma(s)\Delta_y X_{v_r}^{U_{rd}}}{((e_{y2}+\sigma_y y_{\text{int}}^{\text{eq}})^2+\Delta_y^2)^{3/2}} - \frac{\sigma_y\Delta_y^2 X_{v_r}^{U_{rd}}}{((e_{y2}+\sigma_y y_{\text{int}}^{\text{eq}})^2+\Delta_y^2)^2}\right) & \left(Y_{v_r}^{U_{rd}} - \frac{\Delta_y^2 X_{v_r}^{U_{rd}}}{\sqrt{s^2+1}((e_{y2}+\sigma_y y_{\text{int}}^{\text{eq}})^2+\Delta_y^2)^{3/2}}\right) \end{bmatrix} \tag{9.82}$$

9.B. Appendix: Proof of Lemma 9.1

Equation (9.26) is written again:

$$s\sqrt{s^2+1} = \frac{V_z}{U_{rd}}s^2 - \frac{Z_{w_r}}{Y_{w_r}^{U_{rd}}}s + \frac{V_z}{U_{rd}}. \tag{9.83}$$

This Lemma proves that there exists only one real solution to (9.83) if Assumption 9.5 holds. The proof follows along the lines of the proof of Lemma 5.1 given in Appendix 5.A of Chapter 5. First, it is shown that there exist real solutions to (9.83) and then uniqueness is argued. Squaring both sides of (9.83) gives:

$$p(s) \triangleq (M^2 - U_{rd}^2)s^4 + 2MNs^3 + (2MP + N^2 - U_{rd}^2)s^2 + 2NPs + P^2 = 0, \tag{9.84}$$

where $M \triangleq V_z$, $N \triangleq -Z_{w_r}/Y_{w_r}^{U_{rd}}$ and $P \triangleq V_z$. Hence, $M^2 - U_{rd}^2 < 0$ as long as $U_{rd} > V_{\max}$ which is guaranteed by Assumption 9.5. This means that, if Assumption 9.5 holds, the polynomial $p(s) \to -\infty$ as $s \to \pm\infty$. Furthermore, since $P^2 \geq 0$, then $p(0) \geq 0$. Therefore, $p(s)$ has at least one real zero, or at least two real zeros - one positive and one negative - if $P > 0$. This proves the existence of real solutions to (9.83).

The intersections between the curves defined by the two sides of (9.83) are considered next to show uniqueness:

$$L_1(s^*) \triangleq s^*\sqrt{s^{*2}+1}, \tag{9.85}$$

$$L_2(s^*) \triangleq \frac{V_z}{U_{rd}}s^{*2} - \frac{Z_{w_r}}{U_{rd}Y_{w_r}^{U_{rd}}}s^* + \frac{V_z}{U_{rd}}. \tag{9.86}$$

The curve $L_1(s^*)$ is strictly increasing while $L_2(s^*)$ is a parabola. The first derivatives in s^* of $L_1(s^*)$ and $L_2(s^*)$ are analyzed:

$$\frac{dL_1}{ds^*} = \frac{2s^{*2}+1}{\sqrt{s^{*2}+1}}, \tag{9.87}$$

$$\frac{dL_2}{ds^*} = \frac{2V_z}{U_{rd}}s^* - \frac{Z_{w_r}}{U_{rd}Y_{w_r}^{U_{rd}}}, \tag{9.88}$$

The following bound holds:

$$\frac{dL_2}{ds^*} \leq \frac{2V_{\max}}{U_{rd}}|s^*| + \frac{|Z_{w_r}|}{U_{rd}|Y_{w_r}^{U_{rd}}|}. \tag{9.89}$$

Notice that as long as $U_{rd} > 2V_{\max}$ and $U_{rd} > 2|Z_{w_r}|/|Y^{U_{rd}}|$, which are both guaranteed by Assumption 9.5, the following inequality holds:

$$\frac{dL_1}{ds} > \frac{2V_{\max}}{U_{rd}}|s^*| + \frac{|Z_{w_r}|}{U_{rd}|Y_{w_r}^{U_{rd}}|} \geq \frac{dL_2}{ds}, \quad \forall s^*. \tag{9.90}$$

This inequality has two important consequences: if there exist any intersections between L_1 and L_2, these intersections are transverse intersections. Yet, if there exists an intersection between L_1 and L_2, then this intersection is unique: since $dL_1/ds > dL_2/ds$, if the curves intersect in one point, they will never intersect again. The proven existence of real solutions to (9.83) guarantees that L_1 and L_2 intersect each other and hence it is possible to conclude that the intersection point is unique. To conclude, as long as Assumption 9.5 is satisfied, there exists only one real solution s for (9.83).

Chapter 10.

Counter-Current and Co-Current Guidance of Underactuated Marine Vehicles

"Adventure is just bad planning."
— Roald Amundsen, Explorer

In this chapter the problem of steering a marine vessel against the ocean current or with the ocean current is addressed. This is an interesting problem since an autonomous marine vehicle capable of sensing the current and follow the flow could exploit the drift when exact positioning is not as critical as energy efficiency. In fact, such guidance law makes the vehicle determine the direction that guarantees the minimum energy consumption for a given absolute speed. Moreover, an underwater vehicle that can turn against the flow could, for instance, help locate a hydrothermal vent or detect hydrocarbon leaks from subsea oil and gas installations. Furthermore, a control law for counter-current guidance can be integrated into more complex weather optimal heading/positioning control systems (WOHC-WOPC) since it is meant to steer the vessel against the disturbance.

Two guidance laws for counter-current and co-current guidance of underactuated marine vehicles in 3 degrees of freedom (DOF) are presented in this chapter. The proposed solutions can be applied to surface vessels as well as to underwater vehicles and are designed to perform counter-current or co-current guidance in presence of constant and irrotational ocean currents acting in any direction of the inertial frame. The guidance laws are based on the relation between the relative and absolute velocities. In particular, it is shown that the counter-current direction and the co-current direction are two possible steady-state headings having zero absolute sway velocity and zero component of the ocean current acting in the sway direction.

In the first guidance law the absolute sway velocity is viewed as the error signal of the guidance system. In particular, the system integrates the absolute sway velocity signal to define the desired heading and to detect the two directions having zero sway velocity. The vehicle is shown to converge to the counter-current course or to the co-current course depending on the sign of a constant gain parameter. The closed loop stability analysis reveals a pendulum-like system with one of the two mentioned directions as the stable equilibrium point and the other as the unstable equilibrium point. The control system is based on relative velocities with direct control over the vehicle relative speed. In this first case the surge and yaw dynamics are not taken into account in the stability analysis. Finally, local exponential stability (LES) of the closed loop system is proved using Lyapunov perturbation theory theory and simulation results are presented.

In the second guidance law the component of the ocean current acting in the sway direction is chosen as the integrated error signal instead of the absolute sway velocity. It is shown that this separates the underactuated sway dynamics from the closed loop guidance dynamics. This simplifies the control system. Moreover, the sway subsystem is shown to be input-to-state stable (ISS). Again, the closed loop system reveals multiple stable/unstable equilibrium points, corresponding to the counter-current/co-current directions, respectively. The sign of a gain parameter selects which of the two courses is the stable one. Compared to the first guidance law, the complete cascaded closed loop system is considered and uniform semiglobal exponential stability (USES) is shown. Lyapunov theory is used in the proof. Simulation results support the theoretical findings.

The chapter is organized as follows: Section 10.1 presents the control plant model of the vehicle and Section 10.2 identifies the control objective. The feedback linearizing speed and heading controllers are introduced in Section 10.3 while Section 10.4 presents the first proposed guidance law that solves the control task. Its stability properties are analyzed in Section 10.5 and the control system is simulated in Section 10.6. The second proposed guidance law is presented in Section 10.7 and its stability properties are assessed in Section 10.8. Simulation results are shown in Section 10.9. Finally, conclusions are given in Section 10.10.

10.1. The Vehicle Model

The class of marine vehicles described by the 3-DOF maneuvering model presented in Section 2.3 of Chapter 2 are considered:

$$\dot{\boldsymbol{p}} = \boldsymbol{R}(\psi)\boldsymbol{\nu}_r + \boldsymbol{V}_c, \tag{10.1}$$

$$\boldsymbol{M}\dot{\boldsymbol{\nu}}_r + \boldsymbol{C}(\boldsymbol{\nu}_r)\boldsymbol{\nu}_r + \boldsymbol{D}\boldsymbol{\nu}_r = \boldsymbol{B}\boldsymbol{f}. \tag{10.2}$$

Assumption 10.1. The body-fixed coordinate frame b is considered located at a point $(x_g^*, 0)$ from the vehicle's center of gravity (CG) along the center-line of the vessel, where x_g^* is such that $\boldsymbol{M}^{-1}\boldsymbol{B}\boldsymbol{f} = [\tau_u, 0, \tau_r]^T$.

The point $(x_g^*, 0)$ exists for all port-starboard symmetric vehicles, (see Section 2.3 of Chapter 2). Notice that in (10.1-10.2) the effects of the disturbances are integrated into the irrotational ocean current $\boldsymbol{V}_c$. In this chapter the vector $\boldsymbol{w}$ is not taken into account. The following assumption is introduced for clarity and completeness:

Assumption 10.2. The ocean current is defined in the inertial frame i and is assumed constant, unknown, irrotational and bounded. Hence, $\boldsymbol{V}_c \triangleq [V_x, V_y, 0]^T$ and there exists a constant $V_{\max} > 0$ such that $V_{\max} \geq \sqrt{V_x^2 + V_y^2}$.

The state of the surface vessel is given by the vector $[\boldsymbol{p}^T, \boldsymbol{\nu}_r^T]^T$ where $\boldsymbol{p} \triangleq [x, y, \psi]^T$ describes the position and the orientation of the vehicle with respect to the inertial frame i. As shown in Chapter 2, in navigation problems involving irrotational ocean currents it is useful to describe the state of the vessel with the relative velocity vector: $\boldsymbol{\nu}_r = [u_r, v_r, r]^T$. The vector $\boldsymbol{\nu}_r$ is defined in the body frame b, where u_r is the relative surge velocity, v_r is the relative sway velocity and r is the yaw rate. The model (10.1-10.2) describes the kinematics and dynamics of surface vessels as well as underwater vehicles moving in the horizontal plane. The ocean current is constant and irrotational in i, i.e. $\dot{\boldsymbol{V}}_c = \boldsymbol{0}$ and therefore:

$$\dot{\boldsymbol{\nu}}_c = [rv_c, -ru_c, 0]^T. \tag{10.3}$$

The vector $\boldsymbol{f} \triangleq [T_u, T_r]^T$ is the control input vector, containing the surge thrust T_u and the rudder angle T_r. Notice that the model (10.1-10.2) is underactuated in its configuration space since it has fewer control inputs than DOFs. The matrix $\boldsymbol{M} = \boldsymbol{M}^T > 0$ is the mass and inertia matrix and includes hydrodynamic added mass. The matrix $\boldsymbol{C}(\boldsymbol{\nu}_r)$ is the Coriolis and centripetal matrix, $\boldsymbol{D} > 0$ is the hydrodynamic damping matrix and $\boldsymbol{B} \in \mathbb{R}^{3\times 2}$ is the actuator configuration matrix. The structure of the matrices $\boldsymbol{R}(\psi)$, $\boldsymbol{M}$, $\boldsymbol{C}(\boldsymbol{\nu}_r)$ and $\boldsymbol{B}$ is given in Chapter 2. The following assumption defines the properties of the damping matrix $\boldsymbol{D}$:

Assumption 10.3. Damping is considered linear.

Remark 10.1. Nonlinear damping is not considered in order to reduce the complexity of the controllers. However, the passive nature of the non-linear hydrodynamic damping forces should enhance the directional stability of the vessel.

The hydrodynamic damping matrix $\boldsymbol{D}$ is therefore considered to have the following structure [52]:

$$\boldsymbol{D} \triangleq \begin{bmatrix} d_{11} & 0 & 0 \\ 0 & d_{22} & d_{23} \\ 0 & d_{32} & d_{33} \end{bmatrix}. \tag{10.4}$$

The particular structure of $\boldsymbol{D}$ is justified by symmetry arguments (see Section 2.3 of Chapter 2) and Assumption 10.3.

10.1.1. The Model in Component Form

To solve nonlinear underactuated control design problems it is useful to expand (10.1-10.2) into:

$$\dot{x} = u_r \cos(\psi) - v_r \sin(\psi) + V_x, \tag{10.5a}$$

$$\dot{y} = u_r \sin(\psi) + v_r \cos(\psi) + V_y, \tag{10.5b}$$

$$\dot{\psi} = r, \tag{10.5c}$$

$$\dot{u}_r = F_{u_r}(v_r, r) - (d_{11}/m_{11})u_r + \tau_u, \tag{10.5d}$$

$$\dot{v}_r = X(u_r)r + Y(u_r)v_r, \tag{10.5e}$$

$$\dot{r} = F_r(u_r, v_r, r) + \tau_r. \tag{10.5f}$$

The expressions for $F_r(u_r, v_r, r)$, $F_{u_r}(v_r, r)$, $X(u_r)$ and $Y(u_r)$ are given in Appendix 10.A. Notice that the functions $Y(u_r)$ and $X(u_r)$ are bounded for bounded arguments and thus the following notation is used:

$$X^{\max} \triangleq \max_{\Omega} |X(u_r)|, \tag{10.6}$$

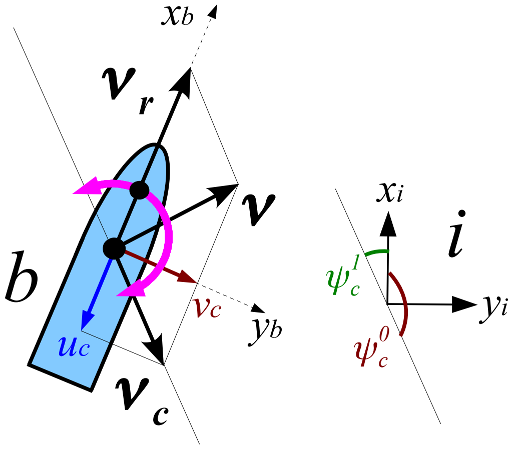

Figure 10.1.: The vehicle has to align its relative velocity vector $\boldsymbol{\nu}_r$ with the current vector $\boldsymbol{\nu}_c$ to perform counter-current or co-current guidance.

where $\Omega \triangleq \{-V_{\max} \leq u_r \leq U_{rd}\}$ and the following assumption is introduced:

Assumption 10.4. The function $Y(u_r)$ satisfies:

$$Y(u_r) \leq -Y^{\min} < 0, \quad \forall u_r \in \Omega.$$

Remark 10.2. Assumption 10.4 is justified by a contradiction: $Y(u_r) \geq 0$ would imply a nominally unstable vehicle in sway which is not the case for commercial vessels by design. Furthermore, notice that no bounds are implied on u_r. The constant $U_{rd} > 0$ is a design parameter and is defined in Section 10.2.

10.2. The Control Objective

This section formalizes the control problem solved in this paper: the control system should make the vessel turn against the current, or follow the current, in the complementary case. In addition, the vehicle should also maintain a desired constant surge relative velocity $U_{rd} > 0$. The ocean current is considered constant and unknown.

The case of a marine vehicle moving at constant speed and holding a constant course ψ_c, in presence of ocean currents, should be considered first to properly define the control objectives. This case has been addressed in [26], [28] and [34], where it has been proven that the relative sway velocity of the vessel, v_r, decays exponentially to zero due to

Assumption 10.4. Furthermore it can be seen that the current component acting in the sway direction v_c becomes $v_c \to v_{c,ss} \triangleq -V_x \sin(\psi_c) + V_y \cos(\psi_c)$, exponentially. Moreover, since $v = v_r + v_c$, at equilibrium $v \to v_{c,ss}$. Therefore, in presence of constant irrotational ocean current, $v_r \to 0$, $v_c \to v_{c,ss}$ and $v_c \to v_{c,ss}$, at steady state.

To achieve counter-current guidance as well as co-current guidance, the vessel is required to align its relative velocity vector $\boldsymbol{\nu}_r$ with the current velocity vector $\boldsymbol{\nu}_c$, as shown in Figure 10.1. At steady state, when the two vectors are parallel, the current vector $\boldsymbol{\nu}_c$ has clearly its sway component $v_{c,ss} = 0$ and thus $v = 0$. It is trivial to show that $v_{c,ss} = 0$ and $v = 0$ if and only if the vessel is pointing against the current or going with the current, i.e. if and only if $\psi_c = \text{atan2}(V_y, V_x) + k\pi,\ k \in \mathbb{Z}$. Hence, the objectives the control system should pursue can be formalized as follows:

$$\lim_{t\to\infty} v(t) = 0, \tag{10.7}$$

$$\lim_{t\to\infty} v_c(t) = 0, \tag{10.8}$$

$$\lim_{t\to\infty} \psi(t) = \text{atan2}(V_y, V_x) + k\pi, \quad k \in \{0, 1\}, \tag{10.9}$$

$$\lim_{t\to\infty} u_r(t) = U_{rd}, \tag{10.10}$$

where $k = 0$ identifies the co-current guidance and $k = 1$ identifies the counter-current guidance. Finally, the following assumption allows the vessel to move against sea currents acting in any directions of the plane:

Assumption 10.5. The propulsion system is rated with power and thrust capacity such that U_{rd} satisfies $U_{rd} > V_{\max}$.

Remark 10.3. For most marine vehicles Assumption 10.5 is easy to meet since their propulsion systems are typically designed to give more than $2 - 3$ [m/s] of relative speed U_{rd}. The ocean current has usually an intensity of less than 1 [m/s].

Remark 10.4. Notice that Assumption 10.5 is strictly necessary for the vessel to be able to move against the current.

Remark 10.5. The properties $v \to 0$ and $v_c \to 0$ can be exploited to search for the current direction. In the first guidance law presented in this chapter the signal v represent the error signal, while the second guidance law considers v_c as the error signal.

10.3. The Surge and Yaw Controllers

According to (10.10), $u_r(t)$ should follow the desired value $u_{rd}(t) \triangleq U_{rd} > 0$. To this end the following controller is used:

$$\tau_u = -F_{u_r}(v_r, r) + \frac{d_{11}}{m_{11}} u_{rd} + \dot{u}_{rd} - k_{u_r}(u_r - u_{rd}). \tag{10.11}$$

The gain $k_{u_r} > 0$ is constant. The controller (10.11) is a feedback linearizing P-controller that in a closed loop configuration with (10.5d) guarantees exponential tracking of $u_{rd}(t)$. Notice that part of the damping is not canceled in order to guarantee some robustness with respect to model uncertainties. The following controller can be used to track the desired yaw angle ψ_d:

$$\tau_r = -F_r(u_r, v_r, r) + \ddot{\psi}_d - k_\psi(\psi - \psi_d) - k_r(\dot{\psi} - \dot{\psi}_d), \tag{10.12}$$

where $k_\psi, k_r > 0$ are constant gains. The controller (10.12) is a feedback linearizing PD controller that in a closed loop configuration with (10.5c)-(10.5f) makes sure that ψ and r exponentially track ψ_d and $\dot{\psi}_d$.

Remark 10.6. The speed and heading controllers (10.11-10.12) are used in a cascaded configuration with both the guidance laws presented in this chapter.

10.4. The Integral Guidance - First Solution

The first guidance system that solves the control problem defined in Section 10.2 is presented in this section. This first solution integrates the absolute sway velocity v to search for the current direction. Hence, the following heading reference is proposed to achieve counter-current guidance, or alternatively co-current guidance:

$$\psi_{G1} \triangleq -\sigma v_{\text{int}}, \quad \sigma \neq 0, \tag{10.13a}$$

$$\dot{v}_{\text{int}} = v, \tag{10.13b}$$

where $\sigma > 0$ makes the vehicle turn against the flow and $\sigma < 0$ makes the vehicle follow the flow. The integral effect (10.13b) forces the vessel to search for the two directions having zero absolute sway velocity at steady state, while the sign of the gain σ defines whether the counter-current course or the co-current course is the stable equilibrium point of the closed loop system. It is shown in this chapter how the simple and intuitive guidance system (10.13) performs counter-current guidance, or co-current guidance, with strong stability properties. Notice that alternative integral laws, such as the one introduced in [26], can be used to improve the performance of (10.13).

Remark 10.7. The error signal in (10.13b) is the absolute sway velocity and it can be measured or estimated using DVL devices or other sensor fusion techniques [11].

Remark 10.8. Notice that $\dot{\psi}_d$ and $\ddot{\psi}_d$ are well defined if $\psi_d \triangleq \psi_{G1}$ since (10.3) is a consequence of Assumption 10.2.

In this first case the surge and yaw dynamics are not taken into account in the stability analysis since the controllers (10.11-10.12) guarantee exponential tracking of the reference signals u_r, ψ_d and $\dot{\psi}_d$. Hence, the following assumption is introduced:

Assumption 10.6. The controllers (10.11-10.12) are assumed to be fast compared to the guidance law (10.13).

Remark 10.9. The gains k_u, k_ψ and k_r can be set so that the closed loop surge and yaw dynamics do not affect the guidance system significantly.

Remark 10.10. Applying Assumptions 10.6 decouples the sway dynamics from the surge and yaw closed loop dynamics. In particular, the convergence rate of the guidance (10.13) is proportional to σ (see Section 10.5). Therefore, qualitatively, Assumption 10.6 is valid as long as σ is chosen small enough.

10.5. Closed Loop Stability Analysis - First Solution

This section presents the conditions under which the first proposed guidance law (10.13) in a cascaded configuration with the controllers (10.11-10.12) achieves the objectives (10.7-10.10). The notation $X^{U_{rd}} \triangleq X(U_{rd})$ and $Y^{U_{rd}} \triangleq Y(U_{rd})$ is introduced and the euclidean norm $\|\cdot\| \triangleq \|\cdot\|_2$ is used. The following stability analysis considers the counter-current guidance case only ($\sigma > 0$). The same discussion can be repeated for the co-current case ($\sigma < 0$).

Theorem 10.1. *Given an underactuated marine vehicle described by the dynamical system (10.5). If Assumptions 10.2-10.6 hold, there exists a small enough* σ *satisfying*

$$0 < \sigma < |Y^{U_{rd}}|/|X^{U_{rd}}|, \tag{10.14}$$

such that the guidance law (10.13) *and the controllers (10.11-10.12), where* $u_{rd} \triangleq U_{rd}$*, guarantee achievement of the control objectives (10.7-10.10).*

Proof. The actuated dynamics (10.5d) and (10.5f) of the ship in closed loop configuration with the controllers (10.11) and (10.12) are considered first. Given the vector $\boldsymbol{\zeta} \triangleq [\tilde{u}_r, \tilde{\psi}, \dot{\tilde{\psi}}]^T$ where $\tilde{u}_r \triangleq u_r - U_{rd}$, $\tilde{\psi} \triangleq \psi - \psi_d$ and $\dot{\tilde{\psi}} \triangleq \dot{\psi} - \dot{\psi}_d$, the dynamics of $\boldsymbol{\zeta}$ are obtained by combining the system equations (10.5c), (10.5d) and (10.5f) with the control laws (10.11) and (10.12):

$$\dot{\boldsymbol{\zeta}} = \begin{bmatrix} -k_{u_r} - \frac{d_{11}}{m_{11}} & 0 & 0 \\ 0 & 0 & 1 \\ 0 & -k_\psi & -k_r \end{bmatrix} \boldsymbol{\zeta} \triangleq \boldsymbol{\Sigma}\boldsymbol{\zeta}. \tag{10.15}$$

The system (10.15) is linear and time-invariant. Furthermore, since the gains k_{u_r}, k_ψ, k_r and the term d_{11}/m_{11} are all strictly positive, the system matrix $\boldsymbol{\Sigma}$ is Hurwitz and the origin $\boldsymbol{\zeta} = \mathbf{0}$ is globally exponentially stable. Therefore the control goal (10.10) is achieved with exponential converging properties in any ball of initial conditions.

The dynamics of the sway velocity v are analyzed next. The v, v_{int} subsystem is obtained combining (10.5e) and (10.13b). Then, the equations $\boldsymbol{\nu} = \boldsymbol{\nu}_r + \boldsymbol{\nu}_c$, $\boldsymbol{\nu}_c = \boldsymbol{R}^T(\psi)\boldsymbol{V}_c$ and (10.13) lead to:

$$\dot{v}_{\text{int}} = v, \tag{10.16}$$

$$\begin{aligned} \dot{v} = {} & \big[X(U_{rd} + \tilde{u}_r) - (V_x \cos(\psi_d + \tilde{\psi}) + V_y \sin(\psi_d + \tilde{\psi}))\big](\dot{\psi}_d + \dot{\tilde{\psi}}) \\ & + Y(U_{rd} + \tilde{u}_r)v - Y(U_{rd} + \tilde{u}_r)(-V_x \sin(\psi_d + \tilde{\psi}) + V_y \cos(\psi_d + \tilde{\psi})), \end{aligned} \tag{10.17}$$

where $\psi_d = -\sigma v_{\text{int}}$ and $\dot{\psi}_d = -\sigma v$, from (10.13). Since $\boldsymbol{\zeta} \to \mathbf{0}$ exponentially, it is possible to apply Assumption 10.6 and consider $\boldsymbol{\zeta} = \mathbf{0}$. Moreover, according to Assumption 10.4, $Y(U_{rd}) = -|Y(U_{rd})|$. Therefore, the system (10.16-10.17) becomes:

$$\dot{v}_{\text{int}} = v, \tag{10.18}$$

$$\begin{aligned} \dot{v} = {} & -\big[|Y(U_{rd})| + \sigma X(U_{rd})\big]v + |Y(U_{rd})|\big[V_x \sin(\sigma v_{\text{int}}) + V_y \cos(\sigma v_{\text{int}})\big] \\ & + \sigma(V_x \cos(\sigma v_{\text{int}}) - V_y \sin(\sigma v_{\text{int}}))v. \end{aligned} \tag{10.19}$$

The equilibrium points of (10.18-10.19) are:

$$v_{\text{int},k}^{\text{eq}} = -\frac{1}{\sigma}\left[\operatorname{atan2}\left(V_y, V_x\right) + k\pi\right], \quad v_k^{\text{eq}} = 0, \tag{10.20}$$

where $k \in \mathbb{Z}$. The system (10.18-10.19) has two physical equilibrium points: the counter-current direction and the co-current direction. This is clearly seen if the course held by the ship at equilibrium is calculated:

$$\psi_k^{\text{eq}} = \operatorname{atan2}\left(V_y, V_x\right) + k\pi, \quad k \in \mathbb{Z}. \tag{10.21}$$

The equilibrium point that corresponds to the counter-current course, $(v_{\text{int},1}^{\text{eq}}, v_1^{\text{eq}})$, is considered. The variable $e \triangleq v_{\text{int}} - v_{\text{int},1}^{\text{eq}}$ is introduced to move the equilibrium point to the origin. This is in fact a rotation of the inertial frame i against the current. The system (10.18-10.19) can then be rewritten in the following form:

$$\dot{\boldsymbol{\chi}} = \boldsymbol{F}(\boldsymbol{\chi}) + \boldsymbol{G}(\boldsymbol{\chi}), \tag{10.22}$$

where $\boldsymbol{\chi} \triangleq [e, v]^T$. The vectors $\boldsymbol{F}(\boldsymbol{\chi})$ and $\boldsymbol{G}(\boldsymbol{\chi})$ are:

$$\boldsymbol{F}(\boldsymbol{\chi}) \triangleq \left[\begin{smallmatrix} v \\ -A\sin(\sigma e) - Bv \end{smallmatrix}\right], \tag{10.23}$$

$$\boldsymbol{G}(\boldsymbol{\chi}) \triangleq \left[\begin{smallmatrix} 0 \\ -C\cos(\sigma e)v \end{smallmatrix}\right]. \tag{10.24}$$

The constants $A \triangleq V_c|Y(U_{rd})|$, $B \triangleq |Y(U_{rd})| + \sigma X(U_{rd})$ and $C \triangleq \sigma V_c$, where $V_c \triangleq \sqrt{V_x^2 + V_y^2}$ is the intensity of the current. Notice that $A > 0$ and that $B > 0$ as long as σ satisfies (10.14). In (10.22) the vanishing perturbation $\boldsymbol{G}(\boldsymbol{\chi})$ perturbs the following nominal system:

$$\dot{\boldsymbol{\chi}} = \boldsymbol{F}(\boldsymbol{\chi}). \tag{10.25}$$

The stability of (10.25) is considered first. The system (10.25) is a pendulum-like system and has the same equilibrium points as (10.22). Hence, following [82], it is straightforward to define a positive definite Lyapunov function candidate (LFC):

$$W_1 \triangleq \frac{\sigma}{2}\boldsymbol{\chi}^T\boldsymbol{P}\boldsymbol{\chi} + A(1 - \cos(\sigma e)), \quad \boldsymbol{P} \triangleq \begin{bmatrix} \frac{B^2}{2} & \frac{B}{2} \\ \frac{B}{2} & 1 \end{bmatrix}. \tag{10.26}$$

This gives:

$$\dot{W}_1 = -\frac{\sigma}{2} ABe \sin(\sigma e) - \frac{\sigma}{2} Bv^2. \tag{10.27}$$

As long as $A > 0$ and $B > 0$, $\dot{W}_1$ is negative definite on $0 < |e| < \pi/\sigma$. Therefore, if σ satisfies (10.14), the origin is an asymptotically stable equilibrium point of (10.25). In addition, the following bounds hold globally:

$$\frac{\sigma}{2} \boldsymbol{\chi}^T \boldsymbol{P} \boldsymbol{\chi} \leq W_1 \leq \frac{\sigma}{2} \boldsymbol{\chi}^T \boldsymbol{Q} \boldsymbol{\chi}, \quad \boldsymbol{Q} \triangleq \begin{bmatrix} \sigma A + \frac{B^2}{2} & \frac{B}{2} \\ \frac{B}{2} & 1 \end{bmatrix}, \tag{10.28}$$

where $\boldsymbol{Q}$ is positive definite. Recalling that a positive definite quadratic form $\boldsymbol{\chi}^T \boldsymbol{T} \boldsymbol{\chi}$ satisfies $\lambda_{\min}(\boldsymbol{T}) \boldsymbol{\chi}^T \boldsymbol{\chi} \leq \boldsymbol{\chi}^T \boldsymbol{T} \boldsymbol{\chi} \leq \lambda_{\max}(\boldsymbol{T}) \boldsymbol{\chi}^T \boldsymbol{\chi}$, there exist two constants $c_1 > 0$ and $c_2 > 0$ such that:

$$c_1 \|\boldsymbol{\chi}\|^2 \leq W_1 \leq c_2 \|\boldsymbol{\chi}\|^2, \tag{10.29}$$

globally. Moreover, the time derivative of the LFC satisfies:

$$\dot{W}_1 \leq -\frac{\sigma B c_3}{2} \left[Ae^2 + v^2 \right] \leq -\frac{\sigma B c_3}{2} \min\{A, 1\} \|\boldsymbol{\chi}\|^2, \tag{10.30}$$

for some positive constant $c_3 < 1$, in a neighborhood $D \triangleq \{\boldsymbol{\chi} \mid \sin(\sigma e)/(\sigma e) \geq c_3, 0 < |e| < \pi/\sigma\}$ of the origin. Notice that $D \neq \emptyset$ for every $\sigma > 0$ as long as $c_3 < 1$. Thus, it is possible to conclude [82] that the origin is also a locally exponentially stable equilibrium point of (10.25).

The stability of the perturbed system (10.22) is considered next. The LFC (10.26) satisfies the following bound globally:

$$\left\| \left[\frac{\partial W_1}{\partial e}, \frac{\partial W_1}{\partial v} \right] \right\| \leq \sigma \sqrt{\lambda_{\max}(\boldsymbol{S})} \|\boldsymbol{\chi}\| \leq \sigma c_4 \|\boldsymbol{\chi}\|, \tag{10.31}$$

where the positive constant $c_4 \geq \sqrt{\lambda_{\max}(\boldsymbol{S})}$. The matrix $\boldsymbol{S}$ is positive definite and is given by:

$$\boldsymbol{S} \triangleq \begin{bmatrix} \left(\frac{B_M^2}{2} + A_M \sigma_{\max} \right)^2 + \frac{B_M^2}{4} & \frac{B_M}{2} \left[\left(\frac{B_M^2}{2} + A_M \sigma_{\max} \right) + 1 \right] \\ \frac{B_M}{2} \left[\left(\frac{B_M^2}{2} + A_M \sigma_{\max} \right) + 1 \right] & \frac{B_M^2}{4} + 1 \end{bmatrix}, \tag{10.32}$$

where $\sigma_{\max} \triangleq |Y^{U_{rd}}|/|X^{U_{rd}}|$, $A_M \triangleq V_{\max}|Y^{U_{rd}}|$ and $B_M \triangleq 2|Y^{U_{rd}}|$, from (10.14). Notice that the bounds on c_3 and c_4 do not depend on σ. Furthermore, the perturbation $\boldsymbol{G}(\boldsymbol{\chi})$ satisfies the linear growth bound:

$$\|\boldsymbol{G}(\boldsymbol{\chi})\| \leq \gamma \|\boldsymbol{\chi}\|, \tag{10.33}$$

for a non-negative constant $\gamma \triangleq \sigma V_{\max}$. Given $c_3^* \triangleq (c_3/2)\min\{A, 1\}$, if $\sigma > 0$ is chosen such that:

$$\sigma < \frac{|Y^{U_{rd}}|}{V_{\max}\frac{c_4}{c_3^*} + |X^{U_{rd}}|} < \sigma_{\max}, \tag{10.34}$$

then $\gamma < \frac{Bc_3^*}{c_4}$ for any:

$$c_3 < 1, \tag{10.35}$$

$$c_4 \geq \max\left\{\sqrt{\lambda_{\max}(\boldsymbol{S})}, \frac{|X^{U_{rd}}|}{2V_{\max}}\right\}. \tag{10.36}$$

Therefore, there exists a small enough σ satisfying (10.14) and $\gamma < \frac{Bc_3^*}{c_4}$ for all $\chi \in D$. Hence, according to standard perturbation theory arguments [82, Lemma 9.1], the origin of the perturbed system (10.22) is locally exponentially stable and the objectives (10.7-10.9) are achieved with exponential converging properties with $\psi(t) \to \text{atan2}(V_y, V_x) + \pi$. $\square$

Similarly, the same proof can be repeated for the co-current guidance ($\sigma < 0$).

10.6. Simulations - First Solution

In this section results from numerical simulations are presented. The first guidance law presented in this chapter (10.13) is applied to the HUGIN AUV. The model of the vehicle is given in Section B.4 of Appendix B where the planar motion in 3DOF of the AUV is considered. The objective is to make the vehicle move against the sea current or, complementary, to follow the sea current. The AUV should also hold a desired surge relative speed $U_{rd} = 1$ [m/s]. Notice that the guidance law sets the heading of the vessel only, while its position is unconstrained.

The intensity of the current is $|\boldsymbol{V}_c| = 0.5$ [m/s] and its direction is randomly generated. In this case, its components are $V_x = 0.19$ [m/s] and $V_y = -0.46$ [m/s], giving a direction of -68.2 [deg]. Thus, Assumptions 10.2 and 10.5 are fulfilled with $V_{\max} = 0.6$ [m/s]. Furthermore, it can be verified that Assumption 10.4 is satisfied with $Y^{\min} = 0.60$ [s^{-1}] and that $\sigma_{\max} = 0.104$ [m^{-1}]. The chosen values for the gain σ in the counter-current case and in the co-current case are 0.1 [m^{-1}] and -0.1 [m^{-1}], respectively. Therefore, (10.14) as well as (10.34) are satisfied with $c_3 = 0.9$ and $c_4 = 2.7$. Notice that linearizing (10.22) at the origin gives an overdamped second order system with $\omega_0 \approx 0.2$ [rad/s]. The restoring term $A\sin(\sigma e)e$ is strongest at the origin, thus the guidance dynamics are faster around the stable equilibrium point. The internal controllers (10.11-10.12) are implemented with the following gains: $k_{u_r} = 0.7$, $k_\psi = 1$ and $k_r = 2$. Hence, the $\tilde{u}_r$ first order closed loop system has a time constant of 1.4 [s] while the $\tilde{\psi}$ second order closed loop system is overdamped with $\omega_n = 1$ [rad/s]. The yaw closed loop system is made critically damped to have the fastest possible response without overshoots. The chosen gains make the controllers (10.11-10.12) faster then the guidance system (10.22), as required by Assumption 10.6. Notice that in the simulations saturation is considered for both the rudder and the propeller. The maximum rudder angle is 20 [deg] and the maximum rudder turning rate is 10 [deg/s]. The forward thrust $T_u \in [-T_u^{\max}(u_r), T_u^{\max}(u_r)]$ is dynamically saturated with saturation limits given by $T_u^{\max}(u_r) = T_{nn}n_{\max}^2 - T_{un}n_{\max}u_r$. Here, $n_{\max} = 230/60$ [rps] and $T_{nn} > 0$ and $T_{un} > 0$ are some coefficients given by the propeller characteristics (see [52]).

The AUV is initially located at the origin of the inertial frame and holds zero relative velocity. Its surge axis is parallel to the x axis of the inertial frame. Figures 10.2a and 10.2b show that counter-current and co-current guidance are successfully achieved. Notice that the current is acting in the -68.2 [deg] direction and that the guidance law correctly identifies the counter-current course as well as the co-current course (Figures 10.3a and 10.3b). Figures 10.3c and 10.3d show the relative sway velocity and the absolute sway velocity over time in the two cases. As expected, the absolute sway velocity converges to zero since it is the error signal of the guidance law. The practical implementability of the counter-current/co-current guidance can be assessed by analyzing the rudder angle of the AUV from Figures 10.3a and 10.3b, and the thrust developed by the main propeller in Figures 10.3e and 10.3f. The performance of the speed controller (10.11) is also shown in Figures 10.3e and 10.3f. Figures 10.3a and 10.3b show that the yaw controller (10.12) moves the rudder smoothly without sharp variations. Therefore, it is possible to conclude that the proposed guidance law is implementable for values of the parameter σ satisfying (10.34), as long as reliable measurements of the absolute sway velocity v of the vehicle are available. Furthermore, the controller (10.11) develops the necessary thrust to make the vessel reach the desired water speed of 1 [m/s] (Figures 10.3e and 10.3f).

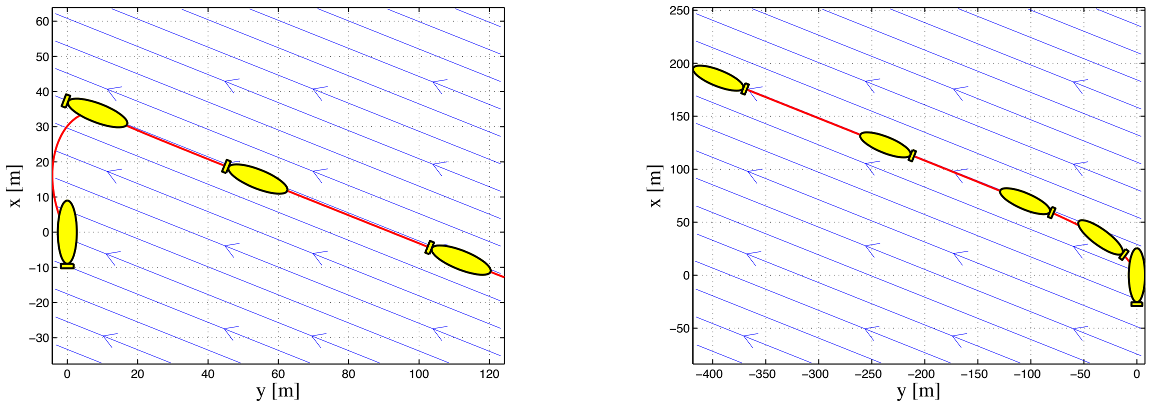

(a) Counter-current guidance of the underactuated HUGIN AUV ($\sigma = 0.1$ [m^{-1}]).

(b) Co-current guidance of the underactuated HUGIN AUV ($\sigma = -0.1$ [m^{-1}]).

Figure 10.2.: Simulation results of the first counter-current/co-current guidance law (10.13).

10.7. The Integral Guidance - Second Solution

The second solution of the guidance system that solves the control problem defined in Section 10.2 is presented in this section. This second solution integrates the current component in the sway direction o achieve counter-current guidance, or alternatively co-current guidance. Hence, the heading reference generator is redefined as:

$$\psi_{G2} \triangleq -\sigma v_{\text{int}}, \quad \sigma \neq 0, \tag{10.37a}$$

$$\dot{v}_{\text{int}} = v_c, \tag{10.37b}$$

where $\sigma > 0$ makes the vehicle turn against the flow and $\sigma < 0$ makes the vehicle follow the flow. The integral effect (10.37b) forces the vessel to search for the two directions having zero current component in the sway direction v_c at steady state, while the sign of the gain σ defines whether the counter-current course or the co-current course is the stable equilibrium point of the closed loop system. It is shown in the following sections how the modified guidance system (10.37) performs counter-current guidance, or co-current guidance, with stronger stability properties than the guidance law presented in Section 10.4. Notice that alternative integral laws can be used to improve (10.37).

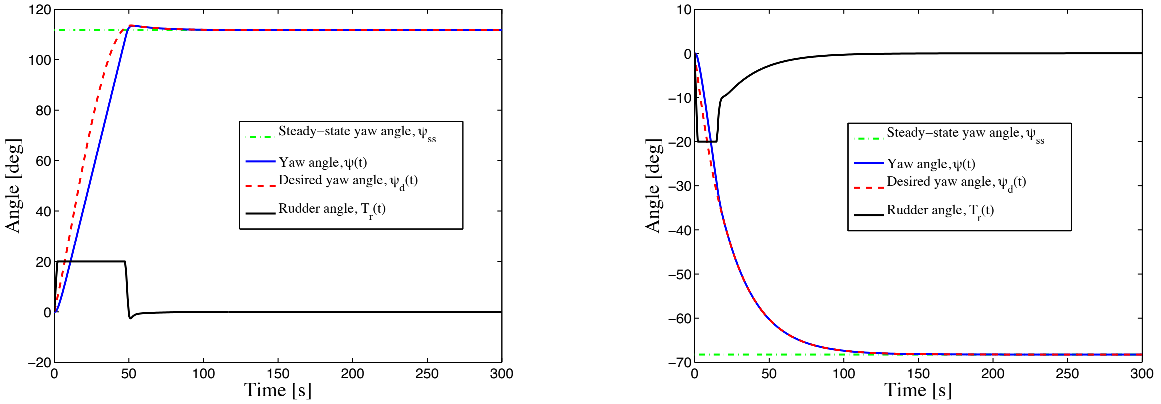

(a) Yaw angle $\psi(t)$ of the vehicle in counter-current guidance mode ($\sigma = 0.1$ [m^{-1}]). Notice that the steady state yaw angle is $\psi_{ss} = 111.8$ [deg] while the current is acting in exactly the opposite direction of -68.2 [deg].

(b) Yaw angle $\psi(t)$ of the vehicle in co-current guidance mode ($\sigma = -0.1$ [m^{-1}]). Notice that the steady state yaw angle is $\psi_{ss} = -68.2$ [deg] which is exactly the current direction.

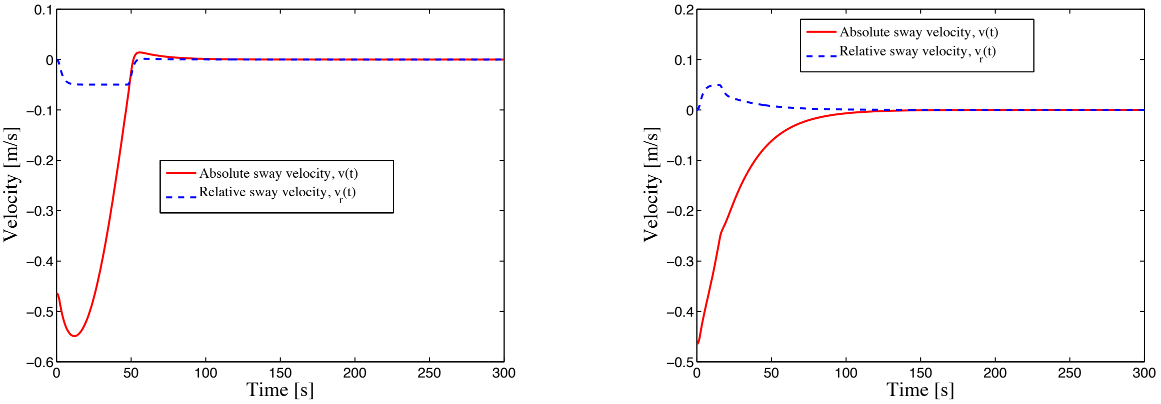

(c) The relative and absolute sway velocities of the AUV in counter-current guidance mode converge to zero as expected ($\sigma = 0.1$ [m^{-1}]).

(d) The relative and absolute sway velocities of the AUV in co-current guidance mode converge to zero as expected ($\sigma = -0.1$ [m^{-1}]).

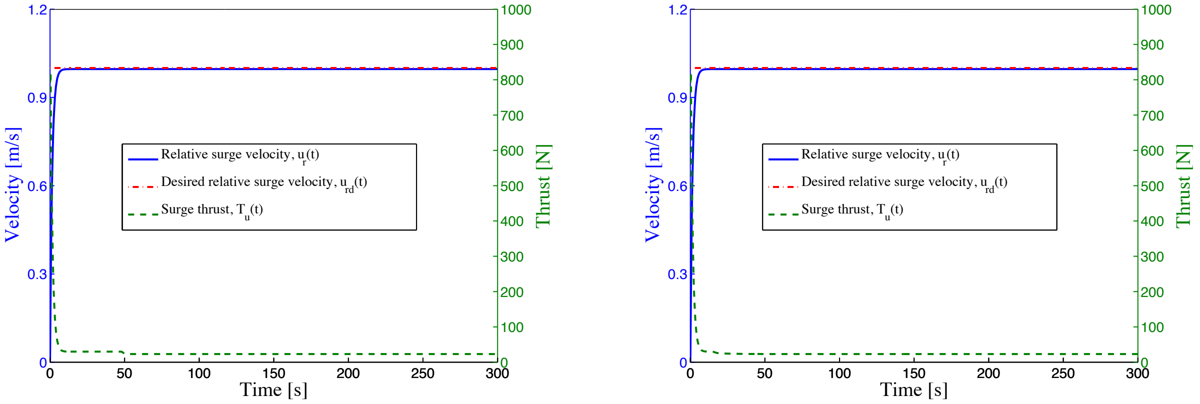

(e) Relative surge velocity $u_r(t)$ and surge thrust $T_u(t)$ of the HUGIN AUV from simulations (counter-current case).

(f) Relative surge velocity $u_r(t)$ and surge thrust $T_u(t)$ of the HUGIN AUV from simulations (co-current case).

Figure 10.3.: Simulation results of the first counter-current/co-current guidance law (10.13).

Remark 10.11. The error signal in (10.37b) is the current component acting in the sway direction. This component can be measured or estimated using DVL devices or other sensor fusion techniques [99].

Remark 10.12. In this second case the actuated surge and yaw dynamics are included in the analysis. Therefore, Assumption 10.6 is removed in this context.

Remark 10.13. The surge and yaw controllers (10.11-10.12) from Section 10.3 are used in a cascaded configuration with the redefined guidance law (10.37) to solve the problem defined in Section 10.2.

10.8. Closed Loop Stability Analysis - Second Solution

This section presents the conditions under which the proposed control system achieves the objectives (10.7-10.10). The counter-current guidance case ($\sigma > 0$) is considered only. However, the same derivations and conclusions can be drawn for the co-current case ($\sigma < 0$).

Theorem 10.2. *Given an underactuated marine vehicle described by the dynamical system (10.5). If Assumptions 10.2-10.5 hold, the controllers (10.11-10.12), with* $k_{u_r}, k_\psi, k_r > 0$, $u_{rd} \triangleq U_{rd}$ *and* $\psi_d \triangleq \psi_{G2}$, *guarantee achievement of the control objectives (10.7-10.10) with USES. The USES properties hold on the parameter set* $\Theta \triangleq \{\sigma > 0\}$.

Proof. The actuated surge and yaw dynamics of the vehicle are considered first. The closed loop surge subsystem is obtained combining (10.5d) with (10.11) and given $\tilde{u}_r \triangleq u_r - U_{rd}$, the $\tilde{u}_r$ dynamics become:

$$\dot{\tilde{u}}_r = -\left(\frac{d_{11}}{m_{11}} + k_{u_r}\right)\tilde{u}_r, \tag{10.38}$$

where $d_{11}, m_{11}, k_{u_r} > 0$. The $\tilde{u}_r$ subsystem is clearly uniformly globally exponentially stable (UGES). Therefore, the control goal (10.10) is achieved with exponential converging properties in any ball of initial conditions. The yaw ψ, r subsystem is obtained from (10.5c) and (10.5f) in closed loop configuration with (10.12). Given the error variables $\tilde{\psi} \triangleq \psi - \psi_d$ and $\tilde{r} \triangleq r - \dot{\psi}_d$, the dynamics of $\tilde{\psi}$ and $\tilde{r}$ are:

$$\dot{\boldsymbol{\xi}} = \left[\begin{smallmatrix} 0 & 1 \\ -k_\psi & -k_r \end{smallmatrix}\right] \boldsymbol{\xi} \triangleq \boldsymbol{\Sigma}\boldsymbol{\xi}, \tag{10.39}$$

where $\boldsymbol{\xi} \triangleq [\tilde{\psi}, \tilde{r}]^T$. The system (10.39) is linear and time-invariant. Furthermore, since the gains k_ψ, k_r are strictly positive, the system matrix $\boldsymbol{\Sigma}$ is Hurwitz and hence the origin $\boldsymbol{\xi} = \mathbf{0}$ is UGES.

The guidance system (10.37) is considered next. Since $\boldsymbol{\nu}_c = \boldsymbol{R}^T(\psi)\boldsymbol{V}_c$ (see Section 10.1) and $\tilde{\psi} \triangleq \psi - \psi_d$, the integrator (10.37b) can be written as:

$$\dot{v}_{\text{int}} = -V_x \sin(\psi_d + \tilde{\psi}) + V_y \cos(\psi_d + \tilde{\psi}), \tag{10.40}$$

where $\psi_d = -\sigma v_{\text{int}}$. The interconnected dynamics of v_{int} are given combining (10.40) with (10.39):

$$\dot{v}_{\text{int}} = V_x \sin(\sigma v_{\text{int}}) + V_y \cos(\sigma v_{\text{int}}) + \boldsymbol{H}_v(v_{\text{int}}, \boldsymbol{\xi})\boldsymbol{\xi}, \tag{10.41a}$$

$$\dot{\boldsymbol{\xi}} = \boldsymbol{\Sigma}\boldsymbol{\xi}, \tag{10.41b}$$

where $\boldsymbol{H}_v(v_{\text{int}}, \boldsymbol{\xi}) \triangleq [h_{v_{\text{int}}}(v_{\text{int}}, \tilde{\psi}),\ 0]$ and the function $h_{v_{\text{int}}}(v_{\text{int}}, \tilde{\psi})$ is given in Appendix 10.A. The system (10.41) is a cascaded system where the linear UGES system (10.41b) perturbs the dynamics (10.41a) through the interconnection term $\boldsymbol{H}_v$.

Remark 10.14. Compared to Section 10.5, the relative sway velocity v_r does not show up in (10.41). This is due to the choice of v_c instead of v as the error signal in (10.37). Complexity of the closed loop stability analysis is therefore reduced.

Analyzing (10.41) at equilibrium shows that $\boldsymbol{\xi}^{\text{eq}} = \mathbf{0}$ and:

$$V_x \sin(\sigma v_{\text{int}}^{\text{eq}}) + V_y \cos(\sigma v_{\text{int}}^{\text{eq}}) = 0, \tag{10.42}$$

therefore:

$$v_{\text{int},k}^{\text{eq}} = -(1/\sigma)\left[\text{atan2}\left(V_y, V_x\right) + k\pi\right], \quad k \in \mathbb{Z}. \tag{10.43}$$

The system (10.41) has multiple equilibrium points that identify two physical directions: the counter-current direction and the co-current direction. This is clearly seen if the course held by the ship at equilibrium is calculated:

$$\psi_k^{\text{eq}} = \text{atan2}\left(V_y, V_x\right) + k\pi, \quad k \in \mathbb{Z}, \tag{10.44}$$

where the equilibrium points with $k = 1 + 2n, n \in \mathbb{Z}$ correspond to the counter-current direction, while the equilibrium points identified by $k = 2n, n \in \mathbb{Z}$ correspond to the co-current direction. In particular, the equilibrium point with $k = 1$ that corresponds to the counter-current course, $v_{\text{int},1}^{\text{eq}}$, is considered.

Remark 10.15. The equilibrium point having $k = 1$ is equivalent to all the counter-current equilibrium points identified by $k = 1 + 2n, n \in \mathbb{Z}$, hence their analysis is identical.

The variable $e \triangleq v_{\text{int}} - v_{\text{int},1}^{\text{eq}}$ is introduced to move the equilibrium point to the origin. This is in fact a rotation of the inertial frame i for an angle ψ_1^{eq}. The cascaded system (10.41) can be then rewritten in the following form:

$$\dot{e} = -V_c \sin(\sigma e) + \boldsymbol{H}_e(e, \boldsymbol{\xi})\boldsymbol{\xi}, \tag{10.45a}$$

$$\dot{\boldsymbol{\xi}} = \boldsymbol{\Sigma}\boldsymbol{\xi}, \tag{10.45b}$$

where $V_c > 0$ is the magnitude of the ocean current, $V_c \triangleq \sqrt{V_x^2 + V_y^2}$, and $\boldsymbol{H}_e \triangleq [h_e(e, \tilde{\psi}),\ 0]$. The function $h_e(e, \tilde{\psi})$ is given in Appendix 10.A.

The following positive definite quadratic Lyapunov function candidate is introduced to analyze the stability properties of the cascaded system (10.45):

$$W_2 \triangleq \boldsymbol{\chi}^T \boldsymbol{P} \boldsymbol{\chi}, \tag{10.46}$$

where $\boldsymbol{\chi} \triangleq [e, \tilde{\psi}, \tilde{r}]^T$ and the matrix $\boldsymbol{P}$ is defined as:

$$\boldsymbol{P} \triangleq \begin{bmatrix} \frac{1}{2} & 0 & 0 \\ 0 & \frac{\rho}{2}\left[\frac{k_\psi}{k_r}\left(1+\frac{1}{k_\psi}\right)+\frac{k_r}{k_\psi}\right] & \frac{\rho}{2k_\psi} \\ 0 & \frac{\rho}{2k_\psi} & \frac{\rho}{2k_r}\left(1+\frac{1}{k_\psi}\right) \end{bmatrix}, \tag{10.47}$$

where $\rho > 0$ is a constant parameter. Notice that the matrix $\boldsymbol{P}$ is symmetric and positive definite. Hence, its eigenvalues $\lambda_1, \lambda_2, \lambda_3$ are real and positive. In particular $\lambda_1 = 1/2$ and the other two are linearly dependent on ρ: $\lambda_2(\rho) = c_2(k_\psi, k_r)\rho$ and $\lambda_3(\rho) = c_3(k_\psi, k_r)\rho$, where $c_2(k_\psi, k_r) > 0$ and $c_3(k_\psi, k_r) > 0$. The time derivative of the LFC (10.46) is:

$$\dot{W}_2 = -\rho\tilde{\psi}^2 - \rho\tilde{r}^2 - V_c e \sin(\sigma e) + e\tilde{\psi}h(e, \tilde{\psi}). \tag{10.48}$$

Notice that the function $h(e, \tilde{\psi})$ is globally bounded, since $|h(e, \tilde{\psi})| \leq 2V_{\max}$. Therefore, in any ball $\mathcal{B}_{1/\sigma} \triangleq \{|e| \leq 1/\sigma\}$, the time-derivative of W_2 satisfies the following inequality:

$$\dot{W}_2 \leq -\rho\tilde{\psi}^2 - \rho\tilde{r}^2 - V_{\max}\sigma\frac{e^2}{2} + 2V_{\max}|e||\tilde{\psi}|. \tag{10.49}$$

The bound (10.49) can be rewritten as:

$$\dot{W}_2 \leq -W_B(|\tilde{r}|, |e|, |\tilde{\psi}|), \tag{10.50}$$

where:

$$W_B(|\tilde{r}|, |e|, |\tilde{\psi}|) \triangleq \begin{bmatrix} |\tilde{r}| & |e| & |\tilde{\psi}| \end{bmatrix} \begin{bmatrix} \rho & 0 & 0 \\ 0 & \frac{V_{\max}\sigma}{2} & -V_{\max} \\ 0 & -V_{\max} & \rho \end{bmatrix} \begin{bmatrix} |\tilde{r}| \\ |e| \\ |\tilde{\psi}| \end{bmatrix} \tag{10.51}$$

It is straightforward to show that W_B is positive definite as long as $\rho > \frac{2V_{\max}}{\sigma}$. Without any loss of generality one can choose for instance $\rho = \frac{3V_{\max}}{\sigma}$, hence making two of the eigenvalues of W linearly dependent on $1/\sigma$ and all the eigenvalues of W_B dependent on $1/\sigma$. Given that the tuning parameter $\sigma > 0$ can be chosen arbitrarily small, this shows exponential stability on a domain of attraction that can be made arbitrarily large by picking σ small enough. Therefore, according to Theorem A.1, it is possible to conclude uniform semiglobal exponential stability on the parameter set $\Theta = \{\sigma > 0\}$ for the system (10.45).

Remark 10.16. Precise definitions of the USES stability property are given in Definition A.5 and in [37, Definition 2.2].

Remark 10.17. Even though the equilibria of (10.45) are multiple, they all can be separated by an arbitrarily large distance by picking $\sigma > 0$ small enough. This explains intuitively why the stability properties of (10.45) hold semiglobally.

Hence, following Remark 10.15, all the counter-current equilibrium points ($k = 1 + 2n, n \in \mathbb{Z}$) have USES and stability properties. Moreover, linearization shows instability of the equilibrium points identifying the co-current direction ($k = 2n, n \in \mathbb{Z}$).

Finally, ISS for the sway dynamics (10.5e) is shown. The underactuated sway subsystem (10.5e) can be rewritten using $r = \dot{\psi}_d + \tilde{r}$:

$$\dot{v}_r = Y(u_r)v_r + X(u_r)f(\boldsymbol{\chi}), \tag{10.52}$$

where:

$$f(\boldsymbol{\chi}) \triangleq \sigma V_c \sin(\sigma e) - \sigma\tilde{\psi} h_e(e,\tilde{\psi}) + \tilde{r}, \tag{10.53}$$

and it can be shown that:

$$|f(\boldsymbol{\chi})| \leq g(||\boldsymbol{\chi}||) \triangleq \kappa(|e| + |\tilde{\psi}| + |\tilde{r}|), \tag{10.54}$$

for some $\kappa > 0$. Notice that $\boldsymbol{\chi}(t)$ perturbs the sway subsystem and that $f(\mathbf{0}) = 0$. The unforced sway subsystem is $\dot{v}_r = Y(u_r)v_r$. Applying (10.54) and Assumption 10.4 to the time derivative of the quadratic function $W_3 \triangleq (1/2)v_r^2$ yields the following bound:

$$\dot{W}_3 = Y(u_r)v_r^2 + X(u_r)f(\boldsymbol{\chi})v_r \leq -Y^{\min}v_r^2 + X^{\max}g(||\boldsymbol{\chi}||)|v_r|. \tag{10.55}$$

Given $0 < \theta < 1$, (10.55) becomes:

$$\dot{W}_3 \leq -(1-\theta)Y^{\min}v_r^2, \ \forall |v_r| \geq \frac{1}{\theta}\frac{X^{\max}}{Y^{\min}}g(||\boldsymbol{\chi}||) > 0. \tag{10.56}$$

Hence, following [82, Theorem 4.19], the sway subsystem (10.5e) is ISS with respect to $\boldsymbol{\chi}$.

Remark 10.18. The use of Assumption 10.4 in the proof of above is justified by the fact that u_r is bounded, as clearly shown at the beginning of this section. See [26, 34] for similar arguments.

To conclude, the guidance (10.37) in a cascaded configuration with the controllers (10.11-10.12) guarantee USES on the parameter set $\Theta = \{\sigma > 0\}$ of the counter-current equilibrium points ($k = 1 + 2n, n \to \mathbb{Z}$) of the closed loop system (10.45). Hence, for any ball of initial conditions $\boldsymbol{\chi}_o$ there exists a small enough $\sigma > 0$ such that the objectives (10.7-10.10) are achieved exponentially. Notice that the goal (10.7) is included as a direct consequence of the relation $v = v_r + v_c$. □

Similarly, the same proof can be repeated for the co-current guidance ($\sigma < 0$).

10.9. Simulations - Second Solution

In this section results from numerical simulations are presented where the second solution of the counter-currant/co-current guidance law (10.37) is applied to the HUGIN AUV in a similar way as done with the guidance law (10.13) in Section 10.6. The model of the vehicle is given in Section B.4 of Appendix B and the objective is to make the vehicle move against the sea current or, complementary, to follow the sea current. The AUV should also hold a desired surge relative speed $U_{rd} = 1$ [m/s]. Notice that the guidance law sets the heading of the vessel only, while its position is unconstrained. The intensity of the current is $|\boldsymbol{V}_c| = 0.5$ [m/s] and its direction is randomly generated. In this case, its components are $V_x = -0.41$ [m/s] and $V_y = 0.29$ [m/s], giving a direction of 144.2 [deg]. Thus, Assumptions 10.2 and 10.5 are fulfilled with $V_{\max} = 0.6$ [m/s]. Furthermore, it can be verified that Assumption 10.4 is satisfied with $Y^{\min} = 0.60$ [s^{-1}] and $X^{\max} = 1.08$ [m/s].

The chosen values for the gain σ in the counter-current case and in the co-current case are 0.1 [m^{-1}] and -0.1 [m^{-1}], respectively. Choosing too high values for σ may induce chattering due to saturation in the magnitude and the turning rate of the rudder actuators. Linearizing the system (10.45) in the origin shows that the convergence rate of the guidance law is in first approximation dependent on the constant σV_c. Given that $V_c = 0.5$ [m/s] and $|\sigma| = 0.1$ [m^{-1}], this gives a time constant of 20 [s]. In particular, the restoring term $V_c \sin(\sigma e)$ is strongest at the origin, thus the guidance dynamics are faster close to the stable equilibrium point. The internal controllers (10.11-10.12) are implemented with the following gains: $k_{u_r} = 0.7$, $k_\psi = 1$ and $k_r = 2$. Hence, the $\tilde{u}_r$ first order closed loop system (10.38) has a time constant of 1.4 [s] while the $\tilde{\psi}$ second order closed loop system (10.39) is critically damped with $\omega_n = 1$ [rad/s].

The ship is initially located at the origin of the inertial frame and holds zero relative velocity. Its surge axis is parallel to the x axis of the inertial frame. Figures 10.4 and 10.5 show how counter-current and co-current guidance are successfully achieved. Notice that the current is acting in the 144.2 [deg] direction and that the guidance law correctly identifies the counter-current course as well as the co-current course (Figures 10.5a and 10.5b). Figures 10.5c and 10.5d show the relative sway velocity and the sway current component over time in the two cases. As expected, the sway current component converges to zero since it is the error signal of the guidance law. The practical implementability of the counter-current/co-current guidance can be assessed by analyzing the rudder angle of the vessel from Figures 10.5a and 10.5b. The performance of the speed controller (10.11) is also shown in Figures 10.5e and 10.5f. Notice that in the simulations saturation is taken into account for both the rudder and the propeller as described in Section 10.6. Figures 10.5a and 10.5b show that the controller moves the rudder smoothly without sharp variations. This illustrates that the proposed guidance is implementable as long as reliable measurements of the v_c current component are available.

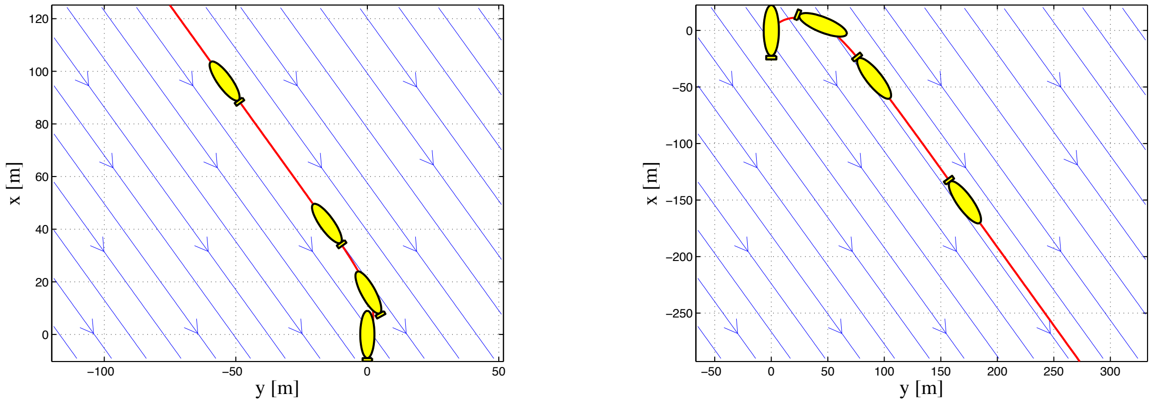

(a) Counter-current guidance of the underactuated HUGIN AUV ($\sigma = 0.1$ [m^{-1}]).

(b) Co-current guidance of the underactuated HUGIN AUV ($\sigma = -0.1$ [m^{-1}]).

Figure 10.4.: Simulation results of the second counter-current/co-current guidance law (10.37).

10.10. Conclusions

Two guidance laws for counter-current and co-current guidance of underactuated marine vehicles in 3DOF have been presented in this chapter. The proposed solutions can be applied to surface vessels as well as to underwater vehicles and are based on the relation between the relative and absolute velocities. In particular, the counter-current direction and the co-current direction are two possible steady-state headings having zero absolute sway velocity and zero sway current component.

The first presented guidance law integrates the absolute sway velocity. This makes the vessel determine the two possible directions: the counter-current course and the co-current course. It has been shown that the two directions represent a set of stable equilibrium points and a set of unstable equilibrium points of a closed loop pendulum-like system. The sign of the gain σ defines whether the vehicle converges to the counter-current direction or to the co-current direction. Explicit conditions upon the guidance law parameter σ have been derived using standard Lyapunov arguments as well as perturbation theory

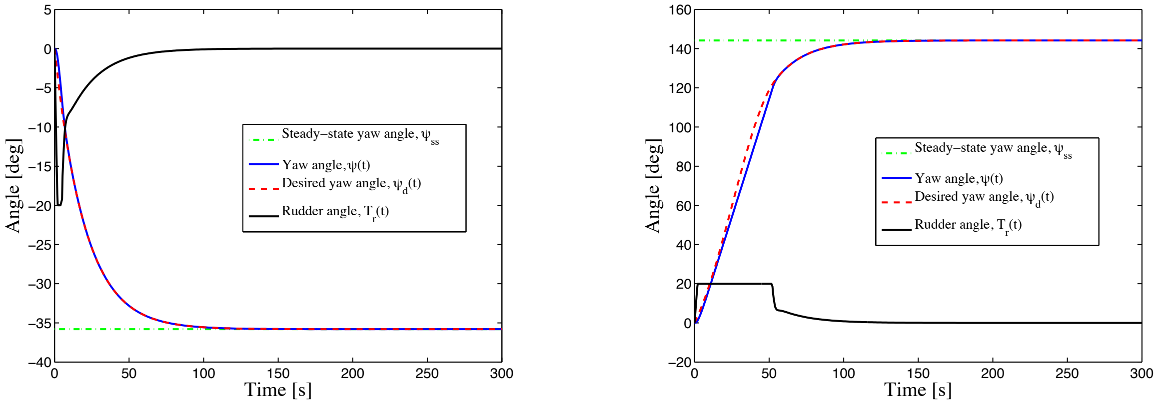

(a) Yaw angle $\psi(t)$ of the vehicle in counter-current guidance mode ($\sigma = 0.1$ [m^{-1}]). Notice that the steady state yaw angle is $\psi_{ss} = -35.8$ [deg] while the current is acting in exactly the opposite direction of 144.2 [deg] [deg].

(b) Yaw angle $\psi(t)$ of the vehicle in co-current guidance mode ($\sigma = -0.1$ [m^{-1}]). Notice that the steady state yaw angle is $\psi_{ss} = 144.2$ [deg] [deg] which is exactly the current direction.

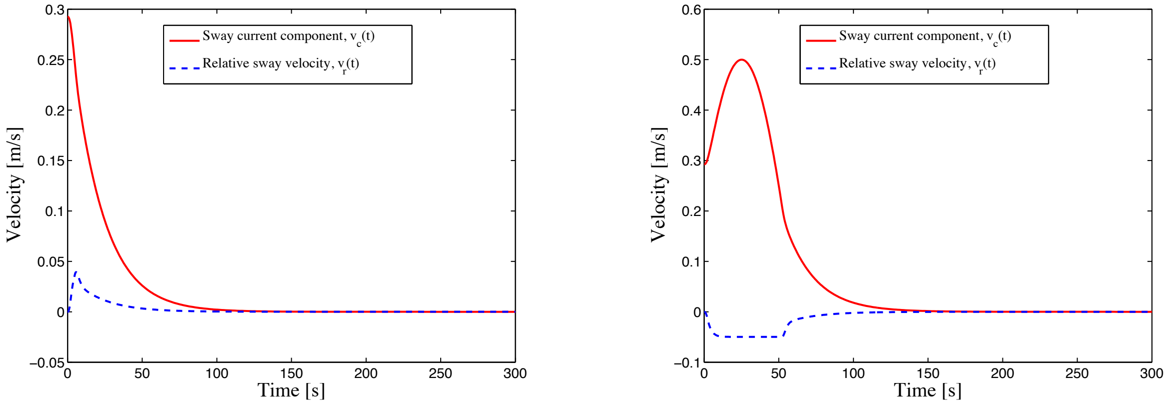

(c) The relative and absolute sway velocities of the AUV and the sway current component in counter-current guidance mode converge to zero as expected ($\sigma = 0.1$ [m^{-1}]).

(d) The relative and absolute sway velocities of the AUV and the sway current component in co-current guidance mode converge to zero as expected ($\sigma = -0.1$ [m^{-1}]).

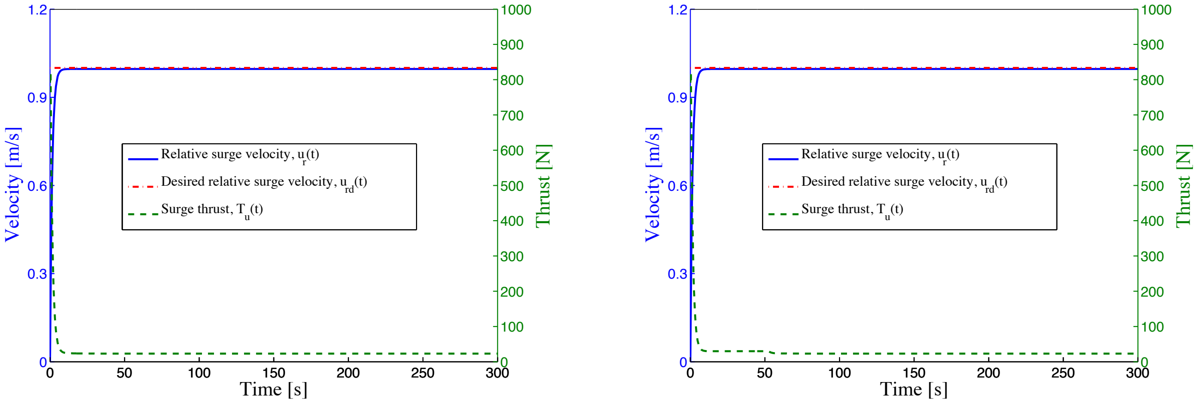

(e) Relative surge velocity $u_r(t)$ and surge thrust $T_u(t)$ of the HUGIN AUV from simulations (counter-current case).

(f) Relative surge velocity $u_r(t)$ and surge thrust $T_u(t)$ of the HUGIN AUV from simulations (co-current case).

Figure 10.5.: Simulation results of the second counter-current/co-current guidance law (10.37).

elements to guarantee local exponential stability for both the counter-current guidance as well as the co-current guidance. However, the surge and yaw dynamics have not been included in the analysis.

The second presented guidance law represents an improvement of the first. It integrates the sway current component and as a result it determines the two possible directions having zero absolute sway velocity: the counter-current course and the co-current course. Again, the two directions represent a set of stable equilibrium points and a set of unstable equilibrium points. In this case the closed loop system is analyzed without neglecting the surge and yaw dynamics and the stronger stability property of USES is shown for the complete multiple-equilibria closed loop system. The sign of the gain σ defines whether the vehicle converges to the counter-current direction or to the co-current direction. No upper bounds on the gain σ have been derived. However high values should be avoided not to cause chattering.

Results from numerical simulations have been presented to verify the theoretical results and compare the two guidance laws. Their transient as well as steady state response are very similar, suggesting that stronger stability properties may hold for the first guidance law as well. The choice between the two is then left to the available feedback signal: the absolute sway velocity v or the sway current component v_c. Given the increasing number of sensors mounted on board of ships and unmanned marine vehicles (GPS, DVL, IMU, $\dots$), it should be possible to have at least one of them available. This however should be well filtered and processed before being fed into the integrator. Finally, notice that the stronger the current, the faster both the guidance laws react.

10.A. Appendix: Functional Expressions

$$F_{u_r}(v_r, r) \triangleq \frac{1}{m_{11}}(m_{22}v_r + m_{23}r)r, \tag{10.57}$$

$$X(u_r) \triangleq \frac{m_{23}^2 - m_{11}m_{33}}{m_{22}m_{33} - m_{23}^2}u_r + \frac{d_{33}m_{23} - d_{23}m_{33}}{m_{22}m_{33} - m_{23}^2}, \tag{10.58}$$

$$Y(u_r) \triangleq \frac{(m_{22} - m_{11})m_{23}}{m_{22}m_{33} - m_{23}^2}u_r - \frac{d_{22}m_{33} - d_{32}m_{23}}{m_{22}m_{33} - m_{23}^2}, \tag{10.59}$$

$$\begin{aligned} F_r(u_r, v_r, r) \triangleq{}& \frac{m_{23}d_{22} - m_{22}(d_{32} + (m_{22} - m_{11})u_r)}{m_{22}m_{33} - m_{23}^2}v_r \\ &+ \frac{m_{23}(d_{23} + m_{11}u_r) - m_{22}(d_{33} + m_{23}u_r)}{m_{22}m_{33} - m_{23}^2}r. \end{aligned} \tag{10.60}$$

The functions $h_{v_{\text{int}}}(v_{\text{int}}, \tilde{\psi})$ and $h_e(e, \tilde{\psi})$ are:

$$\begin{aligned} h_{v_{\text{int}}}(v_{\text{int}}, \tilde{\psi}) \triangleq{}& -\frac{1 - \cos(\tilde{\psi})}{\tilde{\psi}}\left(V_x \sin(\sigma v_{\text{int}}) + V_y \cos(\sigma v_{\text{int}})\right) \\ &- \frac{\sin(\tilde{\psi})}{\tilde{\psi}}\left(V_x \cos(\sigma v_{\text{int}}) - V_y \sin(\sigma v_{\text{int}})\right), \end{aligned} \tag{10.61}$$

$$h_e(e, \tilde{\psi}) \triangleq V_c\frac{1 - \cos(\tilde{\psi})}{\tilde{\psi}}\sin(\sigma e) + V_c\frac{\sin(\tilde{\psi})}{\tilde{\psi}}\cos(\sigma e), \tag{10.62}$$

where the limits of $h_{v_{\text{int}}}$ and h_e for $\tilde{\psi} \to 0$ exist and are finite. The constant $V_c > 0$ is the magnitude of the current: $V_c \triangleq \sqrt{V_x^2 + V_y^2}$. Notice that the following identities are used when moving the equilibrium point $v_{\text{int},1}^{\text{eq}}$ to the origin in Section 10.8 (recall that $e = v_{\text{int}} - v_{\text{int},1}^{\text{eq}}$):

$$V_x \sin(\sigma v_{\text{int}}) + V_y \cos(\sigma v_{\text{int}}) = -V_c \sin(\sigma e), \tag{10.63}$$

$$V_x \cos(\sigma v_{\text{int}}) - V_y \sin(\sigma v_{\text{int}}) = -V_c \cos(\sigma e), \tag{10.64}$$

$$\sin(\text{atan2}\,(V_y, V_x)) = V_y/V_c, \tag{10.65}$$

$$\cos(\text{atan2}\,(V_y, V_x)) = V_x/V_c. \tag{10.66}$$

Chapter 11.

Conclusions and Future Work

"At the end of the project, we should all be able to look ourselves in the eye... in the mirror... and honestly say: I gave it my very best shot!"
— Sir Peter Blake, Yachtsman

This dissertation has focused on the Integral Line-of-Sight (ILOS) guidance solution for path following applications of underactuated marine vessels in presence of environmental disturbances. Path following of straight lines is considered and some of the obtained results closely relate to bounded control and modeling of marine crafts. Furthermore, the problem of steering a vehicle against the ocean current or with the ocean current is addressed as well.

The ILOS guidance law from [26] has been improved, revisited, extended and validated through full scale experiments. The improvements introduced to the ILOS guidance law from [26] relate to the redefinition of the vessel state in terms of its relative velocity. As shown in [67, 52] it is possible to rewrite the model of the vessel in terms of the relative velocity vector as long as the ocean current disturbance is assumed constant and irrotational. Since the constant and irrotational current is a widely accepted description of slowly varying disturbances [52, 51], the property presented in [67, 52] is here applied. In Chapter 6 the model of the vessel in terms of the relative velocity vector allows to prove stronger stability properties compared to [26]. In [26] both the relative velocity vector and the absolute velocity vector are present in the system dynamics forcing the introduction of adaptive control systems to estimate the unknown terms, hence increasing complexity and weakening stability. In the cases presented and analyzed in this thesis it is shown that having the state of the vessel described with relative velocities only, makes the adaptive terms unnecessary since the unknown current terms do not show up.

In Chapter 6 the designed control system consists of the 2D ILOS guidance law in a cascaded configuration with two feedback linearzing controllers. It is hence possible to prove the stronger stability properties of uniform global asymptotic stability (UGAS) and uniform local exponential stability (ULES) for the 3 degrees of freedom (DOFs) case of an underactuated ship or vehicle in a planar motion configuration. The full state of the closed loop system is analyzed, including the actuated and the underactuated dynamics. Furthermore, it is shown that in steady state it is possible to estimate the unknown current by using the integral term of the ILOS guidance law as well as measurements of the absolute and relative speeds of the vessel. The theoretical analysis is strongly supported by results from simulations and field experiments where the ILOS guidance has been applied to the CART Unmanned Semi-Submersible Vehicle (USSV) for sea trials. Furthermore, different models of a supply ship are used to simulate the control system and to assess its robustness with respect to parameter uncertainties and process noise.

The same theoretical results are obtained in Chapter 9 for the more complex case of an underactuated underwater vehicles moving in a 3D environment in the presence of constant irrotational ocean currents acting in any direction. In this case a 3D ILOS guidance law is used with integral action in both the vertical and horizontal directions, hence extending the previous findings and the vehicle is described by a 5-DOFs control plant model where the state is given by the its relative velocity. The three dimensional ILOS is combined with three feedback controllers in a cascaded configuration and the full kinematic-dynamic closed loop system is analyzed using Lyapunov techniques and nonlinear cascaded systems theory. In particular, the analysis gives explicit conditions on the control design parameters to guarantee UGAS and ULES stability. The theoretical results are supported and completed with an extensive set of simulations and sea trials where the LAUV vehicle is used. In particular, the presented guidance law shows good path following performance, comparable to the vector field guidance low, it does not stress the actuators and it gives smooth servo signals.

In Chapter 7 a combined control strategy for path following of fully actuated surface marine vehicles in presence of constant irrotational ocean currents has been developed. This extends the results of 6 to fully actuated surface vessels. Saturation of the sway actuators is analytically taken into account yielding a partially bounded control problem. The guidance system is based on the ILOS guidance law developed in Chapter 6 and a sway nonlinear bounded PI controller. In particular, it is shown in Chapter 5 that the ILOS guidance can effectively compensate for disturbances in sway and this property is here exploited to combine the ILOS with a bounded sway controller. The control system compensates for the current and guarantees path following even when the sway thrusters are saturated, by making the ship side-slip. The analysis of the full state closed loop system through Lyapunov techniques and nonlinear cascaded systems theory gives explicit conditions to guarantee exponential stability. Numerical simulations support the theoretical results.

In Chapter 8 it is shown that the ILOS guidance law developed in Chapter 6 for path following purposes of underactuated surface vehicles effectively compensates for kinematic disturbances, such as irrotational ocean currents, as well as dynamic disturbances, such as the heading dependent wind forces. Theoretical results and simulations have been presented in a unified manner for this purpose. In particular, a 3-DOFs control plant model for maneuvering purposes that includes environmental disturbances has been introduced. The disturbances are modeled as a combination of a constant irrotational ocean current and constant heading dependent wind forces. Furthermore, it has been shown that the ILOS guidance guarantees path following with UGAS and ULES (global κ-exponential stability) properties in closed loop configuration with an adaptive surge-yaw controller, in presence of both the disturbances. The full kinematic-dynamic closed loop system has been considered and explicit conditions to guarantee stability have been derived. The theoretical results are supported by numerical simulations.

The first methods of analysis and interpretations presented in this thesis are however linked to simple kinematic models of underactuated vehicles. These methods make it possible to develop simple and intuitive arguments that explain the results developed in the chapters mentioned above. In particular, in Chapter 3 the ILOS guidance has been presented and applied to a simple kinematic model of surface vessels. An intuitive approach has been followed to explain the problem of disturbance compensation for underactuated marine vessels. In particular, constant irrotational ocean currents have been considered and it has been shown that the problem has one possible solution only. The ILOS guidance is used to achieve side-slipping and compensate for the current where the closed loop system has been analyzed as a pure nonlinear kinematic problem. The analysis reveals UGAS as well as ULES stability properties and explicit conditions upon the choice of the integral gain σ are derived but no conditions upon the look-ahead distance Δ are derived since the dynamics are not taken into account within this kinematic approach. A similar kinematic approach is followed in Chapter 4 to first introduce the

3D version of the ILOS guidance later analyzed in details in Chapter 6. The intuitive approach followed in Chapter 3 is repeated and extended for underactuated underwater vehicles moving in a 3D space. In particular, 3D constant irrotational ocean currents are considered and it is shown that the problem has one possible solution only. The integral LOS guidance is used to hold non-zero pitch and yaw angles at equilibrium and thus compensate for the current. The closed loop system has been analyzed revealing a cascaded structure with UGAS and ULES stability properties. Explicit conditions upon the choice of the integral gains σ_y and σ_z are derived but no conditions upon the look-ahead distances Δ_y and Δ_z are derived since the dynamics are neglected within this kinematic approach. Explicit bounds for the choice of the ILOS guidance look-ahead distance are derived in Chapter 5 by including the underactuated dynamics into the Lyapunov analysis where disturbances in the form of constant irrotational ocean currents and constant dynamic, attitude dependent, forces have been also taken into account and their maximum ratings show up in the bounds derived for the guidance law parameters.

Finally two guidance laws for counter-current and co-current guidance of underactuated marine vehicles in 3DOF have been presented in Chapter 10. The proposed solutions can be applied to surface vessels as well as to underwater vehicles and are based on the relation between the relative and absolute velocities. In particular, it is shown that the counter-current direction and the co-current direction are two possible steady-state headings having zero absolute sway velocity and zero sway current component. In the first guidance law the absolute sway velocity is the error signal of the guidance system, while in the second guidance law the sway current component is the error signal. The two laws show different stability properties: local exponential stability (LES) for the first and uniform semiglobal exponential stability (USES) for the second. In both the cases the closed loop system reveals multiple stable/unstable equilibrium points, corresponding to the counter-current/co-current directions depending on the setting. Results from numerical simulations have been presented that support the theoretical results and compare the two guidance laws. Their transient as well as steady state responses are very similar, suggesting that stronger stability properties may hold for the first guidance law as well. The choice between the two is then left to the available feedback signal: the absolute sway velocity v or the sway current component v_c. Given the increasing number of sensor mounted on board of ships and unmanned marine vehicles (GPS, DVL, IMU, ...), it should be possible to have at least one of them available. This however should be well filtered and processed before being fed into the integrator.

Future developments of this thesis include several aspects of the guidance methods developed in the mentioned chapters. The extension of the ILOS guidance law to curved paths for path following purposes in presence of environmental disturbances should be considered since this dissertation has focused exclusively on path following of straight lines. The use of different controllers such as sliding mode, backstepping, PID or passivity based for the steering of the vehicle and the speed control represents a possible future development as well. It would be also interesting to test the control system that combines the ILOS guidance law with the bounded sway controller presented in Chapter 7 on a fully actuated vehicle. Additional tests and simulations with more complex process plan models can be also considered to further test the ILOS guidance and validate the control plant models used in this dissertation, in particular the model from Chapter 8 or to see how a complete system based on relative velocities behaves. Future extensions related to the counter-current and co-current guidance laws presented in Chapter 10 include on the field testing and their integration into more complex weather optimal heading control/weather optimal postion control (WOHC/WOPC) systems. Finally, future developments and additional validation of the control plant models discussed in Chapter 2 can be considered as well.

Appendix A.

Mathematical Tools

Several mathematical concepts and tools from nonlinear control theory are used throughout this dissertation. This appendix presents the notation, the definitions and the theorems that are of relevance to the results and analysis given in the previous chapters.

A.1. Notation

In this thesis the space $\mathbb{R}^n$ is the Euclidean space of dimension n and $\mathbb{R}^+$ is the set of all non-negative real numbers. The p norm of a vector $\boldsymbol{x} \in \mathbb{R}^n$ is denoted as $\|\boldsymbol{x}\|_p$, for $p \in [1, +\infty]$. When a norm is written without subscript, such as $\|\boldsymbol{x}\|$, the 2-norm is implied. The induced p-norm of a real matrix $\boldsymbol{A} \in \mathbb{R}^{n\times n}$ is defined as $\|\boldsymbol{A}\|_p = \max_{\|\boldsymbol{x}\|_p=1} \|\boldsymbol{A}\boldsymbol{x}\|_p$. Finally, the following definitions are taken from [82]:

Definition A.1. A continuous function $\alpha : \mathbb{R}^+ \to \mathbb{R}^+$ is said to belong to class $\mathcal{K}$ if it is strictly increasing and $\alpha(0) = 0$. It is said to belong to class $\mathcal{K}_\infty$ if $\alpha(r) \to \infty$ as $r \to \infty$.

Definition A.2. A continuous function $\beta : \mathbb{R}^+ \times \mathbb{R}^+ \to \mathbb{R}^+$ is said to belong to class $\mathcal{KL}$ if, for each fixed s, the mapping $\beta(r, s)$ belongs to class $\mathcal{K}$ with respect to r and, for each fixed r, the mapping $\beta(r, s)$ is decreasing with respect to s and $\beta(r, s) \to 0$ as $s \to \infty$.

A.2. General Stability

Some important definitions of stability for nonlinear systems are given in this section. Given the nonlinear time-varying system:

$$\dot{\boldsymbol{x}} = \boldsymbol{f}(t, \boldsymbol{x}), \quad \boldsymbol{x} \in \mathbb{R}^n, \tag{A.1}$$

where $\boldsymbol{f} : \mathbb{R}^+ \times \mathbb{R}^n \to \mathbb{R}^n$ is assumed as piecewise continuous in t and locally Lipschiz in $\boldsymbol{x}$. Since some of the systems analyzed in this thesis are time-varying, the concept of uniform stability is introduced. The following definitions of uniform stability are taken from [82] and [23].

Definition A.3 (Uniform stability)**.** The equilibrium point $\boldsymbol{x} = \boldsymbol{0}$ of the system (A.1) is said to be:

- uniformly locally stable (ULS) if there exists a class $\mathcal{K}$ function α and a positive constant c, independent of t_0, such that:

$$\|\boldsymbol{x}(t)\| \leq \alpha(\|\boldsymbol{x}(t_0)\|), \quad \forall t \geq t_0 \geq 0, \quad \forall \|\boldsymbol{x}(t_0)\| < c. \tag{A.2}$$

- uniformly globally stable (UGS) if the inequality (A.2) is satisfied fora any initial state $\boldsymbol{x}(t_0)$.
- uniformly locally asymptotically stable (ULAS) if there exists a class $\mathcal{KL}$ function β and a positive constant c, independent of t_0, such that:

$$\|\boldsymbol{x}(t)\| \leq \beta(\|\boldsymbol{x}(t_0)\|, t - t_0), \quad \forall t \geq t_0 \geq 0, \quad \forall \|\boldsymbol{x}(t_0)\| < c. \tag{A.3}$$

- uniformly globally asymptotically stable (UGAS) if the inequality (A.3) is satisfied fora any initial state $\boldsymbol{x}(t_0)$.
- uniformly locally exponentially stable (ULES) if there exists the positive constants c, k and λ such that:

$$\|\boldsymbol{x}(t)\| \leq k\|\boldsymbol{x}(t_0)\|e^{-\lambda(t-t_0)}, \quad \forall t \geq t_0 \geq 0, \quad \forall \|\boldsymbol{x}(t_0)\| < c. \tag{A.4}$$

- uniformly globally exponentially stable (UGES) if the inequality (A.4) is satisfied fora any initial state $\boldsymbol{x}(t_0)$.

Definition A.4 (Exponential stability in any ball of initial conditions)**.** The equilibrium point $\boldsymbol{x} = \mathbf{0}$ of the system (A.1) is said to be exponentially stable in any ball of initial conditions if there exists a positive constant γ and a class $\mathcal{K}$ function α such that for any initial state $\boldsymbol{x}(t_0)$:

$$\|\boldsymbol{x}(t)\| \leq \alpha(\|\boldsymbol{x}(t_0)\|)e^{-\lambda(t-t_0)}, \quad \forall t \geq t_0 \geq 0. \tag{A.5}$$

Remark A.1. Definition A.4 is equivalent to the definition of global κ-exponential stability introduced in [129].

Remark A.2. Definition A.4 and the concept of global κ-exponential stability are equivalent to the origin of the system (A.1) being UGAS and ULES [88].

Remark A.3. Robustness with respect to disturbances leads to the notion of uniform stability. If the time-varying nonlinear system (A.1) is ULAS and ULES and locally Lipschitz in t, is also locally Input-to-State Stable (ISS) [94]. Therefore, the concept of uniform stability is instrumental when analyzing stability of perturbed systems and of nonlinear time-varying systems in cascade.

A.3. Practical Stability

The term practical stability has different meanings in literature: see [37, 38, 65, 64] for a discussion on the matter. In this thesis the definition of practical stability given in [37] and [65] is used. According to [37] and [65], semiglobal and practical stability properties relate to parametrized nonlinear time-varying systems of the form:

$$\dot{\boldsymbol{x}} = \boldsymbol{f}(t, \boldsymbol{x}, \boldsymbol{\theta}), \tag{A.6}$$

where $\boldsymbol{\theta} \in \mathbb{R}^m$ is a vector of constant parameters and $\boldsymbol{f} : \mathbb{R}^+ \times \mathbb{R}^n \times \mathbb{R}^m \to \mathbb{R}^n$ is assumed as piecewise continuous in t and locally Lipschiz in $\boldsymbol{x}$, for any $\boldsymbol{\theta}$ under consideration. $\boldsymbol{\theta}$ is a free tuning parameter, such as a control gain. The concept of practical stability is applicable when the domain of attraction of the equilibrium point $\boldsymbol{x} = \mathbf{0}$ of (A.6) can be arbitrarily enlarged and diminished by a convenient choice of $\boldsymbol{\theta}$. The following definition of uniform semiglobal exponential stability is taken from [65] and [64].

Definition A.5 (Unifrom semiglobal exponential stability)**.** Let $\boldsymbol{\Theta} \subset \mathbb{R}^m$ be a set of parameters. The equilibrium point $\boldsymbol{x} = \mathbf{0}$ of the system (A.6) is said to be uniformly semiglobally exponentially stable (USES) on $\boldsymbol{\Theta}$ if, given any positive constant c, there exists a parameter $\boldsymbol{\theta}^\star(c) \in \boldsymbol{\Theta}$ and the positive constants $k(c)$ and $\lambda(c)$ such that:

$$\|\boldsymbol{x}(t, \boldsymbol{\theta}^\star)\| \leq k(c)\|\boldsymbol{x}(t_0)\|e^{-\lambda(c)(t-t_0)}, \quad \forall t \geq t_0 \geq 0, \quad \forall \|\boldsymbol{x}(t_0)\| < c. \tag{A.7}$$

Remark A.4. Definition A.5 differs from UGES since the choice of the parameter $\boldsymbol{\theta}^\star(c)$ and the constants $k(c)$ and $\lambda(c)$ depend on the positive constant c.

The following theorem from [65] gives the sufficient condition for the USES property to hold:

Theorem A.1 ([65, Theorem 2]). *Let $\boldsymbol{\Theta}$ be a subset of $\mathbb{R}^m$ and suppose that, given any constant $c > 0$, there exists a parameter $\boldsymbol{\theta}^\star \in \boldsymbol{\Theta}$, a continuous differentiable Lyapunov function $V_c : \mathbb{R}^+ \times \mathbb{R}^n \to \mathbb{R}^+$ and the positive constants $\kappa(c)$, $\underline{\kappa}(c)$, $\overline{\kappa}(c)$ such that, for all $\boldsymbol{x} \in \{\boldsymbol{x} \in \mathbb{R}^n : \|\boldsymbol{x}\| \leq c\}$ and all $t \geq 0$:*

$$\underline{\kappa}(c)\|\boldsymbol{x}\|^q \leq V_c(t, \boldsymbol{x}) \leq \overline{\kappa}(c)\|\boldsymbol{x}\|^q, \tag{A.8}$$

$$\frac{\partial V_c(t, \boldsymbol{x})}{\partial t} + \frac{\partial V_c(t, \boldsymbol{x})}{\partial \boldsymbol{x}} \boldsymbol{f}(t, \boldsymbol{x}, \boldsymbol{\theta}^\star) \leq -\kappa(c)\|\boldsymbol{x}\|^q, \tag{A.9}$$

where q is a positive constant. Then, under the condition that:

$$\lim_{c \to \infty} \frac{\underline{\kappa}(c)c^q}{\overline{\kappa}(c)} = \infty, \tag{A.10}$$

the system (A.6) *is USES on the parameter set $\boldsymbol{\Theta}$.*

A.4. Stability of Cascades

Given the nonlinear time-varying cascaded system:

$$\dot{\boldsymbol{x}} = \boldsymbol{f}_1(t, \boldsymbol{x}) + \boldsymbol{g}(t, \boldsymbol{x}, \boldsymbol{y}), \tag{A.11}$$

$$\dot{\boldsymbol{y}} = \boldsymbol{f}_2(t, \boldsymbol{y}), \tag{A.12}$$

where $\boldsymbol{x} \in \mathbb{R}^n$, $\boldsymbol{y} \in \mathbb{R}^m$ and, $\boldsymbol{f}_1(\cdot, \cdot)$ and $\boldsymbol{f}_2(\cdot, \cdot)$ are continuously differnetiable in their arguments. The following results characterize the stability properties of the origin $(\boldsymbol{x}, \boldsymbol{y}) = (\boldsymbol{0}, \boldsymbol{0})$ of the cascade (A.11-A.12).

Lemma A.1 ([106, Lemma 2]). *Given the cascaded system (A.11-A.12), if both* $\dot{\boldsymbol{x}} = \boldsymbol{f}_1(t, \boldsymbol{x})$ *and* $\dot{\boldsymbol{y}} = \boldsymbol{f}_2(t, \boldsymbol{y})$ *are UGAS and the solutions of (A.11-A.12) are globally uniformly bounded, then the cascaded system (A.11-A.12) is UGAS.*
Theorem A.2 ([105, Theorem 2]). *Given the cascaded system (A.11-A.12). Assume that the system* $\dot{\boldsymbol{x}} = \boldsymbol{f}_1(t, \boldsymbol{x})$ *is UGAS with a Lyapunov function* $V(\boldsymbol{x}, t)$ *satisfying:*

$$\left\| \frac{\partial V}{\partial \boldsymbol{x}} \right\| \|\boldsymbol{x}\| \leq c_1 V(\boldsymbol{x}, t), \quad \forall \|\boldsymbol{x}\| \geq \eta > 0, \tag{A.13}$$

where $c_1 > 0$ *and* $\eta > 0$. *If Assumptions (A1) and (A2) below are satisfied as well, then the cascaded system (A.11-A.12) is UGAS.*

(A1) *The function* $\boldsymbol{g}(t, \boldsymbol{x}, \boldsymbol{y})$ *satisfies:*

$$\|\boldsymbol{g}(t, \boldsymbol{x}, \boldsymbol{y})\| \leq \theta_1(\|\boldsymbol{y}\|) + \theta_1(\|\boldsymbol{y}\|)\boldsymbol{x}, \tag{A.14}$$

where $\theta_1, \theta_2 : \mathbb{R}^+ \to \mathbb{R}^+$ *are continuous.*

(A2) *The system* $\dot{\boldsymbol{y}} = \boldsymbol{f}_2(t, \boldsymbol{y})$ *is UGAS and, for all* $t_0 \geq 0$*:*

$$\int_{t_0}^{t} \|\boldsymbol{x}(s)\| ds \leq \phi(\|\boldsymbol{x}(t_0)\|), \tag{A.15}$$

where the function $\phi(\cdot)$ *is a class* $\mathcal{K}$ *function.*

Remark A.5. If the nominal system $\dot{\boldsymbol{x}} = \boldsymbol{f}_1(t, \boldsymbol{x})$ is UGAS with a quadratic Lyapunov function, then the condition (A.13) satisfied trivially.

Remark A.6. If the perturbing system $\dot{\boldsymbol{y}} = \boldsymbol{f}_2(t, \boldsymbol{y})$ is UGAS and ULES (or equivalently exponentially stable in any ball of initial conditions), then the integrability condition (A.15) is satisfied trivially.

Lemma A.2 ([104, Lemma 8]). *If in addition to the assumptions required by Theorem A.2, both* $\dot{\boldsymbol{x}} = \boldsymbol{f}_1(t, \boldsymbol{x})$ *and* $\dot{\boldsymbol{y}} = \boldsymbol{f}_2(t, \boldsymbol{y})$ *are globally* κ*-exponentially stable (exponentially stable in any ball of initial conditions), then the cascaded system (A.11-A.12) is globally* κ*-exponentially stable (exponentially stable in any ball of initial conditions),*

A.5. Robust Control of Mechanical Systems

Systems in the following from include applications in adaptive control of nonlinear time-varying systems, some of whom are presented in this dissertation as well:

$$\dot{\boldsymbol{x}} = \boldsymbol{h}(t, \boldsymbol{x}) + \boldsymbol{G}(t, \boldsymbol{x}, \boldsymbol{y})\boldsymbol{y}, \tag{A.16}$$

$$\dot{\boldsymbol{y}} = -\boldsymbol{P}\boldsymbol{G}(t, \boldsymbol{x}, \boldsymbol{y})^T \left(\frac{\partial W(\boldsymbol{x}, t)}{\partial \boldsymbol{x}}\right)^T, \quad \boldsymbol{P} = \boldsymbol{P}^T > 0, \tag{A.17}$$

where $\boldsymbol{x} \in \mathbb{R}^n$, $\boldsymbol{y} \in \mathbb{R}^m$ and $W : \mathbb{R}^+ \times \mathbb{R}^n \to \mathbb{R}^+$ is a C^1 function. It is furthermore assumed that all the functions in (A.16-A.17) are such that the solutions exist and are unique (for instance, locally Lipschitz in $\boldsymbol{x}$ and $\boldsymbol{y}$, uniformly in t and continuous in both arguments). The following result from [55] characterizes the stability properties of the origin $(\boldsymbol{x}, \boldsymbol{y}) = (\boldsymbol{0}, \boldsymbol{0})$ of the system (A.16-A.17).

Theorem A.3 ([55, Theorem 1])**.** *If Assumptions (A1) and (A2) below hold, then the origin of the system (A.16-A.17) is UGAS.*

(A1) *Given* $\boldsymbol{G}_0(t, \boldsymbol{y}) \triangleq \boldsymbol{G}(t, \boldsymbol{x}, \boldsymbol{y})|_{\boldsymbol{x} \equiv \boldsymbol{0}}$. *Assume that there exist nondecreasing functions* $\theta_j : \mathbb{R}^+ \to \mathbb{R}^+, j \in 1, 2, 3$ *such that, for all* $t \geq 0$, $\boldsymbol{x} \in \mathbb{R}^n$ *and* $\boldsymbol{y} \in \mathbb{R}^m$*:*

$$\max\left\{\|\boldsymbol{h}(t, \boldsymbol{x})\|, \left\|\frac{\partial W(t, \boldsymbol{x})}{\partial \boldsymbol{x}}\right\|\right\} \leq \theta_1(\|\boldsymbol{x}\|)\|\boldsymbol{x}\|, \tag{A.18}$$

$$\max\left\{\|\boldsymbol{G}(t, \boldsymbol{x}, \boldsymbol{y})\|, \|\boldsymbol{G}_0(t, \boldsymbol{y})\|\right\} \leq \theta_2(\|[\boldsymbol{x}^T, \boldsymbol{y}^T]^T\|), \tag{A.19}$$

$$\max\left\{\left\|\frac{\partial \boldsymbol{G}_0(t, \boldsymbol{y})}{\partial (\boldsymbol{y})_i}\right\|, \left\|\frac{\partial \boldsymbol{G}_0(t, \boldsymbol{y})}{\partial t}\right\|\right\} \leq \theta_3(\|\boldsymbol{y}\|)\|, \quad i \in \{1, \ldots, m\}. \tag{A.20}$$

Furthermore, for each compact set $K \in \mathbb{R}^m$ *there exists* $b_m > 0$ *such that:*

$$\boldsymbol{G}_0(t, \boldsymbol{y})^T \boldsymbol{G}_0(t, \boldsymbol{y}) \geq b_m \boldsymbol{I}, \quad \forall (t, \boldsymbol{y}) \in \mathbb{R}^+ \times K. \tag{A.21}$$

(A2) *There exist class* $\mathcal{K}_\infty$ *functions* α_1 *and* α_2*, and a constant* $c > 0$ *such that:*

$$\alpha_1(\|\boldsymbol{x}\|) \leq W(t, \boldsymbol{x}) \leq \alpha_2(\|\boldsymbol{x}\|), \tag{A.22}$$

$$\frac{\partial W(t, \boldsymbol{x})}{\partial t} + \frac{\partial W(t, \boldsymbol{x})}{\partial \boldsymbol{x}} \boldsymbol{h}(t, \boldsymbol{x}, \boldsymbol{\theta}^\star) \leq -c\|\boldsymbol{x}\|^2. \tag{A.23}$$

Moreover, if $\alpha_2(s) \propto s^2$ *for sufficiently small* s *then the origin of (A.16-A.17) is also ULES.*

Appendix B.

Simulations Models

B.1. The Supply Vessel Simulation Model

In this dissertation the 3-DOF simulation model of an offshore supply vessel derived from [58] and [56] is often used. Compared to [58] the model has an improved linear damping matrix which is obtained from more complex nonlinear damping models. The damping model is discussed at the end of the section. The offshore supply vessel is characterized by the dimensions and parameters given in Table B.1.

Figure B.1.: A platform supply vessel underway.

The dynamic model of the vessel in terms of relative velocities (see Chapter 2) is:

$$\boldsymbol{M}\dot{\boldsymbol{\nu}}_r + \boldsymbol{C}(\boldsymbol{\nu}_r)\boldsymbol{\nu}_r + \boldsymbol{D}(\boldsymbol{\nu}_r)\boldsymbol{\nu}_r = \boldsymbol{B}\boldsymbol{f}, \tag{B.1}$$

where $\boldsymbol{\nu}_r = [u_r, v_r, r]^T$, $\boldsymbol{f} = [T_u, \delta]^T$ and:

$$\boldsymbol{M} = \begin{bmatrix} 7.22 \cdot 10^6 & 0 & 0 \\ 0 & 1.21 \cdot 10^7 & -3.63 \cdot 10^7 \\ 0 & -3.63 \cdot 10^7 & 4.75 \cdot 10^9 \end{bmatrix}, \tag{B.2}$$

$$\boldsymbol{C}(\boldsymbol{\nu}_r) = \begin{bmatrix} 0 & 0 & -1.21 \cdot 10^7 v_r + 3.63 \cdot 10^7 r \\ 0 & 0 & 7.22 \cdot 10^6 u_r \\ 1.21 \cdot 10^7 v_r - 3.63 \cdot 10^7 r & -7.22 \cdot 10^6 u_r & 0 \end{bmatrix}, \tag{B.3}$$

$$\boldsymbol{B} = \begin{bmatrix} 1 & 0 \\ 0 & -1.13 \cdot 10^6 \\ 0 & 9.63 \cdot 10^7 \end{bmatrix}. \tag{B.4}$$

The control inputs are the propeller thrust T_u and the rudder deflection angle δ.

B.1.1. The Nonlinear Damping Model

In this section a nonlinear version of the damping term $\boldsymbol{D}(\boldsymbol{\nu}_r)$ is given. It is obtained as the sum of the linear zero-speed damping matrix from [56] and the nonlinear surge resistance, and cross flow drag [52]:

$$\boldsymbol{D}(\boldsymbol{\nu}_r)\boldsymbol{\nu}_r = \boldsymbol{D}_l\boldsymbol{\nu}_r + \boldsymbol{D}_n(\boldsymbol{\nu}_r), \tag{B.5}$$

where:

$$\boldsymbol{D}_l = \begin{bmatrix} 8.22 \cdot 10^4 & 0 & 0 \\ 0 & 2.72 \cdot 10^5 & -2.17 \cdot 10^6 \\ 0 & -7.17 \cdot 10^5 & 4.11 \cdot 10^8 \end{bmatrix}. \tag{B.6}$$

The nonlinear damping forces are calculated as:

$$\boldsymbol{D}_n(\boldsymbol{\nu}_r) = \begin{bmatrix} \frac{1}{2}\rho S(1+k)C_f(u_r)|u_r|u_r \\ \frac{1}{2}\rho \int_{-L_{pp}/2}^{L_{pp}/2} T C_d^{2D}(x)|v_r + xr|(v_r + xr)dx \\ \frac{1}{2}\rho \int_{-L_{pp}/2}^{L_{pp}/2} T C_d^{2D}(x)x|v_r + xr|(v_r + xr)dx \end{bmatrix}. \tag{B.7}$$

The coefficients and parameters used to calculate (B.7) are given in Table B.2. As an alternative to (B.5), the following formulation for nonlinear damping can be used to discriminate between the linear and nonlinear damping, and their speed regimes [52]:

$$\boldsymbol{D}(\boldsymbol{\nu}_r)\boldsymbol{\nu}_r = \boldsymbol{D}_l \begin{bmatrix} \exp(-\beta_1 u_r^2) & 0 & 0 \\ 0 & \exp(-\beta_2(v_r^2+r^2)) & 0 \\ 0 & 0 & \exp(-\beta_2(v_r^2+r^2)) \end{bmatrix} \boldsymbol{\nu}_r + \boldsymbol{D}_n(\boldsymbol{\nu}_r), \tag{B.8}$$

where $\beta_1, \beta_2 > 0$ can be both set to 0.5, for example.

B.1.2. The Linear Damping Model

As an approximation of the nonlinear damping model (B.8) over the intervals $u_r \in [0, u_r^{\max}]$, $v_r \in [0, 2]$ and $r \in [0, 0.5]$, the linear damping model $\boldsymbol{D}(\boldsymbol{\nu}_r)\boldsymbol{\nu}_r = \boldsymbol{D}\boldsymbol{\nu}_r$ is introduced, where:

$$\boldsymbol{D} = \begin{bmatrix} 1.74 \cdot 10^5 & 0 & 0 \\ 0 & 1.25 \cdot 10^6 & 2.14 \cdot 10^6 \\ 0 & -6.24 \cdot 10^7 & 1.35 \cdot 10^9 \end{bmatrix}. \tag{B.9}$$

Table B.1.: Dimensions and parameters of the offshore supply vessel.

symbol	description	value
m	mass	$6.4 \cdot 10^6$ [kg]
L_{pp}	length between the perpendiculars	76.20 [m]
L_{oa}	length overall	82.45 [m]
B	beam	18.80 [m]
T	draught	6.25 [m]
k_m	form factor - maneuvering	0.1
k_{DP}	form factor - DP	0.25
$T_u^{\max}$	maximum surge thrust	1600 [kN]
$u_r^{\max}$	maximum relative speed - at maximum surge thrust	7 [m/s]

Table B.2.: Coefficients and parameters used to calculate (B.7).

symbol	description	value/formula
ρ	seawater density	1025 [kg/m^3]
V	volume of displaced seawater	$m\rho$
C_b	Block coefficient	$V/(L_{pp}BT)$
S	wetted surface hull - Denny-Mumford formula	$V/(1.7T + BC_b)$
k	form factor - function of u_r, varies between k_{DP} and k_m	$\frac{\lvert k_{DP}-k_m\rvert 1.5^4}{(u_r^2+1.5^2)^2} + k_m$
ν_{vis}	kinematic viscosity at 10 [°C]	$1.3 \cdot 10^{-6}$ [m/s^2]
R_n	Reynolds number	$u_r L_{pp}/\nu_{vis}$
$R_n^{\min}$	minimum R_n to avoid singularities	10^6
C_R	surge residual friction - calculated at $u_r^{\max}$, $T_u^{\max}$, k_m	≈ 0.03
$C_f(u_r)$	surge friction coefficient	$\frac{0.075}{(\log_{10} R_n - 2)^2} + C_R$
C_d^{2D}	constant 2D current coefficient - estimated	Hoerner's curve [52]

B.1.3. Purpose of the Supply Vessel Simulation Model

The presented model is a maneuvering model for speeds higher than 3 [knots] [130]. In this thesis, the linear damping matrix of Section B.1.2 is used in control plant models, while the nonlinear damping of Section B.1.1 is used in process plant models to assess robustness of the designed control systems.

B.2. The Cybership II Simulation Model

In this thesis the 3-DOF simulation model of the Cybership II vessel from [24] and [93] is used. The Cybership II is a 1:70 scale model of a fully actuated supply vessel.

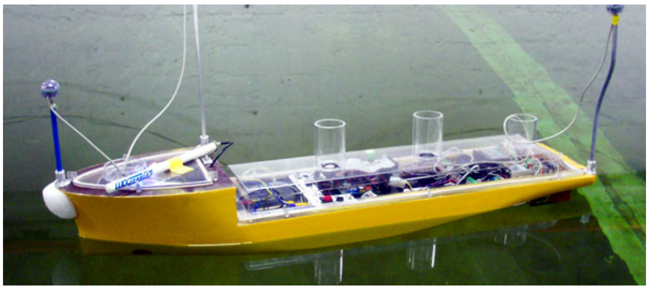

Figure B.2.: Cybership II in the pool at the MCLab.

The dynamic model of the vessel in terms of relative velocities (see Chapter 2) is:

$$\boldsymbol{M}\dot{\boldsymbol{\nu}}_r + \boldsymbol{C}(\boldsymbol{\nu}_r)\boldsymbol{\nu}_r + \boldsymbol{D}\boldsymbol{\nu}_r = \boldsymbol{B}\boldsymbol{f}, \tag{B.10}$$

where $\boldsymbol{\nu}_r = [u_r, v_r, r]^T$, $\boldsymbol{f} = [T_u, T_v, T_r]^T$ and:

$$\boldsymbol{M} = \begin{bmatrix} 25.8 & 0 & 0 \\ 0 & 33.8 & -11.748 \\ 0 & -11.748 & 6.813 \end{bmatrix}, \tag{B.11}$$

$$\boldsymbol{C}(\boldsymbol{\nu}_r) = \begin{bmatrix} 0 & 0 & -33.8v_r + 11.748r \\ 0 & 0 & 25.8u_r \\ 33.8v_r - 11.748r & -25.8u_r & 0 \end{bmatrix}, \tag{B.12}$$

$$\boldsymbol{D} = \begin{bmatrix} 2.0 & 0 & 0 \\ 0 & 7.0 & -2.5425 \\ 0 & -2.5425 & 1.422 \end{bmatrix}. \tag{B.13}$$

The control inputs are the surge thrust T_u, the sway thrust T_v and the yaw moment T_r. The model (B.10) is defined along the centerline of the vessel, in the point laying 25 [cm] aft of the bow, or 33.5 [cm] fore of the center of gravity [23]. It is assumed that in this point the configuration of the actuators is such that the matrix $\boldsymbol{B}$ is:

$$\boldsymbol{B} = \begin{bmatrix} 1 & 0 & 0 \\ 0 & 1 & -1.7244 \\ 0 & -0.3476 & 1 \end{bmatrix}, \tag{B.14}$$

and hence $\boldsymbol{M}^{-1}\boldsymbol{B}\boldsymbol{f} = [k_1 T_u, k_2 T_v, k_3 T_r]^T$ for some constant coefficients k_1, k_2, k_3.

B.2.1. Purpose of the Cybership II Simulation Model

The presented model is a low-speed maneuvering model for speeds lower than 2 [m/s]

B.3. The LAUV Simulation Model

In this dissertation the 5-DOF simulation model of the LAUV underwater vehicle from [40] and [85] is used. The LAUV is a torpedo-shaped light autonomous underwater vehicle developed and designed by the Laboratório de Sistemas e Tecnologia Subaquática (LSTS) from the University of Porto in cooperation with OceanScan-MST Lda.

Figure B.3.: The LAUV vehicle during underwater operations.

The dynamic model of the AUV in terms of relative velocities (see Chapter 2) is:

$$\boldsymbol{M}\dot{\boldsymbol{\nu}}_r + \boldsymbol{C}(\boldsymbol{\nu}_r)\boldsymbol{\nu}_r + \boldsymbol{D}\boldsymbol{\nu}_r + \boldsymbol{g}(\boldsymbol{\eta}) = \boldsymbol{B}\boldsymbol{f}, \tag{B.15}$$

where $\boldsymbol{\nu}_r = [u_r, v_r, w_r, q, r]^T$, $\boldsymbol{\eta} = [x, y, z, \theta, \psi]^T$, $\boldsymbol{f} = [T_u, \delta_D, \delta_S]^T$ and:

$$\boldsymbol{M} = \begin{bmatrix} 19.0 & 0 & 0 & 0 & 0 \\ 0 & 34.0 & 0 & 0 & 0 \\ 0 & 0 & 34.0 & 0 & 0 \\ 0 & 0 & 0 & 2.1 & 0 \\ 0 & 0 & 0 & 0 & 2.1 \end{bmatrix}, \tag{B.16}$$

$$\boldsymbol{D} = \begin{bmatrix} 2.4 & 0 & 0 & 0 & 0 \\ 0 & 23.0 & 0 & 0 & -11.5 \\ 0 & 0 & 23.0 & 11.5 & 0 \\ 0 & 0 & -3.1 & 9.7 & 0 \\ 0 & 3.1 & 0 & 0 & 9.7 \end{bmatrix}, \tag{B.17}$$

$$\boldsymbol{g}(\boldsymbol{\eta}) = \begin{bmatrix} 0 & 0 & 0 & BG_z W \sin(\theta) & 0 \end{bmatrix}^T, \tag{B.18}$$

$$\boldsymbol{B} = \begin{bmatrix} 1.0 & 0 & 0 \\ 0 & 0 & -39.8783 \\ 0 & 39.8783 & 0 \\ 0 & 18.1446 & 0 \\ 0 & 0 & 18.1446 \end{bmatrix}. \tag{B.19}$$

Here, $BG_z = 0.017$ [m] is the vertical distance between the center of gravity (CG) and the center of buoyancy (CB). The term $W = mg$ is the weight of the vehicle in air, where $m = 18$ [kg] is the mass and $g = 9.81$ [m/s^2] is the acceleration of gravity. The control inputs are the propeller thrust T_u, the yaw rudder angle δ_D and the pitch rudder angle δ_S.

B.3.1. Purpose of the LAUV Simulation Model

The presented model is a maneuvering model for speeds lower than 2 [m/s].

B.4. The HUGIN AUV Simulation Model

In this dissertation the 5-DOF simulation model of the HUGIN AUV is used. The HUGIN is a torpedo-shaped survey AUV developed and designed by the Norwegian Defense Research Establishment (FFI) and Kongsberg Maritime AS.

Figure B.4.: The HUGIN AUV. Courtesy of Kongsberg Maritime AS.

The dynamic model of the AUV in terms of relative velocities (see Chapter 2) is:

$$\boldsymbol{M}\dot{\boldsymbol{\nu}}_r + \boldsymbol{C}(\boldsymbol{\nu}_r)\boldsymbol{\nu}_r + \boldsymbol{D}\boldsymbol{\nu}_r + \boldsymbol{g}(\boldsymbol{\eta}) = \boldsymbol{B}\boldsymbol{f}, \tag{B.20}$$

where $\boldsymbol{\nu}_r = [u_r, v_r, w_r, q, r]^T$, $\boldsymbol{\eta} = [x, y, z, \theta, \psi]^T$, $\boldsymbol{f} = [T_u, \delta_D, \delta_S]^T$ and:

$$\boldsymbol{M} = \begin{bmatrix} m_{11} & 0 & 0 & 0 & 0 \\ 0 & m_{22} & 0 & 0 & m_{25} \\ 0 & 0 & m_{33} & m_{34} & 0 \\ 0 & 0 & m_{34} & m_{44} & 0 \\ 0 & m_{25} & 0 & 0 & m_{55} \end{bmatrix}, \tag{B.21}$$

$$\boldsymbol{D} = \begin{bmatrix} d_{11} & 0 & 0 & 0 & 0 \\ 0 & d_{22} & 0 & 0 & d_{25} \\ 0 & 0 & d_{33} & d_{34} & 0 \\ 0 & 0 & d_{43} & d_{44} & 0 \\ 0 & d_{52} & 0 & 0 & d_{55} \end{bmatrix}, \tag{B.22}$$

$$\boldsymbol{g}(\boldsymbol{\eta}) = \begin{bmatrix} 0 & 0 & 0 & BG_z W \sin(\theta) & 0 \end{bmatrix}^T, \tag{B.23}$$

$$\boldsymbol{B} = \begin{bmatrix} 1 & 0 & 0 \\ 0 & 0 & Y_\delta \\ 0 & Z_\delta & 0 \\ 0 & M_\delta & 0 \\ 0 & 0 & N_\delta \end{bmatrix}. \tag{B.24}$$

Here, BG_z is the vertical distance between the center of gravity (CG) and the center of buoyancy (CB). The term $W = mg$ is the weight of the vehicle in air, where m is the mass and g is the acceleration of gravity. The control inputs are the propeller thrust T_u, the yaw rudder angle δ_D and the pitch rudder angle δ_S. The parameters of the HUGIN simulation model are confidential and cannot be given in this thesis.

The surge thrust T_u is generated by a propeller and is given by the following expression (see [116] and [52]):

$$T_u = T_{nn} n|n| - T_{un} u_r n, \tag{B.25}$$

where n is the angular speed of the propeller and $T_{nn} > 0$ and $T_{un} > 0$ are some coefficients given by the propeller characteristics.

B.4.1. Purpose of the HUGIN Simulation Model

The presented model is a maneuvering model for speeds lower than 2 [m/s].

Appendix C.

Semi-empirical functions for wind loads on ships

In Chapter 8 wind disturbances on surface vessels are taken into account where the semi-empirical functions from [15] are used to describe wind loads on a platform supply vessel. Following extensive wind tunnel tests, [15] presents the following parametrical wind load coefficients in surge (C_X), sway (C_Y) and yaw (C_N):

$$C_X(\gamma_e) = -CD_{l,A_F}(\gamma_e)\frac{\cos(\gamma_e)}{1-\frac{\delta}{2}\left(1-\frac{CD_l(\gamma_e)}{CD_t}\right)\sin^2(2\gamma_e)}, \tag{C.1}$$

$$C_Y(\gamma_e) = CD_t\frac{\cos(\gamma_e)}{1-\frac{\delta}{2}\left(1-\frac{CD_l(\gamma_e)}{CD_t}\right)\sin^2(2\gamma_e)}, \tag{C.2}$$

$$C_N(\gamma_e) = \left[\frac{s_L}{L_{OA}} - 0.18\,\pi\,\mathrm{trg}\left(\frac{\gamma_e}{\pi}+\frac{1}{2}\right)\right], \tag{C.3}$$

where:

$$\begin{aligned} CD_{l,A_F}(\gamma_e) &= \frac{CD_{l,A_F,bow}+CD_{l,A_F,stern}}{2} \\ &\quad + (CD_{l,A_F,bow}-CD_{l,A_F,stern})\,\mathrm{sqr}\left(\frac{\gamma_e}{\pi}-\frac{1}{2}\right), \end{aligned} \tag{C.4}$$

$$CD_l(\gamma_e) = \frac{A_F}{A_L}CD_{l,A_F}(\gamma_e), \tag{C.5}$$

and γ_e is the angle of attack of the wind with respect to the bow. The functions trg($\cdot$) and sqr($\cdot$) are the standard triangular and square odd wave functions limited between $[-1,1]$ with period 2. The parameters to calculate (C.1-C.3) for the case of platform supply vessels are taken from [15] and are given in Table C.1.

If needed, the functions $\pi\ \mathrm{trg}\left(\frac{\gamma_e}{\pi}+\frac{1}{2}\right)$ and $\mathrm{sqr}(\frac{\gamma_e}{\pi}-\frac{1}{2})$ can be smoothened with the following differentiable smooth functions:

$$\mathrm{trg}_{\pi,smooth} = \cos^{-1}\Big((1-\eta)\cos(\gamma_e)\Big) - \frac{\pi}{2}, \tag{C.6}$$

$$\mathrm{sqr}_{smooth} = \frac{1}{\pi}\tan^{-1}\left(\frac{\cos(\gamma_e)}{\eta}\right), \tag{C.7}$$

where η is an approximation parameter and can be set for instance to 0.01.

symbol	value
A_F	137.50 [m^2]
A_L	336.80 [m^2]
s_L	7.95 [m]
L_{OA}	62.00 [m]
CD_t	0.90
$CD_{l,A_F,bow}$	0.55
$CD_{l,A_F,stern}$	0.80
δ	0.55

Table C.1.: Parameters from [15] used to calculate (C.1-C.3) for supply vessels.

Bibliography

[1] A. P. Aguiar and J. P. Hespanha. Trajectory-tracking and path-following of underactuated autonomous vehicles with parametric modeling uncertainty. *IEEE Transactions on Automatic Control*, 52(8):1362–1379, 2007.

[2] A. P. Aguiar and A. M. Pascoal. Modeling and control of an autonomous underwater shuttle for the transport of benthic laboratories. In *Proc. of MTS/IEEE Conference OCEANS '97*, pages 888–895, 1997.

[3] M. Aicardi, G. Casalino, A. Bicchi, and A. Balestrino. Closed loop steering of unicycle like vehicles via lyapunov techniques. *IEEE Robotics & Automation Magazine*, 2(1):27–35, 1995.

[4] M. Aicardi, G. Casalino, and G. Indiveri. On a closed loop time invariant position control solution for an underactuated 3d underwater vehicle: implementation, stability and robustness considerations. In *Proc. of IEEE International Symposium on Underwater Technology.*, pages 485–490, 2000.

[5] M. Aicardi, G. Casalino, and G. Indiveri. Closed loop time invariant control of 3D underactuated underwater vehicles. In *Proc. of IEEE International Conference on Robotics and Automation*, pages 903–908, 2001.

[6] G. Antonelli. On the use of adaptive/integral actions for six-degrees-of-freedom control of autonomous underwater vehicles. *IEEE Journal of Oceanic Engineering*, 32(2):300–312, April 2007.

[7] G. Antonelli, F. Caccavale, S. Chiaverini, and G. Fusco. A novel adaptive control law for underwater vehicles. *IEEE Transactions on Control Systems Technology*, 11(2):221–232, March 2003.

[8] F. Arrichiello, G. Antonelli, A. P. Aguiar, and A. M. Pascoal. An observability metric for underwater vehicle localization using range measurements. *Sensors*, 13(12):16191–16215, 2013.

[9] H. Ashrafiuon, K. R. Muske, and L. C. McNinch. Review of nonlinear tracking and setpoint control approaches for autonomous underactuated marine vehicles. In *Proc. of American Control Conference*, pages 5203–5211, 2010.

[10] V. Bakarić, Z. Vukić, and R. Antonić. Improved basic planar algorithm of vehicle guidance through waypoints by the line of sight. In *Proc. of the First International Symposium on Control, Communications and Signal Processing*, pages 541–544, 2004.

[11] P. Batista, C. Silvestre, and P. Oliveira. Optimal position and velocity navigation filters for autonomous vehicles. *Automatica*, 46(4):767–774, 2010.

[12] M. Bibuli, G. Bruzzone, M. Caccia, G. Indiveri, and A. A. Zizzari. Line following guidance control: Application to the charlie unmanned surface vehicle. In *Proc. of IEEE/RSJ International Conference on Intelligent Robots and Systems*, pages 3641–3646, 2008.

[13] M. Bibuli, M. Caccia, L. Lapierre, and G. Bruzzone. Guidance of unmanned surface vehicles: Experiments in vehicle following. *IEEE Robotics & Automation Magazine*, 19(3):92–102, 2012.

[14] M. Bibuli, W. Caharija, K. Y. Pettersen, G. Bruzzone, M. Caccia, and E. Zereik. ILOS guidance - experiments and tuning. In *Proc. of the 19th IFAC World Congress*, pages 4209–4214, 2014.

[15] W. Blendermann. Parameter identification of wind loads on ships. *Journal of Wind Engineering and Industrial Aerodynamics*, 51(3):339–351, 1994.

[16] M. Breivik. *Topics in Guided Motion Control of Marine Vehicles.* PhD thesis, NTNU, Trondheim, Norway, 2010. NTNU thesis 2010: 63.

[17] M. Breivik and T. I. Fossen. Path following of straight lines and circles for marine surface vessels. In *Proc. of the 6th IFAC Conference on Control Applications in Marine Systems*, pages 65–70, 2004.

[18] M. Breivik and T. I. Fossen. Principles of guidance-based path following in 2D and 3D. In *Proc. of the 44th IEEE Conference on Decision and Control*, pages 627 – 634, 2005.

[19] M. Breivik and T. I. Fossen. Guidance laws for planar motion control. In *Proc. of the 47th IEEE Conference on Decision and Control*, pages 570–577, 2008.

[20] M. Breivik and T. I. Fossen. *Guidance Laws for Autonomous Underwater Vehicles*, chapter 4, pages 51–76. A. V. Inzartsev, IN-TECH Education and Publishing, 2009.

[21] M. Breivik and T.I. Fossen. Guidance-based path following for autonomous underwater vehicles. In *Proc. of MTS/IEEE Conference OCEANS '05*, pages 2807–2814, 2005.

[22] G. Bruzzone, M. Bibuli, M. Caccia, and E. Zereik. Cooperative robotic maneuvers for emergency ship towing operations. In *Proc. of MTS/IEEE Conference OCEANS '13 - Bergen*, pages 1–7, 2013.

[23] E. Børhaug. *Nonlinear Control and Synchronization of Mechanical Systems*. PhD thesis, NTNU, Trondheim, Norway, 2008. NTNU thesis 2008: 298.

[24] E. Børhaug, A. Pavlov, E. Panteley, and K. Y. Pettersen. Straight line path following for formations of underactuated marine surface vessels. *IEEE Transactions on Control Systems Technology*, 19(3):493–506, May 2011.

[25] E. Børhaug, A. Pavlov, and K. Y. Pettersen. Straight line path following for formations of underactuated underwater vehicles. In *Proc. of the 46th IEEE Conference on Decision and Control*, pages 2905–2912, 2007.

[26] E. Børhaug, A. Pavlov, and K. Y. Pettersen. Integral LOS control for path following of underactuated marine surface vessels in the presence of constant ocean currents. In *Proc. of the 47th IEEE Conference on Decision and Control*, pages 4984–4991, 2008.

[27] E. Børhaug and K. Y. Pettersen. LOS path following for underactuated underwater vehicle. In *Proc. of the 7th IFAC Conference on Manoeuvring and Control of Marine Craft*, 2006.

[28] W. Caharija, M. Candeloro, K. Y. Pettersen, and A. J. Sørensen. Relative velocity control and integral LOS for path following of underactuated surface vessels. In *Proc. of the 9th IFAC Conference on Manoeuvring and Control of Marine Craft*, pages 380–385, 2012.

[29] W. Caharija, K. Y. Pettersen, M. Bibuli, E. Zereik, J. T. Gravdahl, A. J. Sørensen, and G. Bruzzone. Integral los for path following control of underactuated surface vessels: Theory, simulations and experiments. *IEEE Transactions on Control System Technology*, 2014. submitted.

[30] W. Caharija, K. Y. Pettersen, P. Calado, J. Braga, M. Milovanović, and J. B. Sousa. Path following control of underactuated AUVs in the presence of ocean currents: Theory, simulations and experiments. *IEEE Transactions on Control System Technology*, 2014. to be submitted.

[31] W. Caharija, K. Y. Pettersen, and J. T. Gravdahl. Path following of marine surface vessels with saturated transverse actuators. In *Proc. of American Control Conference*, pages 546–553, 2013.

[32] W. Caharija, K. Y. Pettersen, and J. T. Gravdahl. Path following of underactuated surface vessels in presence of uknown constant environmental forces: Preliminary results. In *Proc. of the 9th IFAC Conference on Control Applications in Marine Systems*, pages 85–90, 2013.

[33] W. Caharija, K. Y. Pettersen, J. T. Gravdahl, and E. Børhaug. Integral LOS guidance for horizontal path following of underactuated autonomous underwater vehicles in the presence of vertical ocean currents. In *Proc. of American Control Conference*, pages 5427–5434, 2012.

[34] W. Caharija, K. Y. Pettersen, J. T. Gravdahl, and E. Børhaug. Path following of underactuated autonomous underwater vehicles in the presence of ocean currents. In *Proc. of the 51st IEEE Conference on Decision and Control*, pages 528–535, 2012.

[35] W. Caharija, K. Y. Pettersen, J. T. Gravdahl, and A. J. Sørensen. Topics on current compensation for path following applications of underactuated underwater vehicles. In *Proc. of the 3rd IFAC Workshop on Navigation, Guidance and Control of Underwater Vehicles*, pages 184–191, 2012.

[36] W. Caharija, K. Y. Pettersen, A. J. Sørensen, M. Candeloro, and J. T. Gravdahl. Relative velocity control and integral LOS for path following of ASVs: Merging intuition with theory. *Proc. of the Institution of Mechanical Engineers, Part M: Journal of Engineering for the Maritime Environment*, 228(2):180–191, 2014. DOI:10.1177/1475090213512293.

[37] A. Chaillet and A. Loría. Necessary and sufficient conditions for uniform semiglobal practical asymptotic stability: Application to cascaded systems. *Automatica*, 42(11):1899–1906, 2006.

[38] A. Chaillet and A. Loría. Uniform semiglobal practical asymptotic stability for non-autonomous cascaded systems and applications. *Automatica*, 44(2):337–347, 2008.

[39] J. E. Da Silva and J. B. Sousa. A dynamic programming approach for the motion control of autonomous vehicles. In *Proc. of the 49th IEEE Conference on Decision and Control*, pages 6660–6665, 2010.

[40] J. E. Da Silva, B. Terra, R. Martins, and J. B. Sousa. Modeling and simulation of the LAUV autonomous underwater vehicle. In *Proc. of the 13th IEEE IFAC International Conference on Methods and Models in Automation and Robotics*, 2007.

[41] K. D. Do, Z. P. Jiang, and J. Pan. Universal controllers for stabilization and tracking of underactuated ships. *Systems & Control Letters*, 47(4):299 – 317, 2002.

[42] K. D. Do and J. Pan. Global tracking control of underactuated ships with off-diagonal terms. In *Proc. of the 42nd IEEE Conference on Decision and Control*, volume 2, pages 1250–1255, 2003.

[43] K. D. Do, J. Pan, and Z. P. Jiang. Robust and adaptive path following for underactuated autonomous underwater vehicles. *Ocean Engineering*, 31:1967–1997, 2004.

[44] K.D. Do, Z. P Jiang, and J. Pan. Underactuated ship global tracking under relaxed conditions. *IEEE Transactions on Automatic Control*, 47(9):1529–1536, 2002.

[45] K.D. Do and J. Pan. Underactuated ships follow smooth paths with integral actions and without velocity measurements for feedback: theory and experiments. *IEEE Transactions on Control Systems Technology*, 14(2):308–322, 2006.

[46] P. Encarnação and A. M. Pascoal. 3D path following for autonomous underwater vehicle. In *Proc. of the 39th IEEE Conference on Decision and Control*, pages 2977–2982, 2000.

[47] P. Encarnação and A. M. Pascoal. Combined trajectory tracking and path following: an application to the coordinated control of autonomous marine craft. In *Proc. of the 40th IEEE Conference on Decision and Control*, pages 964–969, 2001.

[48] P. Encarnação, A. M. Pascoal, and M. Arcak. Path following for autonomous marine craft. In *Proc. of the 5th IFAC Conference on Manoeuvring and Control of*

Marine Craft, pages 117–122, 2000.

[49] P. Encarnação, A. M. Pascoal, and M. Arcak. Path following for marine vehicles in the presence of unknown currents. In *Proc. of the 6th IFAC International Symposium on Robot Control*, pages 469–474, 2000.

[50] O. M. Faltinsen. *Sea Loads on Ships and Offshore Structures.* Cambridge University Press, 1990.

[51] S. Fan and C. A. Woolsey. Underwater vehicle control and estimation in nonuniform currents. In *Proc. of American Control Conference*, pages 1400–1405, 2013.

[52] T. I. Fossen. *Handbook of Marine Craft Hydrodynamics and Motion Control.* John Wiley & Sons, Inc., Hoboken, NJ, 2011.

[53] T. I. Fossen and S. P. Berge. Nonlinear vectorial backstepping design for global exponential tracking of marine vessels in the presence of actuator dynamics. In *Proc. of the 36th IEEE Conference on Decision and Control*, pages 4237–4242, 1997.

[54] T. I. Fossen, M. Breivik, and R. Skjetne. Line-of-Sight path following of underactuated marine craft. In *Proc. of the 6th IFAC Conference on Manoeuvring and Control of Marine Craft*, pages 244–249, 2003.

[55] T. I. Fossen, A. Loría, and A. R. Teel. A theorem for ugas and ules of (passive) nonautonomous systems: robust control of mechanical systems and ships. *International Journal of Robust and Nonlinear Control*, 11(2):95–108, 2001.

[56] T. I. Fossen, S. I. Sagatun, and A. J. Sørensen. Identification of dynamically positioned ships. In *Proc. of the 3rd IFAC Workshop on Control Applications in Marine Systems*, pages 362–369, 1995.

[57] T. I. Fossen and J. P. Strand. Nonlinear passive weather optimal positioning control (WOPC) system for ships and rigs: experimental results. *Automatica*, 37(5):701–715, 2001.

[58] E. Fredriksen and K. Y. Pettersen. Global κ-exponential way-point manoeuvering of ships. In *Proc. of the 43rd IEEE Conference on Decision and Control*, pages 5360–5367, 2004.

[59] E. Fredriksen and K. Y. Pettersen. Global κ-exponential way-point maneuvering of ships: theory and experiments. *Automatica*, 42(4):677–687, 2006.

[60] R. Freeman and L. Praly. Integrator backstepping for rounded controls and control rates. *IEEE Transactions on Automatic Control*, 43(2):258–262, 1998.

[61] J. Godhavn. Nonlinear tracking of underactuated surface vessels. In *Proc. of the 35th IEEE Conference on Decision and Control*, pages 975–980, 1996.

[62] H. Goldstein, C. Poole, and J. Safko. *Classical Mechanics*. Pearson Education International inc., Upper Saddle River, NJ, USA, 3rd edition, 2002.

[63] A. Gruszka, M. Malisoff, and F. Mazenc. On tracking for the PVTOL model with bounded feedbacks. In *Proc. of American Control Conference*, pages 1428–1433, 2011.

[64] E. I. Grøtli. *Robust Stability and Control of Spacecraft Formations*. PhD thesis, NTNU, Trondheim, Norway, 2010. NTNU thesis 2010: 1.

[65] E. I. Grøtli, A. Chaillet, and J. T. Gravdahl. Output control of spacecraft in leader follower formation. In *Proc. of the 47th IEEE Conference on Decision and Control*, pages 1030–1035, 2008.

[66] A. J. Healey and D. Lienard. Multivariable sliding mode control for autonomous diving and steering of unmanned underwater vehicles. *IEEE Journal of Oceanic Engineering*, 18(3):327–339, July 1993.

[67] Ø. Hegrenæs. *Autonomous Navigation for Underwater Vehicles*. PhD thesis, NTNU, Trondheim, Norway, 2010. NTNU thesis 2010: 101.

[68] Ø. Hegrenæs, O. Hallingstad, and B. Jalving. Comparison of mathematical models for the HUGIN 4500 AUV based on experimental data. In *Proc. of IEEE International Symposium on Underwater Technology and Workshop on Scientific Use of Submarine Cables and Related Technologies*, pages 558–567, 2007.

[69] E. Y. Hong, T. K. Meng, and M. Chitre. Online system identification of the dynamics of an autonomous underwater vehicle. In *Proc. of IEEE International Symposium on Underwater Technology*, pages 1–10, 2013.

[70] I.-A. F. Ihle, M. Arcak, and T. I. Fossen. Passivity-based designs for synchronized path-following. *Automatica*, 43(9):1508–1518, 2007.

[71] G. Indiveri. Kinematic time-invariant control of a 2D nonholonomic vehicle. In *Proc. of the 38th IEEE Conference on Decision and Control*, pages 2112–2117, 1999.

[72] G. Indiveri, M. Aicardi, and G. Casalino. Robust global stabilization of an underactuated marine vehicle on a linear course by smooth time-invariant feedback. In *Proc. of the 39th IEEE Conference on Decision and Control*, pages 2156–2161, 2000.

[73] G. Indiveri, S. Creti, and A. A. Zizzari. A proof of concept for the guidance of 3D underactuated vehicles subject to constant unknow disturbances. In *Proc. of the 9th IFAC Conference on Manoeuvring and Control of Marine Craft*, pages 307–312, 2012.

[74] G. Indiveri, M. Pino, M. Aicardi, and G. Casalino. Nonlinear time-invariant feedback control of an underactuated marine vehicle along a straight course. In *Proc. of the 5th IFAC Conference on Manoeuvring and Control of Marine Craft*, pages 221–226, 2000.

[75] G. Indiveri and A. A. Zizzari. Kinematics motion control of an underactuated vehicle: A 3D solution with bounded control effort. In *Proc. of the 2nd IFAC Workshop on Navigation, Guidance and Control of Underwater Vehicles*, pages 73–78, 2008.

[76] R. M. Isherwood. Wind resistance of merchant ships. *Transcripts of the Royal Institution of Naval Architects*, 115:327–338, 1972.

[77] M. V. Jakuba. *Stochastic mapping for chemical plume source localization with application to autonomous hydrothermal vent discovery.* PhD thesis, MIT and WHOI, 2007.

[78] T. A. Johansen and T. I. Fossen. Control allocation - a survey. *Automatica*, 49(5):1087–1103, 2013.

[79] J. Jouffroy, Q. Zhou, and O. Zielinski. Towards selective tidal-stream transport for lagrangian profilers. In *Proc. of MTS/IEEE Conference OCEANS '11*, pages 1–6, 2011.

[80] B. H. Jun, J. Y. Park, F. Y. Lee, P. M. Lee, C. M. Lee, K. Kim, Y. K. Lim, and J. H. Oh. Development of the AUV 'ISiMI' and a free running test in an ocean engineering basin. *Ocean Engineering*, 36(1):2–14, 2009.

[81] I. Kaminer, A. M. Pascoal, and O. Yakimenko. Nonlinear path following control of fully actuated marine vehicles with parameter uncertainty. In *Proc. of the 16th IFAC World Congress*, 2005.

[82] H. Khalil. *Nonlinear Systems.* Pearson Education International inc., Upper Saddle River, NJ, USA, 3rd edition, 2000.

[83] Ø. K. Kjerstad and M. Breivik. Weather optimal positioning control for marine surface vessels. In *Proc. of the 8th IFAC Conference on Control Applications in Marine Systems*, 2010.

[84] M. Kurowski and B. Lampe. AGaPaS: A new approach for search-and-rescue-operations at sea. *Proc. of the Institution of Mechanical Engineers, Part M: Journal of Engineering for the Maritime Environment*, 2014. DOI:10.1177/1475090213504392 accepted.

[85] Laboratório de Sistemas e Tecnologia Subaquática (LSTS). DUNE: Unified navigation environment. http://lsts.fe.up.pt/software/dune, April 2014. University of Porto.

[86] L. Lapierre and B. Jouvencel. Robust nonlinear path-following control of an AUV. *IEEE Journal of Oceanic Engineering*, 33(2):89–102, April 2008.

[87] L. Lapierre, D. Soetanto, and A. M. Pascoal. Nonlinear path following with applications to the control of autonomous underwater vehicles. In *Proc. of the 42nd IEEE Conference on Decision and Control*, pages 1256–1261, 2003.

[88] E. Lefeber. *Tracking Control of Nonlinear Mechanical Systems.* PhD thesis, University of Twente, Enschede, The Netherlands, 2000.

[89] E. Lefeber, K. Y. Pettersen, and H. Nijmeijer. Tracking control of an underactuated ship. *IEEE Transactions on Control Systems Technology*, 11(1):52–61, 2003.

[90] A. M. Lekkas and T. I. Fossen. A time-varying lookahead distance guidance law for path following. In *Proc. of the 9th IFAC Conference on Manoeuvring and Control of Marine Craft*, pages 398–403, 2012.

[91] A. M. Lekkas and T. I. Fossen. Integral LOS path following for curved paths based on a monotone cubic hermite spline parametrization. *IEEE Transactions on Control Systems Technology*, 2014. DOI: 10.1109/TCST.2014.2306774 accepted.

[92] Z. Li, J. Sun, and S. Oh. Design, analysis and experimental validation of a robust nonlinear path following controller for marine surface vessels. *Automatica*, 45(7):1649–1658, 2009.

[93] K.-P. Lindegaard. *Acceleration Feedback in Dynamic Positioning.* PhD thesis, NTNU, Trondheim, Norway, 2003. NTNU thesis 2003: 74.

[94] A. Loría and E. Panteley. Cascaded nonlinear time-varying systems: Analysis and design. In F. Lamnabhi-Lagarrigue, A. Loría, and E. Panteley, editors, *Advanced Topics in Control Systems Theory*, volume 311 of *Lecture Notes in Control and Information Science*, chapter 2, pages 23–64. Springer London, 2005.

[95] Kongsberg Maritime. Kogsberg K-Pos DP dynamic positioning system. Technical Report 301093/B, 2006.

[96] F. Mazenc and S. Bowong. Backstepping with bounded feedbacks for time-varying systems. In *Proc. of the 44th IEEE Conference on Decision and Control*, pages 4560–4565, 2005.

[97] F. Mazenc and A. Iggidr. Backstepping with bounded feedbacks. *Systems & Control Letters*, 51(3-4):235–245, 2004.

[98] A. Micaelli and C. Samson. Trajectory tracking for unicycle-type and two-steering-wheels mobile robots. Technical Report 2097, Institut National De Recherche En Informatique Et En Automatique, Sophia Antipolis, France, 1993.

[99] M. Morgado, P. Batista, P. Oliveira, and C. Silvestre. Position USBL/DVL sensor-based navigation filter in the presence of unknown ocean currents. *Automatica*, 47(12):2604–2614, 2011.

[100] D. R. Nelson, D. B. Barber, T. W. McLain, and R. W. Beard. Vector field path following for miniature air vehicles. *IEEE Transactions on Robotics*, 23(3):519–529, 2007.

[101] S. G. Nelson. AKPO: The subsea production system. In *Proc. of Offshore Technology Conference*, 2010.

[102] Ø. Netland and A. Skavhaug. Two pilot experiments on the feasibility of telerobotic inspection of offshore wind turbines. In *Proc. of the 2nd Mediterranean Conference on Embedded Computing*, pages 46–49, 2013.

[103] OCIMF. *Prediction of Wind and Current Loads on VLCCs.* Oil Companies International Marine Forum, London, UK, 1977.

[104] E. Panteley, E. Lefeber, A. Loría, and H. Nijmeijer. Exponential tracking control of a mobile car using a cascaded approach. In *Proc. of IFAC Workshop on Motion*

Control, pages 221–226, 1998.

[105] E. Panteley and A. Loría. On global uniform asymptotic stability of nonlinear time-varying systems in cascade. *Systems and Control Letters*, 33(2):131–138, 1998.

[106] E. Panteley and A. Loría. Growth rate conditions for uniform asymptotic stability of cascaded time-varying systems. *Automatica*, 37(3):453–460, 2001.

[107] F. A. Papoulias. Bifurcation analysis of line of sight vehicle guidance using sliding modes. *International Journal of Bifurcation and Chaos*, 1(4):849–865, 1991.

[108] L. Paull, S. Saeedi, M. Seto, and H. Li. AUV navigation and localization: A review. *IEEE Journal of Oceanic Engineering*, 39(1):131–149, 2014.

[109] T. Perez and T. I. Fossen. A Matlab Toolbox for Parametric Identification of Radiation-Force Models of Ships and Offshore Structures. *Modeling, Identification and Control*, 30(1):1–15, 2009.

[110] K. Y. Pettersen and E. Lefeber. Way-point tracking control of ships. In *Proc. of the 40th IEEE Conference on Decision and Control*, pages 940–945, 2001.

[111] K. Y. Pettersen and H. Nijmeijer. Tracking control of an underactuated surface vessel. In *Proc. of the 37th IEEE Conference on Decision and Control*, pages 4561–4566, 1998.

[112] K. Y. Pettersen and H. Nijmeijer. Semi-global practical stabilization and disturbance adaptation for an underactuated ship. In *Proc. of the 39th IEEE Conference on Decision and Control*, pages 2144–2149, 2000.

[113] E. H. Peymani and T. I. Fossen. 2D path following for marine craft: A least-square approach. In *Proc. of the 9th IFAC Symposium on Nonlinear Control Systems*, pages 98–103, 2013.

[114] J. A. Pinkster and U. Nienhuis. Dynamic positioning of large tankers at sea. In *Proc. of the 18th Offshore Technology Conference*, 1986.

[115] J. Pinto, P. S. Dias, R. Gonçalves, E. Marques, J. B. Sousa, and F. Pereira. Neptus-A framework to support a mission life cycle. In *Proc. of the 7th IFAC Conference on Manoeuvring and Control of Marine Craft*, 2006.

[116] L. Pivano. *Thrust Estimation and Control of Marine Propellers in Four-Quadrant Operations.* PhD thesis, NTNU, Trondheim, Norway, 2008. NTNU thesis 2008: 20.

[117] J. E. Refsnes, A. J. Sørensen, and K. Y. Pettersen. Output feedback control of slender body underwater vehicles with current estimation. *International Journal of Control*, 80(7):1136–1150, 2007.

[118] K. Reichert, K. Hessner, J. C. Nieto Borge, and J. Dittmer. WaMoS II: A radar based wave and current monitoring system. In *Proc. of International Offshore and Polar Engineering Conference*, pages 139–143, 1999.

[119] D. Ribas, N. Palomeras, P. Ridao, M. Carreras, and A. Mallios. Girona 500 AUV: From survey to intervention. *IEEE/ASME Transactions on Mechatronics*, 17(1):46–53, 2012.

[120] G. Roussos and K.J. Kyriakopoulos. Towards constant velocity navigation and collision avoidance for autonomous nonholonomic aircraft-like vehicles. In *Proc. of the 48th IEEE Conference on Decision and Control.*, pages 5661–5666, 2009.

[121] C. Samson. Path following and time-varying feedback stabilization of a wheeled mobile robot. In *Proc. of the 2nd International Conference on Control, Automation, Robotics and Vision*, 1992.

[122] L. Sciavicco and B. Siciliano. *Modeling and Control of Robot Manipulators.* Springer London ltd., 2nd edition, 2002.

[123] R. Skjetne, T. I. Fossen, and P. V. Kokotović. Robust output maneuvering for a class of nonlinear systems. *Automatica*, 40(3):373–383, 2004.

[124] R. N. Smith, Y. Chao, P. P. Li, D. A. Caron, B. H. Jones, and G. S. Sukhatme. Planning and implementing trajectories for autonomous underwater vehicles to track evolving ocean processes based on predictions from a regional ocean model. *International Journal of Robotics Research*, 29(12):1475–1497, 2010.

[125] R. N. Smith, M. Schwager, S. L. Smith, B. H. Jones, D. Rus, and G. S. Sukhatme. Persistent ocean monitoring with underwater gliders: Adapting sampling resolution. *Journal of Field Robotics*, 28(5):714–741, 2011.

[126] A. Sousa, L. Madureira, J. Coelho, J. Pinto, J. Pereira, J. B. Sousa, and P. Dias. Lauv: The man-portable autonomous underwater vehicle. In *Proc. of the 3rd IFAC Workshop on Navigation, Guidance and Control of Underwater Vehicles*, pages 268–274, 2012.

[127] P. B. Sujit, S. Saripalli, and J. B. Sousa. Unmanned aerial vehicle path following: A survey and analysis of algorithms for fixed-wing unmanned aerial vehicles. *IEEE Control Systems Magazine*, 34(1):42–59, 2014.

[128] O. J. Sørdalen and C. C. De Wit. Exponential control law for a mobile robot: extension to path following. *IEEE Transactions on Robotics and Automation*, 9(6):837–842, 1993.

[129] O. J. Sørdalen and O. Egeland. Exponential stabilization of nonholonomic chained systems. *IEEE Transactions on Automatic Control*, 40(1):35–49, 1995.

[130] A. J. Sørensen. Structural issues in the design and operation of marine control systems. *Annual Reviews in Control*, 29(1):125–149, 2005.

[131] A. J. Sørensen, S. I. Sagatun, and T. I. Fossen. Design of a dynamic positioning system using model-based control. *Control Engineering Practice*, 4(3):359–368, 1996.

[132] A. J. Sørensen, Ø. N. Smogeli, and E. Pedersen. Simulation-based design and testing of dynamically positioned marine vessels. In *Proc. of International Conference on Marine Simulation and Ship Maneuverability*, 2003.

[133] A. R. Teel. Global stabilization and restricted tracking for multiple integrators with bounded controls. *Systems & Control Letters*, 18(3):165–171, 1992.

[134] J. Tsinias. Input to state stability properties of nonlinear systems and applications to bounded feedback stabilization using saturation. *ESAIM: Control, Optimisation and Calculus of Variations*, 2:57–87, 1997.

[135] E. Xargay, I. Kaminer, A. M. Pascoal, N. Hovakimyan, V. Dobrokhodov, V. Cichella, A. P. Aguiar, and R. Ghabcheloo. Time-critical cooperative path following of multiple unmanned aerial vehicles over time-varying networks. *Journal of Guidance, Control, and Dynamics*, 36(2):499–516, 2013.

[136] D. R. Yoerger, M. Jakuba, A. M. Bradley, and B. Bingham. Techniques for deep sea near bottom survey using an autonomous underwater vehicle. *The International Journal of Robotics Research*, 26(1):41–54, 2007.

[137] E. Zereik, M. Bibuli, G. Bruzzone, and M. Caccia. Jacobian task priority-based approach for path following of unmanned surface vehicles. In *Proc. of the 9th IFAC Conference on Control Applications in Marine Systems*, pages 114–119, 2013.